Aix-Marseille Université

THÈSE

presentée pour obtenir le titre de
DOCTEUR
d'Aix-Marseille Université

Ecole doctorale : Sciences pour l'ingénieur
Laboratoire : Mécanique, Modélisation et Procédés Propres (M2P2)
Unité de recherche : CERFACS
Spécialité : Mécanique des Fluides

par

Thomas ASTOUL

Towards improved lattice Boltzmann aeroacoustic simulations with non-uniform grids: application to landing gears noise prediction

---

soutenue le 17/06/2021 devant le jury composé de :

Pierre SAGAUT	Aix-Marseille Université	Directeur
Jean-François BOUSSUGE	CERFACS	Co-directeur
Jonas LATT	Université de Genève	Rapporteur
Damiano CASALINO	Université de Technologie de Delft	Rapporteur
Véronique FORTUNÉ	Université de Poitiers	Examinatrice
Stéphane MOREAU	Université de Sherbrooke	Examinateur
Éric MANOHA	ONERA	Examinateur
Alois SENGISSEN	Airbus Operations	Examinateur

Résumé

La prédiction de bruit de train d'atterrissage est un enjeu majeur pour un constructeur aéronautique, puisqu'il contribue à environ 40% du bruit total de l'aéronef lors des phases d'approche. Les essais en vol et ceux réalisés en souffleries anéchoïques ont permis de comprendre les mécanismes de génération du bruit, ainsi que de développer des dispositifs permettant de le réduire. Cependant, ces méthodes sont très longues et coûteuses à mettre en œuvre. Les méthodes de simulation numériques (CFD) émergent ainsi comme un complément essentiel à ces approches expérimentales. L'écoulement autour des trains d'atterrissage est complexe et fortement instationnaire, et le bruit généré est de nature large bande. De part ces caractéristiques, il est nécessaire de se tourner vers des méthodes instationnaires de modélisation de la turbulence, comme la simulation aux grandes échelles (LES), pour prédire ces sources acoustiques. La méthode de Boltzmann sur réseau (LBM) est une méthode numérique qui a récemment montré un fort potentiel pour ce type d'applications, grâce à sa précision, son faible temps de restitution et sa capacité à gérer des géométries complexes, et de ce fait, est adoptée pour cette thèse.

Les simulations aéroacoustiques nécessitent une grande précision puisque les fluctuations acoustiques, qui sont de plusieurs ordres de grandeur inférieures aux fluctuations aérodynamiques, doivent être correctement capturées et propagées. Néanmoins, les raccords de maillages non conformes utilisés en LBM ont l'inconvénient de générer de la vorticité et de l'acoustique parasites se propageant au coeur du fluide, au risque d'affecter les prédictions de bruit. L'objectif de cette thèse est de développer de nouveaux modèles de transition de maillage dans le code LBM "LaBS/proLB", et de les valider sur des cas d'application d'aéroacoustique de train d'atterrissage. Deux axes principaux sont étudiés pour remédier à ces phénomènes : 1/ Une étude du schéma numérique au cœur du fluide est effectuée, mettant en exergue la responsabilité des modes non-hydrodynamiques, spécifiques à la LBM, dans la génération de vorticité et d'une portion de l'acoustique parasite émise aux raccords de maillages. Après une étude approfondie de l'implication de ces modes, un modèle de collision approprié (H-RR) est selectionné pour filtrer ces derniers lors d'une simulation. La stabilité et la précision de ce modèle ainsi que d'autres schémas LBM dans des conditions typiques de simulations aéroacoustiques sont également investiguées. Cette étude met en évidence des problèmes de stabilité, ainsi qu'une précision discutable de nombreux schémas LBM avancés disponibles dans la littérature. 2/ Un algorithme de couplage direct entre deux grilles de résolution différentes est proposé. Cet algorithme permet de grandement améliorer la précision des raccords non-conformes et, de ce fait, de réduire l'émission acoustique parasite produite par la traversée de ces interfaces par des tourbillons composant les sillages.

Enfin, le train d'atterrissage LAGOON permet de valider ces ingrédients numériques. Une étude aérodynamique puis aéroacoustique *via* un couplage avec un code de propagation acoustique basé sur l'analogie de Ffowcs Williams and Hawkings (FW-H) sont menées. Les limites de cette analogie dans sa formulation solide, généralement utilisée pour prédire le bruit de train d'atterrissage, sont soulignées. Enfin, l'effet de composants additionnels de complexité croissante sur le bruit généré est étudié.

Abstract

Predicting landing gear noise is a major concern for an aircraft manufacturer, since it contributes to about 40% of the total aircraft noise during the approach phases. Flight tests and those carried out in anechoic wind tunnels have enabled the understanding of noise generation mechanisms, as well as the design of low noise devices. However, these methods are time consuming and costly to set up. The use of computational fluid dynamics (CFD) is thus emerging as an essential complement to these experimental approaches. The flow around landing gears is complex and highly unsteady, and the noise generated is broadband by nature. Given these characteristics, it is therefore necessary to use unsteady methods with high-fidelity turbulence modeling such as Large Eddy Simulation (LES), to predict these acoustic sources. The lattice Boltzmann method (LBM) is a numerical approach that has recently shown a strong potential for this type of application, thanks to its accuracy, its low restitution time and its ability to handle complex geometries. It is consequently adopted for this thesis.

Aeroacoustic simulations require a high level of accuracy since acoustic fluctuations, which are several orders of magnitude smaller than aerodynamic ones, must be properly captured and propagated. Nevertheless, the non-conforming grid interfaces used in LBM have the inconvenience of generating spurious vorticity and acoustics that propagate in the fluid core, which may affect the noise predictions. The PhD objective is to develop new grid coupling models in the "LaBS/ProLB" LBM solver, and to validate them in the context of landing gears aeroacoustics. Two main directions are addressed to overcome these phenomena: 1/ A study of the numerical scheme in the fluid core is performed, highlighting the involvement of non-hydrodynamic modes, specific to the LBM, in the generation of vorticity and of a portion of the spurious acoustics generated at mesh interfaces. After a thorough study of the implication of these modes, an appropriate collision model (H-RR) is chosen to filter them out during a simulation. The stability and accuracy of several LBM schemes including the H-RR one under typical aeroacoustic simulation conditions are also investigated. This study highlights stability issues, as well as questionable precision of many advanced LBM schemes available in the literature. 2/ A direct coupling algorithm between two grids of different resolution is proposed. This algorithm allows to greatly improve the accuracy of the non-conforming grid interfaces, and hence to reduce the spurious acoustic emission produced by the crossing of vortices composing the wakes.

Finally, the LAGOON landing gear allows for the validation of these numerical ingredients. An aerodynamic study and then an aeroacoustic one *via* a coupling with an acoustic propagation code based on the Ffowcs Williams and Hawkings analogy (FW-H) are conducted. The limitations of this analogy in its solid formulation, mostly used to predict landing gear noise, are exposed. Lastly, the effect of extra components of increasing complexity on the noise generated is investigated.

Remerciements

Je tiens tout d'abord à remercier les membres du jury pour avoir accepté d'évaluer mes travaux de thèse et pour les échanges constructifs qui en ont découlé. J'ai eu la chance d'avoir un jury de très grande qualité, avec Stéphane Moreau en tant que président, Véronique Fortuné et Eric Manoha en tant qu'examinateur, ainsi que Jonas Latt et Damiano Casalino à qui j'adresse une mention particulière pour avoir pris le temps d'une lecture approfondie de ce manuscrit.

Mes remerciements s'adressent ensuite naturellement à mes encadrants de thèse, Pierre et Jean-François pour m'avoir permis de réaliser cette thèse dans les meilleures conditions. Pierre, pour ta grande réactivité malgré la distance entre nos laboratoires, et pour tes conseils scientifiques avisés. Jeff, pour ces cinq années partagées au cours de trois contrats différents, merci pour ton optimisme, ta franchise, la confiance que tu m'as accordée qui m'a permis de vraiment m'épanouir, et pour le quotidien très agréable dans lequel on évolue notamment grâce à une super équipe LBM! Normalement, notre collaboration devrait encore durer quelques années, ce dont je me réjouis.

Cette thèse CIFRE a été financée par Airbus, et notamment le service des méthodes numériques pour l'acoustique IPA6 au sein duquel j'ai été vraiment bien accueilli, et où j'ai passé de très belles années. Vous êtes une super team: Jean-Yves, Nolwenn, Bast, Greg, JP, Fabien, Katrina, Aurel, les deux Sebs, Thomas, Johanna, Lloris, Yann et Vianney, avec un humour d'une finesse rarement égalée! Parmi cette équipe, il y a bien évidemment aussi Alois, à qui je dois (presque) tout! De l'initiation à la LBM, à la découverte, puis au goût pour la recherche: tu avais bien raison, une thèse, c'est un peu de souffrance, mais aussi beaucoup de plaisir et de liberté et j'ai vraiment apprécié ces années! Tu as toujours suivi mes travaux avec beaucoup d'attention et su apporter un regard critique et pertinent quels que soient les sujets, et je ne compte même pas les heures que tu as passées pour me simplifier la tâche et me sauver la mise au quotidien! Quoi qu'il en soit IPA6 et la LBM ça n'est pas fini, puisqu'une nouvelle aventure démarre ensemble très prochainement! (Ça y est Greg, tu vas enfin pouvoir te venger de la conversion de Muscat à la LBM, en me faisant goûter à ta charette! ;-)).

Je tiens également à remercier d'autres personnes avec qui j'ai eu la chance de pouvoir travailler: JC pour tout le support en début de thèse sur les trains d'atterrissage, Felix pour l'apport inestimable sur les transitions et l'aéroacoustique en LBM, Denis, Sébastien, Florian, Hatem, Jean-Pierre et Romain pour nos nombreux échanges et le support exceptionnel que vous m'avez toujours apporté.

Au CERFACS, je remercie chaleureusement l'équipe admin: Michèle, Chantal, Marie, Jade et Lydia pour votre bonne humeur qui égaye nos journées, et votre efficacité. La redoutable équipe CSG: Patrick, Isabelle, Gérard, Fabrice et Fred pour qui le mot problème ne subsiste jamais plus de 5 minutes. Je remercie également l'équipe CFD pour la su-

per ambiance au quotidien: Maxou notre grand chef pâtissier, Laulau_du_13 pour faire résonner la cité phocéenne dans les couloirs du CERFACS, JF pour les blagues, les barbeucs, et les fameuses éponges parties, Minh pour ses inestimables relectures, et ses soirées babyfoots mémorables, Paul pour ses stratégies cyclistes implacables, Thomas G pour les tennis du midi, Thomas L pour m'avoir léché la joue, Johan à qui rien ne résiste dans ProLB, PAM le stagiaire incontrôlable, Quentin qui a dû changer de bureau car ses cuisses ne passaient plus la porte, Valou qui a su faire briller l'EAC, Robin que l'on appelle maintenant R. InShape, Majd pour m'avoir montré la Voie, Felix, Dario, Melissa, Guillaume, Omar, Dominik, Alexia, Rémi, Matthieu...

Encore au CERFACS, je tiens à remercier la team LBM pour cette amitié profonde qui s'est créée. Ça a commencé par le cornerstone: l'irréductible Totoff, alias Little Bald Man qui m'a énormément apporté autour de ces innombrables cafés. L'homme teigne à qui j'ai proposé de taper des balles, avant de savoir qu'il ne jouait qu'en coups droits, et bien sûr qu'il courrait d'autant plus qu'il ne buvait de café... Et c'est peu dire! Nous avons ensuite la Wiscotte, alias La Baltringue Malade, dont une bonne partie de ce manuscrit est le fruit de nos discussions, qui se terminaient d'ailleurs souvent autour d'une salade de fruits alcoolisée, où il fallait toujours boire ça vite. Et puis... Perdu dans les couloirs, keyless, et fier dans sa tenue de Wife Beater, Flo alias Le Bobo Marseillais est arrivé, quel chamboulement! J'ai dû quelques fois user de mes stratagèmes les plus poussés (i.e call Mr Sengissen) pour parvenir à mes fins, mais finalement que de bons moments passés ensembles sous le soleil toulousain, toujours au beau fixe! Membre LBM par adoption, nous avons ensuite Dounnish, dont l'alias restera confidentiel. Un co-bureau exceptionnel, discret avant 18h, mais qui peut s'avérer l'être beaucoup moins par la suite, ce qui m'a vraiment aidé à décompresser! Entre les fous rires et les sessions lancers de parpaings (souvent liés d'ailleurs), mes abdos te remercient! Dernier membre par adoption, qui a préféré quitter la technique pour régaler ses copains avec de délicieuses bières (enfin un métier utile!), et dont je suis le plus fervent amateur: Bastibilly! Un guitariste/trompétiste créatif (et avec un vrai instrument...) qui saura animer des soirées houblonnées de folies!

À travers cette team LBM, j'ai eu l'incroyable chance de pouvoir rencontrer Adélie, membre du crew, qui m'a fait découvrir un plat encore plus gras que mon alimentation habituelle: le Welch! Octavie, une pilote hors paire, et d'une patience infinie, souvent dommage collatéral du lourd fardeau qu'elle se traîne... Et enfin Laura, membre éminent de la team grenouille: seule personne que je connaisse dont le plaisir de se rhabiller est supérieur à celui d'une bonne journée de kite, et jeune maman de la petite Emilia! On a passé de précieux moments ensembles, que je ne suis pas près d'oublier!

On en arrive à ma plus grande fierté au CERFACS, la team kite (KSC): Flo le saumon noir: une espèce méconnue en voie de disparition, Bastien la grenouille: un style vestimentaire comme aérien, Kelu le chevreuil au pied (nu) cassé (ohh ça suffit avec les noms d'animaux!), Adèle la reine du backloop à qui il manque juste un leash de planche et généralement la première moitié de la journée, le gros Romain: le plagiste, qu'éole n'arrive pas à soulever et son disciple Cricri, pour des raisons bien différentes mais qui mènent aussi à la bronzette. Dave au style d'Indiana Jones et meilleur adversaire au BP, Thomas Lr pour le combo gagnant escalade + kite, Lucien, première personne que je vais réussir à convertir à la wing, bien malgré moi! Arthur et Thomas, les petits nouveaux, squatteurs de piscine à leurs heures perdues et qui mettent une ambiance de folie. On a aussi les extérieurs, mais tout aussi importants: Louise et Éloi pour les soirées de grande ampleur (#C..DeLaGimone) et pour me forcer à ne pas regarder mes doigts de pieds, Yann pour les sessions déjantées et ton futur accueil en Martinique! Gilda pour représenter fièrement ton petit pays fort sympathique, que j'ai adoré découvrir, et finalement Axel, pour révéler la part démoniaque qui se cache dans la terrible famille Potiers. La liste est bien longue, comme le nombre de moments partagés avec chacun de vous, au travers d'un petit RTT kite, WE ou trip dans des destinations de rêves!

Je remercie également les AHYs: Tony, Valou, Yo, Margot, Galy, Kéké, Rémi, pour ces sardines de folies d'Arcachon à Marseille! C'est impeccable de voir perdurer ce petit groupe d'irrésistible MP, et de maintenir les valeurs qui nous sont chères: le BP et le B&Co! Sans oublier mon fillot Antoine, dont notre plaisir partagé de la table n'a pas cessé de nous rapprocher, ainsi que Robinson, pour l'art de la pétanque loisir.

Il reste évidemment les amis d'enfance: Thib, Matgal, Alitchita, Vincentello, Laulau, Chacha, Laurie et bien sûr les Juliens Garnier... On prend les mêmes et on recommence, même 15ans après! Entre les voyages, les week-ends, les soirées, ce sont toujours des moments inoubliables, remplis de fous rires et de culture, que ce soit avec Corse Matin (ne l'oublions pas!), ou avec l'ABCD des fleurs et champignons. Mention spéciale au Couz, qui était déjà un cador des fameux "modes non-hydrodynamiques" avant même la soutenance! J'ai eu l'impression de me sentir écouté lors de nos longues heures de discussions (passionnantes...), que l'on a pu avoir au cours des nombreux treks réalisés ensembles.

Pour finir, je tiens à remercier mes parents, ma sœur et tous les membres de ma famille pour leur soutien inconditionnel, sans oublier mon grand-père qui serait fier de voir un deuxième Dr Astoul dans la famille! Et je remercie également la famille de Mai, notamment pour avoir réalisé un excellent buffet post-soutenance. Mes derniers remerciements s'adressent à Mai, dont la présence m'a énormément aidé au cours de cette thèse, et pour le bonheur partagé au quotidien.

Nomenclature

Miscellaneous variables and constants

$\boldsymbol{S}$	Strain tensor ($= \frac{1}{2}(\partial u_\alpha/\partial x_\beta + \partial u_\beta/\partial x_\alpha)$)
$\boldsymbol{u}$	Fluid velocity
$\boldsymbol{x}$	Space variable
Δx, Δt	Discrete mesh size and time step
κ	Thermal conductivity
μ, ν	Dynamic and kinematic viscosities ($\nu = \mu/\rho$)
μ_b	Bulk viscosity
ρ	Fluid density
c_p	$\gamma r_g/(\gamma - 1)$, Heat capacity at constant pressure
c_v	$r_g/(\gamma - 1)$, Heat capacity at constant volume
c_0	Air sound speed
D	Number of spatial dimensions
E	Total energy ($= \boldsymbol{u}^2/2 + e$)
e	Internal energy ($= c_v T$)
I	Acoustic intensity
i	Complex number ($i^2 = -1$)
p	Thermodynamic (static) pressure
p'	Relative pressure ($p - p_\infty$)
r_g	Specific gas constant
T	(Static) temperature ($= e/c_v$)

Variables related to lattice Boltzmann

$\bar{\tau}$	Relaxation time after the variable change ($= \tau + \Delta t/2$)
$\boldsymbol{\mathcal{H}}^{(n)}$	n^{th}-order multi-dimensional Hermite polynomial
$\boldsymbol{\Pi}$	Stress tensor
$\boldsymbol{\tau}$	Shear stress tensor
$\boldsymbol{\xi_i}$, $\boldsymbol{e_i}$	Dimensional and dimensionless lattice velocities
$\boldsymbol{\xi}$	Velocity space variable
$\boldsymbol{a}^{(n)}$, $\boldsymbol{a}_{eq}^{(n)}$	n^{th}-order Hermite moments of f and f^{eq} ($= \int \boldsymbol{\mathcal{H}}^{(n)} f \, \mathrm{d}\boldsymbol{\xi}$ and $\int \boldsymbol{\mathcal{H}}^{(n)} f^{eq} \, \mathrm{d}\boldsymbol{\xi}$)
$\boldsymbol{Q}$	Heat flux tensor
$\boldsymbol{q}$	Heat flux ($= \int \frac{1}{2}(\boldsymbol{\xi} - \boldsymbol{u})(\boldsymbol{\xi} - \boldsymbol{u})^2 f \, \mathrm{d}\boldsymbol{\xi}$)
$\mathcal{L}$	Free mean path
R	Fine to coarse rescaling factor ($= \overline{\tau_f}/2\overline{\tau_c}$)
Ω	Collision operator
τ	Relaxation time of the collision model
θ	T/T_0, Normalized temperature
c_s	Lattice constant
f	Mass distribution function
$f^{(k)}$	Order of f in the Chapman-Enskog expansion
$f^{eq,N}$	Truncated equilibrium distribution function at order N in Hermite polynomials
f^{eq}	Maxwell-Boltzmann equilibrium distribution function
f_i, g_i	Discrete distribution functions before and after explicit change of variable
$g_i^{(1),S}, g_i^{(1),G}$	Second and higher projection order of the off-equilibrium function $g_i^{(1)}$
$g_i^{(1)}$	Discrete first-order off-equilibrium function after explicit variable change
N	Truncation order of the equilibrium distribution function (in Hermite polynomials)
Q	Quadrature order of the lattice of velocities

T_0	Reference temperature
V	Number of discrete velocities
$w(\boldsymbol{\xi})$	Weight function
w_i	Lattice weights

Variables related to linear stability analyses

$\boldsymbol{k}$	Wavenumber vector
$\hat{\rho}, \hat{\boldsymbol{u}}$	Complex amplitude of the density and velocity
$\hat{g}_i$	Complex amplitude of g_i'
$\mathcal{V}$	Vector of macroscopic variables
ω	Pulsation of the wave (complex for a temporal analysis)
$\overline{\rho}, \overline{\boldsymbol{u}}$	Mean flow density and velocity
$\overline{g_i}$	Mean flow distribution function
g_i'	Fluctuating distribution function
v_ϕ	Phase velocity
v_g	Group velocity

Dimensionless numbers

γ	Heat capacity ratio ($(D+2)/D$ for a monatomic gas, 1.4 for the air)
ϵ	$\mathcal{L}/l_0$, Knudsen number
Ma	$u/\sqrt{\gamma r_g T}$, Mach number
Pr	$\mu c_p/\kappa$, Prandtl number
Re	Reynolds number
St	Strouhal number

Abbreviations

Ac+	Downstream Acoustic mode
Ac-	Upstream Acoustic mode
BGK	Bhatnagar Gross and Krook
CAA	Computational AeroAcoustics
CFD	Computational Fluid Dynamics
DC	Direct Coupling algorithm
DDES	Delayed-Detached Eddy Simulation
DES	Detached Eddy Simulation
DNS	Direct Numerical Simulation
DRT	Dual Relaxation Time
DVBE	Discrete Velocity Boltzmann Equation
FP	Fractional Propagation
FW-H	Ffowcs-Williams and Hawkings
H-RR	Hybrid-Recursive Regularized
H-RR$_\psi$	Corrected Hybrid-Recursive Regularized
LB	Lattice Boltzmann
LBM	Lattice Boltzmann Method
LDV	Laser Doppler Velocimetry
LES	Large Eddy Simulation
LSA	Linear Stability Analysis
MRT	Multiple Relaxation Time
NS	Navier-Stokes
OASPL	Overall Sound Pressure Level
PIV	Particle Image Velocimetry
PR	Projected Regularization

PSD	Power Spectral Density
RANS	Reynolds Average Navier-Stokes
RD	Resolution Domain
RR	Recursive Regularized
RR_ψ	Corrected Recursive Regularized
S-A	Spalart Allmaras
SISM	Shear Improved Smagorinsky Model
STD	Standard grid coupling algorithm
WL	Wall Law
WMLES	Wall-Modeled Large Eddy Simulation
WRLES	Wall-Resolved Large Eddy Simulation
WTT	Wind Tunnel Test
ZDES	Zonal Detached Eddy Simulation

Contents

Chapter 1

Introduction

Contents

1.1 Industrial context: Airframe noise reduction

Noise pollution has a harmful effect on humans. According to the 1999 World Health Organization's estimate, nearly half of the European population lives in "areas that do not allow for acoustic comfort of residents" [1]. Aircraft noise is one of the major sources of urban noise annoyance, so it is important to characterize it in order to reduce its impact. Moreover, air traffic is (except for the recent tremendous decrease due to COVID-19 disease, which will hopefully be temporary) in strong growth since the beginning of civil aviation (*cf.* Fig. 1.1). Actually, traffic doubles every 15 years on average, regardless of previous world crises.

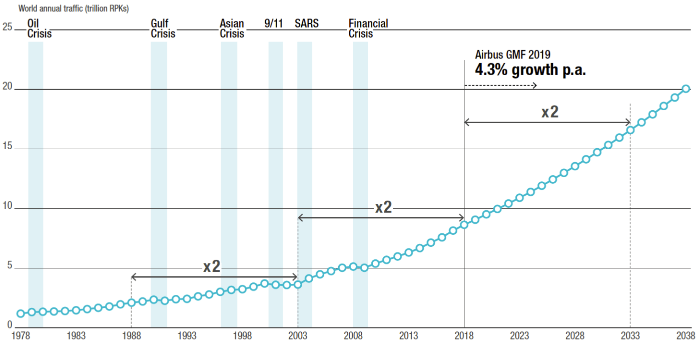

Figure 1.1 – *Evolution of annual air traffic and growth forecast from Airbus [2].*

There is a worldwide certification standard of all international airports, allowing for the homogenization of rules, especially regarding noise pollution. The latter is the ICAO [3] (for International Civil Aviation Organisation) certification and is guaranteed by each state. This standard evolves regularly and exerts significant pressure on aircraft manufacturers to reduce their noise emissions. There are also local regulations, specific to each airport or city. For example, since 1993, London airports have adopted a "Quota Count" system [4], followed by Madrid, Brussels and Aberdeen. This measure aims to rate aircraft according to the noise they emit during takeoff and landing phases, and thus to limit the number of operations accordingly, or even to stop the operations during nights (curfew) when a given threshold is exceeded. For instance, Fig. 1.2 shows the noise footprint of a Boeing 747-400 compared to a recent and less noisy Airbus A350 aircraft. It can be seen that the reduction of the noise footprint is considerable. Thus, noisy aircraft like the Boeing 747-400 can see their use reduced during the night in airports using this system.

Globally, cities want to reduce the current noise footprint of airplanes but considering the growing trend of global air traffic (*cf.* Fig. 1.1) at the same time. For an aeronautics manufacturer like Airbus, the financial stakes are therefore substantial, because the noise footprint is becoming a decisive commercial criterion for an airline company in its aircraft selection. Considerable noise reduction was accomplished in the early 1970s with the appearance of the first twin cycle bypass turbofan engines that reduced jet noise. In the

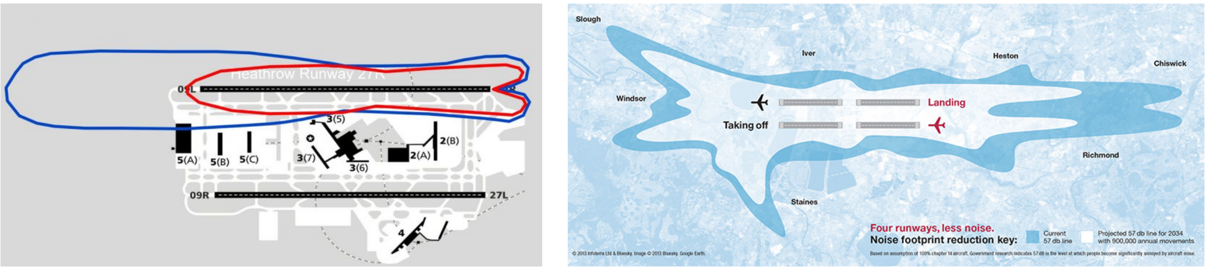

Figure 1.2 – *Left: Noise footprint of a 747-400 (blue) and an A350 (red) during take-off at Heathrow airport. Perceived noise on the ground is greater than 85dB in the surrounded areas [5]. Right: Noise footprint reduction target for Heathrow Airport from 2019 to 2034 [6].*

last decades, the bypass ratios of the following generations of turbofan engines have been continuously increased to optimize specific fuel consumption, leading as a side-benefit to noise decrease. Nowadays, engine noise has been reduced to a level comparable to that generated by aerodynamic fluctuations during the approach and landing phases, known as "airframe noise". During these flight phases, high-lift devices are deployed along with the landing gears. As illustrated in Fig. 1.3 airframe noise is responsible for over half of the noise emissions during the approach phases. Landing gears in particular, of very complex shape and extremely non-streamlined aerodynamics are the first contributor to airframe noise and will be studied in this thesis.

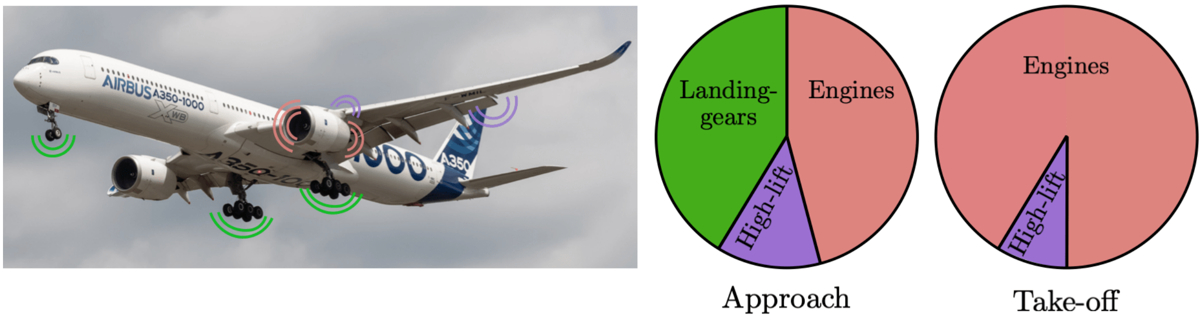

Figure 1.3 – *Typical noise source distribution of an Airbus family long-haul aircraft at take-off and in approach phases. Adapted from [7].*

1.2 Landing gear noise

The landing gears allow the aircraft to move on the ground, steer, and support the landing by cushioning the aircraft and then allowing it to stop over a short distance through efficient braking systems.

The main elements composing a nose and a main landing gear are described in Fig. 1.4:

- The main strut also referred as leg. It is composed of the shock absorber piston and its casing that connects the axle to the aircraft.
- The steering actuator: it allows the aircraft to be directed during ground operation and is obviously present only on nose landing gear.
- The torque link: a structural element linking the main strut and the piston of the shock absorber. It prevents the piston from turning inside the cylinder while enabling it to move up and down. This element is most visible on Fig. 7.1.
- The shock absorber: allows to absorb the landing and taxi shocks.
- The drag stay: holds the landing gear locked in the extended position. It prevents from an axial movement.
- The side stay: holds the landing gear locked in the extended position. It prevents from a lateral movement.
- The tow bar: enables to push/pull the aircraft on the tarmac.
- The axle: It connects the wheels to the landing gear leg.
- The braking system: it is usually located on the main landing gear for weight and load purposes. It obviously helps to stop the aircraft, especially during landing phases.
- Dressings: include all the electrical wiring and hydraulic harnesses.

The two types of landing gear are rather similar. However, the nose one is used to steer the aircraft while the main landing gear is able to brake the aircraft and support significantly more load.
As can be imagined, all these elements are an aerodynamic aberration (which by the way is beneficial for braking the aircraft) and involve elements of very different sizes ranging from the wheel diameter to that of the electrical and hydraulic wires. Additionally, the landing gear geometries are very diversified according to the aircraft models. For instance, the main landing gear can have from two to six wheels for Airbus aircraft and even up to eight for the Antonov An 255.

Given this statement, one can guess that predicting the noise generated by the flow around landing gear is very tough. The greatest advances in the understanding of noise

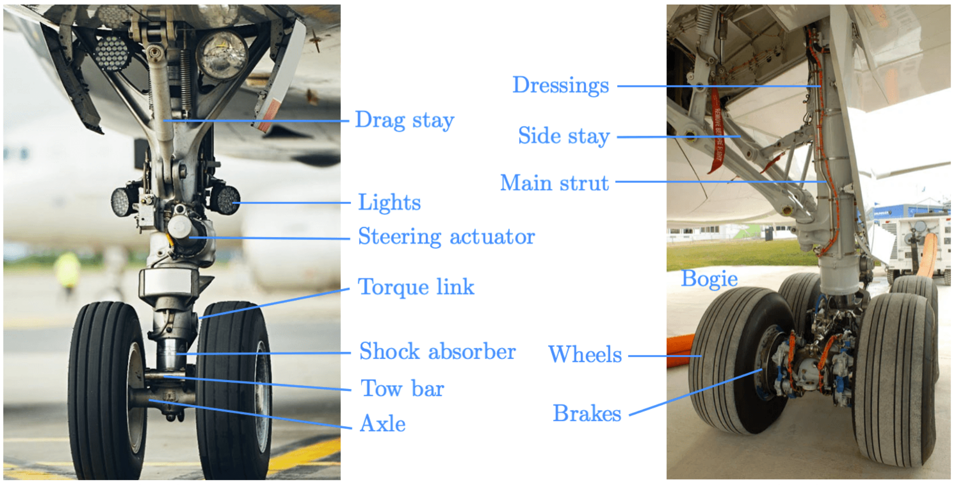

Nose landing gear Main landing gear

Figure 1.4 – *Left: Nose landing gear of an A320. Right: B787 Dreamliner Main landing gear.*

generation mechanisms for such configurations have come from wind tunnel tests and are summarized in [8, 9].

The main features to remember about landing gear noise are [8]:

- It is essentially broadband in nature. However, some small diameter components may give rise to distinct tonal noise due to coherent vortex shedding from Reynolds number flows of less than 5.10^5. This is for instance the case of the tow-bar that will be studied in Chap. 8. Additionally, cavities can also produce tonal peaks due to eigenmodes.

- The broadband noise originates from 1) the turbulent flow separation of the variety of bluff-body structural components, and 2) the interaction of such turbulent wake flows with downstream located gear elements. More generally, the noise emitted is the result of distorted vortices [10].

- The different landing gear components contribute to broadband noise in various frequency ranges depending on their size. For example, dressings mainly contribute to high frequencies, while larger components, such as tires and large struts contribute to low-middle frequencies.

- Landing gear noise is strongly affected by the installation effect [11, 12]. This last is characterized by 1) a modification of the acoustic source of the landing gear due to the circulation effect that induces a reduction of the local flow velocity under the wing, and 2) acoustic reflections and diffractions by the full wing with high-lift appendices deployed which modified the noise directivity [13].

The wind tunnel tests (WTT) are a reliable tool for understanding the mechanisms of noise generation and for estimating the noise levels of the various components. Additionally, they enable the testing of low-noise designs. They are generally carried out in open-jet anechoic wind tunnels (*cf.* Fig. 7.2). A detailed review of wind tunnel tests performed on landing gears aiming at understanding noise generation mechanisms or at reducing them can be found in Giret's PhD thesis [9]. However, because of the limited dimensions of wind tunnels, small-scale models are generally studied and the Reynolds effect is still a source of error when transposing to full scale [8]. Furthermore, WTT are time consuming and costly.

Alternatively, it is even possible to perform flight tests with microphones installed in the cabin and on the ground as shown on Fig. 1.5. Indeed, increasingly advanced beam forming methods [14–16] allow to locate more and more precisely the sources and to estimate their levels. In addition, they allow evaluating the installation effect. However, even with these methods, flight tests do not always enable to precisely isolate noise sources, or to effectively test noise reduction devices. They are nonetheless very accurate for determining the aircraft's noise footprint, and are used in the certification stage.

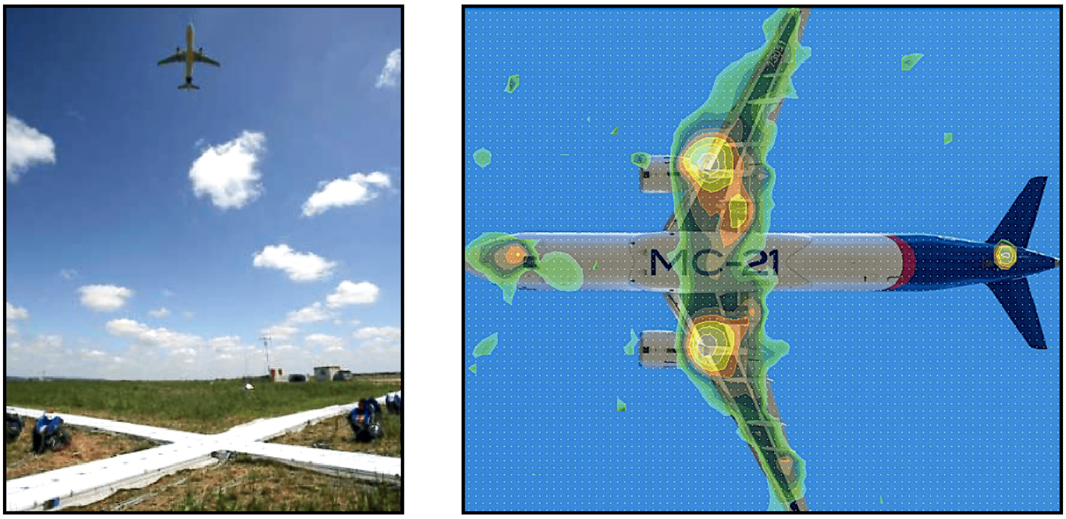

Figure 1.5 – *Left: Ground microphone installation for noise sources location from Airbus internal report. Right: Two-dimensional localization maps of noise sources. Frequency range* 315Hz-5kHz*, display dynamic range of 15*dB*. Extracted from [17].*

These experimental methods are reliable and very relevant, since they allow taking into account the geometric complexities and the installation effects. However, they require significant costs and set-up time. This is why analytical [18–20] or numerical methods have been simultaneously elaborated. The analytical methods, although attractive by their costs, do not allow to take into account complex hydrodynamic interactions and require validation and *a posteriori* calibration. This condition does not allow to be used for design phases. Computational Fluid Dynamics (CFD), by numerically approximating the fluid mechanics equations, is able to characterize and localize the landing gear noise without prior calibration. Ideally, the aeronautical manufacturer would like to carry out fast (a day) and accurate simulations, and dispense with experiments. It is towards these methods that this thesis turns to.

1.3 Numerical methods for landing gear noise prediction

Numerical simulation aims to approximate the fluid mechanics equations to solve any kind of flow within the bounds of a given set of assumptions. For this purpose, the equations need to be discretized in space and time on a grid. This thesis is a follow-up of two previous theses dealing with landing gear noise [9, 21], and from the start we have a clear idea of the numerical ingredients we intend to use. Thus, we will not detail the so-called Navier-Stokes "finite volume" numerical methods that have been previously explored and that are described in [9, 21]. In this thesis, we will focus on an alternative approach: The Lattice Boltzmann Method (LBM). Before discussing the latter, the main concepts of turbulence modeling will be introduced, with their application to landing gear simulations.

1.3.1 Turbulence modeling approaches

A flow around a landing gear is complex and highly turbulent with Reynolds numbers of several million. A turbulent flow can be seen as a three-dimensional and multi-scale flow involving eddies of various sizes. The size of the smallest scales of turbulence is inversely proportional to the Reynolds number, which characterizes the laminar/turbulent nature of a flow [22]. A flow around a landing gear therefore involves very small characteristic vortex sizes, and the number of grids points required to capture such flows would be staggering without modeling. Such a simulation where all scales are solved is commonly called Direct Numerical Simulation (DNS), and is currently only suitable for simple academic cases. To overcome this problem, there are different methods to account for turbulence at more affordable costs:

- **Reynolds Averaged Navier-Stokes (RANS):** It consists in solving the time-averaged Navier-Stokes equations using the Reynolds decomposition [23]. This decomposition allows to separate an unsteady quantity into a time-averaged and a fluctuating quantity. A non-linear term called Reynolds stress tensor appears which requires additional modeling to close the RANS equations. This closure problem has given birth to many turbulence models. To mention only the most famous, one can distinguish models that use the Boussinesq approximation and introduce a turbulent viscosity (Spalart-Allmaras [24], $k-\epsilon$ [25], $k-\omega$ [26]), and those who do not need this assumption and introduce a transport equation for each term of the Reynolds tensor (Reynolds Stress Models). RANS methods fully model turbulence and offer the advantage of being very inexpensive. They are widely used in the industry and often provide satisfactory results for attached and stationary flows [27]. However, if the unsteady flow data are relevant for the study carried out, or if the flow is inherently highly unsteady, this modeling will not be adequate. For landing gear simulations, only the very first study [28] used this modeling or the Unsteady-RANS version which allows to capture large variations of the flow [29].

- **Large Eddy Simulation (LES):** This method is based on Kolmogorov's postulate that turbulent scales can be segregated for large Reynolds numbers. The large scales are those whose carry the most of energy and are specific to the case studied. Then, there is a variety of eddies sizes where a universal behavior is encountered, with a famous decay of kinetic energy in '$-5/3$ slope'. These large scales are generally referred to as integral scales [22]. Finally, smaller scales have a universal and essentially dissipative behavior. The idea behind LES is therefore to explicitly compute the large scales while modeling the smaller ones. Practically, a spatial filtering of the Navier-Stokes equations is applied. As for the RANS, a closure model is required, to take into account the effect of small scales on the resolved ones. The best known is that of Smagorinsky [30]. This method significantly reduces the cost of a DNS. However, the number of grid points necessary to correctly resolve a boundary layer is proportional to $\mathrm{Re}^{1.86}$ [31] which makes Wall Resolved LES (WRLES) hardly affordable in practice for aeronautical applications. To date, only Giret [32] has realized a WRLES on a landing gear, but with insufficient parietal resolution to correctly resolve the boundary layers. The results were nevertheless reliable for predicting the LAGOON landing gear noise. To overcome this dependency in $\mathrm{Re}^{1.86}$, boundary layer models have been developed to use a coarser resolution in the near wall-region. The Wall-Modeled LES (WMLES) allows to keep a number of mesh proportional to the Reynolds number [31], and thus make aeronautical simulations more affordable. To the gain associated with the reduction of the cell number comes a gain on the time step used for an explicit LES [33], where the time step is based on the smallest cell size. Thus, for landing gear noise prediction, WMLES has recently been successfully employed by Zhang [21] and Hou [34, 35]. Satisfying WMLES near-field results were also obtained by Sengissen [36] and Brionnaud [37].
- **Detached Eddy Simulation (DES):** This method consists in hybridizing the RANS and LES to benefit from the advantages of each method: Use a RANS model close to the wall and in the attached areas, which is accurate and less constraining regarding the mesh density, then a LES modeling in the detached and fully turbulent regions. Originally, this method was proposed by Spalart [38] as a modification of its RANS turbulence model S-A [24], by modifying the destruction term of its transport equation. Thus, the S-A turbulence model degenerates into a LES subgrid scale model away from the wall. Yet, the transition from one model to the other contains a "grey area" and could, in its original form, create grid-induced separation [39]. This was corrected in 2006 with Spalart's Delayed-DES model (DDES) [40] allowing the boundary layer to be protected in RANS mode. Many similar methods have emerged, among them, the Zonal-DES (ZDES) methods have been developed and allow the hand selection of RANS and LES zones [41] but require prior knowledge of the flow. Deck has also proposed a formulation of ZDES which removes this constraint [27, 42]. The RANS-LES hybrid method has been widely used to predict landing gear noise. Considering only the simplified LAGOON landing gear studied in Chap. 7, there are no less than ten references [43–52]. Hybrid RANS/LES is a very good compromise in terms of CPU cost, but requires wise use, sometimes with a good knowledge of the flow beforehand.

1.3.2 The lattice Boltzmann method: an alternative to Navier-Stokes based solvers

The latter turbulence modeling approaches have been developed within the framework of solvers solving the Navier-Stokes equations mostly using finite volume methods. Over the past two decades, solvers based on the resolution of the Boltzmann equation have emerged. Specifically, the PowerFLOW solver which has been the only one able to perform industrial and accurate simulations [53–55] until the last decade when concurrent solvers have emerged. These solvers are based on the lattice Boltzmann method (LBM) which is derived from the Boltzmann equation and will be detailed in Chap. 2, and which will be widely studied through this manuscript. This method has the advantage of being very fast and has enabled a step forward in the simulation of unsteady flows, gaining about an order of magnitude on the restitution time [56, 57]. In terms of turbulence handling, the LBM solvers can use exactly the same turbulence modeling as the Navier-Stokes solvers [58–60] described in Sec. 1.3.1. Moreover, this method is natively discretized on a Cartesian grid, which greatly facilitates the meshing of complex geometries [61], but does not allow to make body-fitted meshes. Because of these mesh constraints, industrial LBM solvers use wall laws, which they associate with LES models in the case of the solvers Xflow [37], ultraFluidX [62], LaBS/ProLB [63], and even with DES models for the PowerFLOW solver [64].

The main challenges currently encountered by LBM solvers for landing gear aeroacoustics are:

- The stability of the method: in its most common formalism called "standard LBM", the LBM allows to simulate athermal and low Mach number flows ($\mathrm{Ma} < 0.4$) [65]. And yet, we will see in Chap. 5 that for low viscosity flows, this limit is even very optimistic if one does not use adequate models.

- Boundary conditions: since solvers cannot be body-fitted, it is essential to use wall laws. However, their implementation can be complex in a LBM framework [66–68], and physics is obviously highly dependent on the implementation strategy.

- Mesh refinement: the construction of LBM meshes imposes an integer mesh jump between two resolution domains. The precision of such interfaces is crucial to avoid spurious acoustic sources [69, 70].

With the PowerFLOW solver, the LBM has been successfully applied to the prediction of simplified landing gear noise [51, 52] as well as complex ones [54, 56, 61, 71–74] with remarkable restitution times [75]. Only this LBM solver has allowed far-field aeroacoustic results (acoustic propagation zone outside of hydrodynamic fluctuations). There are also three studies that do not yet present far-field datas, but exhibit very good near-field results (region where the acoustic sources are computed). The one performed with the LAVA solver from NASA [56] compared to their Cartesian Navier-Stokes solver embedded in the same environment. They underline an order of magnitude on the restitution time, with a higher precision. Brionnaud has shown preliminary results on LAGOON with the Xflow solver [37], and Sengissen with LaBS/ProLB [36].

Far-field acoustic prediction requires a very high accuracy and was, in the context of Sengissen's simulations in 2015 [36], not reacheable for the reasons that will be discussed in Sec. 1.4.2. **This PhD thesis aims at enabling the realization of accurate aeroacoustic simulations with the LaBS/ProLB solver** which is detailed below.

1.4 LaBS/ProLB a lattice Boltzmann solver

1.4.1 LaBS/ProLB v2.5 in a nutshell

The LaBS solver and its commercial release named ProLB is an industrial LBM code developed within a consortium of industrialists (Renault, Airbus, CS), academic laboratories (Aix-Marseille University, UPMC, Ecole Centrale de Lyon), and in close collaboration with other research entities (CERFACS, ONERA, Alstom, Université Paris-Sud, Gantha, Matelys) through several French projects: "LaBS" (2010-2013), "CLIMB" (2015-2018) , "ALBATROS" (2019-2021), "BALBUZARD" (2021-2024) and "SCALABLE" (2021-2024).

Description of LaBS/ProLB v2.5:

The v2.5 version of LaBS/ProLB, was the commercial version available at the beginning of the PhD thesis. It is coded in C++, and uses the MPI (Message Passing Interface) parallelization library. The main components of interest to perform industrial simulations are:

- **LBM core**: an athermal formulation based on a D3Q19 lattice [65] (see Sec. 2.3.3). This lattice offers a great trade-off between stability, precision and CPU performance [76]. The solver integrates the DRT (Dual Relaxation Time) collision model [63] presented in Sec. 4.7 and studied in Chap. 5.

- **Turbulence modeling:** two models are available, the DNS (without any turbulence model) or the LES using the SISM sub-grid scale model (for Shear Improved Smagorinsky Model [77]). Near wall turbulence is handled using wall laws accounting for adverse pressure gradient [78] and curvature effects. Implementation details are given in section III. C. of [66]. Besides, the Sengissen paper [36] illustrates the benefits of wall law and the adverse pressure gradient effects on the simplified LAGOON landing gear. Alongside this thesis, an other thesis was conducted by Johan Degrigny [68] on the adaptation of LaBS/ProLB to a WMDES turbulence modeling. Thus, the turbulence modeling will not be questioned thorough the manuscript.

- **Boundary conditions:** Dirichlet, wall-law, and non-reflective [79] boundary conditions are available. These last ones allow to damp acoustic reflections at the domain boundaries, and to improve the convergence. They are essential for performing aeroacoustic simulations. All boundary conditions are implemented using a full reconstruction of the distribution functions using finite differences [80–82] and implementation strategy is detailed in [66–68].

- **Octree based meshes:** an octree mesher is directly integrated in the solver. This mesher allows the generation of "layers" of cells around objects in addition to more simple refinements inside closed construction surfaces, which is very efficient for meshing almost automatically complex geometries [36, 57]. Furthermore, a cell-vertex algorithm based on an overlapping area to couple two meshes of different resolution is used, with an explicit filtering step during the transfer from the fine mesh to the coarse one [59,83]. This algorithm is detailed in Sec. 3.5 and evaluated in Chap. 6.

This solver offers very attractive models for performing industrial simulations. However, aeroacoustics is a field that requires a high level of accuracy, and some of the current ingredients do not meet the required precision level. The weaknesses of the solver will be qualitatively highlighted in the following section.

1.4.2 Current weaknesses for aeroacoustic applications

Following the very convincing results of Ribeiro, Casalino *et al.* for the two-wheels LAGOON landing gear [51,52], Sengissen has carried out this study with the LaBS/ProLB solver [36]. The results were very promising for computing the acoustic sources of the LAGOON gear. However, far-field acoustic prediction requires a precise scheme, and an absence of spurious acoustic sources. The Fig. 1.6 shows, for the same settings as Sengissen [36], a velocity dilatation field obtained on a slice, allowing to visualize the acoustic waves involved in the simulation. One can observe that in addition to the expected acoustic source, centered on the landing gear, many spurious sources emanate from the mesh resolution domains (RD). Furthermore, plane spurious waves occurs even upstream of the landing gear, as well as near the ceiling on which the landing gear stands. These two phenomena are quite distinct, and will be studied separately.

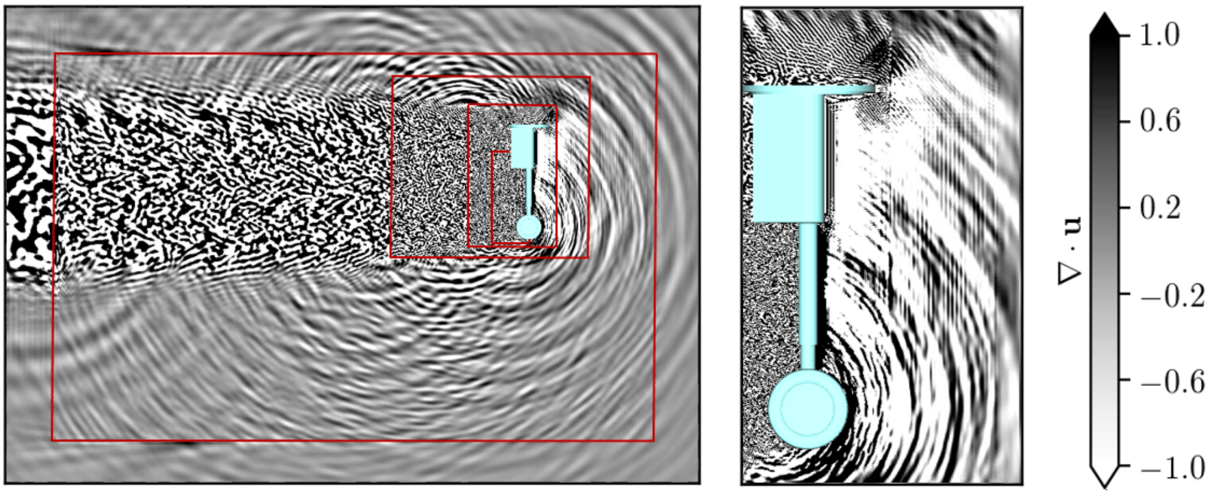

Figure 1.6 – *Velocity divergence field of the flow around the* LAGOON *landing gear in the Y-plane with LaBS/ProLB v2.5. The resolution domains* (RD) *are depicted in red* (□).

The Fig. 1.7 exhibits a vorticity field on this same slice. The vorticity colormap is tightened, allowing the appearance of spurious vorticity waves. Surprisingly, the resolution transitions generate spurious vorticity even upstream of the gear, without any incoming hydrodynamic disturbance. This phenomenon strongly reminds the numerical artefacts observed in Fig. 9.6 of Hasert's thesis [84]. The latter has minimized this phenomenon by reducing to one the order of precision of his refinement algorithm, which is obviously not a satisfactory solution.

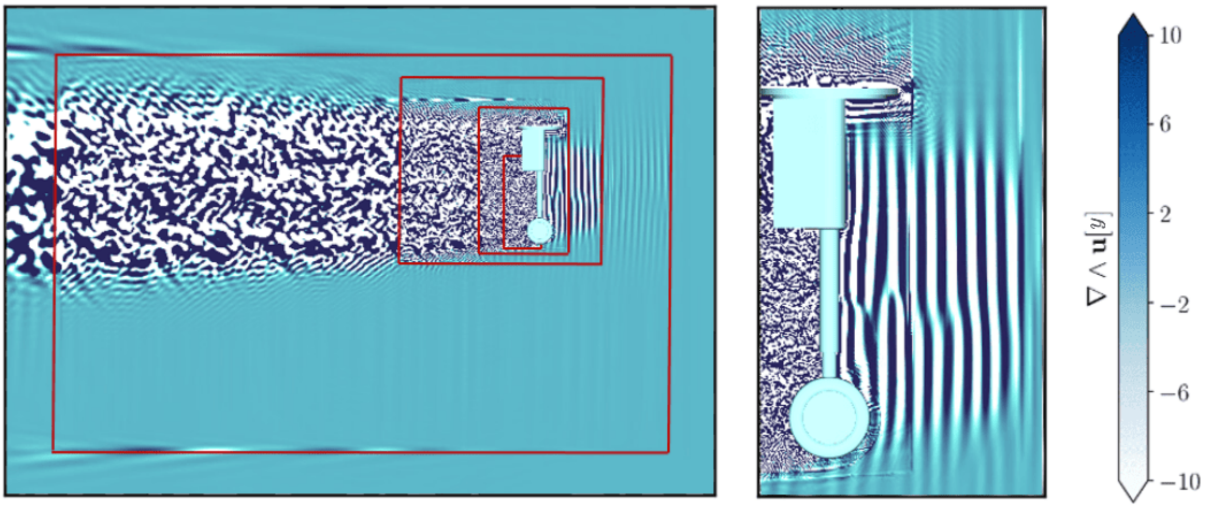

Figure 1.7 – *Y-component of the vorticity field around the* LAGOON *landing gear in the Y-plane with LaBS/ProLB v2.5. The resolution domains* (RD) *are depicted in red* (□).

Obviously, such spurious waves are completely non-physical and are not at all acceptable in a simulation. In view of these first observations, before being able to perform aeroacoustic simulations of landing gears, the **academic objectives of this thesis** will consist in:

1. **Understand where these non-physical waves originate**, apparently related to resolution transitions, and **find a suitable way to get rid of them**.
2. **Assess and improve the accuracy of the grid coupling algorithm**, partially responsible for the spherical spurious waves visible on Fig. 1.6.
3. **Evaluate the stability and precision of LBM schemes** for typical landing gear flow configuration.

These different items are identified as mandatory steps for the realization of aeroacoustic simulations and will be addressed in separate chapters.

1.5 Outline of this manuscript

The manuscript is divided in two parts: a part dedicated to the study and improvement of LBM models to perform aeroacoustic simulations with non-uniform meshes (Chap. 2 to Chap. 6) and a part devoted to the models validation and landing gear noise prediction in Chap. 7 and Chap. 8. In these last two chapters, the three LAGOON landing gear configurations of increasing complexity will be studied. Other landing gears have been investigated during this thesis but will not be addressed in this manuscript:

1. The OPENAIR gear [85] which is a $1:7.5$ scale of an A320 landing gear. This study was performed at the beginning of the thesis with the LaBS/ProLB v2.5 in the framework of the CLIMB project and was limited to aerodynamic results.
2. The ARTEM [86] gear, which is a realistic $1:11$ scale A320 landing gear installed underneath a fully deployed high-lift wing. These simulations have been carried out at the end of this thesis with using the aeroacoustic compliant models developed. Due to the confidentiality of this configuration, and the poor amount of aerodynamic experimental data available, it was not chosen to present these results in the manuscript.

The outline of the manuscript is the following:

- **Chapter 2** is dedicated to the derivation of the LBM starting with the Boltzmann equation and the physical assumptions associated with it. The limitations related to the most basic LB model will be highlighted in a turbulent simulation involving non-uniform grids, in terms of stability and accuracy.
- **Chapter 3** is focused on the spectral analysis of a simple LBM model and the establishment of tools and elementary test cases allowing to highlight the harmful effect of the so-called "non-hydrodynamic modes" when a change in resolution occurs. This chapter constitutes the first part of a study published during the present thesis [87].
- **Chapter 4** introduces advanced LBM models allowing to minimize or even suppress (with an adequate model) these non-hydrodynamic modes and the associated deleterious effects on resolution transitions. This last model will answer point 1. exposed in Sec. 1.4.2. A validation will be carried out with a simulation of a cylinder with a high Reynolds number flow. This chapter forms the second part of a study published during this thesis [87], and has been enriched in the present manuscript with other models from the literature to generalize the conclusions.
- **Chapter 5** aims to study the stability and accuracy of different LBM models in an aeroacoustic framework by means of stability analysis and numerical experiments. The need to provide a correction term to the model chosen in Chapter 4 for improving its stability will be shown, and its properties for aeroacoustics will be validated. This chapter will address point 3. outlined in Sec. 1.4.2.

- **Chapter 6** presents the development of a new and more precise grid coupling algorithm, enabling to overcome an overlapping area between two grids. This model will be assessed and compared to the one used in LaBS/ProLB v2.5. A massive reduction of the spurious acoustic sources appearing during wake crossing through transitions will be achieved. This chapter will fulfill point 2. of Sec. 1.4.2 identified as a barrier for performing aeroacoustic simulations. This work has been submitted for publication during this thesis [88].

- **Chapter 7** is devoted to the study of the LAGOON 1 landing gear. In a first step, a bibliographical review of the previous studies will be carried out. In a second step, an aerodynamic analysis is carried out for three grids of increasing resolution. Then, the LBM model chosen in chapter 4, as well as the grid coupling algorithm developed in chapter 6 will be validated for the prediction of landing gear noise. Finally, the coupling with a FW-H solver (*c.f* Sec. 7.1.2) will be investigated and the flaws of the solid formulation, commonly used for landing gear noise, will be pointed out and subsequent recommendations will be issued.

- **Chapter 8** deals with the LAGOON 2 and LAGOON 3 configurations which integrate additional components (tow-bar, steering actuator, lights, torque-link, rim cavity caps). Aerodynamic and aeroacoustic validations are achieved based on the best practices proposed in Chap. 7. The objective is to capture the effect of these various components on the broadband noise, as well as the tonal peak resulting from the interaction between the tow-bar wake and the axle.

Chapter 2

The lattice Boltzmann method

Contents

This chapter is dedicated to the derivation of the lattice Boltzmann method starting from the Boltzmann equation. To this end, reminders will be provided on kinetic theory and on statistical modeling of gases. Then, the hydrodynamic limits of the Boltzmann equation will be investigated and the macroscopic behavior of this equation will be retrieved thanks to a Chapman-Enskog development. Subsequently, this equation will be discretized in velocity using a Hermite polynomial development of the equilibrium function and a Gauss-Hermite quadrature. Afterwards, a space and time discretization will be carried out to get to the famous lattice Boltzmann scheme. Finally, the simple model thus derived will be evaluated within the framework of aeronautical aeroacoustic simulation.

2.1 Introduction

The lattice Boltzmann method (LBM) has emerged as a very efficient approach for computational fluid dynamics over the last two decades. Its high degree of versatility makes it applicable to a large variety of highly complex physical phenomena, such as turbulence [58,89], multiphase flows [90,91], porous media [92] or even hemodynamics [93], and it has increasingly interested both industrial and academic actors. In its standard formulation, the main advantages are, *inter alia:*

- a very simple and reasonably dissipative numerical scheme representing weakly compressible flows which makes the LBM suitable for aeroacoustic simulations,
- a local and efficient space and time discretization allowing a massive parallelization on high-performance computers and offer promising perspectives on GPUs [94–96],
- a discretization based on the well known collide and stream algorithm that requires a Cartesian grid allowing for a seamless way to handle complex geometries through an automated octree meshes [61] and non body fitted boundary conditions.

The lattice Boltzmann (LB) method relies on a fluid description at the mesoscopic scale, instead of classical methods that deals with macroscopic variables like the density, the velocity or the temperature. This relatively recent method is based on kinetic theory of gases dating back more than a century, pioneered by James C. Maxwell [97] and Ludwig Boltzmann [98] and on studies conducted in the 1980s on lattice gas cellular automata (LGCA). The first cellular automatons are the HPP model by Hardy, Pomeau and Pazzis [99], the FHP model by Frisch, Hasslacher and Pomeau [100], or the 3D lattice gas model proposed by d'Humières [101]. These models allowed to find an attractive macroscopic behavior but were polluted by a significant numerical noise. The LGCA were then improved by McNamara and Zanetti [102], who modeled the fluid using particle distributions with the help of the Maxwell-Boltzmann equilibrium distribution to retrieve the Galilean invariance principle, and with the use of floating operations to reduce the numerical noise. This last piece of work is generally described as the first LBM model but was suffering at that time from a complex collision operator. The appearance of the current LB models will take place progressively with the linearization of the collision operator by Higuera and Jimnez in 1989 [103]. Finally, Chen [104] and Qian [65] have adopted the simple BGK collision operator in 1992, developed forty years ago by Bhatnagar, Gross and Krook [105]. So far, these models are intended to be an improvement of the LGCA and the LBM allows the recovery of the Navier-Stokes behavior in an *a posteriori* way. It is only in 1996 with the work of He and Luo [106] that an *a priori* link between the LBM and the Boltzmann equation (BE) was directly established, without involving the LGCA models.

In the rest of this chapter, reminders will be provided on the kinetic theory of gases with the introduction of the probability density function of particles and the Boltzmann equation which governs the evolution of this function. Then, the hydrodynamic limits of the Boltzmann equation will be studied. Finally, this equation will be discretized in velocity on a so-called lattice, then in space and time to give rise to the LB scheme directly exploitable numerically.

2.2 Basics of kinetic theory

The kinetic theory of gases took a big step forward in the middle of the 19th century with the work of James C. Maxwell [97] and Ludwig Boltzmann [98]. These two physicists have adopted a statistical description of a fluid, at the so-called mesoscopic scale. This representation lies between the microscopic scale, where the gas dynamics is governed by Newton's equations, in which particles are tracked on arbitrary trajectory, and the macroscopic scale, which is governed by Euler's or Navier-Stokes equations for viscous fluids. In what follows, only a brief introduction to the kinetic theory of gases will be presented, for more details, the reader may refer to [107, 108].

2.2.1 The probability density function and the Boltzmann-BGK equation

In such modeling, a set of particles can be described by a particle distribution function $f_N\left(\boldsymbol{x},\boldsymbol{\xi},t\right)$ as

$$dN = f_N\left(\boldsymbol{x},\boldsymbol{\xi},t\right)\mathrm{d}\boldsymbol{x}\mathrm{d}\boldsymbol{\xi}, \tag{2.2.1}$$

where dN is the total number of particles located at a position $\boldsymbol{x}$, traveling at microscopic velocity $\boldsymbol{\xi}$ and at time t within a mesoscopic volume $\mathrm{d}\boldsymbol{x}$. Assuming the gas with particles of identical mass m, one can define $f_N\left(\boldsymbol{x},\boldsymbol{\xi},t\right)$ in terms of probability density distribution function as

$$f\left(\boldsymbol{x},\boldsymbol{\xi},t\right) = m f_N\left(\boldsymbol{x},\boldsymbol{\xi},t\right). \tag{2.2.2}$$

With this definition, the local density $\rho(\boldsymbol{x},t)$ can be found as the zeroth-order statistical moment of the distribution function. The momentum density $\rho\boldsymbol{u}(\boldsymbol{x},t)$ or the total energy density $\rho E(\boldsymbol{x}, t)$ are recovered by computing first and second-order moments over the velocity space of dimension D.

$$\rho(\boldsymbol{x}, t) = \int_{\mathbb{R}^D} f(\boldsymbol{x}, \boldsymbol{\xi}, t) \mathrm{d}\boldsymbol{\xi}, \tag{2.2.3}$$

$$\rho \mathbf{u}(\boldsymbol{x}, t) = \int_{\mathbb{R}^D} \boldsymbol{\xi} f(\boldsymbol{x}, \boldsymbol{\xi}, t) \mathrm{d}\boldsymbol{\xi}, \tag{2.2.4}$$

$$\rho E(\boldsymbol{x}, t) = \int_{\mathbb{R}^D} \frac{|\boldsymbol{\xi}|^2}{2} f(\boldsymbol{x}, \boldsymbol{\xi}, t) \mathrm{d}\boldsymbol{\xi}. \tag{2.2.5}$$

For a monatomic gas, in which collisions are assumed elastic, the total energy $E(\boldsymbol{x}, t)$ is composed of the internal energy $e(\boldsymbol{x}, t)$ and the kinetic energy as

$$\rho E(\boldsymbol{x}, t) = \rho e(\boldsymbol{x}, t) + \frac{1}{2} \rho |\boldsymbol{u}(\boldsymbol{x}, t)|^2. \tag{2.2.6}$$

The internal energy $e(\boldsymbol{x}, t)$ is linked to the random thermal motion of particles around their mean velocity $\boldsymbol{u}$. It can thus be seen at the standard deviation of the distribution function and then be expressed as

$$\rho e(\boldsymbol{x}, t) = \int_{\mathbb{R}^D} \frac{|\boldsymbol{\xi} - \boldsymbol{u}|^2}{2} f(\boldsymbol{x}, \boldsymbol{\xi}, t) \mathrm{d}\boldsymbol{\xi}. \tag{2.2.7}$$

Furthermore, the thermodynamic temperature $T(\boldsymbol{x}, t)$ can be recovered from the internal energy $e(\boldsymbol{x}, t)$ as

$$T(\boldsymbol{x}, t) = \frac{e(\boldsymbol{x}, t)}{c_v}, \tag{2.2.8}$$

where $c_v = r_g D/2$ is the heat capacity at constant volume for a monatomic gas and r_g is the gas constant.
Finally the pressure can be obtained using the perfect gaz law:

$$p(\boldsymbol{x}, t) = \rho(\boldsymbol{x}, t) r_g T(\boldsymbol{x}, t). \tag{2.2.9}$$

The distribution function f therefore allows to retrieve the macroscopic quantities of interest. The Boltzmann equation dating from 1872 [98] then makes it possible to track the evolution of the particle distribution in space and time, with a transport term on the left-hand side and a collision source term on the right-hand side. This collision term represents the variations of f due to collisions between particles which play an essential part in the evolution of the gas towards a thermodynamic equilibrium. By neglecting any external forces that can influence the motion of particles, such as gravity, the Boltzmann equation is expressed as

$$\frac{\partial f}{\partial t} + \boldsymbol{\xi} \cdot \frac{\partial f}{\partial \boldsymbol{x}} = \Omega(f), \tag{2.2.10}$$

where the center dot denotes the scalar product over $\mathbb{R}^D$.

Considering elastic collision between particles, the collision model $\Omega(f)$ must conserve the mass, momentum and energy during the collision process. These constraints are the collision invariants and could be expressed as

$$\int \Omega(f)\Phi(\boldsymbol{\xi})\mathrm{d}\boldsymbol{\xi} = \mathbf{0}. \tag{2.2.11}$$

with $\Phi(\boldsymbol{\xi}) = (1, \boldsymbol{\xi}, \xi^2/2)$.

A simple collision operator $\Omega(f)$ satisfies these constraints: The single relaxation time of Bhatnagar-Gross-Krook (BGK) model [105].

$$\Omega(f)^{\mathrm{BGK}} = -\frac{1}{\tau}\left(f - f^{(eq)}\right). \tag{2.2.12}$$

This collision process involves a relaxation of particle distributions at a relaxation time τ towards a thermodynamic equilibrium state described by the equilibrium distribution of Maxwell-Boltzmann

$$f^{(eq)} = \frac{\rho}{(2\pi r_g T)^{D/2}} \exp\left(-\frac{\|\boldsymbol{\xi} - \boldsymbol{u}\|^2}{2 r_g T}\right), \tag{2.2.13}$$

One can thus notice that the equilibrium function is locally entirely defined by the density, the macroscopic velocity and the temperature which are the first three moments of the distribution function f. These last can be derived analytically from Eq. (2.2.13)

$$\int_{\mathbb{R}^D} f^{(eq)}\mathrm{d}\boldsymbol{\xi} = \rho(\boldsymbol{x}, t), \tag{2.2.14}$$

$$\int_{\mathbb{R}^D} \boldsymbol{\xi} f^{(eq)}\mathrm{d}\boldsymbol{\xi} = \rho\mathbf{u}(\boldsymbol{x}, t), \tag{2.2.15}$$

$$\frac{1}{2}\int_{\mathbb{R}^D} |\boldsymbol{\xi}|^2 f^{(eq)}\mathrm{d}\boldsymbol{\xi} = \rho E(\boldsymbol{x}, t) = \frac{D}{2}\rho r_g T(\boldsymbol{x}, t) + \frac{1}{2}\rho|\boldsymbol{u}(\boldsymbol{x}, t)|^2. \tag{2.2.16}$$

The zeroth, first and the trace of the second-order moment of the equilibrium function are equal to those of f. The BGK collision operator thus conserves the mass, momentum, as well as the energy.

The second-order equilibrium moment is also presented as it will be useful in the following.

$$\int_{\mathbb{R}^D} \boldsymbol{\xi}\boldsymbol{\xi} f^{(eq)}\mathrm{d}\boldsymbol{\xi} = \rho r_g T\delta + \frac{1}{2}\rho\boldsymbol{u}\boldsymbol{u}. \tag{2.2.17}$$

The benefit of this collision operator lies in its simplicity and its computational efficiency. Nevertheless, this simple modeling will have repercussions on the conservation laws retrieved as further discussed in Sec. 2.2.2.c.
By substituting the collision operator $\Omega(f)^{\mathrm{BGK}}$ into the Boltzmann equation described in Eq. (2.2.10), the Boltzmann-BGK equation studied in the following becomes

$$\frac{\partial f}{\partial t} + \boldsymbol{\xi} \cdot \frac{\partial f}{\partial \boldsymbol{x}} = -\frac{1}{\tau}\left(f - f^{(eq)}\right). \tag{2.2.18}$$

2.2.2 Hydrodynamic limits of the Boltzmann-BGK equation

2.2.2.a Macroscopic equations and closure problem

In order to find the macroscopic equations governed by the Boltzmann-BGK equation, one can calculate its moments. By taking the zeroth, first and the trace of the second-order moments of Eq. (2.2.18) and considering that $\boldsymbol{x}, \boldsymbol{\xi}, t$ are three independent variables, one obtained

$$\frac{\partial}{\partial t}\int_{\mathbb{R}^D} f \mathrm{d}\boldsymbol{\xi} + \frac{\partial}{\partial x_\beta}\int_{\mathbb{R}^D} \xi_\beta f \mathrm{d}\boldsymbol{\xi} = -\frac{1}{\tau}\int_{\mathbb{R}^D}\left(f - f^{(eq)}\right)\mathrm{d}\boldsymbol{\xi} = 0, \tag{2.2.19}$$

$$\frac{\partial}{\partial t}\int_{\mathbb{R}^D} \xi_\alpha f \mathrm{d}\boldsymbol{\xi} + \frac{\partial}{\partial x_\beta}\int_{\mathbb{R}^D} \xi_\alpha\xi_\beta f \mathrm{d}\boldsymbol{\xi} = -\frac{1}{\tau}\int_{\mathbb{R}^D}\xi_\alpha\left(f - f^{(eq)}\right)\mathrm{d}\boldsymbol{\xi} = 0, \tag{2.2.20}$$

$$\frac{1}{2}\frac{\partial}{\partial t}\int_{\mathbb{R}^D} \xi_\alpha\xi_\alpha f \mathrm{d}\boldsymbol{\xi} + \frac{1}{2}\frac{\partial}{\partial x_\beta}\int_{\mathbb{R}^D} \xi_\alpha\xi_\alpha\xi_\beta f \mathrm{d}\boldsymbol{\xi} = -\frac{1}{2\tau}\int_{\mathbb{R}^D}\xi_\alpha\xi_\alpha\left(f - f^{(eq)}\right)\mathrm{d}\boldsymbol{\xi} = 0, \tag{2.2.21}$$

where the collision invariants of mass, momentum and energy are well respected. Replacing Eq. (2.2.3) to (2.2.5) in the above equations gives

$$\frac{\partial \rho}{\partial t} + \frac{\partial(\rho u_\beta)}{\partial x_\beta} = 0, \tag{2.2.22}$$

$$\frac{\partial(\rho u_\alpha)}{\partial t} + \frac{\partial \Pi_{\alpha\beta}}{\partial x_\beta} = 0, \tag{2.2.23}$$

$$\frac{\partial(\rho e + \frac{1}{2}\rho u_\alpha u_\alpha)}{\partial t} + \frac{1}{2}\frac{\partial Q_{\alpha\alpha\beta}}{\partial x_\beta} = 0, \tag{2.2.24}$$

where $\Pi_{\alpha\beta}$ and $Q_{\alpha\alpha\beta}$ are respectively the second and third-order tensor of f.

Let's now rewrite these tensors in a more convenient form. Firstly, the second-order tensor $\Pi_{\alpha\beta}$ can be expressed as

$$\Pi_{\alpha\beta} = \sigma_{\alpha\beta} + \rho u_\alpha u_\beta, \tag{2.2.25}$$

with $\sigma_{\alpha\beta}$ that is usually referred as the stress tensor. It is computed as second-order tensor centered over the mean local velocity frame $\boldsymbol{u}$.

$$\sigma_{\alpha\beta} = \int_{\mathbb{R}^D}(\xi_\alpha - u_\alpha)(\xi_\beta - u_\beta) f \mathrm{d}\boldsymbol{\xi}. \tag{2.2.26}$$

The $\sigma_{\alpha\beta}$ tensor is composed of a spherical part $\tau_{\alpha\beta}$ and a deviator one $\frac{1}{D}\sigma_{\alpha\alpha}\delta_{\alpha\beta}$

$$\sigma_{\alpha\beta} = \tau_{\alpha\beta} + \frac{1}{D}\sigma_{\alpha\alpha}\delta_{\alpha\beta}, \tag{2.2.27}$$

Using Eq. (2.2.7), one can establish that the deviator part is linked to the internal energy e as

$$\frac{1}{D}\sigma_{\alpha\alpha}\delta_{\alpha\beta} = \frac{2}{D}\rho e\delta_{\alpha\beta} = \rho r_g T\delta_{\alpha\beta} = p\delta_{\alpha\beta}. \tag{2.2.28}$$

Following a similar decomposition, the tensor $Q_{\alpha\alpha\beta}$ might be expressed as

$$\frac{1}{2}Q_{\alpha\alpha\beta} = \rho e u_\beta + \frac{1}{2}\rho u_\alpha^2 u_\beta + u_\alpha\sigma_{\alpha\beta} + q_\beta, \tag{2.2.29}$$

with revealing q_β which will be further identified as the heat flux.

$$q_\beta = \frac{1}{2}\int_{\mathbb{R}} (\xi_\beta - u_\beta)\,|\boldsymbol{\xi} - \boldsymbol{u}|^2 f\,\mathrm{d}\boldsymbol{\xi}. \tag{2.2.30}$$

These expressions can be substituted in Eq. (2.2.22) to (2.2.24). It gives

$$\frac{\partial\rho}{\partial t} + \frac{\partial(\rho u_\beta)}{\partial x_\beta} = 0, \tag{2.2.31}$$

$$\frac{\partial(\rho u_\alpha)}{\partial t} + \frac{\partial(\rho u_\alpha u_\beta)}{\partial x_\beta} + \frac{\partial p}{\partial x_\beta} + \frac{\partial \tau_{\alpha\beta}}{\partial x_\beta} = 0, \tag{2.2.32}$$

$$\frac{\partial(\rho e + \frac{1}{2}\rho u_\alpha u_\alpha)}{\partial t} + \frac{\partial\left(u_\beta\left[\rho e + \frac{1}{2}\rho u_\alpha^2 + p\right]\right)}{\partial x_\beta} + \frac{\partial q_\beta}{\partial x_\beta} + \frac{\partial\left(u_\alpha\tau_{\alpha\beta}\right)}{\partial x_\beta} = 0. \tag{2.2.33}$$

The mass, momentum and energy conservation equations are retrieved. These equations involve the tensors $\tau_{\alpha\beta}$ and q_β, that are implicit since their expressions are dependent on the distribution functions. This system of equations is therefore not closed as it stands, since it involves too many variables. A closure was proposed by Hilbert [109] and then by Chapman and Enskog in the 1970s [110].

2.2.2.b The Chapman-Enskog expansion

The idea behind the development of Chapman-Enskog is to extend the distribution functions according to the Knudsen number ϵ. This dimensionless number is the ratio between the mean free path $\mathcal{L}$ of particles, *i.e.* a mean distance over which no collision occurs and the characteristic length scale l_0 of the flow.

$$\epsilon = \frac{\mathcal{L}}{l_0} = \frac{\tau_0\sqrt{r_g T_0}}{l_0} = \frac{\tau_0}{t_0}, \tag{2.2.34}$$

with τ_0 the mean time between two collisions. Furthermore, a characteristic time of the flow $t_0 = l_0/\sqrt{r_g T_0}$ can be defined as well as a sound velocity $c_0 = \sqrt{r_g T_0}$ corresponding to an isothermal sound velocity at a reference temperature T_0.

The Chapman-Enskog development expands the distributions f in Knudsen number ϵ around an equilibrium state referred as $f^{(0)}$.

$$f = f^{(0)} + \epsilon f^{(1)} + \epsilon^2 f^{(2)} + \ldots = \sum_{k=0}^{k=\infty} \epsilon^k f^{(k)}, \tag{2.2.35}$$

This asymptotic expansion was first introduced by Hilbert [109] a decade before the works of Chapman and Enskog. The originality of Chapman and Enskog works is that in their expansion, the distribution functions f are sought to be dependent of the conserved hydrodynamic moments $(\rho, \rho\mathbf{u}, \rho e)$ only [111].

A specific expansion of the time-derivative operator is proposed by Enskog.

$$\frac{\partial}{\partial t} = \sum_{k=0}^{k=\infty} \epsilon^k \frac{\partial}{\partial t^{(k)}}, \tag{2.2.36}$$

Furthermore, the moments of f can be expanded in Knudsen number around their equilibrium value. In order to retrieve the Navier-Stokes behavior, one has to expand the development up to the first-order.

$$\mathbf{\Pi} \simeq \mathbf{\Pi}^{(0)} + \epsilon \mathbf{\Pi}^{(1)}, \tag{2.2.37}$$

$$\boldsymbol{Q} \simeq \boldsymbol{Q}^{(0)} + \epsilon \boldsymbol{Q}^{(1)}. \tag{2.2.38}$$

Before going into the development, the Boltzmann-BGK equation (2.2.18) is made dimensionless to introduce ϵ in the relaxation time τ.

$$\tilde{t} = t\frac{c_0}{l_0}; \quad \tilde{\boldsymbol{x}} = \frac{\boldsymbol{x}}{l_0}; \quad \tilde{\tau} = \frac{\tau}{\tau_0}; \quad \tilde{\boldsymbol{\xi}} = \frac{\boldsymbol{\xi}}{c_0}; \quad \tilde{f} = \frac{f c_0^3}{\rho_0}. \tag{2.2.39}$$

with ρ_0 a reference density. The macroscopic variables turn into

$$\tilde{\rho} = \frac{\rho}{\rho_0} \quad ; \quad \tilde{\boldsymbol{u}} = \frac{\boldsymbol{u}}{c_0} \quad ; \quad r_g\tilde{T} = \frac{r_g T}{c_0^2} = \tilde{c_0}^2. \tag{2.2.40}$$

Hence, the equation (2.2.18) becomes

$$\frac{\partial \tilde{f}}{\partial \tilde{t}} + \tilde{\boldsymbol{\xi}} \cdot \frac{\partial \tilde{f}}{\partial \tilde{\boldsymbol{x}}} = -\frac{1}{\epsilon\tilde{\tau}}\left(\tilde{f} - \tilde{f}^{(eq)}\right). \tag{2.2.41}$$

For the sake of clarity, unless explicitly stated, dimensionless variables will be noted without the tilde in the following.

By injecting Eq. (2.2.35) and Eq. (2.2.36) into the dimensionless Boltzmann-BGK equation (2.2.41), and retaining only the first two orders in Knudsen number, one obtains:

$$\epsilon^{-1}: \quad f^{(0)} = f^{(eq)}, \tag{2.2.42}$$

$$\epsilon^{0}: \quad \frac{\partial f^{(0)}}{\partial t^{(0)}} + \boldsymbol{\xi} \cdot \frac{\partial f^{(0)}}{\partial \boldsymbol{x}} = -\frac{1}{\tau} f^{(1)}, \tag{2.2.43}$$

$$\epsilon^{1}: \quad \frac{\partial f^{(0)}}{\partial t^{(1)}} + \frac{\partial f^{(1)}}{\partial t^{(0)}} + \boldsymbol{\xi} \cdot \frac{\partial f^{(1)}}{\partial \boldsymbol{x}} = -\frac{1}{\tau} f^{(2)}. \tag{2.2.44}$$

Now let's analyze the contributions of the Boltzmann-BGK equation to the different orders in Knudsen, starting with the zeroth-order. To this extend, the zeroth, first and (the trace of the) second-order moments of Eq. (2.2.43) are computed. Thanks to the calculation of equilibrium moments ($f^{(0)} = f^{(eq)}$) given by Eq. (2.2.14) to (2.2.17), one obtains

$$\frac{\partial \rho}{\partial t^{(0)}} + \frac{\partial(\rho u_\beta)}{\partial x_\beta} = 0, \tag{2.2.45}$$

$$\frac{\partial(\rho u_\alpha)}{\partial t^{(0)}} + \frac{\partial\left(\rho u_\alpha u_\beta\right)}{\partial x_\beta} + \frac{\partial p}{\partial x_\beta} = 0, \tag{2.2.46}$$

$$\frac{\partial(\rho e + \frac{1}{2}\rho u_\alpha u_\alpha)}{\partial t^{(0)}} + \frac{\partial\left(u_\beta\left[\rho e + \frac{1}{2}\rho u_\alpha^2 + p\right]\right)}{\partial x_\beta} = 0. \tag{2.2.47}$$

Noticing that, from the explicit computation of equilibrium moments: $\sigma^{(0)} = p\boldsymbol{I}$ and $q^{(0)} = 0$. Moreover, the right-hand side terms vanish, since they are collision invariants following Eq. (2.2.11).
Truncating the Chapman-Enskog development to the zeroth-order in Knudsen, the Boltzmann equation leads to the Euler equations. This system is closed since the pressure p is linked to the internal energy e through Eq. (2.2.8) and Eq. (2.2.9).

Now the development is pushed further to the first-order in Knudsen:

$$\frac{\partial \rho}{\partial t^{(1)}} = 0, \tag{2.2.48}$$

$$\frac{\partial(\rho u_\alpha)}{\partial t^{(1)}} + \frac{\partial \Pi^{(1)}_{\alpha\beta}}{\partial x_\beta} = 0, \tag{2.2.49}$$

$$\frac{\partial(\rho e + \frac{1}{2}\rho u_\alpha u_\alpha)}{\partial t} + \frac{\partial q^{(1)}_\beta + u_\alpha \sigma^{(1)}_{\alpha\beta}}{\partial x_\beta} = 0, \tag{2.2.50}$$

with $\Pi^{(1)}_{\alpha\beta} = \sigma^{(1)}_{\alpha\beta}$. The off-equilibrium tensors $\sigma^{(1)}_{\alpha\beta}$ and $q^{(1)}_\beta$ can be obtained by computing the second and third-order moments of Eq. (2.2.43). For instance, the $\Pi^{(1)}_{\alpha\beta}$ computation gives

$$\Pi^{(1)}_{\alpha\beta} = -\tau \int_{\mathbb{R}} \xi_\alpha \xi_\beta \left(\frac{\partial f^{(0)}}{\partial t^{(0)}} + \xi_\gamma \frac{\partial f^{(0)}}{\partial x_\gamma} \right) \mathrm{d}\boldsymbol{\xi}. \tag{2.2.51}$$

The above equation (2.2.51) indicates that in order to compute the second-order off-equilibrium moment, it is necessary to have access to the third-order moment of the equilibrium function $f^{(0)}$. If one desires to compute $q^{(1)}_\beta$ by calculating the third-order moment of Eq. (2.2.43), the fourth-order equilibrium moment will be required. More generally, the calculation of an off-equilibrium moment of order n, requires the knowledge of an equilibrium moment of order $n + 1$ [112].

Afterwards, the temporal derivatives obtained are replaced by spatial derivatives using the aforementioned Euler equations (2.2.45) to (2.2.47).

Finally, after some tedious algebra that can be found in [70, 113], an explicit expression is obtained for the shear stress tensor $\sigma_{\alpha\beta}$ and heat flux tensors q_β

$$\sigma^{(1)}_{\alpha\beta} = -\tau p \left(2S_{\alpha\beta} - \frac{2}{D}\frac{\partial u_\gamma}{\partial x_\gamma}\delta_{\alpha\beta} \right), \tag{2.2.52}$$

$$q^{(1)}_{\beta} = -\tau p c_p \frac{\partial T}{\partial x_b}, \tag{2.2.53}$$

with $c_p = (1 + D/2)r$ the heat capacity at constant pressure and $S_{\alpha\beta}$ the velocity strain tensor defined as

$$S_{\alpha\beta} = \frac{1}{2}\left(\frac{\partial u_\alpha}{\partial x_\beta} + \frac{\partial u_\beta}{\partial x_\alpha} \right). \tag{2.2.54}$$

From the above equations (2.2.52) and (2.2.53), the dynamic viscosity is identified from the shear stress tensor as

$$\mu = \tau p, \tag{2.2.55}$$

and the thermal conductivity is identified from the hear flux tensor as

$$\kappa = \tau p c_p, \tag{2.2.56}$$

Adding the contributions from the zeroth and first-order of the Knudsen development, the Navier-Stokes Fourier equations are retrieved from the Boltzmann (Eq. (2.2.31) to Eq. (2.2.33)). This time, the system of equation is closed since $\sigma_{\alpha\beta}$ and $q^{(1)}$ are explicitly determined with Eq. (2.2.52) and Eq. (2.2.53).

2.2.2.c Discussion on the hydrodynamic limit of the Boltzmann equation

The Chapman-Enskog development carried out in the previous section provides more information on the hydrodynamic limits of the Boltzmann-BGK equation. Accordingly, several remarks may be raised:

- The Knudsen number is a fundamental parameter to describe a flow dynamic. For low Knudsen number values, fluids are considered as continuous and the effect of collisions between particles is dominant. In such situations, the flow dynamic is near equilibrium. Conversely, the greater the Knudsen number is, sparser the medium will be. The Navier-Stokes equations are retrieved from the Boltzmann equation when considering a small deviation from equilibrium, with a first-order truncation of the Chapman-Enskog development. Thus the range of validity of this hydrodynamic limit is restricted to flows with a small Knudsen number $< 10^{-2}$. For higher Knudsen numbers, it becomes necessary to extend the Knudsen development to the second-order and Burnett's equations can be retrieved [112, 114].

- The full knowledge of the equilibrium distribution function is not required to recover a given macroscopic behavior. Only the moments are involved in the Chapman-Enskog development and equilibrium moments up to the fourth-order ($\boldsymbol{Q}^{(0)}$) are needed to recover the Navier-Stokes Fourier equations. More generally, a Chapman-Enskog development at k-order reveals that for calculating a moment of order n of the distribution function f, one must be able to calculate exactly an equilibrium moment of order $n+k$. Since the Navier-Stokes equations correspond to a truncation at the first-order in Knudsen number, it is necessary to be able to calculate fourth-order equilibrium moments in order to retrieve the energy equation. If one does not wish to preserve the energy equation and retrieve only the isothermal Navier-Stokes equations, only the knowledge of the first three moments of $f^{(eq)}$ are needed. Consequently, the athermal hypothesis is frequently chosen in LBM since it allows to minimize the constraints on the velocity space discretization of the Boltzmann equation (see Sec. 2.3.3), and thus to increase the numerical efficiency of the method.

- The single relaxation time τ is involved in the calculation of both the dynamic viscosity $\mu = \tau p$ as well as the thermal conductivity $\kappa = \tau p c_p$. This implies the Prandtl number is fixed

  $$\mathrm{Pr}^{\mathrm{BGK}} = \frac{\mu c_p}{\kappa} = 1. \tag{2.2.57}$$

  This very strong assumption means the BGK model cannot be used to simulate correct thermal behavior. For this purpose, multiple relaxation time (MRT) collision operator [115, 116], double distribution functions (DDF) models [117–119] or hybrid finite-difference/LBM models [120–122] should be preferred.

2.3 The discrete velocities Boltzmann equation

In the previous section, it has been seen that the Boltzmann equation allows to retrieve the Navier-Stokes equations under certain constraints. In order to numerically solve this equation, a discretization is necessary. In addition to the time and space discretization that is classically found to discretize the Navier-Stokes equations, the Boltzmann equation involves a velocity space $\boldsymbol{\xi}$. Therefore, let's start here by discretizing the velocity space, which will lead to the discrete velocities Boltzmann equation (DVBE).

An efficient method for discretizing it is based on a Gauss-Hermite quadrature. In 1998, Shan and He [123] show that it is possible to discretize the velocity space based on the work of Grad and his 13-moments' equations [124]. Grad proposes a fluid model from an expansion of the distribution functions in Hermite polynomial. Later, this expansion is repeated by He and Luo in 1997 [106], then Shan and He one year later [123]. Finally, the construction of complete model with discretized on a lattice using a Gauss-Hermite quadrature is presented by Shan et al. in 2006 [112].

2.3.1 Hermite polynomial expansion and moments of the distribution function

Let's start by defining the Hermite polynomials of order n noted $\boldsymbol{\mathcal{H}}^n(\boldsymbol{\xi})$ with the weight function (or generating function) $w(\boldsymbol{\xi})$ of these polynomials. Both are make dimensionless to be consistent with Eq. (2.2.39).

$$\boldsymbol{\mathcal{H}}^{(n)}(\boldsymbol{\xi}) = \frac{(-r_gT_0)^n}{w(\boldsymbol{\xi})}\nabla^n_{\boldsymbol{\xi}} w(\boldsymbol{\xi}), \qquad \text{with} \qquad w(\boldsymbol{\xi}) = \frac{1}{(2\pi r_g T_0)^{D/2}} \exp\left(-\frac{\xi^2}{2r_gT_0}\right), \tag{2.3.1}$$

where $1/\left(r_gT_0\right)^{D/2}$ has been added to $w(\boldsymbol{\xi})$ to ensure that $\int w(\boldsymbol{\xi})\mathrm{d}\boldsymbol{\xi} = 1$. Furthermore, $\nabla^n_{\boldsymbol{\xi}}$, denotes the nth-order gradient tensor obtained by n-successive derivations with respect to the vector $\boldsymbol{\xi}$.

The first Hermite polynomials are:

$$\mathcal{H}^{(0)}(\boldsymbol{\xi}) = 1, \tag{2.3.2}$$

$$\mathcal{H}^{(1)}_{\alpha}(\boldsymbol{\xi}) = \xi_\alpha, \tag{2.3.3}$$

$$\mathcal{H}^{(2)}_{\alpha\beta}(\boldsymbol{\xi}) = \xi_\alpha\xi_\beta - r_gT_0\delta_{\alpha\beta}, \tag{2.3.4}$$

$$\mathcal{H}^{(3)}_{\alpha\beta\gamma}(\boldsymbol{\xi}) = \xi_\alpha\xi_\beta\xi_\gamma - r_gT_0(\delta_{\alpha\beta}\xi_\gamma + \delta_{\alpha\gamma}\xi_\beta + \delta_{\beta\gamma}\xi_\alpha), \tag{2.3.5}$$

$$\begin{aligned}\mathcal{H}^{(4)}_{\alpha\beta\gamma\delta}(\boldsymbol{\xi}) = {} & \xi_\alpha\xi_\beta\xi_\gamma\xi_\delta - r_gT_0(\delta_{\alpha\beta}\xi_\gamma\xi_\delta + \delta_{\alpha\gamma}\xi_\beta\xi_\delta + \delta_{\alpha\delta}\xi_\beta\xi_\gamma + \delta_{\beta\gamma}\xi_\alpha\xi_\delta \\ & + \delta_{\beta\delta}\xi_\alpha\xi_\gamma + \delta_{\gamma\delta}\xi_\alpha\xi_\beta) + (r_gT_0)^2\left(\delta_{\alpha\beta}\delta_{\gamma\delta} + \delta_{\alpha\gamma}\delta_{\beta\delta} + \delta_{\alpha\delta}\delta_{\beta\gamma}\right).\end{aligned} \tag{2.3.6}$$

The Hermite polynomials form an orthogonal basis with respect to the following scalar product:

$$\langle a|b\rangle = \int w(\boldsymbol{\xi})a(\boldsymbol{\xi})b(\boldsymbol{\xi})\mathrm{d}\boldsymbol{\xi}, \qquad \forall a, b \in \mathcal{L}^2, \tag{2.3.7}$$

where $\mathcal{L}^2$ is the space of square-integrable functions. Every function $\phi(\boldsymbol{x},\boldsymbol{\xi},t) \in \mathcal{L}^2$, can be decomposed on the orthogonal basis of Hermite polynomials as

$$\phi(\boldsymbol{x},\boldsymbol{\xi},t) = \sum_{n=0}^{\infty} \frac{1}{n!(r_gT_0)^n} \left\langle \phi|\boldsymbol{\mathcal{H}}^{(n)}\right\rangle \boldsymbol{\mathcal{H}}^{(n)}(\boldsymbol{\xi}). \tag{2.3.8}$$

Hence, if $\phi = f^{(0)}/w$, the equilibrium function $f^{(0)}$ can be decomposed on the orthogonal Hermite basis as

$$f^{(0)}(\boldsymbol{x},\boldsymbol{\xi},t) = w(\boldsymbol{\xi}) \sum_{n=0}^{\infty} \frac{1}{n!(r_gT_0)^n} \boldsymbol{a}_0^{(n)}(\boldsymbol{x},t) : \boldsymbol{\mathcal{H}}^{(n)}(\boldsymbol{\xi}). \tag{2.3.9}$$

where the equilibrium expansion coefficients $\boldsymbol{a}_0^{(n)}(\boldsymbol{x},t)$ are given by

$$\boldsymbol{a}_0^{(n)}(\boldsymbol{x},t) = \left\langle \frac{f^{(0)}}{w} \mid \mathcal{H}^n \right\rangle = \int f^{(0)}(\boldsymbol{x},\boldsymbol{\xi},t)\mathcal{H}^{(n)}(\boldsymbol{\xi})\mathrm{d}\boldsymbol{\xi}, \tag{2.3.10}$$

Here one understands why the development of $f^{(0)}$ in Hermite polynomials is interesting. Indeed, the expansion coefficients $\boldsymbol{a}_0^{(n)}(\boldsymbol{x},t)$ correspond to the Hermite moments of the equilibrium function.

The first four equilibrium expansion coefficients (or Hermite equilibrium moments) are :

$$\boldsymbol{a}_0^{(0)} = \rho, \tag{2.3.11}$$

$$\boldsymbol{a}_0^{(1)} = \rho\boldsymbol{u}, \tag{2.3.12}$$

$$\boldsymbol{a}_0^{(2)} = \rho\left[\boldsymbol{u}^2 + r_g T_0(\theta-1)\boldsymbol{\delta}\right], \tag{2.3.13}$$

$$\boldsymbol{a}_0^{(3)} = \rho\left[\boldsymbol{u}^3 + r_g T_0(\theta-1)\boldsymbol{u}\boldsymbol{\delta}\right], \tag{2.3.14}$$

$$\boldsymbol{a}_0^{(4)} = \rho\left[\boldsymbol{u}^4 + r_g T_0(\theta-1)\boldsymbol{\delta}\boldsymbol{u}^2 + (r_g T_0)^2(\theta-1)\boldsymbol{\delta}^2\right], \tag{2.3.15}$$

where $\theta = T/T_0$. A direct link between the raw moments and the Hermite moments can be easily achieved [125], and both are function of the thermodynamic variables. Hence, the conclusions that emerged during the Chapman-Enskog development in Sec. 2.2.2.c concerning the moments involve in the recovery of a given macroscopic behavior are still valid with the Hermite formalism.

One can note that in the isothermal case ($\theta = 1$), these formulas are reduced to recursive formula given by Malaspinas [126]:

$$\boldsymbol{a}_0^{(n)} = \boldsymbol{a}_0^{(n-1)}\boldsymbol{u} = \rho\boldsymbol{u}^{(n)} \tag{2.3.16}$$

Finally, thanks to the orthogonality properties of the Hermite polynomials [112], it is possible to truncate the development of $f^{(0)}$ to an order N, while keeping intact the values of the N lower-order Hermite moments

$$f^{(0)}(\boldsymbol{x},\boldsymbol{\xi},t) \simeq f^{(0),N}(\boldsymbol{x},\boldsymbol{\xi},t) = w(\boldsymbol{\xi})\sum_{n=0}^{N}\frac{1}{n!(r_g T_0)^n}\boldsymbol{a}_0^{(n)}(\boldsymbol{x},t) : \mathcal{H}^{(n)}(\boldsymbol{\xi}). \tag{2.3.17}$$

2.3.2 Truncation of the distribution functions

As previously discussed in Sec. 2.2.2.c, the equilibrium moments up to the fourth-order ($N = 4$) are needed to recover the full Navier-Stokes Fourier equations. However, it is very common to truncate the equilibrium expansion to a lower level in order to reduce the CPU-costs (*cf.* Sec. 2.3.3) but this will induce error terms in the macroscopic equations.

For $N = 3$, there is an error in the energy equations since the fourth-order equilibrium moment is not preserved by the truncation. With the isothermal approximation $\theta = 1$, the isothermal Navier-Stokes equations are recovered without error terms.

For $N = 2$, too many error terms are introduced in the energy equation, this last cannot be used anymore. The isothermal hypothesis ($\theta = 1$) becomes mandatory and an error term appears in the viscous stress tensor within the momentum equation due to a wrong third-order equilibrium moment.

$$\Pi^{(1)}_{\alpha\beta} = -\tau \int_{\mathbb{R}} \xi_\alpha \xi_\beta \frac{\partial f^{(0),2}}{\partial t^{(0)}} + \underbrace{\xi_\alpha \xi_\beta \xi_\gamma \frac{\partial f^{(0),2}}{\partial x_\gamma}}_{=\Pi'^{(1)}} \mathrm{d}\boldsymbol{\xi}, \tag{2.3.18}$$

$$\Pi'^{(1)}_{\alpha\beta} = \underbrace{\int_{\mathbb{R}} \mathcal{H}^{(3)}_{\alpha\beta\gamma} \frac{\partial f^{(0),2}}{\partial x_\gamma} \mathrm{d}\boldsymbol{\xi}}_{=0 \neq \nabla\cdot(\rho \boldsymbol{u}^3)} + r_g T_0 \int_{\mathbb{R}} (\delta_{\alpha\beta}\xi_\gamma + \delta_{\alpha\gamma}\xi_\beta + \delta_{\beta\gamma}\xi_\alpha) \frac{\partial f^{(0),2}}{\partial x_\gamma} \mathrm{d}\boldsymbol{\xi}. \tag{2.3.19}$$

Due to the orthogonality properties of the Hermite polynomials, the first term vanish, since it must be present in the stress tensor. A $\mathcal{O}\left(Ma^3\right)$ error term is therefore present in the stress tensor of the momentum equation leading to the well known weakly compressible limit of the athermal LBM that is mostly employed [106].

2.3.3 Gauss-Hermite quadrature

Up to now, it has been seen that the Hermite expansion is a useful basis to expand the equilibrium distribution function since the expansion coefficients correspond to the Hermite velocity moments of the equilibrium distribution function. Furthermore, the orthogonality properties allows truncating the expansion up to a given order without affecting the lower-order moments. Another convenient point is the possibility to preserve exactly the moments of $f^{(0)}$ by integrating them on a finite number of discrete velocities $\boldsymbol{\xi}_i$ by means of a Gauss-Hermite quadrature.

Indeed, following [112], the integrand of Eq. (2.3.10) with $f^{(0),N}$ the truncated development of $f^{(0)}$ at an order $N \geq n$ can be written as:

$$f^{(0),N}(\boldsymbol{x}, \boldsymbol{\xi}, t)\boldsymbol{\mathcal{H}}^{(n)}(\boldsymbol{\xi}) = w(\boldsymbol{\xi})\mathcal{P}(\boldsymbol{x}, \boldsymbol{\xi}, t), \tag{2.3.20}$$

where $\mathcal{P}(\boldsymbol{x}, \boldsymbol{\xi}, t)$ is a polynomial in $\boldsymbol{\xi}$ of a degree not greater than $n+N \geq 2n$. Furthermore, the orthogonality properties of the Hermite polynomials allow writing

$$\boldsymbol{a}_0^{(n)}(\boldsymbol{x}, t) = \int f^{(0),N}(\boldsymbol{x}, \boldsymbol{\xi}, t)\boldsymbol{\mathcal{H}}^{(n)}(\boldsymbol{\xi})\mathrm{d}\boldsymbol{\xi} = \int w(\boldsymbol{\xi})\mathcal{P}(\boldsymbol{x}, \boldsymbol{\xi}, t)\mathrm{d}\boldsymbol{\xi}. \tag{2.3.21}$$

It is then possible to integrate the latter expression using a Gauss-Hermite quadrature [106]. This quadrature allows to evaluate exactly the integral (Eq. 2.3.21) by its values at a set of discrete abscissae. The $\boldsymbol{a}_0^{(n)}$ expansion coefficients can be expressed as a weighted sum of $\mathscr{P}(\boldsymbol{x},\boldsymbol{\xi},t)$ values estimated at specific discrete velocities $\boldsymbol{\xi}_i$, $i \in [0, V-1]$

$$\int w(\boldsymbol{\xi})\mathscr{P}(\boldsymbol{x},\boldsymbol{\xi},t)\mathrm{d}\boldsymbol{\xi} = \sum_{i=0}^{V-1} w_i \mathscr{P}(\boldsymbol{x},\boldsymbol{\xi}_i,t), \tag{2.3.22}$$

where w_i and $\boldsymbol{\xi}_i$ are the discrete Gaussian weights and the abscissae respectively. In such case, the quadrature has a $Q \geq 2n$ order of accuracy. V is the number of points used to exactly integrate Eq. (2.3.22). If one goes back to the calculation of the equilbrium moments of interest, using a discrete set of velocities, one gets

$$\boldsymbol{a}_0^{(n)}(\boldsymbol{x},t) = \int w(\boldsymbol{\xi}) \underbrace{\frac{f^{(0),N}(\boldsymbol{x},\boldsymbol{\xi},t)}{w(\boldsymbol{\xi})}\mathscr{H}^{(n)}(\boldsymbol{\xi})}_{p(\boldsymbol{x},\boldsymbol{\xi},t)}\mathrm{d}\boldsymbol{\xi} = \sum_{i=0}^{V-1} w_i \underbrace{\frac{f^{(0),N}(\boldsymbol{x},\boldsymbol{\xi}_i,t)}{w(\boldsymbol{\xi}_i)}\mathscr{H}^{(n)}(\boldsymbol{\xi}_i)}_{p(\boldsymbol{x},\boldsymbol{\xi}_i,t)}, \tag{2.3.23}$$

if we define $f_i^{(0),N}(\boldsymbol{x},t) = w_i \frac{f^{(0),N}(\boldsymbol{x},\boldsymbol{\xi}_i,t)}{w(\boldsymbol{\xi}_i)}$, the discrete Hermite equilbrium moments $\boldsymbol{a}_0^n$ can be expressed as

$$\boldsymbol{a}_0^{(n)}(\boldsymbol{x},t) = \sum_{i=0}^{V-1} f_i^{(0),N}(\boldsymbol{x},t)\mathscr{H}_i^{(n)}, \tag{2.3.24}$$

where $\mathscr{H}_i^{(n)} = \mathscr{H}^{(n)}(\boldsymbol{\xi}_i)$. Incidentally, one can remark from Eq. (2.3.24) that the unit of $f_i^{(0)}$ has changed with the velocity discretization. If the first moment is compute, it gives $\sum_{i=0}^{V-1} f_i^{(0)} = \rho$, thus $\tilde{f}_i^{(0)} = f_i^{(0)}/\rho_0$ instead of the non-dimensionalization proposed in Eq. (2.2.39).

Eventually Eq. (2.3.17) can be rewritten in its form with discretized velocities. For instance, the equilibrium distribution function reads

$$f_i^{(0),N}(\boldsymbol{x},t) = w_i \sum_{n=0}^{N} \frac{1}{n!(r_g T_0)^n} \boldsymbol{a}_0^{(n)}(\boldsymbol{x},t) : \mathscr{H}_i^{(n)}. \tag{2.3.25}$$

Finally, from the above velocity discretization of the distribution functions, the discrete velocity Boltzmann equation (DVBE) is obtained

$$\frac{\partial f_i}{\partial t} + \boldsymbol{\xi}_i \cdot \frac{\partial f_i}{\partial \boldsymbol{x}} = -\frac{1}{\tau}\left(f_i - f_i^{(0),N}\right). \tag{2.3.26}$$

This equation involves both a truncation of the equilibrium function up to an order N, and a velocity discretization obtained through the Gauss-Hermite quadrature. This discretization is performed on a discrete velocity set, called velocity lattice. One can thus notice that Eq. (2.3.26) is composed of as many equations as the number of discrete velocities. Obviously, the bigger the order of the quadrature, the more discrete velocities the lattice will contain and therefore the more equations will have to be solved to integrate exactly the $f^{(0)}$ moments up to an order N.

The lattices are generally denoted with the $\mathrm{D}_D\mathrm{Q}_V$ convention, and are associated to a $E^V_{D,Q}$ quadrature [112], where V is the number of discrete velocities, D is the number of space dimension and Q is the accuracy order of the quadrature.

Several quadratures with a given accuracy order are listed bellow:

- $\underline{Q = 9}$: These quadratures allow the exact moments of the equilibrium function $f^{(0),N}$ to be recovered up to the fourth-order ($N = 4$) since $Q \geq 2N$. This kind of quadrature is thus required to recover the full Navier-Stokes Fourier equations. The most common quadratures are $E^{37}_{2,9}$ and $E^{103}_{3,9}$ for the D2Q37 (see Fig. 2.1) and D3Q103 lattices respectively [127]. These kinds of quadratures requires to solve a very large number of equations since the above velocity discretization involves to solve one equation per discrete velocity. Moreover, the velocity norms are such that third-order neighbors will be necessary in the LB scheme during the streaming step which will be described in Sec. 2.4. These two reasons make the $Q = 9$ quadrature too expensive to solve numerically and will not be studied in the present thesis.

- $\underline{Q = 7}$: These quadratures allow the exact moments of the equilibrium function $f^{(0),N}$ to be recovered up to the third-order ($N = 3$) since $Q \geq 2N$. This kind of quadrature is thus required to recover the Navier-Stokes equations with no-error terms in the momentum equation. Furthermore, the energy equation could be recovered with an error term in the heat flux term q. The most common quadratures are $E^{17}_{2,7}$ and $E^{39}_{3,7}$ for the D2Q17 (see Fig. 2.1) and D3Q39 lattices respectively [112].

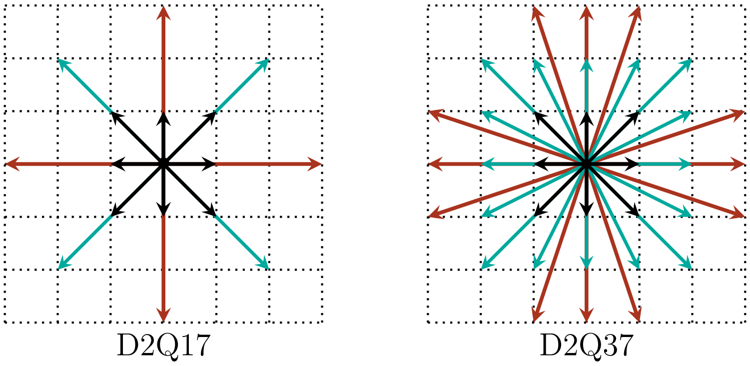

Figure 2.1 – D2Q17 *and* D2Q37 *lattices.*

- $\underline{Q = 5}$: These quadratures allow the exact moments of the equilibrium function $f^{(0),N}$ to be recovered up to the second-order ($N = 2$) since $Q \geq 2N$. The athermal Navier-Stokes equations ($\theta = 1$) with a cubic Mach error terms in the momentum equation can be retrieved. The most common quadratures are $E^{9}_{2,5}$ and $E^{27}_{3,5}$ or $E^{19}_{3,5}$ for the D2Q9 and D3Q27 or D3Q19 lattices respectively [112].

Lattice		$\boldsymbol{\xi}_i/\sqrt{3}$ (permutations)	w_i	$1/c_s$
D2Q9	$E^9_{2,5}$	$(0,0)$	$4/9$	$\sqrt{3}$
		$(\pm1,0)$	$1/9$	
		$(\pm1,\pm1)$	$1/36$	
D3Q19	$E^{19}_{3,5}$	$(0,0,0)$	$1/3$	$\sqrt{3}$
		$(\pm1,0,0)$	$1/18$	
		$(\pm1,\pm1,0)$	$1/36$	

Table 2.1 – *Summary of gaussian weight* w_i *and set of discrete velocities* $\boldsymbol{\xi}_i$ *for the* D2Q9 *and* D3Q19 *lattice. The constant* c_s *is a characteristic of the lattice.*

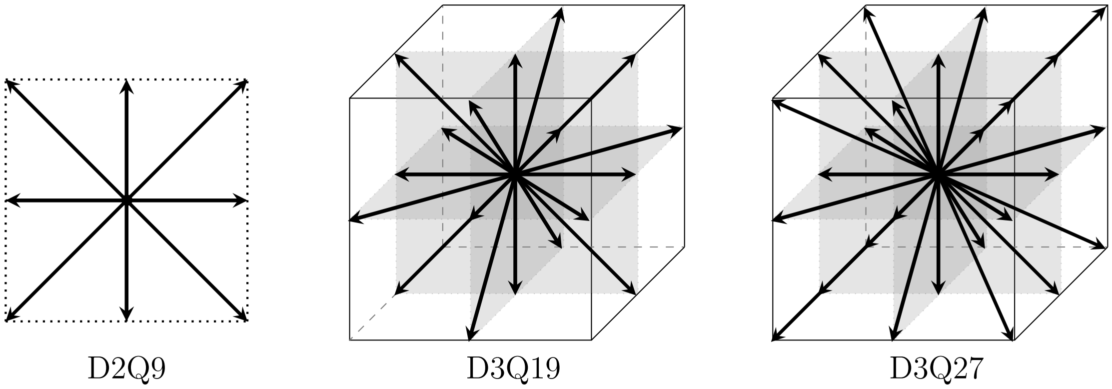

Figure 2.2 – D2Q9 *and* D3Q19 *and* D3Q27 *lattices.*

The D2Q9 and D3Q19 lattices will be used through this manuscript. This last is the widely used in the tridimensional standard athermal lattice Boltzmann method, since it is more CPU-efficient and less memory consuming than the D3Q27 [76].

The Gaussian weight w_i and the discrete velocities $\boldsymbol{\xi}_i$ are summarized in the Table. 2.1

So far, we have seen that there is a particle distribution function f which allows to find usual macroscopic quantities (ρ,$\boldsymbol{u}$,T) through the computation of its moments. Furthermore, the Boltzmann's equation, governing the evolution of this distribution function and involving a Ω collision operator was introduced. The simplified BGK collision operator was presented and it was shown that the hydrodynamic limits of the Boltzmann equation with this collision operator allowed the Navier-Stokes Fourier equations with a fixed Prandtl number of $Pr^{\text{BGK}} = 1$ to be recovered. Subsequently, the equilibrium distribution functions were developed in a Hermite formalism whose expansion coefficients are directly related to the moments of the distribution function. This development allows to take advantage of the orthogonality properties of Hermite polynomials, very useful to truncate this development to an order N. Furthermore, it allows integrating exactly the moments on a finite number of discrete velocity called lattice. These lattices have a discrete velocity number that defines the accuracy of the quadrature. Thus, the higher the discrete velocity number, the more exactly $f^{(0)}$ moments can be integrated up to a given order, but the higher the CPU-cost for solving the DVBE numerically will be. In this thesis, isothermal simulations with a relatively low Mach number will be sufficient to study flows around landing gears that are generally below Mach 0.5. This is why a quadrature of order $Q = 5$ with lattices D2Q9 and D3Q19 will be preferred. These quadratures bring too much error in the energy equation, so an isothermal hypothesis $\theta = 1$ (or athermal since temperature has no physical meaning) is made. In the next section the consequences of such hypothesis will be discussed.

2.3.4 The athermal hypothesis

The choice of a fifth-order quadrature imposes that the energy conservation equation (2.2.33) cannot be correctly retrieved due to the too large number of error terms appearing in it. Thus, the choice to set $\theta = T/T_0 = 1$ becomes mandatory, which replaces the energy equation by a scalar constraint.

The main consequences are:

- The ideal equation of state defined in Eq. (2.2.9) becomes

  $$p = \rho r_g T_0 \tag{2.3.27}$$

  and the speed of sound differs from the standard speed of sound derived at constant entropy $c_0^{therm} = \sqrt{\gamma r_g T}$ that involves the heat capacity ratio $\gamma = c_p/c_v$. In the isothermal case, it reads

  $$c_0 = \sqrt{r_g T_0} \tag{2.3.28}$$

  and the dimensionless temperature defined in Eq. (2.2.40) reduces to

  $$r_g \tilde{T} = 1. \tag{2.3.29}$$

  A factor $\sqrt{\gamma}$ is missing in the definition of the sound velocity, but fortunately a correct sound velocity can be imposed in the isothermal case by modifying the reference temperature T_0 as shown in Sec. 2.4.

- The macroscopic equations recovered during the Chapman-Enskog development differs than from the one obtained in the thermal case. Firstly, the energy equation has no more physical sense, and secondly, as explained in the article by Dellar [128], in the athermal case, the term in $\frac{2}{D}\frac{\partial u_\gamma}{\partial x_\gamma}\delta_{\alpha\beta}$ present in $\sigma_{\alpha\beta}^{(1)}$ of Eq. (2.2.52) is null and the stress tensor is reduced to

  $$\sigma_{\alpha\beta}^{(1)} = -2\mu S_{\alpha\beta}, \tag{2.3.30}$$

This expression differs from the one used by Dellar [128] or Landau & Lifshitz [129]

$$\sigma_{\alpha\beta}^{(1)} = -\mu\left(2S_{\alpha\beta} - \frac{2}{D}\frac{\partial u_\gamma}{\partial x_\gamma}\delta_{\alpha\beta}\right) - \mu_b\frac{\partial u_\gamma}{\partial x_\gamma}\delta_{\alpha\beta}, \tag{2.3.31}$$

where μ_b is referred as the second or bulk viscosity. In the thermal case, the right term associated to the bulk viscosity is null ($\mu_b = 0$), whereas in the athermal case, $\mu_b = \frac{2}{D}\mu$. Practically speaking, since the dissipation of acoustic waves is related to the bulk viscosity, these waves will be slightly more dissipated in the isothermal case.

Now that the Boltzmann's equation has been discretized in velocity space and the assumptions engendered by this discretization have been seen, the discretization in space and time is detailed in the following section.

2.4 Space and time discretization: The lattice Boltzmann method

The aim of this section is to discretize in space and time the DVBE described by Eq. (2.3.26) to arrive to the LB scheme. Generally, the left-hand side (LHS) term which is linear and corresponds to an advection of the distribution functions f at a constant velocity $\boldsymbol{\xi}_i$, is integrated exactly using the method of characteristics. The collision operator on the right-hand side (RHS) is often discretized using the trapezoidal rules to ensure a second-order accuracy in time.
The integration along the characteristic line $(\boldsymbol{x} + \boldsymbol{\xi}_i, t + s)$ reads

$$\int_0^{\Delta t}\left(\frac{\partial f_i}{\partial t} + \boldsymbol{\xi}_i\cdot\frac{\partial f_i}{\partial \boldsymbol{x}}\right)\mathrm{d}s = \int_0^{\Delta t}\Omega_i(\boldsymbol{x} + \boldsymbol{\xi}_i s, t + s)\,\mathrm{d}s, \tag{2.4.1}$$

The LHS term can be integrated exactly. The RHS term is evaluated by a trapezium rule:

$$f_i(\boldsymbol{x} + \boldsymbol{\xi}_i\Delta t, t + \Delta t) - f_i(\boldsymbol{x}, t) = \frac{\Delta t}{2}\Big[\Omega_i(\boldsymbol{x} + \boldsymbol{\xi}_i\Delta t, t + \Delta t) + \Omega_i(\boldsymbol{x}, t)\Big] + O(\Delta t^2) \tag{2.4.2}$$

This scheme is implicit and can be made explicit by an appropriate variable change [117].

$$g_i = f_i - \frac{\Delta t}{2}\Omega_i. \tag{2.4.3}$$

Injecting Eq. (2.4.3) into Eq. (2.4.2), an explicit scheme is obtained

$$g_i(\boldsymbol{x} + \boldsymbol{\xi}_i\Delta t, t + \Delta t) - g_i(\boldsymbol{x}, t) = \Delta t\Omega_i(\boldsymbol{x}, t), \tag{2.4.4}$$

This change of variable requires an adaptation of the BGK collision operator to be consistent with the new distributions g_i.

$$
\begin{aligned}
\Omega_i^{\mathrm{BGK}} &= -\frac{1}{\tau}\left(f_i - f_i^{(0),N}\right) = -\frac{1}{\tau}\left(g_i + \frac{\Delta t}{2}\Omega_i^{\mathrm{BGK}} - f_i^{(0),N}\right) \\
&= -\frac{1}{\tau + \Delta t/2}\left(g_i - f_i^{(0),N}\right).
\end{aligned} \tag{2.4.5}
$$

Hence, substituting Eq. (2.4.5) in Eq. (2.4.4), the LB equation for the BGK collision operator is obtained

$$
g_i(\boldsymbol{x} + \boldsymbol{\xi}_i \Delta t, t + \Delta t) - g_i(\boldsymbol{x}, t) = -\frac{\Delta t}{\bar{\tau}}\left(g_i(\boldsymbol{x}, t) - f_i^{(0),N}(\boldsymbol{x}, t)\right), \tag{2.4.6}
$$

with $\bar{\tau} = \tau + \Delta t/2$ the discrete relaxation time. A fully explicit and discretized LB-BGK scheme is obtained with modified g_i distribution functions.
Since the variable change described in Eq. (2.4.3) involves the collision operator that must respect the collision invariants, f_i and g_i share the same conserved moments.

$$
\sum_{i=0}^{V-1} g_i = \sum_{i=0}^{V-1} f_i = \rho, \tag{2.4.7}
$$

$$
\sum_{i=0}^{V-1} \boldsymbol{\xi}_i g_i = \sum_{i=0}^{V-1} \boldsymbol{\xi}_i f_i = \rho \boldsymbol{u}, \tag{2.4.8}
$$

The advection term on the LHS of Eq. (2.4.6) with such discretization in space, time and velocity on the aforementioned lattice, gives a link between the time step Δt, the mesh size Δx, and the microscopic velocity norm $||\boldsymbol{\xi}_i||$:

$$
\Delta x = ||\boldsymbol{\xi}_i||\Delta t \tag{2.4.9}
$$

This equality imposes the distribution functions g_i, to move from one node at position $\boldsymbol{x}$ to their neighbors at position $\boldsymbol{x} + \boldsymbol{\xi}_i \Delta t$, during one time step on a Cartesian grid.
Usually in a LB solver, these values are set to $\Delta x = \Delta t = 1$ to simplify the code and make the implementation more efficient. It is then convenient to normalize the velocities $\boldsymbol{e}_i = \boldsymbol{\xi}_i c_s$ with c_s the constant characteristic of the lattice given in Table 2.1.

These normalizations give rise to the famous lattice units (noted with a superscript *). In the athermal hypothesis ($T = T_0$, $c_0 = \sqrt{r_g T_0}$) and by employed the previous notation to make dimensionless the DVBE in Eq. (2.2.39), it reads

$$
\boldsymbol{e}_i = \frac{\boldsymbol{\xi}_i}{c_0} c_s = \tilde{\boldsymbol{\xi}}_i c_s \quad ; \quad \bar{\tau}^* = \frac{\bar{\tau}}{\tau_0 \Delta t} = \frac{\tilde{\bar{\tau}}}{\Delta t} \quad ; \quad \boldsymbol{x}^* = \frac{\boldsymbol{x}}{l_0 \Delta x} = \frac{\tilde{\boldsymbol{x}}}{\Delta x} \tag{2.4.10}
$$

$$
t^* = \frac{t c_0}{l_0 \Delta t} = \frac{\tilde{t}}{\Delta t} \quad ; \quad \boldsymbol{g}_i^* = \tilde{\boldsymbol{g}}_i \quad ; \quad c_0^* = \frac{c_0}{\sqrt{r_g T_0}} = \tilde{c}_0 c_s. \tag{2.4.11}
$$

and, following Eq. (2.2.40) the macroscopic variables in lattice units are given by

$$\rho^* = \frac{\rho}{\rho_0} = \tilde{\rho} \quad ; \quad \boldsymbol{u}^* = \frac{\boldsymbol{u} c_s}{c_0} = \tilde{\boldsymbol{u}} c_s \quad ; \quad r_g T^* = \frac{r_g T c_s^2}{c_0^2} = r \tilde{T}_g c_s^2 \tag{2.4.12}$$

With the lattice units convention previously defined, the LB-BGK scheme becomes

$$g_i^*(\boldsymbol{x}^* + \boldsymbol{e}_i, t^* + 1) - g_i^*(\boldsymbol{x}^*, t^*) = -\frac{1}{\overline{\tau}^*}\left(g_i^*(\boldsymbol{x}^*, t^*) - f_i^{*,(0),N}(\boldsymbol{x}^*, t^*)\right), \tag{2.4.13}$$

This numerical scheme can be seen as a collision & propagation (or collide & stream) algorithm. In a LB solver, this scheme is generally divided into two steps:

1. A collision step:

$$g_i^{*,coll}(\boldsymbol{x}^*, t^*) = g_i^*(\boldsymbol{x}^*, t^*) - \frac{1}{\overline{\tau}^*}\left(g_i^*(\boldsymbol{x}^*, t^*) - f_i^{*,(0),N}(\boldsymbol{x}^*, t^*)\right), \tag{2.4.14}$$

2. A propagation step:

$$g_i^*(\boldsymbol{x} + \boldsymbol{e}_i, t + 1) = g_i^{*,coll}(\boldsymbol{x}, t), \tag{2.4.15}$$

where the first step is purely local. Although very simple here with the BGK collision operator, it will be seen later in Chap. 4 that the use of more advanced collision operators, necessary to perform realistic aeroacoustic simulations, will require much more operations to perform the collision step. The second step is merely a copy of the g_i values from the current node to the neighboring ones. In Eq. (2.4.15) it is expressed in the so-called push convention. This step is also frequently expressed in the pull convention (*i.e.* from the neighboring nodes to the current one $g_i(\boldsymbol{x}, t+1) = g_i^{coll}(\boldsymbol{x} - \boldsymbol{e}_i, t)$) for formulating boundary conditions.

An important point in the LBM is the physical sound speed c. Indeed, since in the athermal formulation, the temperature has no meaning, the question of the speed of sound is to be considered.

$$c = c_0^* \frac{\Delta x}{\Delta t} = \tilde{c}_0 c_s \frac{\Delta x}{\Delta t} \qquad \text{with } \tilde{c}_0 = 1 \text{ in the athermal case.} \tag{2.4.16}$$

Thus, because the mesh size is fixed to reach a given resolution, the speed of sound is imposed by the timestep Δt. This relation is called *"acoustic scaling"* [130].
Last but not least, since $r\tilde{T} = 1$, the pressure in lattice units is expressed as

$$p^* = \rho^* c_s^2, \tag{2.4.17}$$

and from Eq. (2.2.55) the kinetic viscosity after the variable change defined in Eq. (2.4.3) gets

$$\overline{\nu}^* = c_s^2 \left(\overline{\tau}^* - 0.5\right), \tag{2.4.18}$$

For the sake of clarity, the * superscripts are removed in the following and, apart from an explicit mention, the lattice units will always be used until Chap. 6.

2.5 Summary: From Boltzmann to the lattice Boltzmann method

In this chapter, the main steps to move from the Boltzmann equation to the LB method are described, along with the associated physics modeling assumptions. The procedure can be summarized on Fig. 2.3, with in green, the choices retained for this thesis.

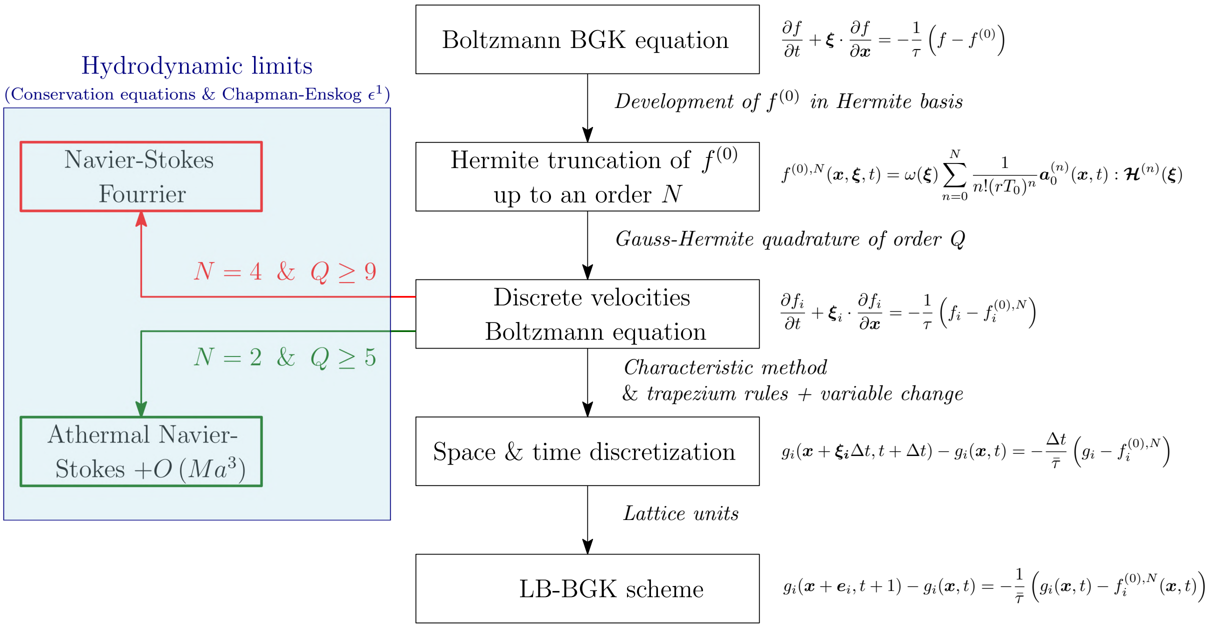

Figure 2.3 – *Summary of the main steps to go from the Boltzmann equation to the LBM scheme. Green: Choice retained for this thesis. Red: Choice declined for this thesis.*

It was decided to use a quadrature of $Q = 5$ order which restricts the limits of the physics obtained to the athermal Navier-Stokes equations, with a cubic Mach error in the stress tensor. This choice in theory restricts the LBM to Ma < 0.732 [113, 114] which are in the scope of landing-gear simulations. In practice, space and time discretization reduces the range of stability as shown in Chap. 5. This quadrature allows for efficient CPU-time simulations, as it enables the use of lattices with small number of discrete velocities (9 in two dimensions and 19 in three dimensions).

Finally, the LBM scheme without boundary conditions can be simply summarized with four steps:

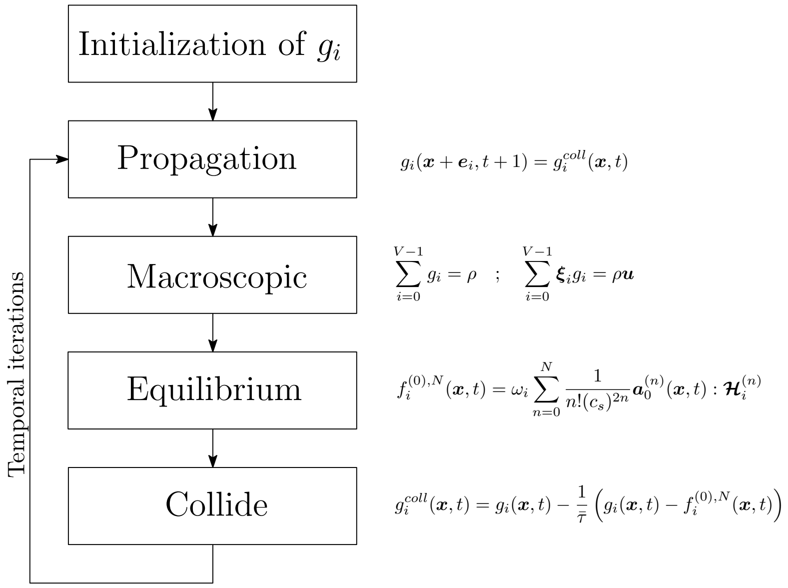

Figure 2.4 – *Main steps of a LBM-BGK scheme*

The initialization of the distribution functions g_i can be made at equilibrium $g_i = f_i^{(0),N}$. It can also be accomplished by imposing the non-equilibrium part $g_i^{(1)}$ but once the notions of regularization will be introduced in Sec. 4.1.

The final LB scheme is very basic and local, the only step that involves neighboring nodes is the propagation step that requires only the direct neighbors. There are many optimizations for this step, including memory address exchanges. These optimizations are summarized here [131,132]. The simplicity and locality of the LB algorithm makes it very easy to parallelize, and gives promising perspectives on GPUs [94,95,132,133].

However, this very simple BGK model is rarely used in practice for stability issues in particular, and many more advanced collision models have been developed to overcome these weaknesses. Some of these models will be presented in Chap. 4, but we will here illustrate how this model is limiting for aeroacoustic applications. Two aspects will be assessed: the stability and quality of the results obtained with simulation involving non-uniform meshes, since it is a mandatory criterion for industrial applications.

2.6 The BGK collision operator: weaknesses for aeroacoustic simulations

The BGK model is widely known for its simplicity, but also for its stability issues. Indeed, it is well recognized in the literature [134] that the BGK model suffers from severe stability issues, especially due to non-hydrodynamic mode contributions for under-resolved simulations [135].
Nevertheless, we did the exercise of simulating a turbulent flow past a cylinder with non-uniform meshes with a diameter chosen to be representative of the LAGOON landing gear wheel shown on Fig. 7.1. The objective is to see from which pair of Reynolds (Re) and Mach (Ma) number this type of simulation gets unstable, and to examine, in the case of stable simulation, qualitatively the results obtained. Indeed, it is interesting to look at the Mach limit since it is known that the athermal LBM [136] is restricted to low Mach numbers (about Ma< 0.4). This limit will be further studied in Chap. 5.

A sketch of the simulation domain is presented on Fig. 2.5. Three resolution domains (RD) are placed around the cylinder, on which a wall law taking into account adverse pressure gradients and curvature effects is applied [66, 78].

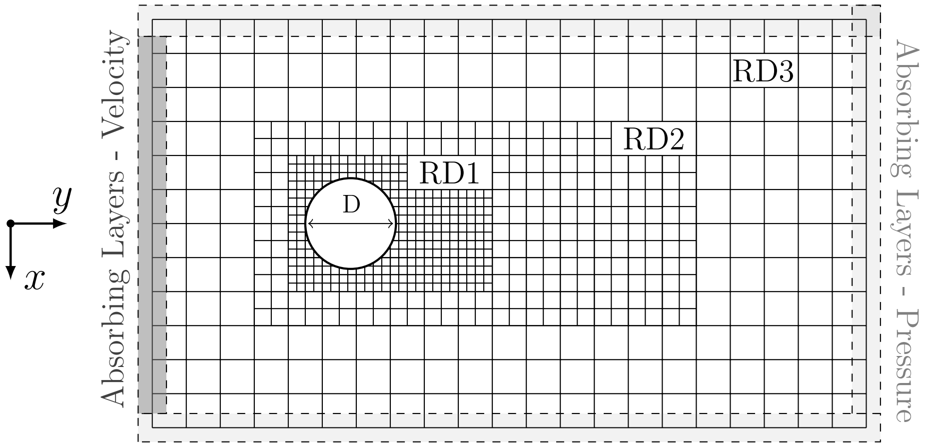

Figure 2.5 – *Sketch of the simulation domain for the cylinder test case. Three refinement domains* (RD) *are used. Absorbing layers map the domain boundaries to avoid any acoustic reflection.*

The simulation parameters are:

$$\mathrm{M}_\infty \in [0.1-0.3], \quad \rho_\infty = 1.17621\mathrm{kg.m}^{-3}, \quad \Delta x^f = 0.001\mathrm{m}, \quad \mathrm{D} = 0.3\mathrm{m}, \quad \mathrm{T} = 0.5\mathrm{s},$$

where M_∞ is the free stream Mach number imposed at the inlet, D is the cylinder diameter and T the overall simulation time.

		Reynolds number				
		1000	5000	10000	50000	100000
$\mathbf{M}_\infty$	0.1	✓	✓	✓	✓	×
	0.2	✓	✓	✓	×	×
	0.3	✓	×	×	×	×

Table 2.2 – *Summary of the simulation status for the cylinder test case with increasing Reynold and Mach numbers.* ✓*: stable,* ×*: unstable.*

A Dirichlet velocity boundary condition is imposed at the inlet and a Dirichlet density boundary condition at the outlets. Furthermore, absorbing layers [79] map the domain boundaries to avoid acoustic reflections and reduce the spurious noise that may be caused by the impact of the turbulent wake on the outlet Dirichlet condition.

Simulations with Reynolds number ranging from 10^3 to 10^5 and Mach number ranging from 0.1 to 0.3 are performed. The simulation status (stable or not after the overall simulation time) are summarized in Table 2.2. Simulations are stable up to a Reynolds number of $5{\cdot}10^4$ for a Mach number of 0.1. Nevertheless, when the Mach number increases up to 0.3, only the simulation at $\text{Re} = 1000$ is stable, corresponding to the simulation with the highest viscosity. With this modeling, it is clear that it is already impossible to simulate landing gear aeroacoustics, where typical Reynolds are several million and typical Mach number is $\text{Ma} \simeq 0.2$ for isolated landing gear and $\text{Ma} \simeq 0.5$ for installed landing gear under high-lift devices [137].

Now let's focus on the quality of the obtained results for stable simulations. To this purpose, the $\text{M}_\infty = 0.1$ simulations are studied. At first, the velocity divergence fields (or dilatation fields) are considered, allowing to clearly visualize the acoustic waves propagating in the fluid domain. Fig. 2.6 very clearly illustrates that when the Reynolds number increases (here, when the viscosity decreases), the dilatation fields become obstructed by at least two non-physical phenomena:

1. Spurious acoustic sources occur centered in areas of varying refinement level. These last seem to specifically appear as the vortex wake passes through the resolution levels.

2. High-frequency spurious waves (with a short wavelength) appear and propagate close to vortex shedding and pollute the simulations. They are particularly apparent when the resolution decreases.

It is also interesting to consider the vorticity fields. These allow seeing the von Karman vortices, and especially in this case, the spurious vortices that may appear with the BGK model. As depicted on Fig. 2.7, spurious vorticity waves appear within the fluid even upstream the cylinder. These become more and more prominent as the Reynolds number increases. Hasert in his thesis [84] encountered similar spurious behavior and reduced it using first-order spatial interpolation scheme in the grid coupling algorithm. Obviously this solution is not satisfactory to preserve an accurate scheme.

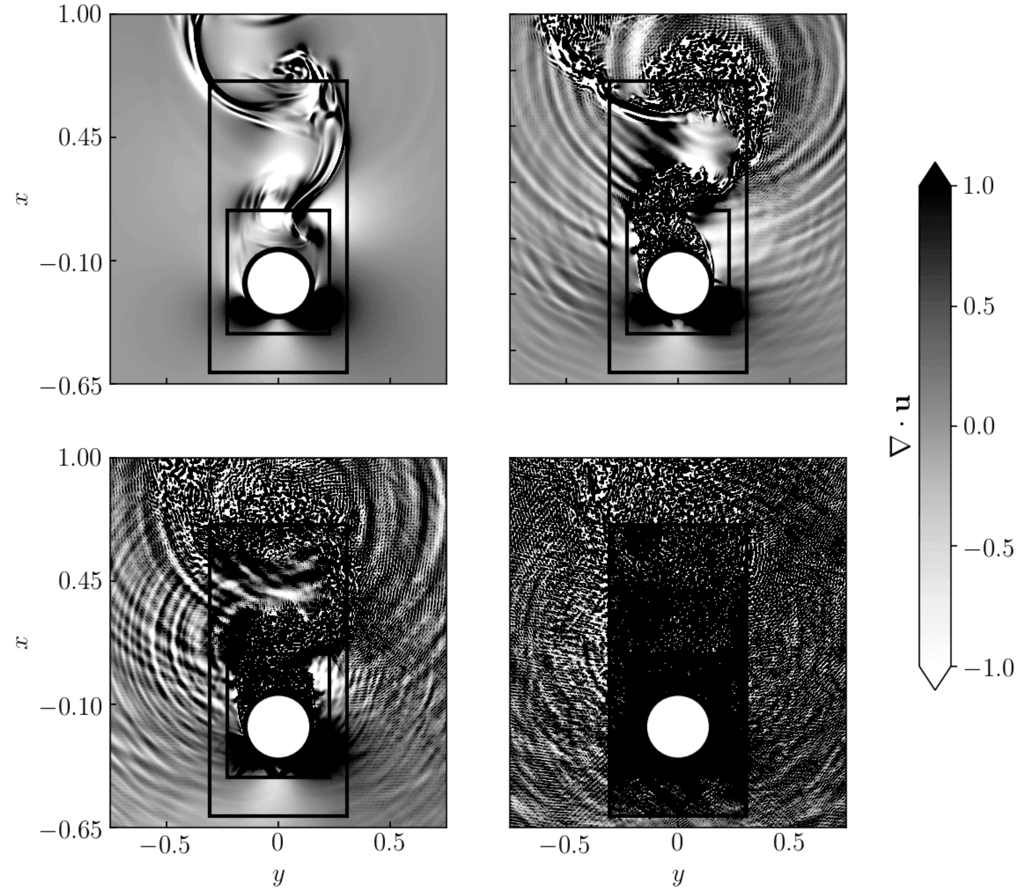

Figure 2.6 – *Velocity dilatation field* $(\nabla \cdot \mathbf{u})$ *of the flow around a cylinder with three resolution levels and increasing Reynolds numbers. The Mach number is fixed to* $\mathrm{M}_\infty = 0.1$*. From top left to bottom right:* $\mathrm{Re} = 1 \cdot 10^3$, $\mathrm{Re} = 5 \cdot 10^3$, $\mathrm{Re} = 1 \cdot 10^4$, $\mathrm{Re} = 5 \cdot 10^4$.

Qualitatively, two distinct sources of spurious waves can be differentiated:

1. Non-physical waves originate from the cylinder wall and propagating in all directions. In particular, these waves can travel up the flow until they reach the resolution domains upstream of the cylinder where they apparently seem attach.
2. High-frequency spurious waves that propagate in the normal direction of vortices and seem to distort physical von Karman vortices.

This test case, although very qualitative, exhibits the stability problems of the BGK model when the Reynolds and Mach number increases. Moreover, spurious waves that pollute simulations are highlighted, with the generation of parasitic vorticity that can interfere with physical vortices, and spurious noise. Furthermore, a generation of unwanted noise appears when a vortex passes through a refinement level. All in all, the BGK model is not suited for aeroacoustic simulations with flow conditions typical of an aeronautical application.

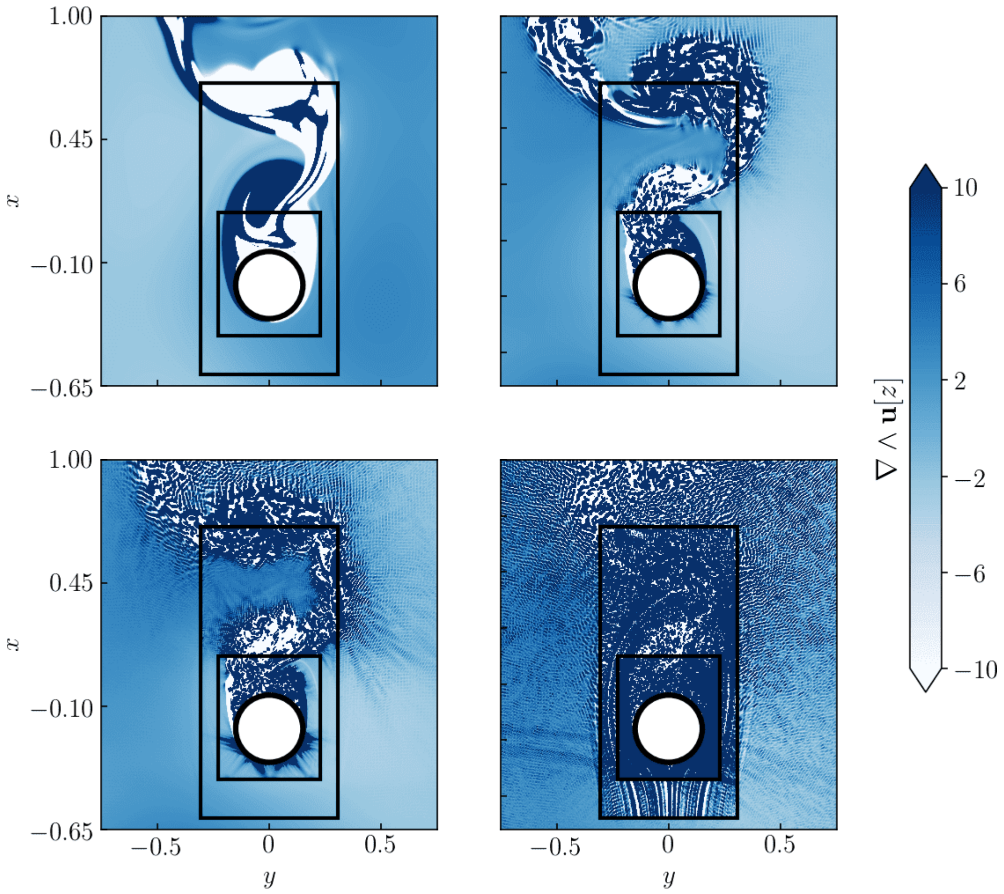

Figure 2.7 – *Z-component of the vorticity field* $(\nabla \wedge \mathbf{u}[z])$ *of the flow around a cylinder with three resolution levels and increasing Reynolds numbers. The Mach number is fixed to* $\mathrm{M}_\infty = 0.1$. *From top left to bottom right:* $\mathrm{Re} = 1 \cdot 10^3$, $\mathrm{Re} = 5 \cdot 10^3$, $\mathrm{Re} = 1 \cdot 10^4$, $\mathrm{Re} = 5 \cdot 10^4$.

The simulations carried out above with the BGK model allow anticipating that **three main problems need to be studied and improved during this PhD thesis** in order to **perform accurate industrial aeroacoustic simulations**.

- **The stability of the numerical scheme needs to be carefully considered** for achieving simulations with high Reynolds numbers and a moderate Mach number up to $\mathrm{Ma} \simeq 0.4$.
- **The obtained macroscopic fields should no longer involve neither spurious vorticity nor spurious acoustic waves** propagating in the fluid domain.
- The **accuracy of the grid coupling algorithm**, that allows an information transfer from grids of various space step, is of paramount importance. It has to be improved for reducing the spurious noise generated by a vortex that crosses such interface.

These points will be dealt within separate chapters. First, we will study the **origin of the spurious waves** that appear on Fig. 2.6 and Fig. 2.7 using the BGK collision model in Chap. 3. To this extend, stability analysis tools will be used and adapted to the analysis of LB schemes with non-uniform resolution. Subsequently, **improvements of the fluid modeling** will be proposed in Chap. 4 to overcome such issues that pollute simulations. The **stability and acoustic properties** of several collision models will then be discussed in Chap. 5. Finally, the **quality of the grid coupling algorithm** will be investigated and improved in Chap. 6 before industrial aeroacoustic simulations can be performed.

Chapter 3

Linear stability analysis: A tool for understanding the BGK model weaknesses for non-uniform simulations

Contents

This chapter is dedicated to the comprehension of the spurious phenomena appearing with the BGK model during LBM simulations with non-uniform grids in Sec. 2.6. For this purpose, linear stability analysis tools are used to highlight the involvement of non-hydrodynamic modes. An extension of this analysis enables to reveal that transfer between physical and non-hydrodynamic modes inevitably exists at resolution transitions. The non-hydrodynamic modes are classified according to the macroscopic quantity they carry and sensors are developed to visualize these modes during simulation. Finally, simple test cases, with non-uniform grids, are carried out with the BGK model to isolate and identify the spurious phenomena related to these modes at grid interfaces.

3.1 Introduction to linear stability analysis

3.1.1 Introduction

The von Neumann analysis [138] (or LSA for Linear Stability Analysis) is a very powerful tool to investigate the behavior of numerical schemes, in terms of stability and accuracy properties. This method consists of evaluating the response of a system, which is described by a given set of either partial or ordinary differential equations, to small disturbances. This analysis quantifies the evolution of these perturbations in terms of growth rate and propagation speed. The former is very useful for qualifying the linear stability of a system, which will be considered stable if this rate is always negative. Moreover, knowing the growth rate of the perturbations will allow to qualify the dissipation properties of a numerical scheme. Such characteristics are essential to determine for propagating a quantity over a distance without it being undesirably attenuated. The second information obtained from the stability analysis is the propagation speed of the waves in the system. If the system alters the wave propagation speed, it is said to disperse.

The LSA is widely used in the Navier-Stokes community. In particular to develop numerical schemes with low dissipation and low dispersion, very valuable for aeroacoustic simulations [139, 140]. Later, Berland *et al.* extended these optimized schemes to boundary conditions and meshes with non-uniform resolutions [141]. They have also developed high-order filters to dissipate the high-frequency oscillations that can arise from boundary conditions and affect the stability of the simulations. Recently, the LSA has been used to stabilize implicit-explicit time couplings, allowing to optimize the computational efficiency of unsteady simulations [142].

Now, if one focuses on the study of the Boltzmann schemes, the LSA has been applied many times to the DVBE or the LB schemes. The first analysis on the DVBE equation was conducted by Marié *et al.* [143] with a D3Q19 lattice. On the latter, the antidissipation due to the cubic Mach error that appears in the viscous stress tensor is clearly visible. Then Coreixas *et al.* [136] have studied the DVBE limits for high-order lattices. Recently, an extensive stability study of the DVBE [114] has highlighted, among other things, a Prandtl error for multiple relaxation time models which can lead to degeneracy of hydrodynamic waves when the Prandtl number is of the order of magnitude of the Knudsen one. Concerning the LB scheme, the LSA has been widely used for choosing the free relaxation times of the MRT models to improve stability [144,145] or to optimize the spectral properties [146, 147]. Additionally, the LSA has recently made it possible to take a step forward in understanding the origin of the BGK model instabilities [148], as well to highlight the incorrect dissipation errors of advanced collision models [149]. Based on the observation that non-physical waves seem to propagate in the fluid core with the BGK model during non-uniform mesh simulations (*cf.* Fig. 2.6 and 2.7), the LSA seems to be a valuable tool to understand these phenomena. In this thesis, the focus will be only restricted to the analysis of the discrete LB schemes, since the space and time discretization will turn out to be root of the spurious behavior highlight in Sec. 2.6.

3.1.2 Principles of the von Neumann analysis

The standard von Neumann analysis principles can be found in [138]. The first step is to linearized Eq. (2.4.13) about a global equilibrium state. To this purpose, Sterling and Chen [150] has proposed to expand the distribution functions into a sum of a stationary part $\bar{g}_i$, and a fluctuating part g_i'

$$g_i = \bar{g}_i + g_i'. \tag{3.1.1}$$

In the LB scheme, the collision operator is not linear in g_i and must be linearized

$$g_i^{coll}\left(g_j\right) = g_i^{coll}\left(\bar{g}_j\right) + \left.\frac{\partial g_i^{coll}}{\partial g_j}\right|_{g_j=\overline{g_j}} g_j' + O\left({g_j'}^2\right). \tag{3.1.2}$$

The advection step in Eq. (2.4.15) is linear, thus keeping only the first-order in distribution functions, the LB scheme reads

$$g_i'\left(\boldsymbol{x}+\boldsymbol{e}_i, t+1\right) = \left.\frac{\partial g_i^{coll}}{\partial g_j}\right|_{g_j=\overline{g_j}} g_j'. \tag{3.1.3}$$

In the particular case of the BGK collision operator, Eq. (3.1.3) becomes

$$g_i'\left(\boldsymbol{x}+\boldsymbol{e}_i, t+1\right) = \left[\delta_{ij} - \frac{1}{\overline{\tau}}\left(\delta_{ij} - J_{ij}^{(0),N}\right)\right] g_i'\left(\boldsymbol{x}, t\right), \tag{3.1.4}$$

with $J_{ij}^{(0)} = \left.\frac{\partial f_i^{(0),N}}{\partial g_j}\right|_{g_j=\overline{g_j}}$ the Jacobian matrix of the equilibrium distribution function.
Once the system of equations to be studied is linearized, the von Neumann analysis consists of injecting complex monochromatic waves of the following form

$$g_i'(x,t) = \hat{g}_i \exp\left(i(\omega t - \boldsymbol{k}\cdot\boldsymbol{x})\right), \tag{3.1.5}$$

in Eq. (3.1.3) (or equivalently Eq. (3.1.4) in the present case). Where $i^2 = -1$, $\hat{g}_i \in \mathbb{C}$, k is the dimensionless wavenumber vector and ω is the dimensionless pulsation of the wave. The physical perturbation corresponds to the real part of this complex wave

$$\Re(g_i') = |\hat{g}_i| e^{-\omega_i t} \cos\left(\omega_r t - \boldsymbol{k} \cdot \boldsymbol{x} + \phi_i\right), \tag{3.1.6}$$

where $\phi_i = \arg(\hat{g}_i)$. The real part $\omega_r = \Re(\omega)$ and the imaginary part $\omega_i = \Im(\omega)$ are respectively linked with the propagation and the dissipation of the perturbation.
Finally, injecting the complex monochromatic perturbations g_i' into Eq. (3.1.3), one obtain the following eigenvalue problem

$$e^{i\omega}\mathbf{F} = \mathbf{M}^{\mathbf{LBM}}\mathbf{F}, \tag{3.1.7}$$

with $\mathbf{M}^{\mathbf{LBM}}$ the time-advance matrix which depends on the collision model and $\mathbf{F} = [\hat{g}_i]^T$ the vector of modal fluctuations. Eigenvalues of Eq. (3.1.7) are then studied to obtain the dissipation (ω_i) and dispersion (ω_r) properties of the LB scheme.

The time-advance matrices $\mathbf{M}^{\mathbf{BGK}}$ for the BGK collision operator reads:

$$M_{ij}^{\mathrm{BGK}} = e^{-i\boldsymbol{k}\cdot\boldsymbol{e}_i}\left[\delta_{ij} - \frac{1}{\bar{\tau}}\left(\delta_{ij} - J_{ij}^{(0),N}\right)\right]. \tag{3.1.8}$$

A similar analysis can be performed on the isothermal Navier-Stokes equations. It gives three linear modes in two dimensions: one shear (or vorticity) mode and two acoustic (one moving upstream Ac- and one moving downstream Ac+) modes. The eigenvalues of these modes are [143, 148]:

$$\begin{aligned}
\omega_{shear} &= \boldsymbol{k} \cdot \bar{\boldsymbol{u}} + i\nu \left\|\boldsymbol{k}\right\|^2, \\
\omega_{Ac+} &= \boldsymbol{k} \cdot \bar{\boldsymbol{u}} + \left\|\boldsymbol{k}\right\| c_s + i\nu \left\|\boldsymbol{k}\right\|^2, \\
\omega_{Ac-} &= \boldsymbol{k} \cdot \bar{\boldsymbol{u}} - \left\|\boldsymbol{k}\right\| c_s + i\nu \left\|\boldsymbol{k}\right\|^2,
\end{aligned} \tag{3.1.9}$$

where $\bar{\boldsymbol{u}}$ is the mean flow velocity.

The von Neumann analysis of the LB-BGK scheme is presented on Fig. 3.1. The analysis is performed with a mean flow of $\bar{u} \cdot \vec{e_x} = 0.1\, c_s$, corresponding to a Mach number $\mathrm{Ma} = 0.1$ along the x axis with an increasing wavenumber k_x ranging from 0 to π. In this figure, only the wave propagating in the $\vec{e_x}$ directions are noticeable. LSAs that take all directions of wave propagation into account will be studied in Chap. 5. For the purpose of this study, one dimension is sufficient to understand and exploit the results.
The dimensionless viscosity is set equal to $\nu = 10^{-6}$. This value is retained for the numerical experiments in the following, since it is in the order of magnitude of viscosity of air for a minimal mesh size of $\Delta x = 0.01$m. It is likely that the mesh will be more resolved, leading to a larger value of dimensionless kinematic viscosity. Here, this very low value is retained to put the emphasis on the spurious phenomena that will arise, knowing that the value of ν will not affect the results and the explanations provided below.

For the sake of clarity, the following analyses will be conducted in two dimensions, using a D2Q9 lattice. It allows reducing the number of waves present in the LSAs (Q waves) and in the numerical experiments, but exactly the same phenomena and conclusions are reached with the D3Q19 lattice used in LaBS/ProLB.

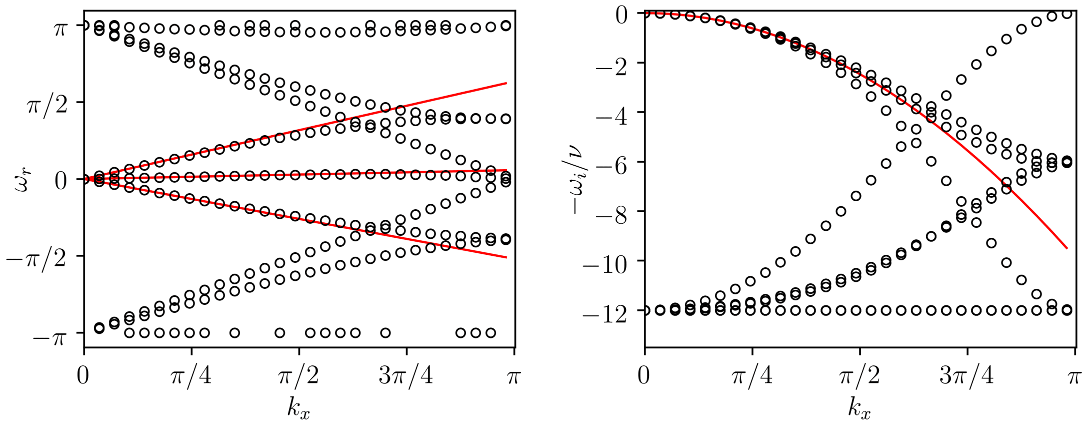

Figure 3.1 – *Propagation (left) and dissipation (right) curves for the BGK collision model.* $\nu = 10^{-6}$, Ma = 0.1. (—) *: Isothermal Navier-Stokes.*

As depicted on Fig. 3.1, nine modes are observed. Furthermore, the imaginary part of the isothermal Navier-Stokes eigenvalues (*cf.* Eq. 3.1.9), is, in the following, taken as the reference for the dissipation curves (—) that physically takes place in real flows. In the propagation curve, the three real part of the isothermal Navier-Stokes eigenvalues are also plotted (—). One can thus recognize three LB waves which seem to coincide with two acoustic waves *Ac*+, *Ac*− and a shear wave propagating at $\bar{\boldsymbol{u}}$, for low wavenumbers at least (when the resolution is the finest).

The phase velocity $\mathbf{v}_\phi$ and the group velocity $\mathbf{v_g}$ of the monochromatic waves are defined as

$$\begin{aligned} \mathbf{v}_\phi &= \frac{\omega_r}{\boldsymbol{k}}, \\ \mathbf{v_g} &= \frac{\mathrm{d}\omega_r}{\mathrm{d}\boldsymbol{k}}. \end{aligned} \tag{3.1.10}$$

Therefore, three modes seem to be identified, at least on the dispersion curves, but six modes remain undetermined. To systematically identify these modes, Wissocq *et al.* [148] have developed a methodology based on the analysis of eigenvectors of the system described in Eq. (3.1.7). The LBM eigenvectors $\mathbf{F}$ are used to give a physical interpretation to modes resulting from the von Neumann analysis. This decomposition is performed by projecting a LBM macroscopic vector $\mathcal{V} = [\hat{\rho}, (\widehat{\rho\boldsymbol{u}})]^T$ composed of moments of $\mathbf{F}$

$$\begin{aligned} \hat{\rho} &= \sum_i \hat{g}_i, \\ (\widehat{\rho\boldsymbol{u}}) &= \sum_i \hat{g}_i \boldsymbol{\xi}_i, \end{aligned} \tag{3.1.11}$$

onto the Navier-Stokes ones. This analysis allows for a systematic identification of the modes carrying a macroscopic information at more than a prescribed ratio η. In the results presented below, this parameter will be set to $\eta = 0.99$.

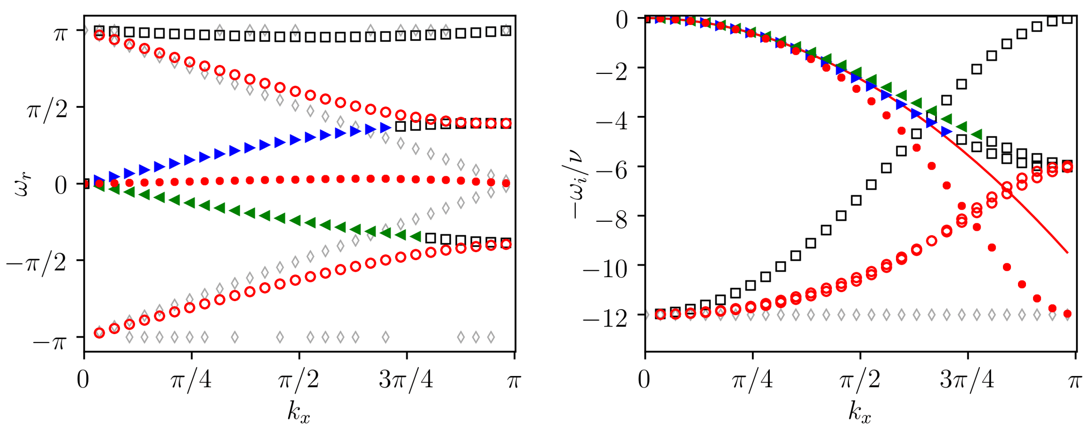

Figure 3.2 – *Propagation and dissipation curves for the BGK collision model.* $\nu = 10^{-6}$*, Ma=0.1.* (▸)*: Ac+ mode,* (◂) *: Ac- mode,* (●) *: Shear mode,* (○) *: SpuriousS modes,* (□) *: SpuriousAc modes,* (◊) *: SpuriousG modes,* (—) *: Isothermal Navier-Stokes.*

As depicted on Fig. 3.2, the eigenvector analysis proposed in [148] allows for the identification of modes carrying more than 99% of an acoustic information identified with (▸) and (◂), and modes carrying a shear information displayed with (●) and (○). Three modes are found for the latter category, while only one shear wave is expected by the Navier-Stokes equations. In the present study, and for a sake of clarity, these shear modes will be further distinguished thanks to their propagation speed. Indeed, on the case illustrated here, only one mode has a propagation speed close the expected one and can be identified as a physical shear mode. Hence, the nine modes observed on Fig. 3.2 can be classified into six categories:

The physical modes:

- (●) The **shear** modes.
- (▸) The acoustic **Ac+** modes.
- (◂) The acoustic **Ac-** modes.

The non-hydrodynamic modes:

- (○) The **SpuriousS** modes that carry a shear quantity (transverse velocity fluctuation) at an incorrect phase velocity.
- (□) The **SpuriousAc** modes thats carry a combination of the two acoustics waves. These modes do not propagate at the sound celerity.
- (◊) The **SpuriousG** modes thats does not carry any physical quantities. These modes are invisible at the macroscopic level.

The "Spurious" terms are related to the non-hydrodynamic modes since they are unexpected in a simulation. Furthermore, as it will be shown in Sec. 3.6, they can have troublesome effects, especially in the presence of non-uniform grids. The SpuriousAc (□) modes have a projection on both the density and the longitudinal velocity, but do not have any contribution on the transversal velocity. As a matter of fact, they can be considered as spurious acoustic modes since their projections on the Navier-Stokes acoustic modes are not null. Moreover, a tight link between the SpuriousAc (□) modes and acoustics (▸,◂) will be shown in Sec. 3.6.2.

3.2 Non hydrodynamic modes: what are they?

Non-hydrodynamic modes [135] (or ghost modes [151]) are modes that appear in the Boltzmann equation but are not contained in the linearized Navier-Stokes equations. Thanks to the recent work of Wissocq *et al.* [148], it has been pointed out that these modes could have a macroscopic contribution, caused by the space and time discretization of the DVBE equation.

This may be verified, as Wissocq does in his PhD thesis [113], by initializing a shear wave in an LB code in order to excite the physical shear mode (●) and non-physical SpuriousS (○) modes that carry shear information. Or in the same way by initializing an acoustic wave for exciting the physical acoustics mode ((▸),(◂)) and non-physical SpuriousAc (□) modes.

A one-dimensional shear wave is initialized as follow in a two dimensional LB code:

$$\begin{cases} \rho\left(x,y\right)=\rho_0, \\ u_x\left(x,y\right)=U_x, \\ u_y\left(x,y\right)=U_y\exp\left(-\frac{(x-x_c)^2}{2R_c^2}\right), \end{cases} \tag{3.2.1}$$

with

$$\rho_0=1, \quad U_x=U_y=0.1c_s, \quad R_c=10, \quad x_c=100, \quad \nu=10^{-6}.$$

Every quantities are given in the dimensionless unit. The LB code used a D2Q9 lattice with a BGK collision operator and an equilibrium distribution function $f_i^{(0),N}$ defined by Eq. (2.3.25) extended to the third-order for stability purposes [148].

After a few iterations, one can see on Fig. 3.3 that the shear wave was correctly advected with a positive velocity u_x. However, two spurious waves with a transverse velocity component (characteristic of shear waves) are also propagating, one downstream, with a positive group velocity, and the other upstream, with a negative group velocity.

This result is consistent with the propagation curve depicted on Fig. 3.2, where two SpuriousS (○) waves with positive and negative group velocities can be distinguished. In the case of the positive group velocity, this last is higher than that of the physical shear wave (○). Hence, the spurious waves which have a macroscopic contribution are well perceptible in LB simulations. Besides, their real pulsation part is near $\omega_r = \pi$. This is manifested by a phase inversion of the spurious waves at each iteration, as shown on Fig. 3.3.

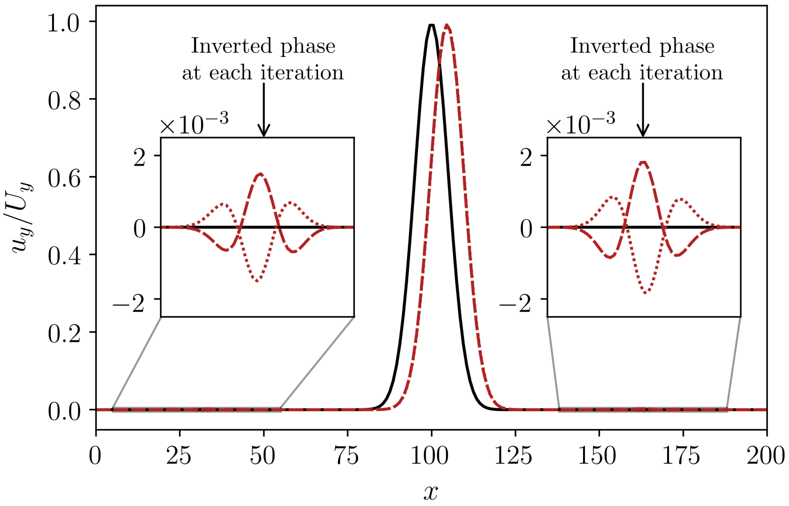

Figure 3.3 – *One dimensional shear wave computed with a two dimensional LB-BGK solver to exhibit the coexistence of physicals and spurious modes.* (—)*: initial solution,* (- - -)*: t=80,* (·····)*: t=81 iterations.*

A very troublesome point of the BGK model is the non-hydrodynamic modes dissipation, which is in the same order than the physical modes as indicated by the dissipation curve on Fig. 3.2. Hence, these last will be very weakly dissipated by the numerical scheme. If we refer to Fig. 2.6 and Fig. 2.7 of the previous chapter, one can already sense that the spurious waves observed on the dilatation and vorticity fields are probably related to these non-hydrodynamic modes.

Up to now, stability analysis has allowed to highlight the existence of non-hydrodynamic modes, characterized by specific dispersion and dissipation properties, and by a given transported quantity. A simple shear plane wave simulation in an LB code has allowed to verify their existence. However, the spectral analysis tools are not systematically applicable in a real simulation, for which the linear hypothesis with plane monochromatic perturbations may not be valid. For this reason, in the next section, a derivation of sensors is proposed to make a systematic link between spectral analysis tool outcomes, and non-hydrodynamic modes observation during a real simulation.

3.3 Non hydrodynamic modes: How can they be highligthed ?

This section aims at proposing different kinds of sensors in order to detect the presence of non-physical modes in a simulation. The objective is to make the link between modes exhibited by the von Neumann analysis and phenomena observed during simulations.

Currently in the literature, the entropic lattice Boltzmann models are based on a similar attempt to systematically identify non-hydrodynamic content [152]. More precisely, it is proposed to decompose the populations g_i into three parts

$$g_i = k_i + s_i + h_i, \tag{3.3.1}$$

where k_i, s_i and h_i respectively refer to a kinematic part, a shear part and the remaining higher-order moments. The kinematic part k_i relies only on conserved variables $(\rho, \mathbf{u})$. The shear part s_i includes second-order moments of g_i, and h_i includes higher-order moments only. Based on this decomposition, Karlin *et al.* [152] proposed to dynamically modify the relaxation time of h_i, especially when interactions appears with the shear moments s_i in order to damp them. This dynamic model is performed using an entropic sensor (referred to as entropic stabilizer), that highlights interactions between the off-equilibrium part of both shear and higher-order moments.
Usually, only the deviatoric stress tensor contribution is included in s_i and the trace of the second-order moment can frequently be found in the h_i part and, thus, its relaxation rate can be a free parameter. The bulk viscosity is then modified and may allow an enhanced behavior in presence of non-uniform grids [153].

However, this entropic sensor allows for detecting only non-hydrodynamic moments of g_i. Yet, the present study focuses on the effects of non-hydrodynamic modes, rather than moments. Before introducing the sensors that will be used below, it is therefore important to emphasize the differences between moments and modes of a LB scheme:

- Moments are macroscopic variables that can be: hydrodynamics and conserved variables (ρ,$\mathbf{u}$) during collisions, non-conserved but hydrodynamic variables (stress tensor components), or non-conserved non-hydrodynamic variables for moments of order greater than two. The latter are usually referred to as "ghost variables" [154]. For many multiple-relaxation-time collision models, the relaxation parameters of these ghost variables are set free regarding the physics [134, 144].

- The modes are built as the eigenvectors of the linear stability analysis applied to the LB scheme. As it has been shown by Wissocq *et al.* [148], they can be "observable" if they carry kinetic variables $(\rho, \mathbf{u})$ or not. In other cases they are "ghost" and are invisible at the macroscopic level. For the purposes of this study, "observable" modes are classified depending on the quantity their carry, as well as on their velocity as proposed in Sec. 3.1.2.

Knowing that the SpuriousAc (□) and SpuriousS (○) modes can have a projection on the macroscopic moments (ρ,$\mathbf{u}$), and since the SpuriousG mode (◊) is linked to non-observable variables, these non-hydrodynamic modes can thus be located during a simulation by building sensors.

SpuriousAc mode (□) sensor:

The first sensor introduced here aims at detecting the SpuriousAc modes (□). These modes carry acoustic disturbances, i.e. compressive waves, thus they can be visualized thanks to the velocity divergence. Furthermore, these modes have a real pulsation ω_r very close to $\omega_r = \pi$ so that their amplitude is inverted at each time step. By using these two properties, one can build a sensor based on the velocity divergence product between two iterations which has to be negative.

$$\vec{\nabla}\cdot\boldsymbol{u}(t-1) * \vec{\nabla}\cdot\boldsymbol{u}(t) \quad \begin{cases} < 0 \;\Rightarrow \text{NHsensor}^{(\square)} = 1,\\ \geq 0 \;\Rightarrow \text{NHsensor}^{(\square)} = 0.\end{cases} \tag{3.3.2}$$

SpuriousS mode (○) sensor:

The second sensor aims to detect the SpuriousS modes (○). These modes carry shear quantity, therefore they can be detected by looking at the vorticity field. As previously, these modes have also a real pulsation ω_r very close to $\omega_r = \pi$ so that their amplitude is inverted at each iteration. Here, it is possible to build a sensor based on the vorticity product between two iterations, which has to be negative. However, the inversion does not occur in strongly sheared areas. Consequently, this sensor enables the detection of SpuriousS mode (○) outside regions with strong hydrodynamic variations.

$$\vec{\nabla}\times\boldsymbol{u}(t-1) * \vec{\nabla}\times\boldsymbol{u}(t) \quad \begin{cases} < 0 \;\Rightarrow \text{NHsensor}^{(\bigcirc)} = 1,\\ \geq 0 \;\Rightarrow \text{NHsensor}^{(\bigcirc)} = 0.\end{cases} \tag{3.3.3}$$

SpuriousG mode (◊) sensor:

The third sensor aims to detect the SpuriousG modes (◊). As stated above, they cannot be detected by looking at the macroscopic quantities. Through the von Neumann analysis, it is possible to show that these ghost modes are linked with “ghost variable” [151]. Therefore, similarly to the entropic LBM sensor, a decomposition of the off-equilibrium distribution functions is proposed in a shear part and a ghost part corresponding to higher-order contributions, as

$$g_i^{(1)} = g_i^{(1),S} + g_i^{(1),G}, \tag{3.3.4}$$

where $g_i^{(1),S}$ is computed by projection of the off-equilibrium populations onto the second-order Hermite polynomials [155]

$$g_i^{(1),S} = \frac{w_i}{2c_s^4}\mathcal{H}_i^{(2)} : \boldsymbol{a}_1^{(2)}. \tag{3.3.5}$$

Using this decomposition, one can detect a SpuriousG mode (◊) when the norm of $g^{(1),G}$ is not null. However, the two previous non-hydrodynamic modes can also be detected with this definition, so it is proposed to withdraw their contributions. The remaining part is, de facto, the SpuriousG mode.

$$\begin{cases} \text{if} \quad \|g^{(1),G}\| > 0 \text{ and } \left(\text{NHsensor}^{(\square)} = 0 \text{ and } \text{NHsensor}^{(\bigcirc)} = 0\right) \Rightarrow \text{NHsensor}^{(\lozenge)} = 1, \\ \text{else NHsensor}^{(\lozenge)} = 0, \end{cases} \tag{3.3.6}$$

with $\|g^{(1),G}\| = \sqrt{\sum \left(g_i^{(1),G}\right)^2}$ the norm of the vector $g^{(1),G}$. This sensor allows to detect the SpuriousG mode (◊) outside the influence of the SpuriousAc (□) and the SpuriousS (○) ones. Since the group velocity of this mode is larger than the other ones, one can expect that they will be well separated with each other, allowing an easier identification.

Sensors to detect non-hydrodynamic modes have been proposed in this section. They allow to make the link between the spectral properties described in Sec. 3.1.2 and unexpected phenomena occurring in simulations. They will be very useful to understand interactions that can appear between physical and spurious modes induced by the drastic change of spectral properties at grid refinement interface.

Before going into numerical experiments, it is therefore interesting to consider the effect of a change of resolution onto these modes, independently of the grid refinement algorithm used. This study is proposed in the next section.

3.4 Energy transfer induced by a change of resolution

The aim of this section is to study the effect of a resolution change on the LBM modes, regardless the grid coupling algorithm. Since the spectral properties of the LBM schemes strongly depend on the dimensionless wavenumber vector $\boldsymbol{k}$, then on the mesh resolution, it is interesting to wonder how a given mode may be affected by a resolution change. To address this question, it is proposed here to study the passage matrix $\mathbf{P}$ between modes with a wavenumber k_x^f and those with a wavenumber $k_x^c = 2k_x^f$.

Let us denote $\mathbf{P}_f$ (respectively $\mathbf{P}_c$) the passage matrix composed of the eigenvectors obtained by the von Neumann analysis at k_x^f (resp. k_x^c) written in the basis of the distribution functions. A given vector $\mathbf{F}$, written in the basis of the distribution functions, can equivalently be represented either by a vector $\mathbf{V}^f$ in the basis of the eigenmodes at k_x^f, or $\mathbf{V}^c$ in the basis of the eigenmodes at k_x^c, where:

$$\mathbf{V}^f = \mathbf{P_f^{-1}F}, \qquad \mathbf{V}^c = \mathbf{P_c^{-1}F}. \tag{3.4.1}$$

Each component of $\mathbf{V}^f = \left[(\blacktriangleright)^f, (\blacktriangleleft)^f, (\square)^f, (\bullet)^f, (\bigcirc)^f, (\bigcirc)^f, (\lozenge)^f, (\lozenge)^f, (\lozenge)^f\right]^T$ (resp. $\mathbf{V}^c$) represents the decomposition of $\mathbf{F}$ in the LBM modes of the fine mesh (resp. the coarse mesh). For example, $\mathbf{V}^f = \left[1, 0, .., 0\right]^T$ denotes a pure downstream acoustic wave at k_x^f. The link between $\mathbf{V}^f$ and $\mathbf{V}^c$ is then straightforward as

$$\mathbf{V}^f = \mathbf{P}\mathbf{V}^c \qquad \text{with} \qquad \mathbf{P} = \mathbf{P_f^{-1}}\mathbf{P_c}. \tag{3.4.2}$$

Coefficient P_{ij} of $\mathbf{P}$ provide the decomposition of the fine modes expressed in the coarse modes basis. For example, the linear decomposition of a fine acoustic Ac+ mode $(\blacktriangleright)^f$ onto the coarse basis reads

$$(\blacktriangleright)^f = P_{11}(\blacktriangleright)^c + P_{12}(\blacktriangleleft)^c + P_{13}(\square)^c + P_{14}(\bullet)^c + P_{15}(\circ)^c + P_{16}(\circ)^c + P_{17}(\lozenge)^c + P_{18}(\lozenge)^c + P_{19}(\lozenge)^c. \tag{3.4.3}$$

Each component of $\mathbf{P}$ is *a priori* complex, whose argument is linked with the phase shift between the modes. Here, only their modulus $|P_{i,j}|$ will be of interest. Moreover, they will be normalized as

$$P_{ij}^* = |P_{ij}|^2 / \sum_k |P_{ik}|^2, \tag{3.4.4}$$

so that $\sum_j P_{i,j}^* = 1$.

Normalized coefficients P_{ij}^* are displayed on Fig. 3.4 for the three physical modes (▸, ◂, ●) obtained with the BGK collision operator. This analysis is performed for several $k_x^c \in [0, \pi]$ and $k_x^f \in [\min(k_x^c)/2, \pi/2]$. It is noticeable that the physical mode of a fine mesh

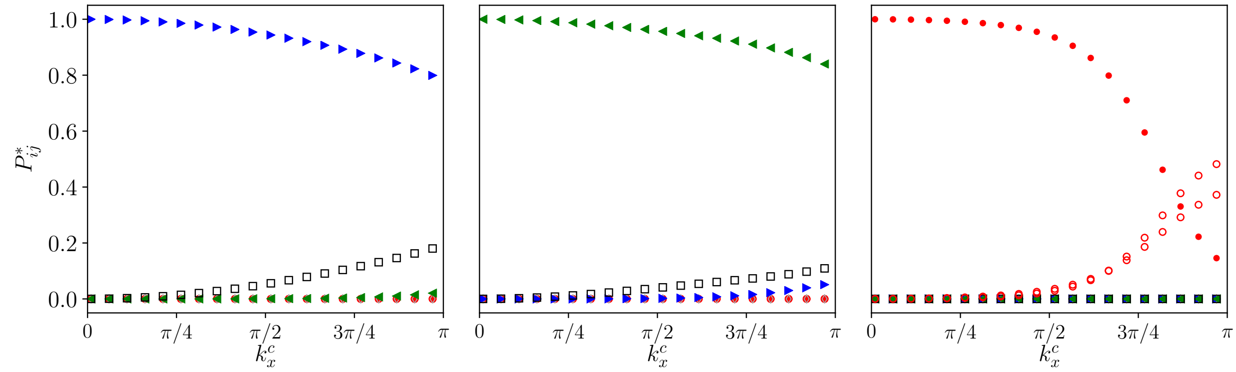

Figure 3.4 – *Normalized coefficients* $P_{i,j}^*$ *for the three physical modes with the BGK collision operator with* $\nu = 10^{-6}$ *and Ma=0.1. Left: Components* P_{1j}^* *of the decomposition of the fine* ***Ac+*** *mode in the coarse eigenbasis, middle:* P_{2j}^* (***Ac-***)*, right:* P_{4j}^* ***Shear****.* (▸)*: Ac+ mode* (P_{i1}^*), (◂)*: Ac- mode* (P_{i2}^*), (●)*: Shear mode* (P_{i4}^*), (○)*: SpuriousS modes* (P_{i5}^* *and* P_{i6}^*), (□)*: SpuriousAc mode* (P_{i3}^*), (◊)*: SpuriousG modes* (P_{i7}^* *to* P_{i9}^*).

at wavenumber k_x^f is not preserved when changing the mesh resolution to the wavenumber k_x^c. It is indeed decomposed into a superposition of coarse modes, hydrodynamic and non-hydrodynamic ones, that carry a quantity of the same nature. Moreover, this phenomenon is amplified as k_x^c increases, *i.e.* as the mode is less resolved. For instance, for the two physical acoustic modes (▶,◀), the decomposition onto the SpuriousAc mode (□) is favored, while shear and ghost modes are not excited. Concerning the shear mode (●), its decomposition is distributed over both SpuriousS modes (○) to reach less than 20% of the projection onto a coarse physical shear mode (●) for high wavenumbers.

The same analysis is performed on Fig. 3.5 for the non-hydrodynamic modes that are projected from a fine resolution (k_x^f) to a coarser one (k_x^c). Here again, the non-hydrodynamic modes are composed only of a combination of modes that carry information of the same nature. The SpuriousAc mode (□) generates acoustics in a significant way. Only one SpuriousS mode (○) and one SpuriousG mode (◊) are plotted since a similar observation is provided for the other ones. The SpuriousG modes are preserved by the change of resolution.

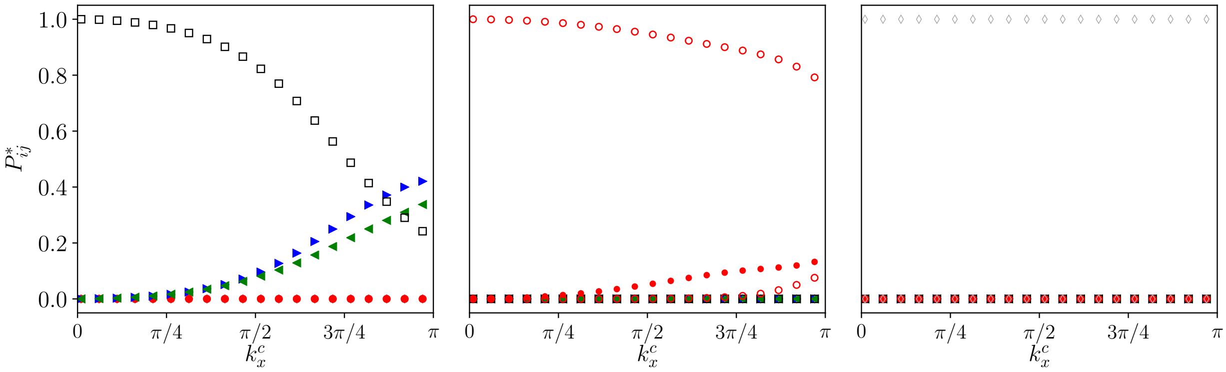

Figure 3.5 – *Normalized coefficients $P^*_{i,j}$ for the non-hydrodynamic modes with the BGK collision operator with $\nu = 10^{-6}$ and Ma=0.1. Left: Components P^*_{3j} of the decomposition of the fine* ***SpuriousAc*** *mode in the coarse eigenbasis, middle: P^*_{5j}* ***SpuriousS****, right: P^*_{7j}* ***SpuriousG****. (▶): Ac+ mode (P^*_{i1}), (◀): Ac- mode (P^*_{i2}), (●): Shear mode (P^*_{i4}), (○): SpuriousS modes (P^*_{i5} and P^*_{i6}), (□): SpuriousAc mode (P^*_{i3}), (◊): SpuriousG modes (P^*_{i7} to P^*_{i9}).*

With these results, it is then possible to rewrite **P** as a block diagonal matrix, with acoustic modes (▶,◀,□) and shear modes (●,○) that form two separated blocks and with the ghost modes (◊) preserved by the transformation:

This short analysis highlights the transfers occurring between both hydrodynamic and non-hydrodynamic modes that carry information of the same nature. This consideration is extremely important and will be further discussed in the numerical experiments of Sec. 3.6. Moreover, it is important to notice that this study has been carried out through von Neumann analyses performed in the fluid core only, regardless of the grid refinement algorithm. These results are therefore generic, and **represent the ideal case of mesh transitions that do not introduce any more numerical errors**. Obviously, it is never the case in practice, where the algorithm may affect the mode redistribution, such as by introducing non-linear effects and high-frequency waves

$$\underbrace{\begin{pmatrix} \blacktriangleright \\ \blacktriangleleft \\ \square \\ \bullet \\ \circ \\ \circ \\ \lozenge \\ \lozenge \\ \lozenge \end{pmatrix}^{f}}_{\mathbf{V}^f} = \underbrace{\begin{bmatrix} P_{11} & P_{12} & P_{13} & 0 & 0 & 0 & 0 & 0 & 0 \\ P_{21} & P_{22} & P_{23} & 0 & 0 & 0 & 0 & 0 & 0 \\ P_{31} & P_{32} & P_{33} & 0 & 0 & 0 & 0 & 0 & 0 \\ 0 & 0 & 0 & P_{44} & P_{45} & P_{46} & 0 & 0 & 0 \\ 0 & 0 & 0 & P_{54} & P_{55} & P_{56} & 0 & 0 & 0 \\ 0 & 0 & 0 & P_{64} & P_{65} & P_{66} & 0 & 0 & 0 \\ 0 & 0 & 0 & 0 & 0 & 0 & 1 & 0 & 0 \\ 0 & 0 & 0 & 0 & 0 & 0 & 0 & 1 & 0 \\ 0 & 0 & 0 & 0 & 0 & 0 & 0 & 0 & 1 \end{bmatrix}}_{\mathbf{P}} \cdot \underbrace{\begin{pmatrix} \blacktriangleright \\ \blacktriangleleft \\ \square \\ \bullet \\ \circ \\ \circ \\ \lozenge \\ \lozenge \\ \lozenge \end{pmatrix}^{c}}_{\mathbf{V}^c} .$$

Figure 3.6 – *Block diagonal projection matrix* $\mathbf{P}$ *of fine modes* $\mathbf{V}^f$ *with resolution* k_x^f *on a coarser resolution* $k_x^c = 2k_x^f$ *to obtain* $\mathbf{V}^c$. P_{1-3}: *bloc of acoustic modes* ($\blacktriangleright$,$\blacktriangleleft$,$\square$), P_{4-6}: *bloc of shear modes* ($\bullet$,$\circ$), P_{7-9}: *ghost modes* ($\lozenge$).

that cannot be predicted by this analysis. In any case, the aforementioned mode transfer seems unavoidable given the spectral properties of the BGK model. In this context, since the **P** matrix is dependent of the collision operator, changing the latter can thus be used to act on the P_{ij} coefficients. This observation will be the key point in the solution proposed in Chap. 4 to improve the behavior of the mesh transition.

Up to now, spectral analysis tools have been used to emphasize some non-hydrodynamic modes with given properties. In addition, **a projection of physical modes onto non-hydrodynamic ones of the same nature and *vice-versa* is very likely to happen at grid interface** as described just above. Subsequently, a grid refinement algorithm classically used in the literature, and which is the one used in LaBS/ProLB v2.5, will be described. It will allow to perform numerical experiments with non-uniform meshes **in an in-house python two dimensional LB code** developed during this phD thesis.

3.5 A standard cell-vertex grid refinement algorithm

Before introducing a particular grid refinement algorithm, it is worth mentioning that the concepts linked to non-hydrodynamic modes presented in the following are independent of the grid refinement algorithm and have been validated for both cell-vertex and cell-centered algorithms. Since the aim of this Chapter is not a comparison of grid coupling algorithms, the one from Lagrava *et al.* [83] is chosen as it is one of the most popular and the one available in both LaBS/ProLB and our in-house LB code. For an assessment of grid refinement algorithms, the interested reader may refer to Chapter 6.

This algorithm is based on the one from Dupuis & Chopard [156] where the distribution functions are rescaled before the collision step in contrast to Filippova *et al.* [157]. An additional Gaussian filtering procedure [59] is applied during the fine to coarse grid transfer to avoid aliasing effects. Grid refinement algorithm details and conversion relations between fine and coarse quantities are described below.

3.5.1 Rescaling of physical quantities

In the following, a plane transition separating a fine and a coarse grid resolution domain is considered. Since the dimensionless convention has been adopted, each resolution level possesses its own "lattice units". This change of scale requires a rescaling of the physical quantities between grids.
Any quantity related to the fine or coarse domain is denoted by a superscript f and c, respectively. The coarse and fine mesh sizes are linked with each other as $\Delta x^c = 2\Delta x^f$. In the case of an acoustic scaling, the timestep is imposed as $\Delta t^c = 2\Delta t^f$ with respect to Eq. (2.4.16). In the following, the coarse scale is chosen to make the space and time steps dimensionless.

The dimensionless viscosity must be rescaled in order to ensure the Reynolds number continuity [157]

$$\nu^f = \frac{\Delta x^c}{\Delta x^f}\nu^c = 2\nu^c, \tag{3.5.1}$$

leading to the following relation between the relaxation times (*cf.* Eq. 2.4.18)

$$\overline{\tau}^f = 2\overline{\tau}^c - \frac{1}{2}. \tag{3.5.2}$$

Unlike the equilibrium part of the distribution function which depends only on macroscopic quantities that are continuous through the interface, the off-equilibrium part $g_i^{(1)}$ has to be rescaled since it depends on velocity gradients through Eq. (2.3.30). By a combination of (3.5.2) and (2.3.30), the relation between the off-equilibrium parts of the fine and coarse populations is

$$g_i^{(1),c} = 2\frac{\overline{\tau}^c}{\overline{\tau}^f} g_i^{(1),f}. \tag{3.5.3}$$

It is worth noting that this relation allows to build distribution functions that are missing at the grid interface after a streaming step:

$$g_i^f = g_i^{(0)} + \frac{\overline{\tau}^f}{2\overline{\tau}^c} g_i^{(1),c}, \tag{3.5.4}$$

$$g_i^c = g_i^{(0)} + \frac{2\overline{\tau}^c}{\overline{\tau}^f} g_{i,filt}^{(1),f}, \tag{3.5.5}$$

where the subscript $g_{filt}^{(1)}$ stands for the filtered value of the off-equilibrium distribution function. This filtering step is highly recommended for stability and accuracy reasons [69, 83]. It is also worth noting that cell-centered algorithms implicitly use a spatial filtering during the coalescence step [70]. The filter used in the present work is the one proposed in [59]. For a D2Q9 lattice, it reads

$$g_{i,filt}^{(1),f}\left(\mathbf{x},t\right)=\frac{1}{4}g_i^{(1),f}\left(\mathbf{x},t\right)+\frac{1}{8}\sum_{\alpha=1}^{4}g_i^{(1),f}\left(\mathbf{x}+\boldsymbol{e}_\alpha,t\right)+\frac{1}{16}\sum_{\alpha=5}^{8}g_i^{(1),f}\left(\mathbf{x}+\boldsymbol{e}_\alpha,t\right), \qquad (3.5.6)$$

where the three contributions correspond respectively to the *center*, *normal* and *diagonal* directions over the neighboring nodes with the convention of dimensionless lattice velocities $\boldsymbol{e}_i$ given in Table. 2.1.

3.5.2 Cell-vertex algorithm with overlapping area

In the standard collide & stream algorithm, some distribution functions are missing at the interface after a streaming step. The use of an overlapping area to couple grids is a very common way to recover the missing populations. This strategy is adopted for most of both cell-centered [158, 159] or cell-vertex [59, 83, 160, 161] algorithms.
The popular algorithm of Lagrava *et al.* [83], that is adopted for this study is based on a cell-vertex formulation and relies on the definition of an overlapping area whose thickness is equal to one coarse cell (Fig. 3.7). Distribution functions from coarse to fine grids are transferred at co-located nodes ● and rescaled using Eq. (3.5.4). Fine to coarse distributions are exchanged at co-located nodes ■ after being filtered with Eq. (3.5.6) and rescaled with Eq. (3.5.5).

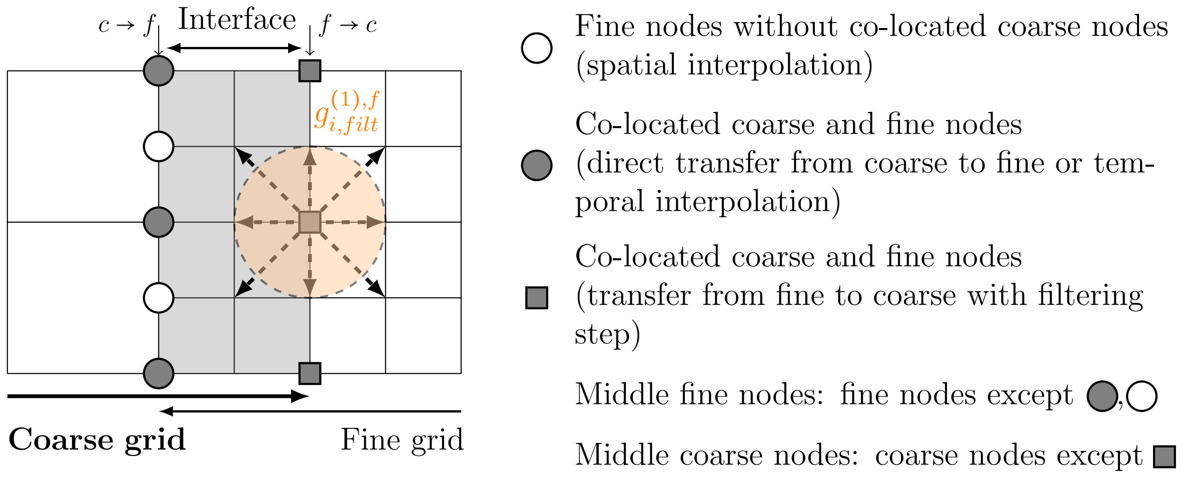

Figure 3.7 – *Two dimensional representation of a plane refinement interface and nodes definition. The overlapping interface is colored in gray. The orange area represents the filter zone to compute* $g_{i,filt}^{(1),f}$.

As there are two fine iterations in one coarse time step, a temporal interpolation of ρ^c, u^c and $g^{(1),c}$ is mandatory to reconstruct the fine missing populations during the asynchronous iterations on nodes ●. A third-order polynomial interpolation is used [59]. For a quantity h, its reads:

$$h\left(\bullet, t+1/2\right) = -\frac{1}{8}h\left(\bullet, t-1/2\right) + \frac{3}{4}h\left(\bullet, t\right) + \frac{3}{8}h\left(\bullet, t+1\right). \tag{3.5.7}$$

At fine nodes ○ which do not have a corresponding coarse node, a third-order spatial interpolation is used to enforce the second-order accuracy of the LBM at the grid interface [83]. In the following, an interface with a normal and tangential vector $e_x(1,0)$ and $e_y(0,1)$ respectively is considered. For a quantity h, the interpolation scheme reads

$$h\left(\circ, t\right) = \frac{9}{16}\left(h\left(\circ + \frac{e_y}{2}, t\right) + h\left(\circ - \frac{e_y}{2}, t\right)\right) - \frac{1}{16}\left(h\left(\circ + \frac{3e_y}{2}, t\right) + h\left(\circ - \frac{3e_y}{2}, t\right)\right). \tag{3.5.8}$$

Now all the notions necessary for the algorithm have been described, the different steps are detailed.

Algorithm steps

1) **Reference state** → Fine grid t ; Coarse grid t
    a. All the distribution functions are known on both grids
2) **Asynchronous iteration** → Fine grid $t+1/2$; Coarse grid $t+1$
    a. Propagation step for fine and coarse middle nodes.
    b. Temporal interpolation of ρ^c, u^c and g^c on ●^{f} nodes using Eq. (3.5.7). g^f are reconstructed using Eq. (3.5.4).
    c. Spatial interpolation of ρ^f, u^f and g^f on ○ nodes with Eq. (3.5.8).
    d. Collision of all fine nodes.
3) **Synchronous iteration** → Fine grid $t+1$; Coarse grid $t+1$
    a. Propagation step for fine middle nodes.
    b. Transfer of ρ^c, u^c, g^c and reconstruction of g^f using Eq. (3.5.4) on ●^{f} nodes.
    c. Spatial interpolation of ρ^f, u^f and g^f on nodes ○ with Eq. (3.5.8).
    d. Filtering step with Eq. (3.5.6) and reconstruction of g^c on ■ nodes using Eq. (3.5.5).
    e. Collision of all nodes.
4) **Repetition of steps 2) to 4) until the end of the simulation**.

Up to now, grid coupling concepts have been introduced and a cell-vertex algorithm has been described. Moreover, stability analyses have revealed the existence of non-hydrodynamic modes with a macroscopic contribution. Additionally, an extended stability analysis for non-uniform meshes was proposed. The latter revealed mode transfers intrinsic to the resolution change, between physical and non-hydrodynamic modes carrying a similar quantity. Finally, sensors have been designed to detect and track non-hydrodynamic modes, allowing to link the LSA to simulations. Now that all the tools have been established, academic test cases will be presented to decompose the non-physical phenomena that occurred during the turbulent cylinder simulations previously introduced in Sec. 2.6.

3.6 Harmful contribution of non-hydrodynamic modes at grid refinement interfaces

The aim of this section is to highlight some issues of grid refinement algorithms on very simple cases. First of all, a convected shear wave will be introduced to characterize the effect of the SpuriousS (○) modes. Then an upstream acoustic wave is studied to look at the influence of the SpuriousAc (□) modes. The simulations will be carried out in an in-house LB-BGK code, with the grid refinement algorithm described in Sec. 3.5.

3.6.1 Convected shear wave

The first test case introduced is a plane convected shear wave, which is one of the most simple cases allowing to have a look at a shear flow across a grid refinement interface.

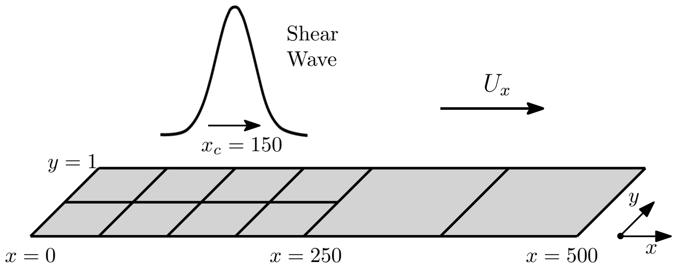

Figure 3.8 – *Schematic representation of the convected shear wave test case.*

The convected plane shear wave is initialized on the fine grid as follow:

$$\begin{cases} \rho\left(x,y\right) = \rho_0, \\ u_x\left(x,y\right) = U_x, \\ u_y\left(x,y\right) = U_y \exp\left(-\frac{(x-x_c)^2}{2R_c^2}\right), \end{cases} \tag{3.6.1}$$

with

$$\rho_0 = 1, \quad U_x = U_y = 0.1c_s, \quad R_c = 5, \quad x_c = 150, \quad \nu = 10^{-6}.$$

Every quantities are given in the coarse dimensionless unit.

The refinement interface is located at $x = 250$ with the fine domain defined between $0 < x < 250$ and the coarse domain for $x > 250$. The simulation domain is extended below

$x < 0$ and above $x > 500$ to avoid any reflection of waves on the domain boundary. Since the case is invariant along the y axis, the domain is defined with a thickness of one coarse cell.

The first numerical experiment results are presented on Fig. 3.9 where, for each plot, the two fine iterations and one corresponding coarse iteration are represented. This allows for the visualization of the amplitude inversion of non-hydrodynamic modes in the fine domain as described on Fig. 3.3.

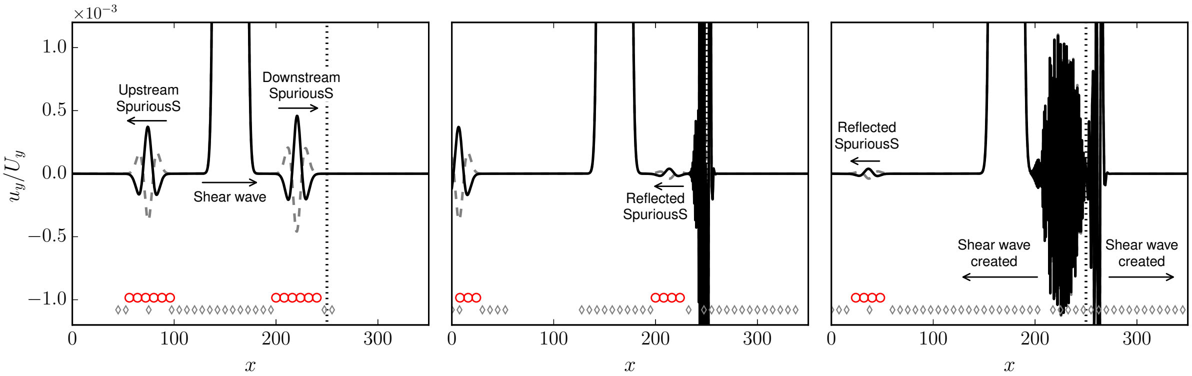

Figure 3.9 – *Convected shear wave with the BGK collision model. The sub-fine iteration* (---) *as well as the coarse iteration* (—) *are plotted to visualize the amplitude inversion of non-hydrodynamic modes. The* (○) *symbols allow detecting the SpuriousS modes and* (◊) *the SpuriousG ones, by the* NHsensor$^{(○)}$ *and* NHsensor$^{(◊)}$ *respectively. Left:* $t = 90$*, Middle:* $t = 170$*, Right:* $t = 380$ *coarse iterations.*

As predicted by the von Neumann analysis (*cf.* Fig. 3.2) and previously observed on Fig. 3.3, after the initialization state, two SpuriousS (○) modes are excited, one going upstream and the other one downstream. The amplitude of these modes is reversed at each iteration, due to the high value of their pulsation ω_r. Furthermore, the wavelength of these modes is about $2R_c$.

At $t = 170$, the SpuriousS (○) mode travelling downstream does not properly cross the interface. A SpuriousS mode detected by the corresponding sensor is reflected on the interface and is advected upstream. However, most of the energy is converted into physical waves going both upstream and downstream as shown at $t = 380$. Indeed, for wavenumbers close to $k_x = \pi$, physical shear modes can be advected upstream due to a negative group velocity.

The shear waves created by the SpuriousS (○) modes are amplified at the interface. An explanation for this amplification may be found on Fig. 3.10 where two coarse iterations are schematically decomposed. Indeed, the SpuriousS modes are reversed at each iteration, and, due to the acoustic scaling of the LBM (*cf.* Eq. (2.4.16)), fine cells are updated twice as frequently as coarse ones. As a matter of fact, the SpuriousS modes are often in phase opposition from one side to the other of the interface. **This leads to a huge error during the temporal interpolation for one dimensional cases, and for both**

space and time interpolations for two dimensional phenomena. Furthermore, significant errors appear on (■) nodes during the fine to coarse reconstruction.

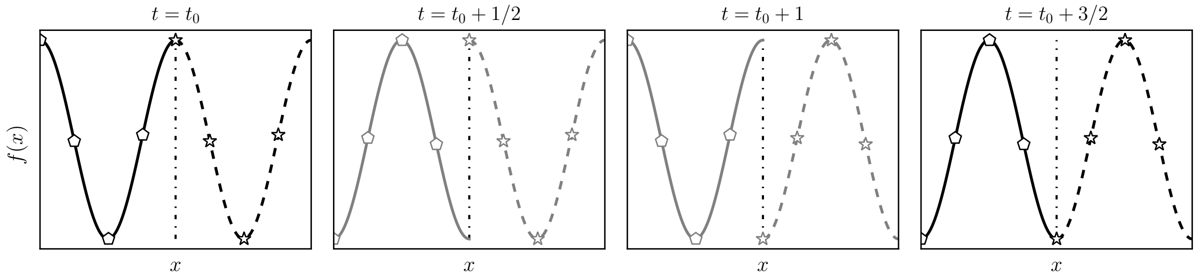

Figure 3.10 – *Schematic representation of a spurious mode at a grid refinement interface during two consecutive coarse iterations. Due to asynchronous time evolution between the two meshes, modes could be in phase or in phase opposition. Phased modes* (–⬠–)*: fine mesh,* (-☆-)*: coarse mesh. Phase opposed modes* (–⬠–)*: fine mesh.* (-☆-)*: coarse mesh.*

One can also notice that at $t = 90$, the SpuriousG (◊) modes going upstream cross the interface without having any impact at the macroscopic level. It is confirmed at $t = 170$ where no variation of transversal velocity is observed downstream the interface (and no variation of density, which remained null every time for this test case). Still, the grid refinement has created upstream and downstream SpuriousG modes, each detected by the corresponding sensor.

The effect of the grid refinement on the convected shear wave is, with the BGK collision model, to redistribute the energy on all shear modes. This behavior is in agreement with the Sec. 3.4 study but some non-linear effects and amplifications are also observed. High frequency physical shear waves are created with a significant amplitude at the interface. Hence, with this collision model, a proper advection of a shear wave through a mesh transition is unlikely to be possible, given the redistribution of energy between physical and non-hydrodynamic modes.

3.6.2 Convected acoustic wave

The second test case introduced is a convected one dimensional acoustic wave. This test case has the advantage of exciting only the modes carrying the acoustics, *i.e.* the physical acoustics Ac+ (▸) and Ac- (◂) modes and the SpuriousAc (□) ones.

Similarly, with the previous shear Gaussian excitation, one expects to generate a well-resolved SpuriousAc mode. According to the spectral analysis of Fig. 3.2, this mode does not have any positive group velocity for low wavenumbers, and the resolved SpuriousAc mode may be advected upstream. Hence, to investigate the effect of this mode across a transition, it is chosen to initialize the wave on the right of the transition. An upstream acoustic wave carried by a mean flow is then initialized as follows:

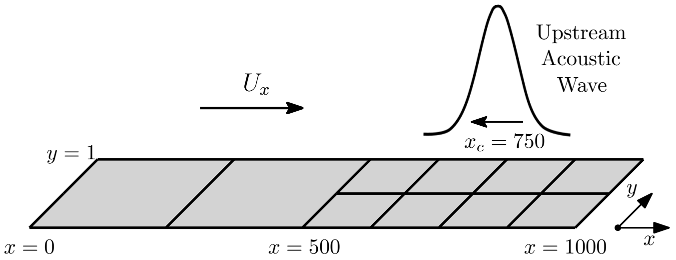

Figure 3.11 – *Schematic representation of the convected acoustic wave test case.*

$$\begin{cases} \rho\left(x\right) = \rho_0\left(1 + A\exp\left(-\frac{(x-x_c)^2}{2R_c^2}\right)\right), \\ u_x\left(x\right) = U_x - A\exp\left(-\frac{(x-x_c)^2}{2R_c^2}\right)c_s, \end{cases} \tag{3.6.2}$$

with

$$\rho_0 = 1\ , \quad U_x = 0.1 \cdot c_s, \quad A = 10^{-4}, \quad R_c = 5, \quad x_c = 750, \quad \nu = 10^{-6}.$$

The refinement interface is located at $x = 500$ with the fine domain located between $500 < x < 1000$ and the coarse domain for $x < 500$. The simulation domain is extended below $x < 0$ and above $x > 1000$ to avoid any wave reflection on the domain boundary. Since the case is invariant along the y axis, the domain is defined with a thickness of one coarse cell.

The numerical experiment results are presented on Fig. 3.12 where, for each plot, the coarse iterations are decomposed with the two fine corresponding sub-iterations. Many phenomena appear, and, for the sake of clarity, they are described one by one as numerated on the Fig. 3.12.

Fig. 3.12-A presents the effect of the upstream acoustic wave that has been advected from $x = 750$ to $x = 270$, and has already passed through the grid interface. As expected [143], a reflected acoustic wave (Fig. 3.12-A_1) appears. Its amplitude is 2000 times less than its corresponding incident acoustic wave. Furthermore, a high wavenumber ($k_x \simeq \pi$) SpuriousAc mode (□) is generated at the interface and advected upstream (*cf.* Fig. 3.12-A_2). Moreover, as intended, SpuriousAc modes (□) have been excited at the initialization with a negative group velocity. Their amplitudes are 10^7 times smaller than that of the upstream acoustic wave (*cf.* Fig. 3.12-A_3). Both SpuriousAc modes are succesfully detected by the NHsensor$^{(\square)}$.

Fig. 3.12-B shows the instant when the incident SpuriousAc mode (□), that was previously described on Fig. 3.12-A_3, has impinged the interface (*cf.* Fig. 3.12-B_1). A huge amplification appears on the density field and a high frequency spurious wave is generated.

In the end, two acoustic waves are generated by the incident SpuriousAc ones, as shown on Fig. 3.12-C: one is going downstream on the fine mesh with an amplitude 100 times smaller than the initial acoustic wave, and the other one is advected upstream with

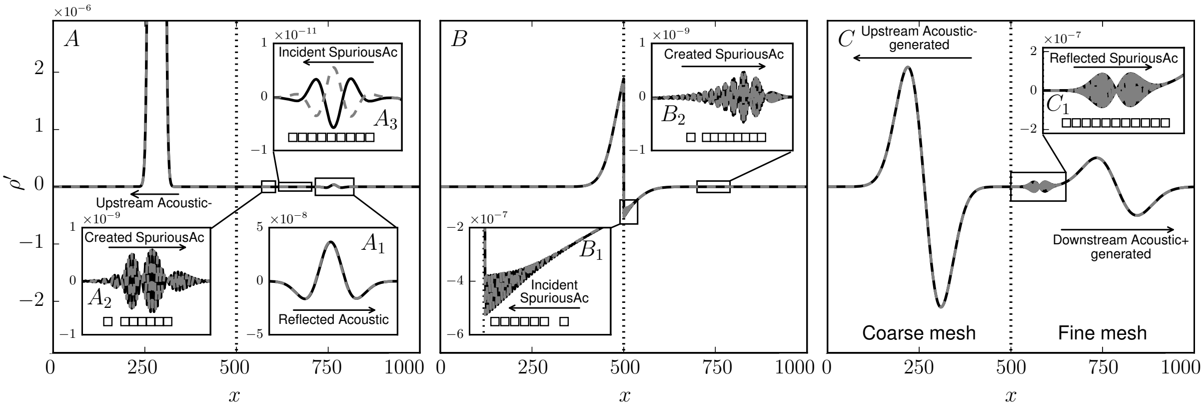

Figure 3.12 – *Relative density evolution* $\rho' = \rho - \rho_0$ *of the upstream acoustic wave with the BGK collision model. The sub-fine iteration* (- - -) *as well as the coarse iteration* (—) *are plotted to visualize the amplitude inversion of non-hydrodynamic modes. The* (□) *symbol allow detecting the SpuriousAc modes by the* NHsensor$^{(\square)}$. *Left:* $t = 900$*, Middle:* $t = 2050$*, Right:* $t = 2620$ *coarse iterations.*

an amplitude 25 times smaller. The incident SpuriousAc modes have been amplified with a factor up to 4.10^5 to reach no less than 4% of the initial acoustic wave amplitude.

This test case highlights the transfer of energy between physical acoustic modes (▸,◂) and the SpuriousAc modes (□) that can appear when a change of mesh resolution occurs. It is in agreement with the analysis performed on Sec. 3.4 where these three modes have non-nul off-diagonal P_{ij} coefficients. This kind of transfer has not been studied until here, as the classical benchmark for acoustic propagation across a grid interface is commonly performed at a null Mach number [69]. In such case, the SpuriousAc (□) mode are static and never cross the interface. This transfer is at the core of a part of the spurious noise emission that can appear when vortices pass through a grid refinement interface [69].

Finally, it has been shown that **transfers occur between modes that carry the same kind of quantity. Acoustic (▸,◂) modes can exchange energy with the SpuriousAc (□) modes and the physical shear mode (●) with the SpuriousS** (○) ones as anticipated in Sec. 3.4.

3.7 Summary and conclusion of this chapter

A summary of the main steps of this chapter is given on Fig. 3.13.

In this chapter, the principles of stability analysis have been introduced, in particular to characterize the non-hydrodynamic content of the LB-BGK scheme. Thanks to the analysis of the eigenvector content, Wissocq *et al.* [148] have shown that a macroscopic quantity could be transported by the non-hydrodynamic modes. According to the quantity transported and their propagation velocity, we have classified these modes as: SpuriousS (○) which carry shear, SpuriousAc (□) modes which haul a combination of acoustic modes, and SpuriousG (◊) modes which are purely ghost. The LSA allowed to anticipate that the BGK model dissipated only very weakly these non-hydrodynamic modes, which seemed to be confirmed by the dilatation and vorticity fields of the cylinder case (*cf.* Fig. 2.6 and Fig. 2.7).

As a complement, sensors based on spectral properties of non-hydrodynamic modes have been designed to link the LSA with the simulations by allowing the latter to be tracked during calculations.

In addition, a linear stability study extended to a change in resolution was proposed for the BGK model. The latter revealed that **transfers between physical and non-physical modes take place, directly attributable to the change in resolution, regardless from the quality of the grid coupling algorithm used**. These transfers are therefore inherent to the collision model and are all the more important when the resolution is poor. However, these **transfers are constrained to modes that carry quantities of the same type**. Thus, a physical shear wave (●) can be transformed into a SpuriousS wave (○) and vice versa, and acoustic waves (▸, ◂) can interact with SpuriousAc waves (□) only.

These conclusions from the LSA have been validated on two academic test cases in an in-house LB code: a shear plane wave and an acoustic plane wave to illustrate these mode transfers. **An additional phenomenon which turns out to be very harmful is the phase inversion of the non-hydrodynamic modes at each iteration**. Due to the acoustic scaling of the LBM, this inversion generates an important discontinuity at the interface which results in a very strong amplification of the spurious modes.

This phenomenon cannot be properly handled by a grid refinement algorithm, unless spatial or temporal smoothing is used, but this would affect the accuracy of such algorithms. The only way is therefore to filter these modes before they interact with a grid interface. For this purpose, advanced collision models will be presented in the next chapter, specifically selected for their non-hydrodynamic mode filtering properties. The BGK model will no longer be practically studied because it is obviously not suitable for industrial aeroacoustic simulations. However, an in-depth analysis of the spectral properties and stability of the BGK model will be carried out in Chap. 5. Indeed, although it is not usable in our study framework, this model has very particular spectral properties that are worthy of interest.

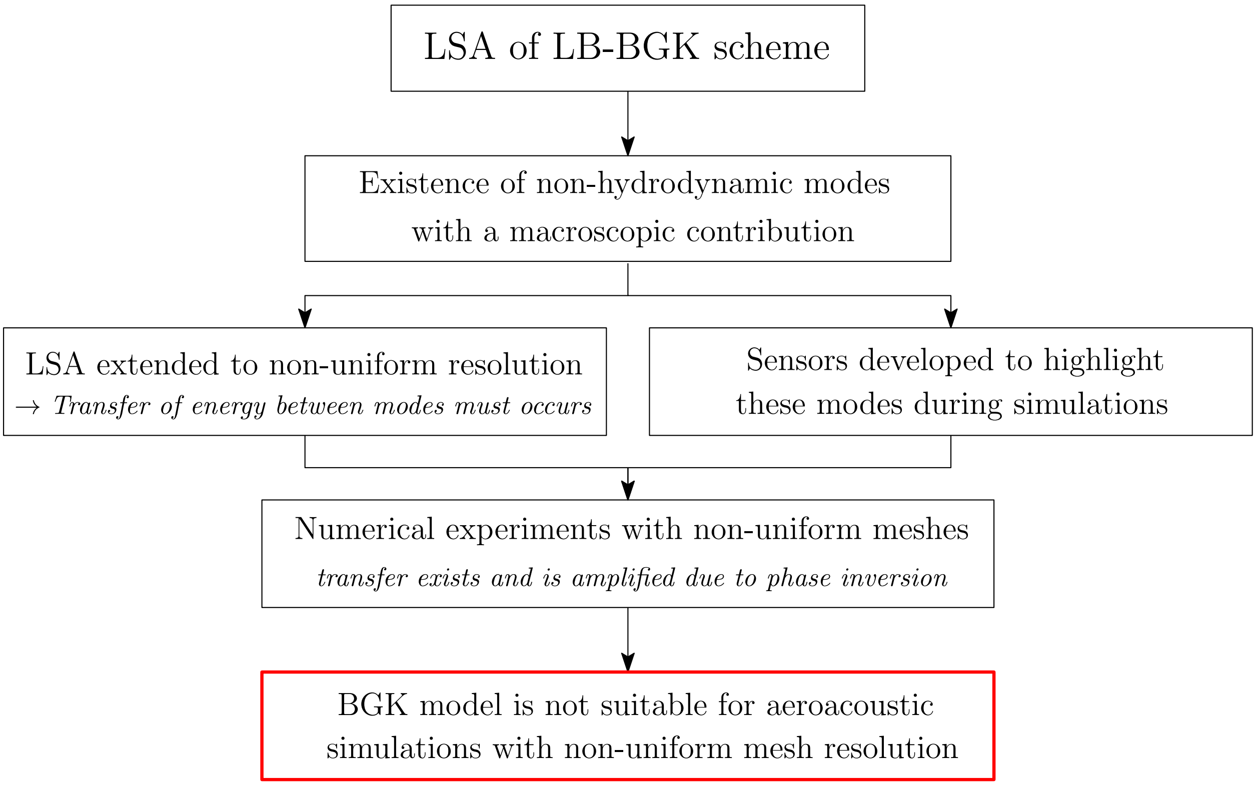

Figure 3.13 – *Summary of the main steps of this chapter.*

Chapter 4

Improved collision operator for aeroacoustic simulations on non-uniform grids

Contents

*This chapter is dedicated to the introduction of advanced collision operators considered for their ability to filter non-hydrodynamic modes in the fluid core. The spectral analysis reveals an excellent filtering property of the non-hydrodynamic modes by reconstructing the stress tensor thanks to the stress rate tensor. This method being too dissipative, hybridization with the recursive regularized model [126] proves to be a good compromise between filtering and accuracy (*H-RR *model [60]). Validations with non-uniform grids are performed for an acoustic pulse, a shear wave, a vortex, and a turbulent flow around a cylinder. The spurious waves of non-hydrodynamic nature visible on Fig. 2.6 and Fig. 2.7 turn out to be completely filtered.*

4.1 Advanced collision operators

The BGK collision model, as discussed in the previous chapter, not only suffers from instability problems, but it also fails in dissipating non-hydrodynamic modes in the fluid core. There are a variety of solutions to increase LB scheme stability and attenuate these modes. One can add low-pass filter [162, 163], use fractional propagation algorithms to suppress high-frequency oscillations [164–166], or adapt the collision model. To improve the stability of the BGK operator, many collision models have been developed. Among them, one can mention the multiple relaxation time (MRT) models in different formalisms. The founders of the MRT models expressed the collision in the *raw-moment* space [134, 144, 167]. Later on, several authors proposed to perform the collision in the *central-moments* space, defined in the co-moving reference frame to improve the stability of LB schemes [168–171]. These models are often referred as *cascaded*. Geier *et al.* have further, expressed the collision in the cumulant space [172]. However, these last two categories, to date, do not have been formulated and validated for a D3Q19 lattice, a D3Q27 is required. In addition, the MRT *raw-moment* cited above in their original formulation, drastically increase the bulk viscosity for stability reasons [70, 146], what should be avoided for acoustics studies.

A well-known family of advanced collision models constructed in order to cancel high-order contributions are the regularized collision models. The standard regularization procedure can be interpreted as a MRT model in the Hermite basis [173] where "ghost variables" are relaxed at a specific value $\bar{\tau}_g = 1$. A recent study have highlighted the capability of regularized collision models to completely filter some non-hydrodynamic modes out of a computation [149]. For instance, the recursive regularized model allows for reducing the number of modes of the D2Q9 lattice to six modes instead of nine [126].

This mode filtering property of regularized operators will be particularly interesting to emphasize the effects of non-hydrodynamic modes crossing a mesh refinement interface. Moreover, the regularized models, by construction, do not increase the bulk viscosity and have already been used for aeroacoustic applications [174]. For these reasons regularized models will be studied in the following. However, additional results with other models are proposed in Sec. 4.7 for the sake of generality.

4.1.1 Recursive regularized collision model: RR

The regularization procedure consists in filtering out high-order moments of the off-equilibrium distribution function to enhance the stability of the LB scheme. This is done by reconstructing the distribution function before the collision step as proposed by Latt and Chopard [155,173]. The reconstruction consists in projecting the off-equilibrium part of the distribution function onto the Hermite basis up to the second-order.

$$g_i^{reg} \equiv g_i^{(0)} + g_i^{(1),reg}, \tag{4.1.1}$$

with

$$g_i^{(1),reg} = w_i \frac{1}{2c_s^4} \boldsymbol{a}_1^{(2)} : \mathcal{H}_i^{(n)}, \tag{4.1.2}$$

where $\boldsymbol{a}_1^{(2)}$ are the off-equilibrium expansion coefficients defined as

$$\boldsymbol{a}_1^{(2)} = \sum \mathcal{H}_i^{(2)} \left(g_i - g_i^{(0)} \right). \tag{4.1.3}$$

This is equivalent with relaxing off-equilibrium moments of order higher than two at equilibrium before the collision step. Furthermore, the regularization method aims at filtering out higher-order contributions in Knudsen number by imposing Eq. (4.1.1) [155]. The LB scheme defined in Eq. (2.4.13) can be modified to apply the regularized procedure to all the distribution functions g_i. Its becomes

$$g_i \left(\boldsymbol{x} + \boldsymbol{e}_i, t+1 \right) = g_i^{(0)} + \left(1 - \frac{1}{\tau} \right) g_i^{(1),reg}. \tag{4.1.4}$$

It has been shown in [126, 136] that this model suffers from stability issues for relatively small Mach numbers which make it not well suited for many aeroacoustic applications.

More recently, it has been proposed by Malaspinas [126] to enhance the content of $g_i^{(1),reg}$ by including some higher-order off-equilibrium expansion coefficients (identified as moments of $g_i^{(1),reg}$ [112]) in the regularization procedure (Eq. (4.1.1)). Following the expansion in Hermite polynomials introduced in Sec. 2.3.1, $g_i^{(1)}$ reads

$$g_i^{(1)} = w_i \sum_{n=2}^{N_1} \frac{1}{c_s^{2n} n!} \boldsymbol{a}_1^{(n)} : \mathcal{H}_i^{(n)}, \tag{4.1.5}$$

where N_1 is the truncation order of the off-equilibrium distribution function. The sum starts at $n = 2$ since Eq. (2.2.11) imposes $\boldsymbol{a}_1^{(0)}=\boldsymbol{a}_1^{(1)}=0$. Moreover, the off-equilibrium expansion coefficients $\boldsymbol{a}_1^{(n)}$ are determined with a recurrence formula [126] obtained thanks to a Chapman-Enskog expansion for $n \geq 3$

$$a_{1,\alpha_1..\alpha_n}^{(n)} = u_{\alpha_n} a_{1,\alpha_1..\alpha_{n-1}}^{(n-1)} + \left(u_{\alpha_1}..u_{\alpha_{n-2}} a_{1,\alpha_{n-1}\alpha_n}^{(2)} + \mathrm{perm}(\alpha_n) \right) \tag{4.1.6}$$

These models are referred to as recursive regularized collision models and have yielded greatly improved stability for the regularization procedure [126, 136, 175]. For the D2Q9 lattice, the off-equilibrium distribution functions $g_i^{(1),reg}$ up to the third-order ($N_1 = 3$) can be expressed as:

$$g_i^{(1),reg} = w_i \left(\frac{1}{2c_s^4} \mathcal{H}_i^{(2)} : \boldsymbol{a}_1^{(2)} + \frac{1}{2c_s^6} \left(\mathcal{H}_{i,xxy}^{(3)} a_{1,xxy}^{(3)} + \mathcal{H}_{i,xyy}^{(3)} a_{1,xyy}^{(3)} \right) \right), \tag{4.1.7}$$

where

$$a_{1,xxy}^{(3)} = 2u_x a_{1,xy}^{(2)} + u_y a_{1,xx}^{(2)}, \qquad a_{1,xyy}^{(3)} = 2u_y a_{1,xy}^{(2)} + u_x a_{1,yy}^{(2)}. \tag{4.1.8}$$

Note that in two dimensions, the recursive regularization procedure can also include fourth-order terms in $g_i^{(1),reg}$ to improve stability. Yet, no difference was observed in this study when including these terms which cannot be take into account with the D3Q19 lattice [126] that is used in LaBS/ProLB. Hence, the RR model will refer to the expression of Eq. (4.1.7) injected into Eq. (4.1.1). For the D3Q19 lattice used for the turbulent test-case in Sec. 4.5, the equilibrium and off-equilibrium functions that are proposed for the D3Q27 lattice in [126] are used, but truncated to the third-order.

4.1.2 Hybrid-recursive regularize collision model: H-RR

The last collision model introduced is chosen for its highly relevant spectral properties that will be presented in Sec. 4.2.2. This recent model proposed by Jacob [60] is based on a hybridization of the recursive regularized collision model with a finite difference reconstruction of the viscous stress tensor. Indeed, a Chapman-Enskog expansion [110] allows to link the off-equilibrium populations $g_i^{(1)} = g_i - g_i^{(0)}$ with the deviatoric tensor $S_{\alpha\beta} = 1/2\left(\nabla\boldsymbol{u} + (\nabla\boldsymbol{u})^T\right)$ through the second-order moments of $g^{(1)}$ (*cf.* Eq. (2.3.30)).

$$\sum_i e_{i,\alpha} e_{i,\beta} g_i^{(1)} \simeq -2\bar{\tau}\rho c_s^2 S_{\alpha\beta}. \tag{4.1.9}$$

It is then possible to hybridize the viscous stress tensor computation as follow

$$\boldsymbol{a}_1^{(2),\mathrm{HRR}} = \sigma \boldsymbol{a}_1^{(2)} + (1-\sigma)\boldsymbol{a}_1^{(2),\mathrm{FD}} \qquad \text{with} \quad [0 \le \sigma \le 1], \tag{4.1.10}$$

where $\boldsymbol{a}_1^{(2)}$ are computed thanks to Eq. (4.1.3) and $\boldsymbol{a}_1^{(2),\mathrm{FD}}$ is estimated with a second-order centered finite-difference scheme as

$$a_{1,\alpha\beta}^{(2),\mathrm{FD}} = -\tau\rho c_s^2 \left(\frac{u_\alpha(\boldsymbol{x}+\boldsymbol{e_\beta}) - u_\alpha(\boldsymbol{x}-\boldsymbol{e_\beta})}{2} + \frac{u_\beta(\boldsymbol{x}+\boldsymbol{e_\alpha}) - u_\beta(\boldsymbol{x}-\boldsymbol{e_\alpha})}{2} \right), \tag{4.1.11}$$

where $\boldsymbol{e_\alpha}, \boldsymbol{e_\beta} \in \{\boldsymbol{e_x}, \boldsymbol{e_y}\}$ are unitary vectors of the Cartesian coordinate system.

Then, third-order off-equilibrium Hermite coefficients are computed recursively using the modified $\boldsymbol{a}_1^{(2),\mathrm{HRR}}$ with Eq. (4.1.8). As in the RR collision model, $g_i^{(1)}$ is computed using Eq. (4.1.7) before the collision step, and injected into the LBM scheme (4.1.4).

The choice of these two collision models is far from exhaustive, and has been motivated by their interesting spectral properties regarding non-hydrodynamic modes that will be highlighted in the next section.

4.2 Analyses of advanced collision operator

In this section, advanced collision model stability analyses will be performed. These analyses, as in Sec. 3.1.2, will be performed for waves propagating in the flow direction only to identify the propagation and dissipation properties of non-hydrodynamic modes. Stability analyses taking into account all propagation directions will be carried out in Chap. 5.

4.2.1 Von Neumann analysis of the RR collision operator

The spectral analysis results for the RR model are displayed on Fig. 4.1 and one can observe many differences with the BGK model presented on Fig. 3.2. In the present case, only six modes are present instead of nine, the eigenvalues associated with the three others having a null modulus. Compared to the BGK model, the two SpuriousG modes (◊) and one SpuriousS mode (○) have been filtered out. Furthermore, the physical shear mode (●) is more attenuated than in the BGK case. However, two spurious modes that carry physical quantities have remained: the SpuriousAc modes (□), with identical dissipation and dispersion properties to those seen with the BGK model, and one SpuriousS mode (○) that is much more attenuated, and has a lower group velocity v_g for low wavenumbers.

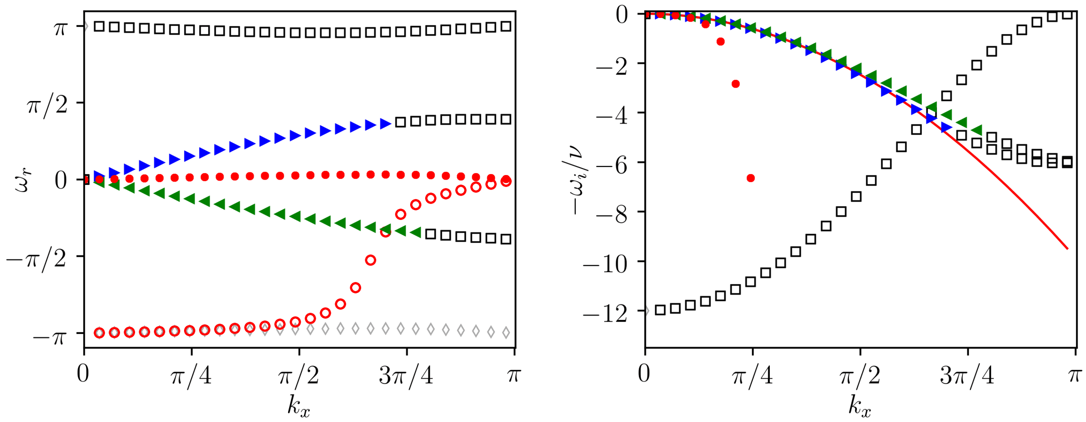

Figure 4.1 – *Propagation and dissipation curves for the RR collision model.* $\nu = 10^{-6}$, *Ma=0.1.* (▸): *Ac+ mode,* (◂) : *Ac- mode,* (●) : *Shear mode,* (○) : *SpuriousS modes,* (□) : *SpuriousAc modes,* (◊) : *SpuriousG modes,* (—) : *Isothermal Navier-Stokes.*

The spectral behavior of this model with respect to non-hydrodynamic modes is interesting since some modes have disappeared and the others that carry shear are much more dissipated (visible on Fig. 4.4). On the contrary, the SpuriousAc (□) one is not influenced by this model. That is one of the reasons why the H-RR model is studied in the following.

4.2.2 Von Neumann analysis of the H-RR collision operator

Before studying the LSA of the H-RR model as it will be used later, it is interesting to consider the effect of a complete reconstruction of the stress tensor with finite differences ($\sigma = 0$) on the spectral properties of the scheme on Fig. 4.2.

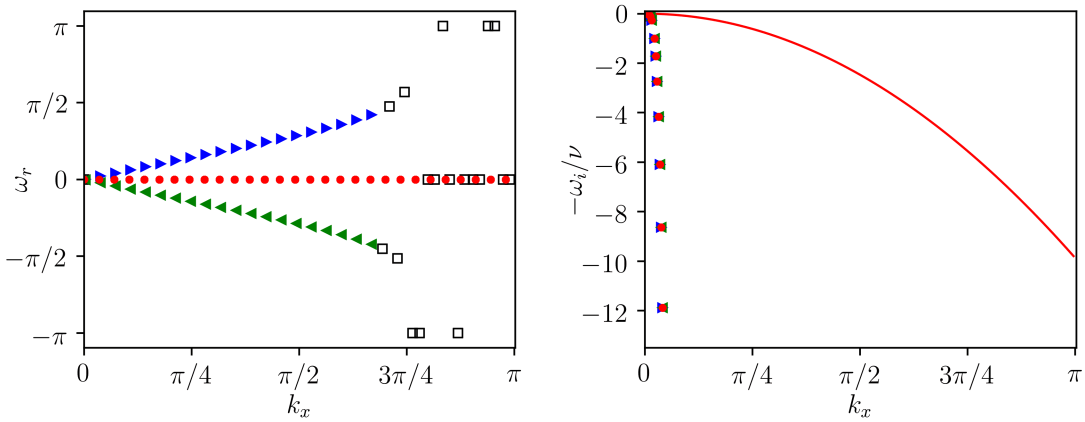

Figure 4.2 – *Propagation and dissipation curves for H-RR collision model with* $\sigma = 0$. $\nu = 10^{-6}$, *Ma=0.* (▶)*: Ac+ mode,* (◀) *: Ac- mode,* (●) *: Shear mode,* (□) *: SpuriousAc modes,* (—) *: Isothermal Navier-Stokes.*

The full reconstruction of the viscous stress tensor has the main advantage making all the spurious modes fully vanish for $k_x < 3\pi/4$. Indeed, whatever the number of velocity of the lattice, the number of remaining modes corresponds to the number of physical modes, as would be the case when solving the isothermal Navier-Stokes equations. In two dimensions, three modes remain, while a fourth mode is observed in three dimensions, corresponding to an additional physical shear wave.

The counterpart of this beneficial effect is the huge dissipation rate of physical modes introduced, which is unbearable for aeroacoustic purposes.

Now, the spectral analysis of the H-RR collision model is presented on Fig. 4.3 with the parameter σ set to $\sigma = 0.995$. This implies that the viscous stress computation is computed at 99.5% with standard approaches (*cf.* Eq. (4.1.3) and with 0.5% with a finite difference estimation of the stress tensor (*cf.* Eq.(4.1.9)).

The value of 0.995 is retained for all the academical numerical experiments since it induces a strong dissipation of non-hydrodynamic modes while keeping a fairly satisfactory dissipation of the physical ones. A value of 0.98 is used for turbulent flows. The consequences of the hybrid reconstruction on physical wave dissipation will be studied in Chap. 5.

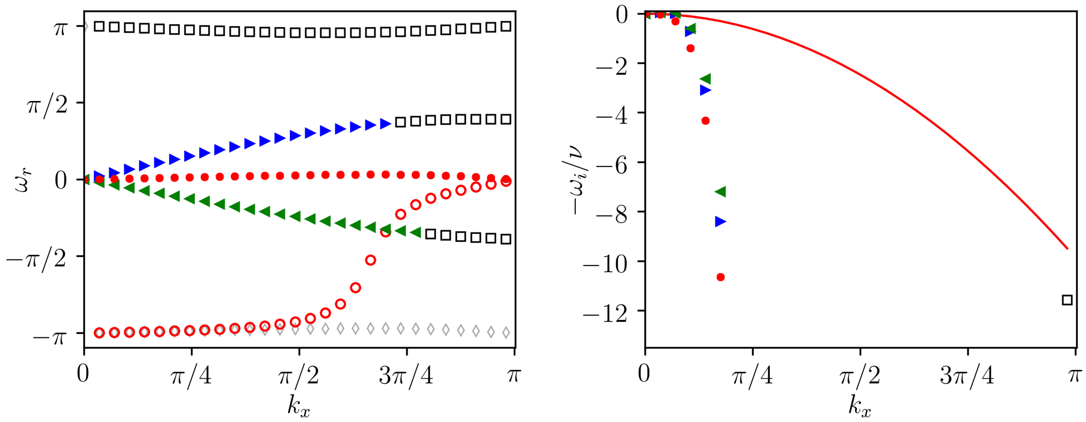

Figure 4.3 – *Propagation and dissipation curves for the H-RR collision model with* $\sigma = 0.995$. $\nu = 10^{-6}$, *Ma=0.1.* (▶)*: Ac+ mode,* (◀) *: Ac- mode,* (●) *: Shear mode,* (○) *: SpuriousS modes,* (□) *: SpuriousAc modes,* (◊) *: SpuriousG modes,* (—) *: Isothermal Navier-Stokes.*

One can observe that dispersion properties are almost identical to that of the RR model. On the other hand, discrepancies appear on the dissipation curves. A better overview is available on Fig. 4.4 where the dissipation rate $-\omega_i/\nu$ is displayed on a logarithmic scale, and compared to the BGK and RR collision models. At first, the remained SpuriousS mode (○) is much more attenuated than for the RR model for low wavenumbers. The SpuriousG modes (◊) have equivalent dissipation properties, but the main differences appear on the SpuriousAc modes (□). The dissipation of this mode is rigorously equivalent for the BGK or RR models, but for the H-RR model it is a lot more dissipated.

For the H-RR collision model, an estimation of the SpuriousAc mode (□) dissipation based on the spectral analysis can be proposed:

$$\nu^{(\square)} \simeq \nu + \frac{1-\sigma}{4} c_s^2, \qquad \forall \sigma > 0. \tag{4.2.1}$$

This estimation seems valid for a dimensionless viscosity $\nu < 0.1$ and is qualitatively assessed on Fig. 4.4 where, among other things, the dissipation of the SpuriousAc (□) mode is compared for the RR and H-RR collision models. For $\nu = 10^{-6}$ and $\sigma = 0.995$, the SpuriousAc mode is damped at a rate $\nu^{(\square)} \simeq 418\nu$. The quality of this estimate will be reinforced later in the application phases by Fig. 4.13.

Since the SpuriousAc mode (□) carries macroscopic information linked with acoustics, it can also be attenuated by increasing the bulk viscosity. This can be easily done by using a multiple relaxation time collision operator [134, 144] for example. However, any modification of the bulk viscosity will also modify the damping of physical acoustic waves. In the present case, the bulk viscosity should be increased by several orders of magnitude to reach the same level of dissipation of the SpuriousAc mode (□) than the one obtained with the H-RR model (Fig. 4.4). This increase is to be banned for any study involving acoustic waves.

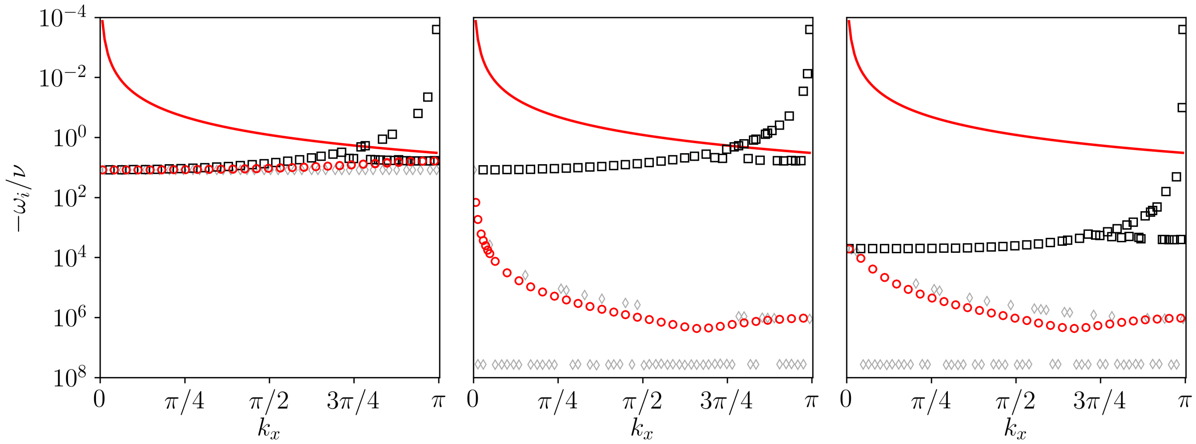

Figure 4.4 – *Comparison of the non-hydrodynamic modes dissipation for the three collision models. Left: BGK, Middle: RR, Right: H-RR ($\sigma = 0.995$). $\nu = 10^{-6}$, Ma=0.1.* (○) *: SpuriousS modes,* (□) *: SpuriousAc modes,* (◊) *: SpuriousG modes,* (—) *: Isothermal Navier-Stokes.*

A summary of the spectral properties of the aforementioned collision models is given in Table. 4.1

		Dissipation of spurious mode		
		SpuriousAc (□)	SpuriousS (○)	SpuriousG (◊)
Collision model	BGK	×	×	×
	RR	×	✓ for high k_x	✓
	H-RR	✓	✓	✓

Table 4.1 – *Summary of the dissipation of non-hydrodynamic modes for the three collision models.* (✓) *high dissipation,* (×) *low dissipation.*

.

This table justifies the choice of these advanced collision models: the dissipation rates of the spurious modes are very different from the BGK one. After a discussion on mode filtering induced by the regularizations in Sec. 4.2.3, a subsequent comparison of their behavior across a mesh refinement interface will be investigated in Sec. 4.4.

4.2.3 Discussions on non-hydrodynamic modes filtering properties of the regularized schemes

The LSAs of the RR and H-RR collision models ($\sigma = 0$) revealed that these models are capable of completely suppressing some non-hydrodynamic modes. An explanation for this filtering properties is given in the recent study by Wissocq *et al.* [149].

Every regularized collision model can be written as two successive steps: (1) a pre-collision regularization using Eq. (4.1.1), followed by (2) a BGK collision with Eq. (4.1.4).

The mode filtering property can be understood by looking at the first step of this procedure. The computation of the equilibrium distribution function involves three macroscopic quantities (ρ, u_x, u_y), hence three moments of the discrete distributions g_i are required. Regarding the non-equilibrium part $g_i^{(1)}$, it depends on the adopted model:

- with the RR model: $g_i^{(1)}$ is a function of six variables: $(\rho, u_x, u_y, a_{1,xx}^{(2)}, a_{1,xy}^{(2)}, a_{1,yy}^{(2)})$, involving six independent moments of the discrete distributions.
- with the H-RR model and $\sigma = 0$: only the first two moments of g_i (ρ, u_x, u_y) are needed to compute $\boldsymbol{a}_1^{(2),\mathrm{FD}}$ with Eq. (4.1.11), required to obtain $g_i^{(1)}$ with Eq. (4.1.5).

Pre-collision regularized distribution functions can be rewritten as

$$\underline{\mathrm{RR}}: \quad g_i^{reg}(\rho, u_x, u_y, a_{1,xx}^{(2)}, a_{1,xy}^{(2)}, a_{1,yy}^{(2)}), \tag{4.2.2}$$

$$\underline{\mathrm{H-RR}}\ (\sigma = 0): \quad g_i^{reg}(\rho, u_x, u_y). \tag{4.2.3}$$

The regularization procedure reduces the number of variables used in the system, and thus the rank of the latter. Only six variables are needed for the RR model and three for the H-RR one with $\sigma = 0$.

In three dimension with a D3Q19 lattice, nineteen modes exists. In the latter, only four are hydrodynamics: The two acoustics modes: $Ac+$, $Ac-$ and two shear modes, thus fifteen are not. The equilibrium distribution function involves four macroscopic quantities (ρ, u_x, u_y, u_z). In such case, the pre-collision regularized distribution functions can be expressed as:

$$\underline{\mathrm{RR}}: \quad g_i^{reg}(\rho, u_x, u_y, u_z, a_{1,xx}^{(2)}, a_{1,xy}^{(2)}, a_{1,xz}^{(2)}, a_{1,yy}^{(2)}, a_{1,yz}^{(2)}, a_{1,zz}^{(2)}), \tag{4.2.4}$$

$$\underline{\mathrm{H-RR}\ }(\sigma = 0): \quad g_i^{reg}(\rho, u_x, u_y, u_z). \tag{4.2.5}$$

The RR model allows keeping only six non-hydrodynamic modes instead of fifteen because of the dependency on ten variables. The full reconstruction of the viscous stress tensor (H-RR with $\sigma = 0$), allows in the same manner, to completely supress all the non-hydrodynamic modes.

In the previous section, the H-RR model adopted contains only 0.5% of finite differences estimation for the stress tensor. Because this last is not fully reconstructed using finite differences, six variables are still needed to reconstruct g_i^{reg} with a D2Q9 lattice. For that matter, three non-hydrodynamic modes are ever observed on Fig. 4.3, as in the case of the RR model (which is equivalent to the H-RR with $\sigma = 1$). However, these three remaining modes are strongly attenuated as shown on Fig. 4.4.

Once advanced collision models have been presented theoretically and their spectral properties have been discussed, the grid coupling algorithm presented in Sec. 3.5 should be adapted to take into account the finite difference estimation of $a_1^{(2),\mathrm{FD}}$ at grid interface. This step is necessary before proceeding to the numerical validations.

4.3 Adaptation of the grid refinement algorithm for the H-RR collision model

The H-RR collision model involves the estimation of velocity gradients using finite difference schemes (Eq. (4.1.11)). To ensure consistency with the numerical scheme used in the whole fluid domain, it is preferable to compute these gradients at the interface with centered second-order schemes instead of a degraded first-order upwind scheme as in [60]. This is all the more true since diffusive terms are usually calculated with centered schemes for stability and accuracy reasons.

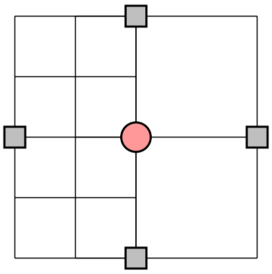

Figure 4.5 – *Two dimensional representation of a plane refinement interface. Nodes used for the estimation of the centered second-order finite difference gradient at the interface: (●): node that requires the gradient computation, (■): nodes used to estimate the gradient.*

The standard configuration of a co-located node is displayed on Fig. 4.5. The difficulty here lies in the fact that there is no fine node placed on the right of the (●) node, which would yet be required to compute the gradient. A coarse stencil is thus necessary.

During even iterations, when the two meshes are synchronized with each other, gradients can be easily estimated with a coarse stencil using either the fine or coarse macroscopic variables. Then, they can be transferred to the fine mesh after being rescaled to the fine scale as

$$S^f_{\alpha\beta} = \frac{1}{2} S^c_{\alpha\beta}. \tag{4.3.1}$$

However, at odd iterations, the velocities are unknown in the coarse mesh. They have to be temporally interpolated using Eq. (3.5.7). These gradients are also estimated with a coarse stencil, they thus need to be rescaled to the fine scale using Eq. (4.3.1).

The algorithm steps become:

1) **Reference state** → Fine grid t ; Coarse grid t

   a. All the distribution functions are known on both grids

2) **Asynchronous iteration** → Fine grid $t+1/2$; Coarse grid $t+1$
   a. Propagation step for fine and coarse middle nodes.
   b. Temporal interpolation of ρ^c, u^c and g^c on ●^{f} nodes using Eq. (3.5.7). g^f are reconstructed using Eq. (3.5.4).
   c. Estimation of the fine strain tensor $S^f_{\alpha\beta}$ on ●^{f} nodes using a second-order centered finite difference scheme following the methodology introduced in the present section.
   d. Spatial interpolation of ρ^f, u^f, g^f and $S^f_{\alpha\beta}$ on ○ nodes with Eq. (3.5.8).
   e. Collision of all fine nodes.
3) **Synchronous iteration** → Fine grid $t+1$; Coarse grid $t+1$
   a. Propagation step for fine middle nodes.
   b. Transfer of ρ^c, u^c, g^c and reconstruction of g^f using Eq. (3.5.4) on ●^{f} nodes.
   c. Estimation of the coarse strain tensor $S^c_{\alpha\beta}$ on ●^{c} using second-order centered finite difference scheme. On ●^{f} nodes, transfer and conversion of $S^c_{\alpha\beta}$ to the fine scale using Eq. (4.3.1).
   d. Spatial interpolation of ρ^f, u^f, g^f and $S^f_{\alpha\beta}$ on nodes ○ with Eq. (3.5.8).
   e. Filtering step using Eq. (3.5.6) and reconstruction of g^c on ■ nodes with Eq. (3.5.5).
   f. Collision of all nodes.
4) **Repetition of steps 2) to 4) until the end of the simulation**.

Since the grid-coupling algorithm is adapted to the H-RR model, numerical validations can be performed. As previously in Sec. 3.6 with the BGK model, the two test cases of a shear wave, followed by an acoustic wave will be conducted before progressing to a more complex case of a two-dimensional barotropic vortex.

4.4 Effect of non-hydrodynamic modes filtering: validation on academic test cases

Previously with the BGK model, it had been seen in Sec. 3.6 that a shear an acoustic wave simulated in a LB code generated SpuriousS (○) or SpuriousAc (□) waves respectively during initialization step or when passing through a refinement interface. The latter are very poorly taken into account by the mesh interface due to their phase inversion at each iteration, resulting in a strong amplification of these modes.

The RR and H-RR collision models have the particularity of filtering in a specific way these non-hydrodynamic modes, as summarized in Table. 4.1. The following numerical validations will allow validating the LSAs presented in Sec. 4.2.1 and Sec. 4.2.2, and to evidence the effect of improving the fluid modeling for enhancing the behavior at grid interfaces.

4.4.1 Assessment of the RR and H-RR model on a convected shear wave

4.4.1.a Convected shear wave with the RR collision model

The identical shear wave test case as presented in Sec. 3.6.1 is simulated using the recursive regularized collision model introduced in Sec. 4.1.1. For the sake of clarity, the SpuriousG modes (◊) are not studied in the following since they do not have any effect at the macroscopic level, even when they pass through an interface.

The von Neumann analysis predictions are, once again, verified on Fig. 4.6. After the initialization state, the SpuriousS (○) mode going upstream is excited, especially for low wavenumbers where it is not strongly attenuated (*cf.* Fig. 4.4). Its amplitude is reversed at each iteration, and it is detected before and after the physical shear wave due to the large range of its group velocity. Indeed, since its group velocity v_g is always positive, v_g is lower than that of the physical shear mode (●) for very low wavenumbers, and higher afterwards.

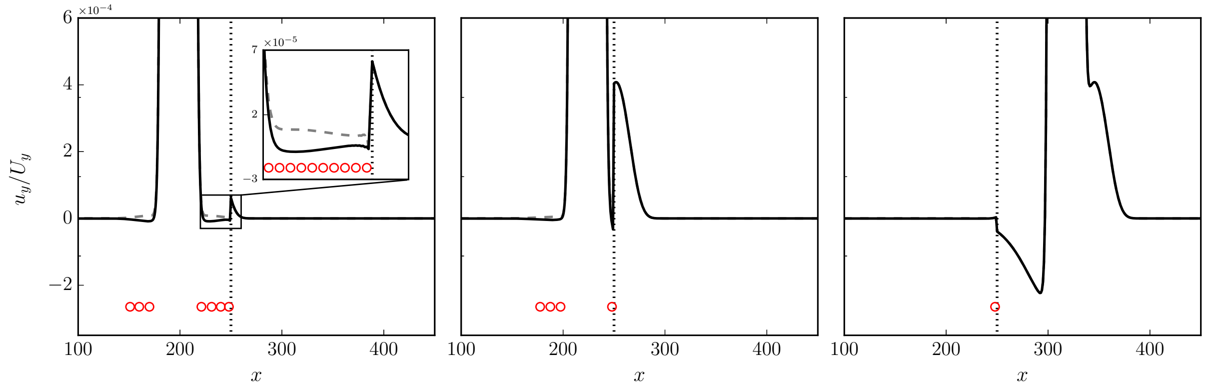

Figure 4.6 – *Convected shear wave with the RR collision model. The sub-fine iteration* (---) *as well as the coarse iteration* (—) *are plotted to visualize the amplitude inversion of non-hydrodynamic modes. The* (○) *symbols allow detecting the SpuriousS modes by the* NHsensor$^{(○)}$. *Left:* $t = 840$, *Middle:* $t = 1280$, *Right:* $t = 2900$ *coarse iterations.*

The SpuriousS (○) mode reaches the refinement interface at $t \simeq 840$ coarse iterations, and a unphysical peak appears on the transversal velocity u_y. The peak grows up to $t = 1280$. Since no mode that carry shear exists with a negative group velocity using the RR collision model, no shear wave is reflected upstream. The SpuriousS (○) mode fails to go over the interface. This last is fully converted into a physical shear mode (●), and after crossing the interface, the convected shear wave is distorted with a positive and a negative transversal velocity component.

The behavior is quite different than for the BGK collision model. No more high frequency waves are generated at the interface. A probable reason might be that these waves are very attenuated by the RR collision model as highlight on Fig. 4.4.

With the RR collision model for a fine to coarse grid crossing, the energy is fully converted from SpuriousS modes (○) to physical shear ones (●). This collision model allows for the shear wave to cross a grid refinement interface with a significant deformation. Note that no spurious noise is observed in this case.

The following section presents the analogous study with the H-RR model.

4.4.1.b Convected shear wave with the H-RR collision model

The aforementioned convected shear wave test case is now performed using the H-RR collision model. As displayed on Fig. 4.7, at $t = 840$, no SpuriousS modes (○) are detected by the NHsensor$^{(\bigcirc)}$, since they have been totally damped by the H-RR model. As a consequence, the convected shear wave perfectly crosses the interface without being deformed.

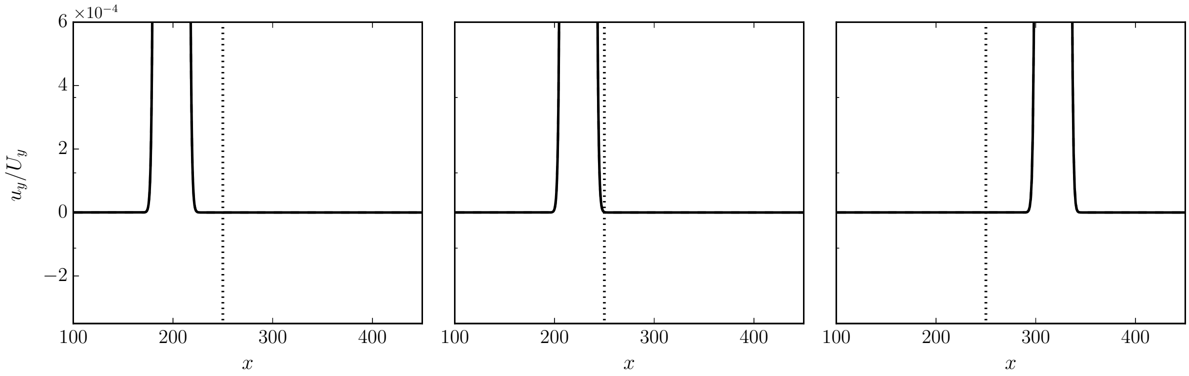

Figure 4.7 – *Convected shear wave with the H-RR collision model with* $\sigma = 0.995$*. No SpuriousS modes* (○) *is detected by the* NHsensor$^{(\bigcirc)}$*. Left:* $t = 840$*, Middle:* $t = 1280$*, Right:* $t = 2900$*.*

The H-RR collision model thus seems to be perfectly capable of dealing with shear flows in the presence of mesh refinement. The next section will compare the two models with a convected acoustic wave.

4.4.2 Assessment of the RR and H-RR model on a convected acoustic wave

The convected acoustic wave is assessed with both the RR and H-RR collision model. The LSA revealed that the RR model had exactly the same spectral properties as the BGK model for SpuriousAc (□) waves propagating in the direction carried by the mean field. It is therefore expected that the results obtained with the RR model are logically identical to those obtained with the BGK model on this test case. The Fig. 4.8 enables validating the LSA results if compared to the Fig. 3.12 obtained with the BGK model. The RR model is thus, as well as the BGK model, not satisfying for damping SpuriousAc modes (□).

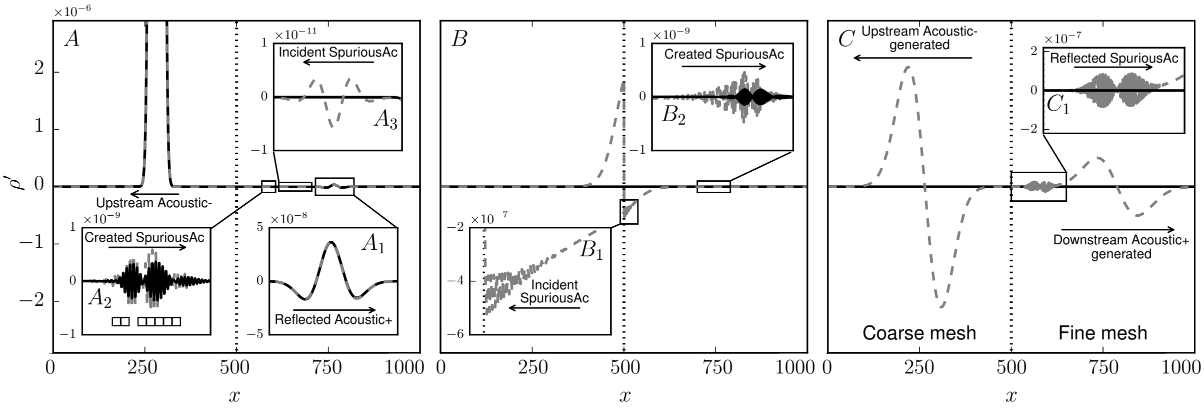

Figure 4.8 – *Comparison of the RR* (---) *and H-RR* (—) *collision models with* $\sigma = 0.995$*. Relative density evolution* $\rho' = \rho - \rho_0$ *for the upstream acoustic wave. The* (□) *symbol allow detecting the SpuriousAc modes by the* NHsensor$^{(\square)}$ *for the H-RR collision model. Left:* $t = 900$*, Middle:* $t = 2050$*, Right:* $t = 2620$*.*

Let's now focus on the H-RR results. The fig. 4.8-A shows the effects of the upstream acoustic wave that has been advected from $x = 750$ to $x = 270$ and has already passed through the grid interface. The reflected acoustic wave (Fig. 4.8-A_1) appears in the same manner as with the RR collision model. This result was expected, since this phenomenon is independent of the non-hydrodynamic contribution. Furthermore, high wavenumber ($k_x = \pi$) SpuriousAc modes (□) are also generated at the interface and advected upstream (*cf.* Fig. 4.8-A_2). These modes are more strongly attenuated with the H-RR model but not fully suppressed as expected by the dissipation curves on Fig. 4.4 for wavenumbers $k_x \to \pi$. Moreover, the SpuriousAc modes (□) generated at the initialization have been fully damped with this last model (*cf.* Fig. 4.8-A_3). This is confirmed by the NHsensor$^{(\square)}$, which does not detect any SpuriousAc mode for the H-RR collision model.

Afterwards, the SpuriousAc modes (□) that have been generated by the upstream acoustic wave is more and more damped with the H-RR collision model (*cf.* Fig. 4.8-B_1). These high frequency modes are not well attenuated by both the RR and H-RR collision model as shown un Fig. 4.4. To enhance this dissipation, the use of low-pass filters might be required as proposed in Sec. 4.7.

No more acoustic emission appears with the H-RR model, since the incident SpuriousAc mode (□) has been fully damped.

The H-RR collision model seems perfectly able to deal with both shear flows and acoustics with non-uniform grids. This outcome is to be confirmed on the subsequent more realistic case: a barotropic convected vortex.

4.4.3 Assessment of the RR and H-RR model on a convected Vortex

The improvements induced by filtering out some non-hydrodynamic modes using the RR and H-RR collision model are now validated considering a convected vortex that crosses a grid refinement interface. This test case is of interest for most aeroacoustic applications. Indeed, this situation appears in many configurations like for the prediction of noise produced by turbulent jet noise [174, 176], turbofan noise [177], cavity noise [178–180], or even landing gears [36, 61, 74] that is of course of interest for this PhD thesis.

One should notice that, in order to avoid a transient adaptation, the convected vortex cannot be initialized here by the common analytical expression of the well-known isentropic Lamb-Oseen vortex [181, 182]. Indeed, these expressions have been derived from the isentropic Euler equations, whereas the notion of 'isentropic' has no meaning in a standard athermal LB solver. In order to avoid a spurious transient adaptation, the vortex is initialized with the more suited batrotropic vortex derived in [183], as follows

$$\left\{\begin{aligned} \rho\left(x,y\right) &= \rho_0 \exp\left[-\frac{\epsilon^2}{2c_s^2}\exp\left(-\frac{(x-x_c)^2+(y-y_c)^2}{R_c^2}\right)\right], \\ u_x\left(x,y\right) &= U_x - \epsilon\left(\frac{y-y_c}{R_c}\right)\exp\left(-\frac{(x-x_c)^2+(y-y_c)^2}{2R_c^2}\right), \\ u_y\left(x,y\right) &= \epsilon\left(\frac{x-x_c}{R_c}\right)\exp\left(-\frac{(x-x_c)^2+(y-y_c)^2}{2R_c^2}\right), \end{aligned}\right. \tag{4.4.1}$$

with

$$\rho_0 = 1., \quad U_x = 0.1c_s, \quad \epsilon = 0.15c_s, \quad R_c = 5, \quad (x_c, y_c) = (100, 75), \quad \nu = 10^{-6}.$$

The refinement interface is located at $x = 150$ with the fine domain defined between $0 < x < 150$ and the coarse domain for $x > 150$.
The convected vortex combines a perturbation on the density field ρ, and the two velocity components u_x, u_y. This leads to an excitation of all kinds of modes that we can find in a LB scheme. Both modes that carry shear quantities (●,○) and acoustics (▶,◀,□) are supposed to be excited. Furthermore, in order to avoid any reflection of spurious waves, Neumann boundary conditions and explicit absorbing layers are added at the domain boundaries in the same way as in [79]. A density probe is also inserted in the simulation domain far from hydrodynamic fluctuations at location $(x = 200,\ y = 125)$ as shown on Fig. 4.9. An estimation of the spurious noise emitted is carried out by computing the power spectral density (PSD) of the density fluctuations recorded on this probe.

Before discussing the results obtained with the H-RR collision model, the two spurious phenomena highlighted with the convected shear and acoustic waves are decomposed for the convected vortex using the RR model. Indeed, since the main property of the H-RR is to damp the spurious modes, it is first interesting to show their negative effect on this case.

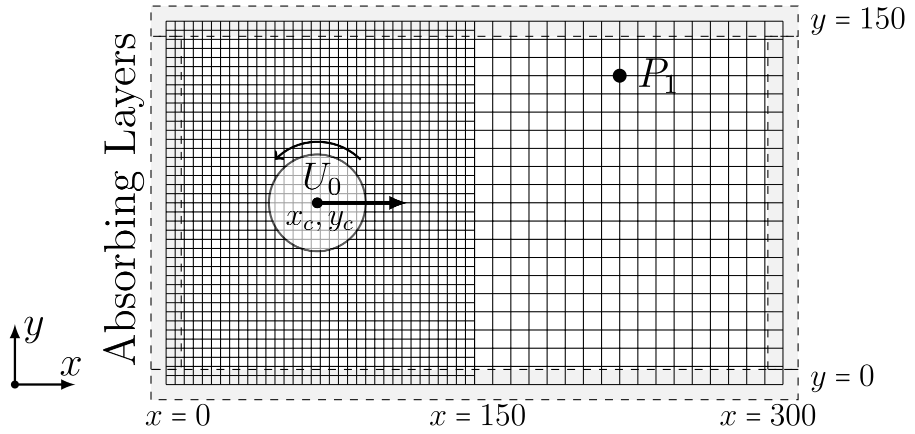

Figure 4.9 – *Schematic representation of the simulation domain for the convected vortex.* $\mathbf{P_1}$ *probe is added for acoustic recording. Absorbing layers map the domain boundaries to avoid reflection of spurious acoustic emission.*

The emphasis is first focused on the shear quantity. Fig. 4.10 shows the vorticity and the SpuriousS modes (○) that are detected by the NHsensor$^{(\bigcirc)}$ inside the isocontours. The sensor allows for the detection of the SpuriousS modes only outside the vortex as explained in Sec. 3.3.

The vortex approaches the transition at $t = 350$ iterations. As it was previously shown for the convected shear wave using this collision model, the SpuriousS modes (○) are completely converted into physical ones for fine to coarse mesh crossing. Exactly the same behavior occurs here. At $t = 780$, the NHsensor$^{(\bigcirc)}$ detects a spreading of the SpuriousS mode (○) along the grid interface, and a quantity of spurious vorticity is generated around the vortex with the same thickness as the previous SpuriousS mode (○) location. In the end, a large deformation of the convected vortex appears after crossing the interface. Previous results obtained on the convected shear wave are then fully recovered on this more complex case.

Next, the focus is put on acoustic modes (▸,◂,□) on Fig. 4.11. The SpuriousAc modes (□) are detected inside the isocontours with the NHsensor$^{(\square)}$. Note that, as predicted by the linear stability analysis, the only SpuriousAc modes advected downstream are high frequency fluctuations in the range $k_x \in [\pi/2, \pi]$. Here, the sensor allows for the detection of the presence of these modes, both inside and outside the vortex. Firstly, when the vortex approaches the refinement interface ($t = 530$), unwanted pressure spots arise on both sides of the interface. These spots appear far from the influence of hydrodynamic fluctuation areas. Their locations correspond to that of the SpuriousAc modes (□) which are converted into physical acoustics.

For a fine to coarse crossing, the modes which are resolved on the fine mesh in the range $k_x \in [\pi/2, \pi]$ cannot exist in the coarse one, due to the resolution change. Therefore, the SpuriousAc modes (□) that do not have a positive group velocity v_g in the range $k_x \in [0, \pi/2]$, cannot cross the interface, and are fully converted into physical acoustics.

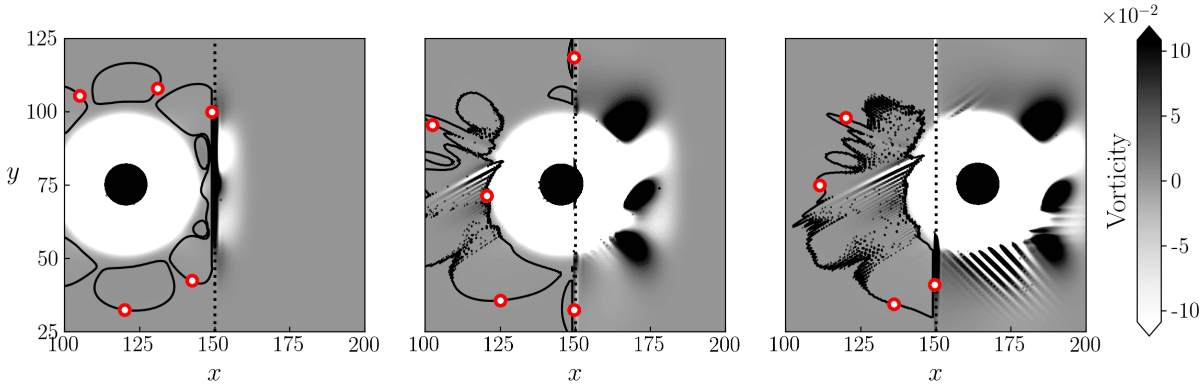

Figure 4.10 – *Vorticity field of the convected vortex that crosses a grid refinement using the RR collision model. Iso-contours denote the presence of SpuriousS* (○) *modes detected by the* NHsensor$^{(\bigcirc)}$. *Left:* $t = 350$, *Middle:* $t = 780$, *Right:* $t = 1100$.

At $t = 780$, a huge spurious emission comes out due to the intensity of the SpuriousAc (□) mode which is higher inside the vortex. At the end, spurious emissions appear on a large frequency range depending on the SpuriousAc mode's wavenumbers.

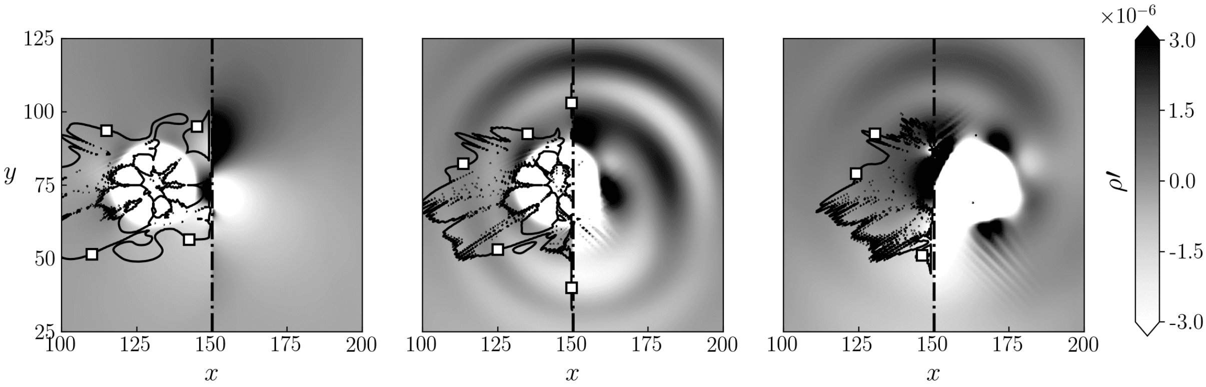

Figure 4.11 – *Density field for the convected vortex test case that crosses a grid refinement using the RR collision model. Iso-contours denote the presence of SpuriousAc*(□) *modes detected by the* NHsensor$^{(\square)}$. *Left:* $t = 530$, *Middle:* $t = 780$, *Right:* $t = 1100$.

The RR and H-RR collision models are now compared on this test case on Fig. 4.12. This time, only physical quantities are displayed on the figure, since for the H-RR model, no more spurious mode is detected by the non-hydrodynamic mode sensors, which proves that they have been fully damped by the collision model. The two displayed quantities are the density, so as to observe the spurious acoustic emission, and the vorticity, to evaluate the vortex deformation.

With the H-RR collision model, no more deformation or pressure spots appear on the grid refinement at $t = 530$. After that, a tiny deformation is observed, and the spurious emission has been drastically reduced. At $t = 780$, a small discontinuity in the pressure field can be noticed on both vortex sides. This deformation is now only due to the ability of the grid refinement algorithm to properly deal with physical waves, which is obviously of crucial importance. Gendre *et al.* [69] have actually described the lack of accuracy of the algorithm adopted here in such conditions and this topic will be discussed in Chap. 6. Without going into such considerations, the phenomena explained in the present study come from the change of mesh resolution, and are independent of the grid refinement algorithm.

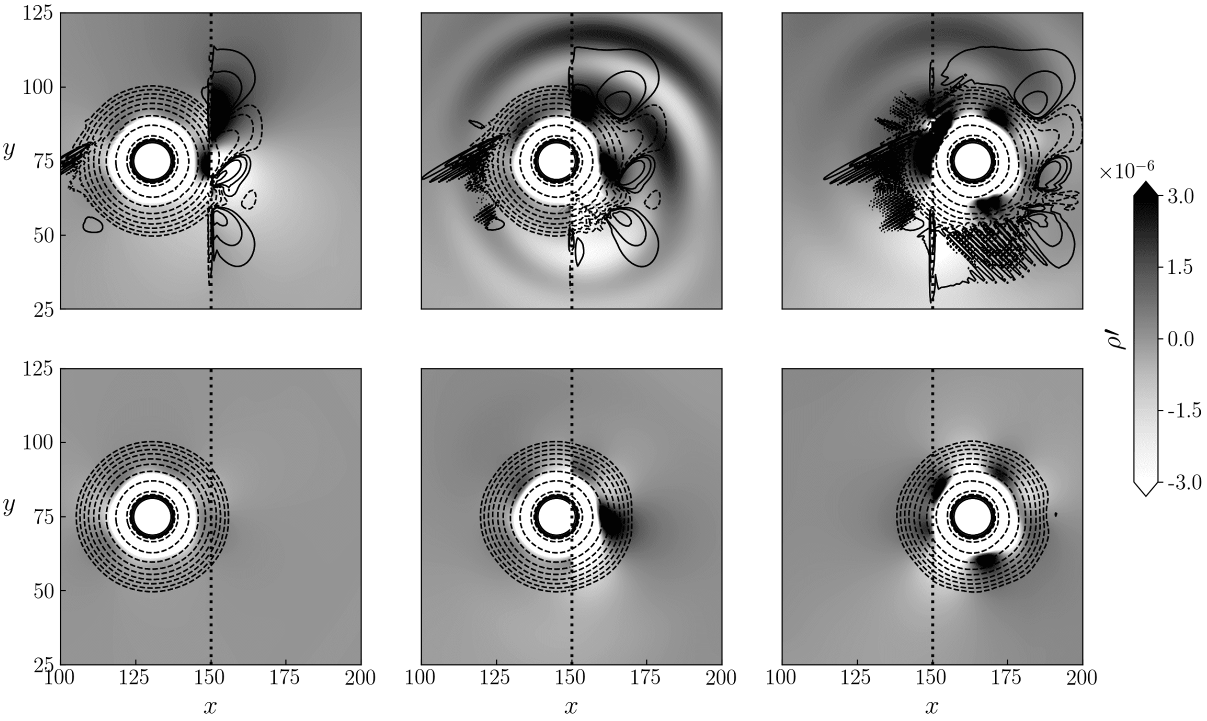

Figure 4.12 – *Maps of relative density fields* $\rho' = \rho - \rho_0$ *with isocontours of vorticity for the vortex convected across a mesh interface, from a fine mesh to a coarse one. Top: RR collision model, bottom: H-RR* ($\sigma = 0.995$)*. Left:* $t = 530$*, Middle:* $t = 780$*, Right:* $t = 1100$*.*

More quantitative results are displayed on Fig. 4.13 where PSD of density fluctuations are displayed. This figure highlights two points:

- A comparison of the spurious noise emitted for the two collision models (---, —) at a fixed dimensionless viscosity $\nu = 10^{-6}$. One can notice an improvement by up to four orders of magnitude for the spurious noise emission on a large frequency range.

- The increase of dimensionless kinetic viscosity that is required to reach the same spurious emission with the RR model. Indeed, as most of the spurious emission is directly linked to the dissipation of the SpuriousAc (□) mode, by increasing the kinetic viscosity using the RR collision model, one can obtain similar results to the one obtained by using the H-RR model with $\sigma = 0.995$. As discussed in Sec. 4.2.2, the strength of the H-RR model is to add an equivalent of the viscosity focused on non-hydrodynamic modes, especially on the SpuriousAc (□) one. An estimation of the dissipation of the SpuriousAc mode (□) was given in Eq. (4.2.1). Using this relation in the present case, to reach the same level of spurious emission, the kinetic viscosity has to be increased by a factor 418.

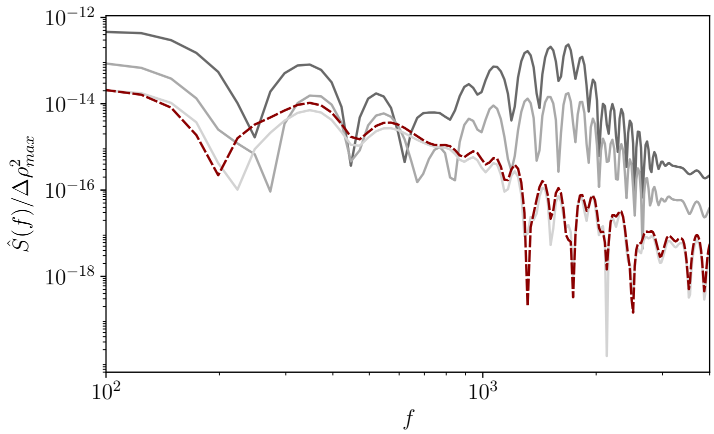

Figure 4.13 – *PSD of spurious density fluctuations recorded at Probe* $\mathbf{P_1}$ *with* $\Delta\rho^2_{max} = \rho_0 - \rho(x_c, y_c, t = 0)$. (1) – *Comparison of RR and H-RR collision model at iso dimensionless kinetic viscosity* $\nu = 10^{-6}$ (---)*: H-RR (*$\sigma = 0.995$*),* (—)*: RR.* (2) – *Influence of the dimensionless kinetic viscosity on the spurious noise emitted for the RR collision model.* (—) *:* $\nu = 10^{-4}$, (—) *:* $\nu = 4.18.10^{-4}$.

It has been shown above that **the acoustic emission comes from the SpuriousAc modes (□) and the deformation from the SpuriousS (○) ones**. As a matter of fact, the intensities of the spurious artifacts are, to a lower degree, linked with the initial position of the vortex. Actually, the greater the distance between the vortex initial position and the refinement interface, the more the spurious modes will be dissipated by the LB scheme. However, as shown on Fig. 4.1, the dissipation of the SpuriousAc mode (□) for the RR collision model is of the same order of magnitude from that of the physical modes. A very long distance is then required to observe a significant effect of the initial location choice.

This remark is of great importance for industrial applications. The same behaviors are expected to appear in wakes where vortices are convected and, often, cross grid refinement interfaces. In such situations, it is crucial to dissipate non-hydrodynamic modes before they impact it. Hopefully, in large eddy simulations (LES), the subgrid scale model has a beneficial effect, because it adds turbulent viscosity inside vortices, and thus helps to dissipate non-hydrodynamic modes. Nevertheless, the range of the turbulent viscosity for LES is about 0 to 50m^2.s^{-1}, which is very far from the order of dissipation obtainable by computing the stress tensor using finite differences as in the H-RR collision model.

4.5 Validation on a high Reynolds number turbulent flow around a cylinder

In this section, a validation is carried out on a three-dimensional high Reynolds turbulent flow around a circular cylinder. The flow physics is not examined here, since it depends mainly on parietal modeling, which is not the subject of this study. The objective is to simulate a low-viscosity turbulent flow across refinement interfaces, minimizing parasitic vorticity and spurious noise. Indeed, previous simulations with the BGK collision model on this test case with a moderate Reynolds number have exhibited many spurious noise (*cf.* Fig. 2.6) and spurious vorticity (*cf.* Fig. 2.7) that pollutes simulations. This test case is purely qualitative and intends to highlight specific problems that may occur when adding solid walls. Quantitative results on the use of H-RR model on a turbulent cylinder can be found in [60]. Furthermore, a quantitative aeroacoustic application on a landing gear using the H-RR collision model can also be found in Chapter 7.

This test case aims at:

- evidencing the impact of non-hydrodynamic modes on mesh transitions in a more realistic case,
- highlighting the parasitic acoustic waves emitted from the wake generated by the cylinder through the grid refinement interface.

The LaBS/ProLB solver is used for this three dimensional test case, where the assessed collision models have been implemented. The subgrid scale viscosity ν_{SGS} is modeled using a Shear improved Smagorinsky model from [77] and computed from the strain-rate tensor. The latter is calculated by the same gradients as those used for the H-RR, which minimizes the cost of this collision model. A wall-law taking into account an adverse pressure gradient and curvature effects [78] is imposed on the cylinder walls. The wall-law is implemented using a full reconstruction of the distribution functions with finite differences estimation [80–82]. This LB code adopts the refinement algorithm described in Sec. 3.5.

A sketch of the simulation domain is displayed on Fig. 4.14. Three levels of refinement are placed in order to evidence the effects of, firstly, the non-hydrodynamic modes generated by the cylinder in the RD1 zone, and secondly, the effect of the wake impinging the RD2 to RD3 interface once it has already passed through the first refinement area. A probe P_2 is added in the domain, far from hydrodynamic fluctuations at location (0, -160) to record acoustic fluctuations.

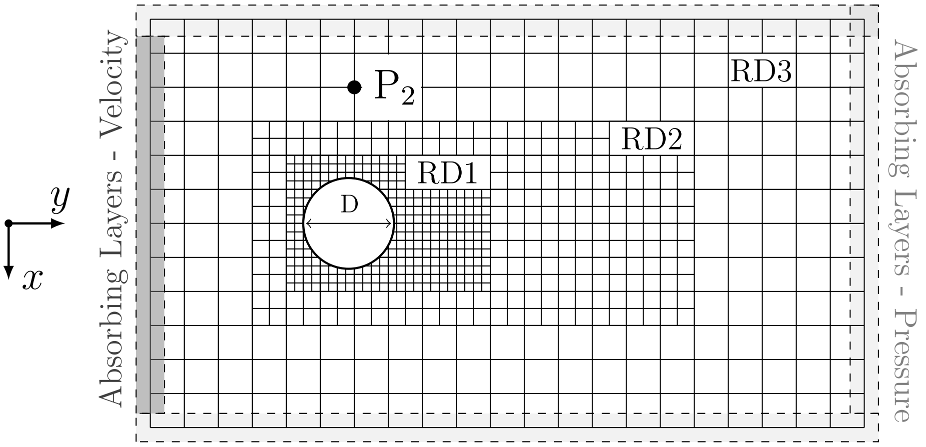

Figure 4.14 – *Schematic representation of the simulation domain for the cylinder test case. Three refinement domains (RD) are used. A* $\mathbf{P_2}$ *probe is added for acoustic recording. Absorbing layers map the domain boundaries to avoid reflection of spurious acoustic emission.*

The operating conditions of the simulation, given in dimensionless units based on the coarser mesh resolution (RD3), are as follows:

$$U_\infty = 0.1c_s, \quad \rho_\infty = 1, \quad \mathrm{D} = 75, \quad \nu = 5.77.10^{-6}, \quad \mathrm{Re} = 750\ 000, \quad \mathrm{T} = 320\ 000,$$

where U_∞ is the inflow velocity upstream the cylinder, D is its diameter (expressed in number of coarse voxels RD3. It means that there are 300 fine cells over a diameter), ν is the dimensionless viscosity (expressed in number of coarse voxels RD3) and T is the number of iterations of the simulation.

The boundary conditions are the following: a velocity Dirichlet U_∞ is imposed at the inlet and a density Dirichlet ρ_∞ is imposed on the domain outlets. Both conditions are implemented using a full reconstruction of distribution functions with finite differences as in [80–82]. The domain is periodic in the spanwise direction (z axis) with a domain span equal to 1.6D to allow the turbulence to be fully developed. The boundaries of the domain are covered with absorbing layers [79] to avoid parasitic wave reflections and so that the turbulent wake generated by the cylinder can be properly evacuated.

Following the same approach as in Sec. 4.4.3, the vorticity and then the acoustic waves emitted are analyzed separately. Only the RR and H-RR ($\sigma = 0.98$) models are compared in this section because the BGK model is unstable at this high Reynolds number. The value of $\sigma = 0.98$ is preferred for turbulent flows, since non-hydrodynamic modes are massively present and need to be quickly attenuated.

The Fig. 4.15 shows that parasitic vorticity fluctuations appear on the Z-component of the vorticity upstream the cylinder. This vorticity is clearly generated at the refinement interface due to SpuriousS modes (○) generated by the walls. Then, it is convected by the flow through the rest of the domain. This observation is consistent with the results obtained on the convected vortex (Fig. 4.10): the SpuriousS (○) modes do not succeed in properly crossing the mesh transitions and are converted into physical shear. This vorticity strongly disturbs the flow. It surrounds the cylinder, may interferes with the boundary layer that develops on it and interacts with the wake in ways that are not physical. Finally, strips of parasitic vorticity induced by the RD3 transition are observed. They are the consequence of parasitic waves generated when the spurious vorticity created upstream of the cylinder intersects the RD1. All of these glitches are greatly improved with the H-RR model which dissipates non-hydrodynamic modes that parasitize the vorticity field. Neither parasitic vorticity upstream, nor any striations around the wake are visible with the H-RR model.

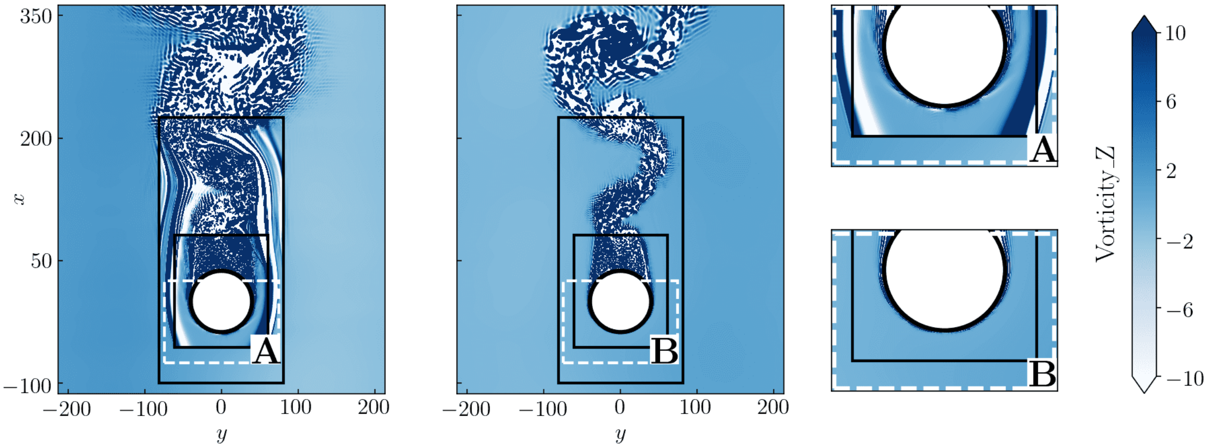

Figure 4.15 – *Field of Z-component of the vorticity generated by the cylinder with two different collision models. Left: RR, Right: H-RR.*

It is also noteworthy to focus on the x-component of the vorticity (*cf.* Fig. 4.16). For this component, there are no more parasitic modes located at the transition upstream of the cylinder with the RR model. However, spurious waves appear around the cylinder and everywhere in the downstream region of RD1. In this resolution domain, parasitic waves propagated in the direction normal to shedding vortices are also observable. These are SpuriousS (○) waves that are continuously generated in the fluid core by the vortices. The same phenomenon has been observed with a uniform mesh simulation and is also filtered by the H-RR model. It is important to filter these waves, especially before they impact another resolution area, as they would create parasitic vorticity again. The fields obtained on the y-component of the vorticity are very similar to those on x-component and are not presented here.

Let us now look at the velocity divergence (Fig. 4.17) in order to highlight the parasitic acoustic waves emitted by the mesh refinement interface. Up to now, it has been shown that two sources of parasitic noise exist at the mesh interface.

The first one is the **conversion of SpuriousAc (□) modes into acoustic waves**.

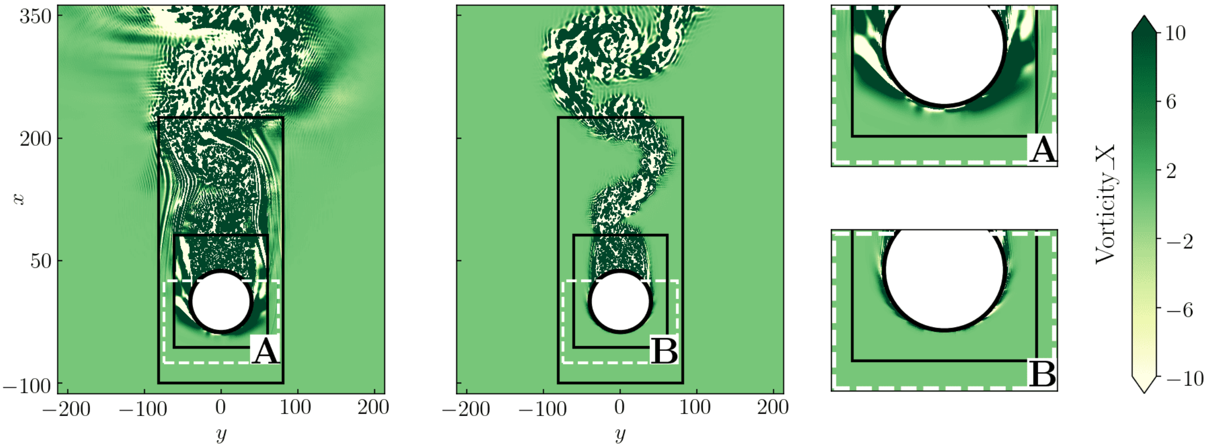

Figure 4.16 – *Field of X-component of the vorticity generated by the cylinder with the two collision models. Left: RR, Right: H-RR.*

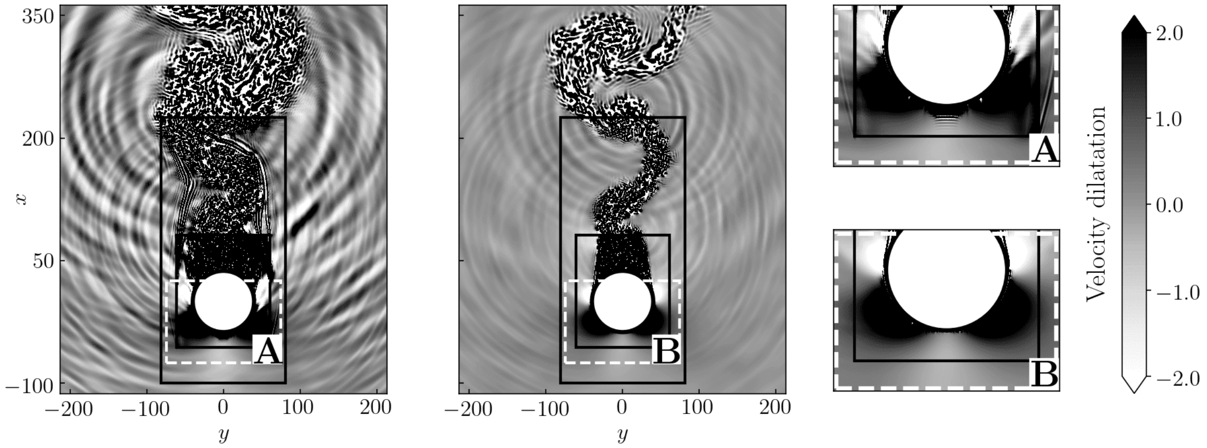

Figure 4.17 – *Velocity divergence field of the flow around the turbulent cylinder with the two collision models. Left: RR, Right: H-RR.*

These modes are present in the vortices generated by the cylinder and contribute significantly to the large parasitic emission that is centered downstream of RD1. These modes are also displayed on zoom (A) of Fig. 4.17, where high-frequency waves are visible.

The second emission is attributed to the **lack of accuracy of the grid refinement algorithm**, where the slightest discontinuity in the transfer of information from one resolution level to another one may result in the emission of acoustic waves. This issue has already been highlighted on the convected vortex test case. To date, the only two refinement algorithms whose acoustic emission due to the passage of a vortex has been quantified are the present one and the *Directional Splitting algorithm* presented in [69]. To act on this second source of noise, the flow that impinges the refinement areas must be as clean as possible since every vortex that impacts the interface will ineluctably generate spurious acoustics. The matter of the refinement algorithm will be dealt with in Chapter 6, where improvements will be provided to overcome this spurious noise source.

As illustrated on the Q-criterion isosurface of Fig. 4.18, the parasitic vorticity created by the RD3 are of an intensity comparable to the vortices generated in the wake of the cylinder. **These vortices interact with the wake and enrich the wake turbulence that crosses the grid interface in an unphysical way.**

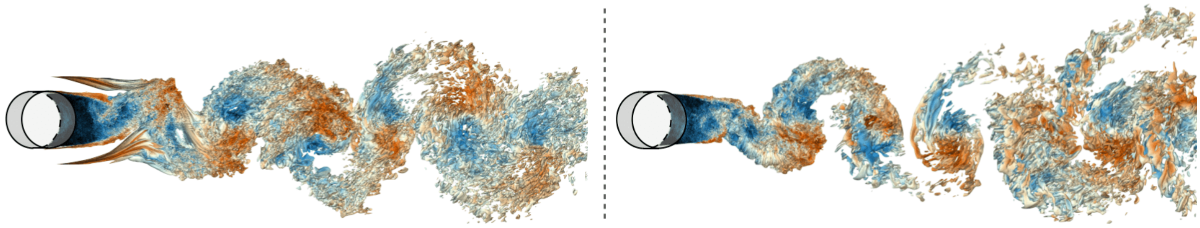

Figure 4.18 – *Isosurface of Q-criterion* $Q = 10^5$ *colored by velocity magnitude for the two collision models. Left: RR, Right: H-RR.*

All of these parasitic phenomena contribute to an increase in the quantity and intensity of the vortices. Thus, they greatly increase the parasitic acoustic emissions induced by grid interfaces positioned in the wake. This is clearly evidenced on Fig. 4.17. Moreover, the parasitic vorticity is, in most cases, under-resolved and will thus be unlikely to transmit properly from one mesh to another.

Although this test case is qualitative and mainly selected to break down the diverse spurious phenomena, a Power Spectral Density (PSD) of pressure fluctuations is displayed on Fig. 4.19. This PSD reveals the tremendous impact of the collision model on the spurious noise emitted over a wide frequency range. Indeed, the two types of acoustic sources mentioned in the previous paragraph have a strong impact on the entire spectrum. The noise induced by the aliasing of SpuriousAc (□) modes is completely suppressed with the H-RR model, and the vortices crossing the transitions are cleaned of parasitic vorticity that also affects the whole spectrum. On this plot, four peaks are also noticeable. They are all physical and correspond to the dipole noise emitted by the cylinder with the associated harmonics.

This turbulent three-dimensional cylinder test case allows for corroborating the observations made on the elementary test cases on a more realistic configuration. It has been demonstrated that solid boundaries can be responsible for the generation of non-hydrodynamic modes that have to be properly handled at the mesh transitions. More generally, it has been observed that any boundary condition, mesh refinement, and even any vortex produces non-hydrodynamic modes that are likely to pollute hydrodynamic and acoustic fields. It is therefore necessary to filter them out by different means through the whole domain, to increase the stability of high Reynolds number computations, as well as the accuracy of simulations.

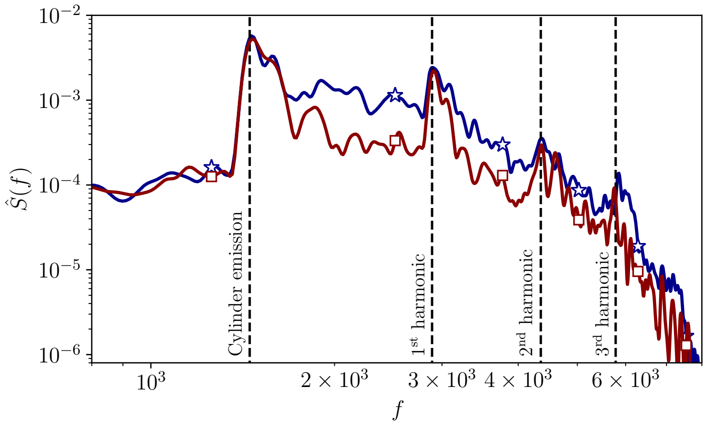

Figure 4.19 – *Power Spectral Density of pressure fluctuations recorded at Probe* $\mathbf{P_2}$*. Comparison of RR* (☆) *and H-RR* (□) *collision model.*

4.6 Conclusion of this study

The present study separated into Chap. 3 and Chap. 4 has investigated the transfer of energy between non-hydrodynamic and physical modes occurring at a grid refinement interface. More precisely, by clearly sorting the modes by their carried macroscopic information, referred to above as shear or acoustic modes, and by systematically identifying them in a simulation thanks to adequate newly proposed sensors, it has been shown that the energy of a LB mode can be redistributed on every LB mode carrying a quantity of the same nature when a change of grid resolution occurs.

This observation was anticipated by spectrally analyzing the projection of a fine mode into a coarser resolution. Furthermore, these exchanges can be harmful and the undesired effects are amplified by the high pulsation ω_r of some modes which leads to a huge discontinuity at the interface, due to the asynchronous evolution of both meshes. Moreover, these non-hydrodynamic modes might suffer from a severe dispersion, which makes their group velocity v_g strongly dependent on the wavenumber k. It can even be reversed depending on the mesh resolution, so that a wave packet travelling in a given direction has no equivalent after the mesh transition: the only solution is then to convert energy into a physical mode. For all these reasons, non-hydrodynamic modes that cross a mesh transition are likely to be a main source of spurious noise emission, whereas the physical waves seem to have a correct behavior in all the simulations carried out. To this extent, major improvements have been observed by changing the collision model in the fluid core in order to damp any non-hydrodynamic mode.

Issues observed in this study are commonly found in industrial simulations. Even when focusing on pure aerodynamic outcomes, it has been proven that the spurious modes carrying the shear quantity can hugely distort vortices, which may have an important impact on wakes shape. Boundary layers are also likely to be strongly affected by the spurious vorticity as in most industrial applications, refinement areas are placed close to walls. Furthermore, spurious vorticity may be created at grid interface, even far from the hydrodynamic areas [84]. It is even more crucial to handle carefully these phenomena for aeroacoustic simulations where, in addition to accurate aerodynamic predictions, the spurious acoustic sources must be avoided as much as possible. To this end, the turbulent cylinder test case has highlighted the necessity to damp both the SpuriousAc (□) modes that are converted into spurious acoustics and the SpuriousS (○) modes to avoid parasitic vorticity that increases the turbulence in a non-physical manner.

A solution to this issue has been introduced by finding a way to strongly dissipate these modes: the reconstruction of the stress tensor using finite differences. As this solution is very dissipative, a hybridization of this reconstruction with the recursive regularized model [60] was chosen to strongly dissipate non-hydrodynamic modes while keeping correct dissipation properties for the physical ones.

Compatibility with large-eddy simulations has been addressed. It appears that although the subgrid scale model works in favor of dissipating non-hydrodynamic modes in sheared areas, the order of dissipation added is far from that introduced by the H-RR model. Furthermore, the non-hydrodynamic modes responsible for spurious acoustic emission are not often directly impacted by the subgrid scale model since they may not be detected by sensors based on turbulent quantities. The H-RR model, or another one capable of dissipating spurious modes, is then strongly advised, especially for aeroacoustic simulations. Furthermore, the additional CPU cost of the H-RR model is reduced when a subgrid scale model based on velocity gradient is used since these quantity are already computed.

The quality of the grid-coupling algorithm has not been considered in this study, but it remains essential. Indeed, noise is always visible on Fig. 4.17, when vortices pass through refinement interface, even when the latter are cleaned of any non-hydrodynamic contribution. This point will be discussed in Chap. 6 where several algorithms will be compared and a significant improvement will be brought with the development of an alternative direct coupling algorithm.

In this study, the focus has been placed on the BGK, RR and H-RR models only for the sake of clarity. However, many other advanced collision models exist. Some additional results using other collision models or stabilization techniques are provided in the next section before the LSA focused on physical waves properties and stability of these models will be carry out in Chap. 5.

4.7 Additional results with other stabilization techniques

Some results of stability analyses and noise generated by a vortex crossing a refinement interface are presented here for various collision models or filters for which a D3Q19 formulation is already available, and most importantly, widely validated through numerous benchmark tests. As a non-exhaustive list, the following collision models or filtering strategy have been selected:

- The original regularized model from Latt and Chopard [81, 155] introduced in Sec. 4.1.1 with $g^{(1),reg}$ given in Eq. (4.1.2) and referred as **PR**. This model is chosen as it is the first regularized model proposed in the literature. In particular, it is at the origin of the dual time relaxation DRT model that is currently employed in LaBS/ProLB v2.5 [63].

- The multiple relaxation time $\mathbf{MRT}^{\boldsymbol{H}}$ model, developed and assessed for aeroacoustic applications in the Gendre phD thesis [70]. The two-dimensional moment matrix $\boldsymbol{M}$ that is used in our in-house LB-code is available in [135,151]. This model reduces to the standard regularized model if high-order moments are imposed at equilibrium value at each iterations.

  This model is expressed as:

  $$\boldsymbol{g}^{coll}(\boldsymbol{x},t) = \boldsymbol{g}(\boldsymbol{x},t) - \boldsymbol{M}^{-1}\boldsymbol{S}\cdot(\boldsymbol{m}(\boldsymbol{x},t) - \boldsymbol{m}^{eq}(\boldsymbol{x},t)), \tag{4.7.1}$$

  with $\boldsymbol{m} = \boldsymbol{M}\boldsymbol{g}$, $\boldsymbol{m}^{eq} = \boldsymbol{M}\boldsymbol{f}^{eq}$ and $\boldsymbol{S}$ is the diagonal relaxation matrix that allows each moment to be relaxed at a given frequency.

  $$\boldsymbol{S} = \mathrm{diag}(0,0,0,s,s,s,1.9,1.9,1.2), \tag{4.7.2}$$

  with $s = 1/\left(\nu/c_s^2 + 0.5\right)$.

- The Dual Relaxation Time (**DRT**) [63] model with and without additional **selective filters** [162] as it is currently implemented in LaBS/ProLB v2.5. It is expressed as:

  $$g_i^{coll}(\boldsymbol{x},t) = g_i(\boldsymbol{x},t) - \frac{1}{\bar{\tau}}g_i^{(1),reg} - \frac{1}{\bar{\tau}^N}g_i^{(1),N}, \tag{4.7.3}$$

  with $g_i^{(1),reg}$ defined in Eq. (4.1.2) and $g_i^{(1),N} = g_i - g_i^{(1),reg} - f_i^{(0)}$ is a non-equilibrium part composed of high-order moments of g_i. It can be view (not rigorously) as the h_i term used in the entropic decomposition described in Sec. 3.2, if the trace of the second-order moment is not included in h_i.

  Without filter, this model reduces to the standard regularized model (PR) if the relaxation time $\bar{\tau}^N$ linked to the relaxation of high-order moments is fixed to $\bar{\tau}^N = 1$

or it reduces to the BGK model if $\bar{\tau}^N = \bar{\tau}$. The value is fixed to $\bar{\tau}^N = 0.55$ as in LaBS/ProLB v2.5.

The selective filters allow improving the stability and minimizing the high-frequency oscillations of the LB schemes [162]. They can be applied either on the distribution functions themselves, on the collision only or on the macroscopic quantities. This last solution is preferred in LaBS/ProLB v2.5. For a given macroscopic variable h it reads:

$$\langle h(\boldsymbol{x}) \rangle = h(\boldsymbol{x}) - \lambda \sum_{j=1}^{d} \sum_{n=-N_f}^{N_f} d_n h\left(\boldsymbol{x} + n\boldsymbol{e}_j \Delta x\right), \tag{4.7.4}$$

where $\boldsymbol{e}_j$ is an unitary vector in the j direction and $\lambda \in [0;1]$ is the filtering strength coefficient. The value of λ is fixed to 0.02. N_f is the number of points used in each direction and d_n are the filter weights given in [162]. This kind of filters use $2N_f + 1$ points and are of order $2N_f$. In LaBS/ProLB v2.5, as well as in the present study, $N_f = 3$, this means that seven points are used for the filter.

- The fractional propagation (**FP**) scheme [164–166, 184], is a LB scheme with a modified propagation step. It is widely used as a low-pass filter and reads:

  $$g_i(\boldsymbol{x}, t+1) = \alpha_0 g_i^{coll}(\boldsymbol{x}, t) + \alpha_1 g_i^{coll}(\boldsymbol{x} + \boldsymbol{e}_i, t) + \alpha_{-1} g_i^{coll}(\boldsymbol{x} - \boldsymbol{e}_i, t), \tag{4.7.5}$$

  with $\alpha_0 = 1 - A^2$, $\alpha_1 = 0.5A(A-1)$, $\alpha - 1 = 0.5A(A+1)$ and $0 < A \leq 1$. If the A parameter is set to $A = 1$, the standard collide and stream algorithm is retrieved. This formulation required a modification of the timestep $\Delta t^{\mathrm{FP}} = A\Delta t$, and thus of the sound velocity and the relaxation time accordingly. The value of A will be set at a very low value of $A = 0.9995$ in the following. The fractional propagation will be combined with the H-RR one to dissipate the remaining SpuriousAc (□) mode for $k_x \to \pi$.

The spectral properties regarding the non-hydrodynamic modes dissipation only of these different models are compared on Fig. 4.20. These dissipation plots anticipate the generation of parasitic acoustics due to the SpuriousAc (□) mode aliasing as it passes through the grid refinement interface. At iso-dissipation for the same mode, the emission or distortion (due to the SpuriousS mode (○) conversion) deviations of the vortex visible on Fig. 4.21, come from variations in the propagation properties. However, a detailed analysis of propagation properties as previously conducted will not be repeated here in order not to overwhelm the reader. Moreover, the LSAs performed are restricted to waves propagating in the flow direction only, which is not sufficient to accurately analyze the different models on a two-dimensional test case.

On Fig. 4.21, the BGK model is not present since it is unstable for this low viscosity test case. Nevertheless, it is interesting to compare the dissipation properties of the advanced models with the BGK one on Fig. 4.20. Moreover, the H-RR model with the fractional propagation algorithm is not depicted on Fig. 4.21 sinces the latter gives apparently the same results as the H-RR model which is sufficient to dissipate the troublesome non-hydrodynamic modes. If for some test cases the SpuriousAc (◻) mode which is not dissipated with the H-RR model when $k_x \to \pi$ is problematic, adding the fractional propagation algorithm may nevertheless solve the issues. In all the test cases carried out during this thesis, the fractional propagation was not required to improve the stability. The latter will therefore not be studied although it is very relevant.

Some conclusions can be drawn from Fig. 4.21. Firstly, the four models that do not filter the SpuriousAc mode (◻) on Fig. 4.20 generate strong spurious acoustics. These models are: PR, RR, MRT^H and DRT. The PR model is the worst because a non-hydrodynamic mode follows the vortex wake and folds in acoustics as it passes through the grid interface. This mode is entirely filtered by the RR model and partially by the MRT^H and DRT ones. Another point to notice is that the MRT^H and DRT are very close to each other. Actually, these two models are identical if the relaxation times of the MRT^H high-order moments are taken equal to $1/\bar{\tau}^N$ instead of 1.9 and 1.2.

The use of selective filtering effectively removes the SpuriousAc (◻) mode in the high-frequency range. This can be seen on Fig. 4.20, as on Fig. 4.21 where the acoustic emission is almost no longer perceptible with the filtered DRT model. However, the ‘checkerboard” spurious modes visible with the DRT model are also present with the addition of filtering. This model, which is present in LaBS/ProLB v2.5, is therefore not satisfactory compared to the H-RR.

A PSD of density fluctuation is shown on Fig. 4.22. This confirms the above remarks. The PR model generates the most spurious noise, followed by the RR one. The MRT^H and DRT models have a similar behavior regarding the handling of non-hydrodynamic modes. Finally, a clear reduction of parasitic noise is obtained with the use of filters or the H-RR model.

These results confirm that the choice of the collision model, or associated stabilization techniques, is of paramount importance and that the treatment of non-hydrodynamic modes must be an integral part of the selection criteria for a fluid model in a LB solver. In the next chapter, stability analyses will be carried out, but this time the focus will be exclusively set on the stability and properties of physical waves. These two points are also fundamental for accurate and stable aeroacoustic simulations.

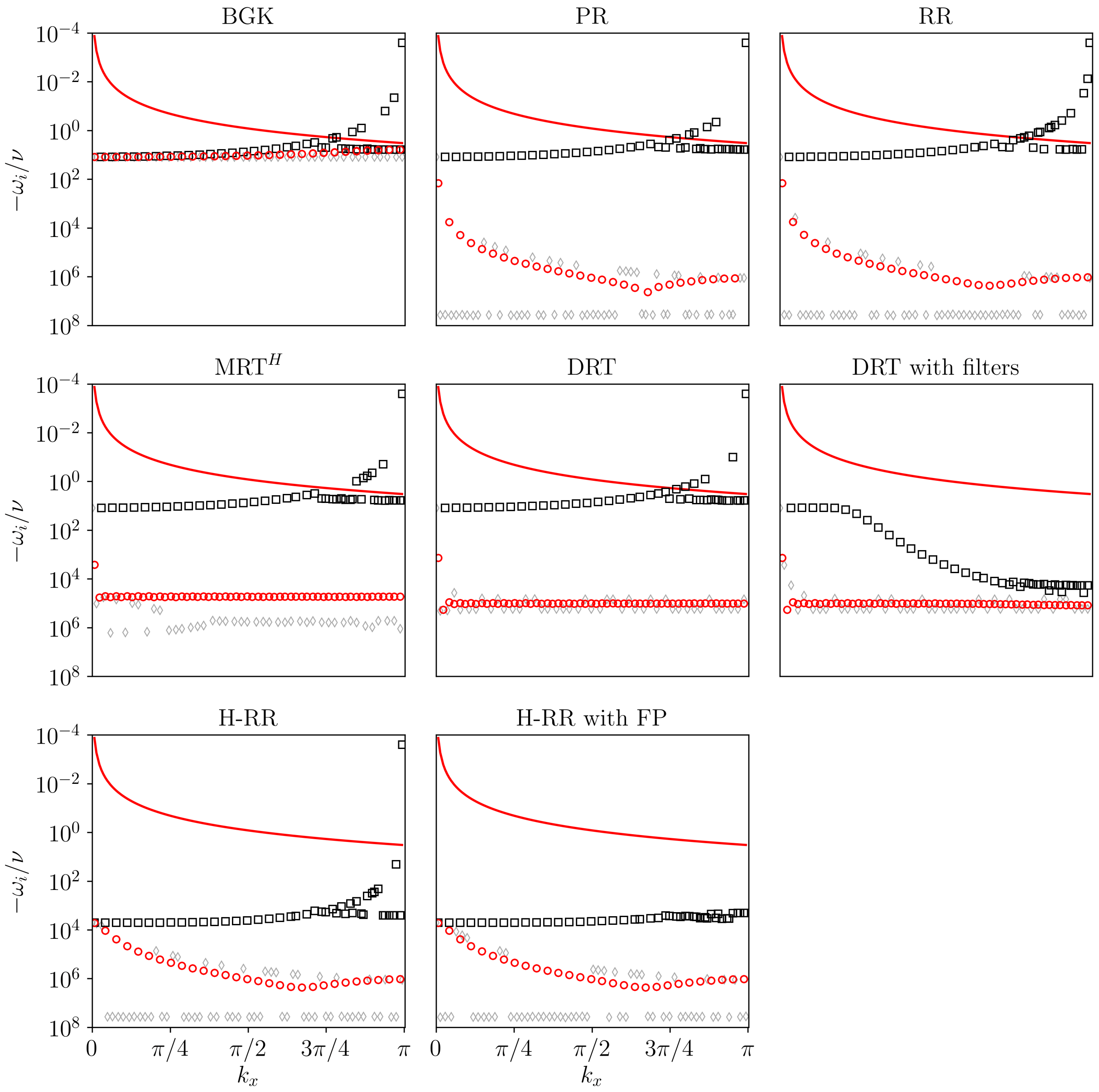

Figure 4.20 – *Comparison of the non-hydrodynamic modes dissipation for several stabilization techniques.* $\nu = 10^{-6}$*, Ma=0.1.* (○) *: SpuriousS modes,* (□) *: SpuriousAc modes,* (◊) *: SpuriousG modes,* (—) *: Isothermal Navier-Stokes.*

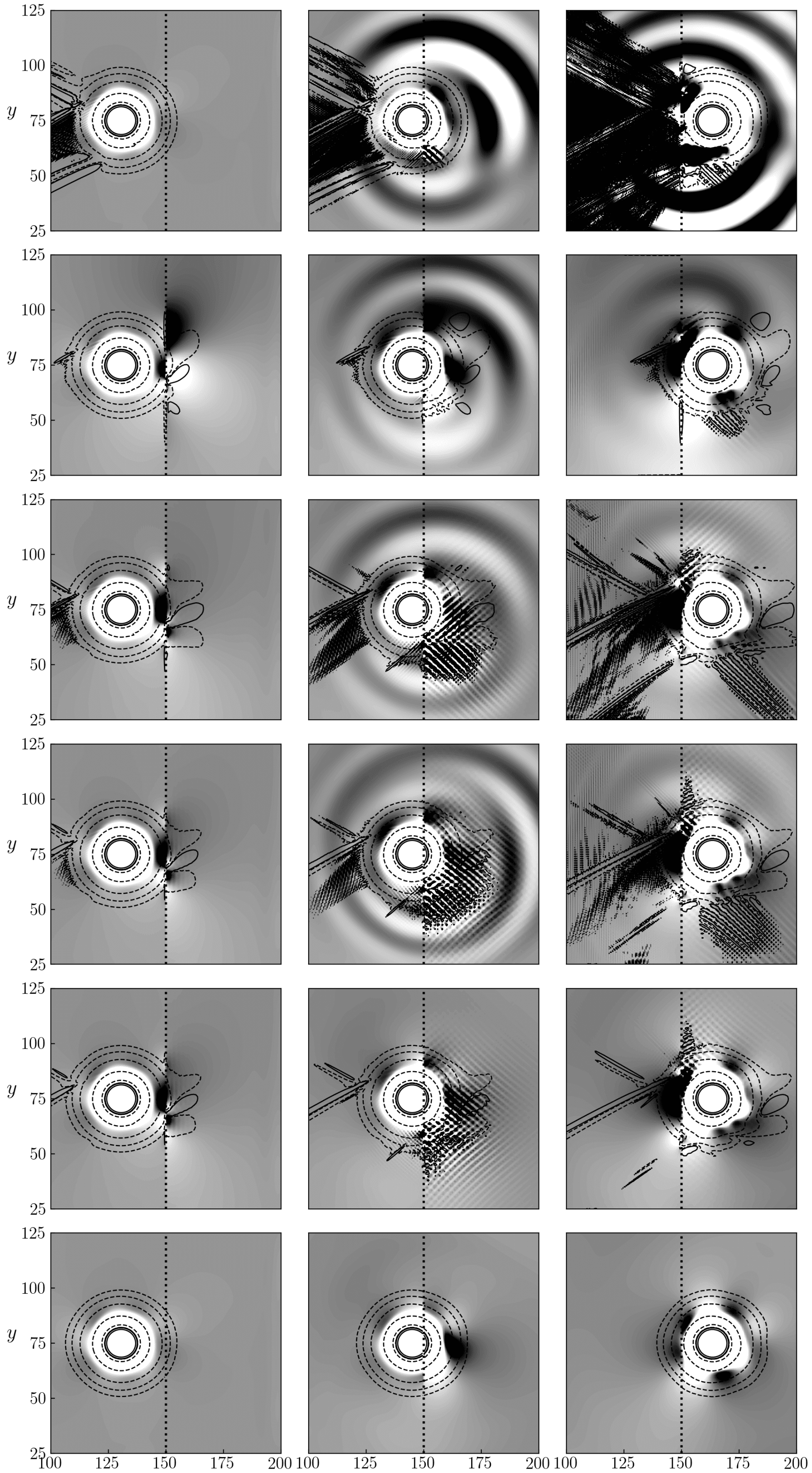

Figure 4.21 – *Maps of relative density fields* $\rho' = \rho - \rho_0$ *with isocontours of vorticity for the vortex convected across a mesh interface, from a fine mesh to a coarse one. From top to bottom:* PR, RR, MRT^H, DRT, DRT with filters, H-RR. *Left:* $t = 530$, *Middle:* $t = 780$, *Right:* $t = 1100$.

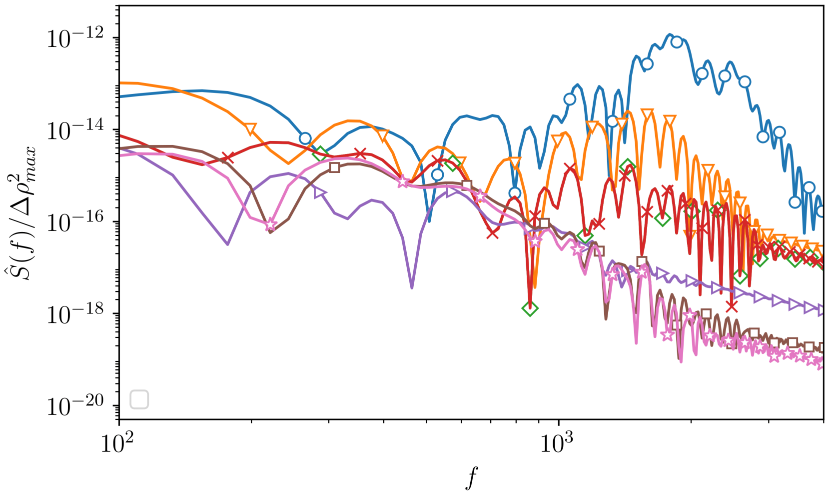

Figure 4.22 – *PSD of spurious density fluctuations recorded at Probe* $\mathbf{P_1}$ *with* $\Delta\rho_{max}^2 = \rho_0 - \rho(x_c, y_c, t = 0)$ *for several stabilization techniques.* PR: (—○—) , RR: (—▽—), MRT^H: (—◇—), DRT: (—✕—), DRT with filters: (—▷—), H-RR: (—□—), H-RR with FP: (—☆—).

Chapter 5

Stability and accuracy of the lattice Boltzmann method

Contents

This chapter is devoted to the analysis of the stability and accuracy of some LBM models. The objective is to verify the ability of the H-RR operator to perform stable and accurate aeroacoustic simulations. It turned out that correcting the Galilean invariance errors of the shear stress tensor is mandatory to increase its stability. The stability of most of the studied models, with a third-order equilibrium function, appears to be quite unsatisfactory and the mechanisms of instabilities are discussed. Then, the LSA of advanced models shows a strong anisotropy in dissipation, which could challenge the low dissipation statements frequently mentioned for LBM models. Finally, test cases of vortex and acoustic pulse are performed in order to validate the LSA results.

This chapter aims to characterize the stability and accuracy of LB models to perform aeronautical aeroacoustic simulations. These two aspects are crucial, but stability is the first criterion, as it is a necessary condition to deliver a simulation. Besides, most industrial solvers add ingredients to stabilize their simulations, which sometimes may affect the accuracy. To give a few examples, the AVBP solver used in the two previous theses dealing with landing gear noise, employs artificial viscosity sensors [9, 21, 185, 186] for enhancing stability. For the same purpose, the elsA solver, widely used for aerodynamic and aeroacoustic applications [187–189] uses high-order selective filters [190, 191]. One can also consider the example of PowerFLOW which alledgedly uses, among others, the fractional propagation method described in Sec. 4.7 to improve its stability [192]. Last but not least, in the same spirit, the commercial version of LaBS/ProLB v2.5 uses selective filters [162] to help stabilize the DRT model. These stabilization approaches are most often added in supplement to the numerical scheme to improve robustness and damp high-frequency non physical waves that can appear at boundaries or mesh interfaces where a change of numerical scheme or resolution occurs [193].

In this chapter, the stability criterion will be studied first. The overall stability of different LB models will be compared and the origin of instabilities will be highlighted. Then the accuracy (i.e. the spectral properties) of the studied models will be evaluated. Accuracy is essential for precise aeroacoustic simulations. A scheme must be able to correctly propagate shear (*i.e.* vortices advected in wakes for instance), as well as acoustics. These two quantities will not necessarily be treated in the same way by the numerical scheme and LSA tools will help to quantify this aspect. Numerical validations will finally complement LSA results.

5.1 Stability of lattice Boltzmann models

Before going into the details of LB model stability, a correction of the H-RR model is introduced in the following section. This correction is proposed by Feng et al. [120] for a high-subsonic thermal version and allows a great improvement of the H-RR model stability as it will be shown in Sec. 5.1.2. It consists in correcting the cubic Mach error present in the viscous stress tensor. This errors appears due to the choice of the equilibrium truncation and the associated velocity discretization as shown in Eq. (2.3.19).

5.1.1 Cubic Mach correction terms for enhancing the H-RR model stability

This correction term noted $\boldsymbol{\psi}$ thereafter enables correcting the biased third-order equilibrium moment and allows recovering a Galilean invariant shear stress tensor in the Navier-Stokes equations. Since it relies on the equilibrium function, this term also depends on the space dimension. Details on the computation of these terms for both two and three dimensional H-RR models are given in [120]. Modifications must therefore be brought to the LB algorithm based on the H-RR collision model according to [120], and associated effects on the numerical properties will be addressed in the next sections.

Firstly, the off-equilibrium regularized distribution function defined in Eq. (4.1.1) is modified as:

$$g_i^{reg} \equiv g_i^{(0)} + g_i^{(1),reg} + \frac{\psi_i}{2}, \tag{5.1.1}$$

and the associated regularized LB scheme described by Eq. (4.1.4) becomes:

$$g_i\left(\boldsymbol{x}+\boldsymbol{e}_i, t+1\right) = g_i^{(0)} + \left(1-\frac{1}{\overline{\tau}}\right) g_i^{(1),reg} + \frac{\psi_i}{2}, \tag{5.1.2}$$

Finally, the off-equilibrium Hermite expansion coefficient $\boldsymbol{a}_1^{(2)}$ defined by Eq. (4.1.3) turns into:

$$\boldsymbol{a}_1^{(2)} = \sum \mathcal{H}_i^{(2)} \left(g_i - g_i^{(0)} + \frac{\psi_i}{2}\right). \tag{5.1.3}$$

The H-RR model with the corrected cubic Mach errors will be subsequently referred to as: **H-RR**$_{\boldsymbol{\psi}}$. The $\boldsymbol{a}_1^{(2)}$ term calculated by Eq. (5.1.3) is, as for the classical H-RR model, injected in Eq. (4.1.10). By extension, the corrected RR model will be referred to as **RR**$_{\boldsymbol{\psi}}$. As a reminder, this collision model is equivalent to H-RR$_{\psi}$ ($\sigma = 1$). **Unless otherwise stated, the value of σ is set to** $\sigma = 0.98$.

5.1.2 Stability of two-dimensional models

The linear stability corresponds to flow conditions where a scheme is considered linearly stable over time, *i.e.* no mode is amplified. The study that will follow will be divided into two parts. First of all, the global linear stability of the different models presented in Sec. 4.7 will be investigated. This stability analysis will consist in studying the stability of each model for all possible directions of the perturbations carried by the wavevector $\boldsymbol{k}$ and for all directions and intensity of the mean field. The linear perturbations that are complex monochromatic waves are defined in Sec. 3.1.2. This kind of analysis is essential to assess the stability of a scheme. The study of perturbations propagating only in the direction of the mean field as performed in Chap. 3 and Chap. 4 is not sufficient. Afterwards, the origin of instabilities will be studied with the help of LSA. It was chosen that the stability of three-dimensional models would not be studied by means of LSA since it requires a very high CPU cost to be able to characterize the entire parameter space. However, observations made from LSA in two dimensions can be retrieved numerically in three dimensions. Therefore, only numerical validations will be performed for three dimensional models.

5.1.2.a Stability domains

The stability domains are studied for wavevectors $\boldsymbol{k}$ discretized with $k_x \in [-\pi, \pi]$ and $k_y \in [0, \pi]$ and with a step $\Delta k = 0.005$. The eigenvalue problem in Eq. (3.1.7) is solved for increasing dimensionless viscosities, growing Mach numbers and various orientation angles of the mean field $\theta \in [0°, 45°]$ with a step $\Delta\theta = 1°$ as it is done in [136,144,149,194,195]. A scheme is considered unstable and reaches its critical Mach number for a given viscosity if $\max(\omega_i > 0)$.

The stability ranges of several models are displayed on Fig. 5.1 for a D2Q9 lattice and a third-order Hermite equilibrium function. This figure indicates that:

- Increasing the dimensionless viscosity improves the stability of LB models.
- The LB models studied are at best capped at a critical Mach of 0.732 which is the theoretical limit of the DVBE for this velocity discretization as shown in [113,114].

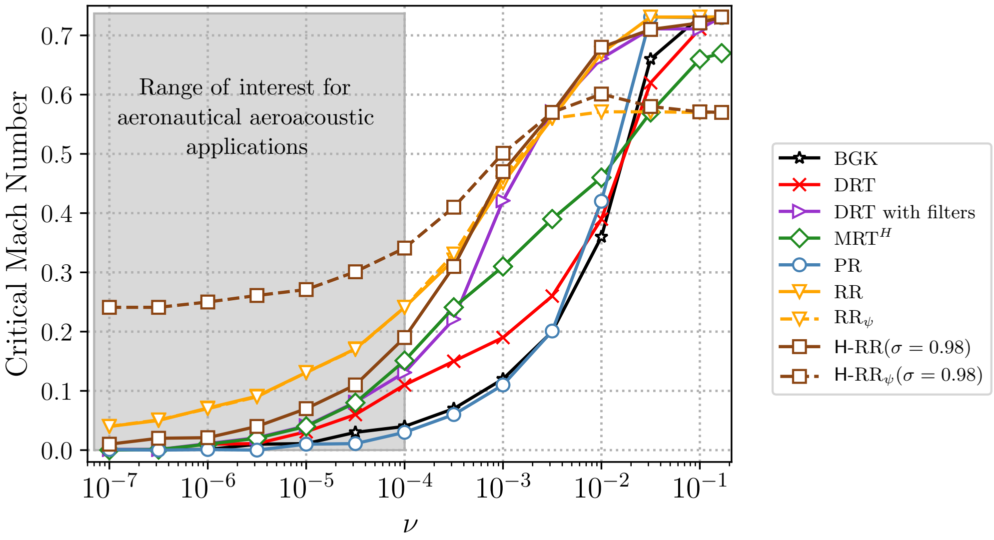

Figure 5.1 – *Critical Mach number reachable for a given dimensionless viscosity ν with several two-dimensional LB models on a D2Q9 lattice, with a third-order Hermite equilibrium function.*

In a LB scheme, the dimensionless viscosity scales in $\sim 1/\Delta x$ when an acoustic scaling is considered. Consequently, when a simulation with non-uniform meshes is carried out, the fine resolution zones benefit from a higher dimensionless viscosity and hence an improved stability compared to the coarse resolution. This is an important remark to keep in mind when considering the stability of a scheme used for aeronautical applications. Indeed, for a minimum mesh size of about 0.1mm, frequently used in this type of LB application and for a kinematic viscosity of air, this results in a maximum dimensionless viscosity of interest of about 10^{-4}. Thus, on Fig. 5.1, the range of interest for stability goes to values of viscosity below this limit.

In this range of interest, the H-RR$_\psi$ model, which incorporates cubic Mach corrections, offers the greatest stability. All the other models have much lower stability. The PR model has a range of stability that is even lower than the BGK model for $\nu < 10^{-3}$ as already shown in [149]. In this paper, as in these two PhD thesis [113,136], it is also found that the stability of the RR model strongly depends on the order of the equilibrium and off-equilibrium distribution function. In this manuscript, the choice was made to truncate this development to the third-order, so that it is directly extensible to a D3Q19 lattice [60,120]. This choice reduces the stability of the RR and consequently, of the H-RR models. It should also be noted that adding filters to the DRT model allows to slightly improve its stability range, but this model which is currently implemented in LaBS/ProLB v2.5 is clearly not satisfactory for the targeted aeroacoustic applications.

The $\boldsymbol{\psi}$ correction terms greatly improve the stability of the H-RR$_\psi$ model for low-viscosities. However, these terms have a destabilizing effect when the viscosity is higher than $\nu > 2.10^{-3}$, which is not a concern for aeronautics applications. However, it can be seen that, once corrected, the stress rate tensor reconstruction part of the H-RR$_\psi$ model increases the overall stability of the scheme.

The RR model, will later be studied only in its form with the $\boldsymbol{\psi}$ correction terms (RR$_\psi$). Indeed, the effect of the $\boldsymbol{\psi}$ terms on this collision model are infinitesimal for low viscosities but the terms greatly stabilize the H-RR$_\psi$ model. Analyzing the RR$_\psi$ scheme instead of the RR one is equivalent to analyzing the H-RR$_\psi$ scheme with $\sigma = 1$, which is more relevant for our study.

5.1.2.b Nature of instabilities

The origin of instabilities for the different models is discussed here. For that purpose, the particular case of LSA with a mean field of Ma= 0.2 oriented towards $\theta = 0°$ ($M_x = 0.2$) and a dimensionless viscosity $\nu = 10^{-6}$ is studied, since it corresponds to typical landing gear simulations. First of all, maximum amplification maps for the various possible directions of the wavevector $\mathbf{k}$ are presented on Fig. 5.2. In this particular case where the flow is aligned with the horizontal direction, the symmetry properties of the lattice allow to reduce the discretization of the wavevector in the horizontal direction to $k_x \in [0, \pi]$ [149]. At first glance, one can already notice that the BGK model has an average maximum amplification rate much more homogeneous and close to $\max(\omega_i)/\nu \sim -1$ compared to the other models, which means a much lower dissipation. Moreover, its instability region over the $\mathbf{k}$ space is very small compared to other models. Indeed, the kind of instability of the BGK model that appears here is particular and is attributable to an eigenvalue collision as it is widely discussed in [148]. This form of instability is characterized by a destructive interaction between two modes and results in a very strong amplification for one and a very strong dissipation for the other. This phenomenon is illustrated on Fig. 5.3 where a slice is made through this instability bubble and shows a destructive interaction between two SpuriousAc (□) modes. The other models have much wider instability ranges. These instabilities are attributable to incorrect dissipation behavior of physical or non-hydrodynamic modes. This dissipation error has already been observed for the different regularized models [126,149]. A possible explanation is proposed in [149] with a *a priori* derivation of the PR model. This derivation proves that the PR scheme is only first-order accurate in time for high-order moments instead of second-order. This loss of one accuracy order does not seem to have any consequence on the global order of the PR model which is second-order accurate [126,173,196–198], thus additional investigations are required. To our knowledge, there is currently no further explanation in the literature.

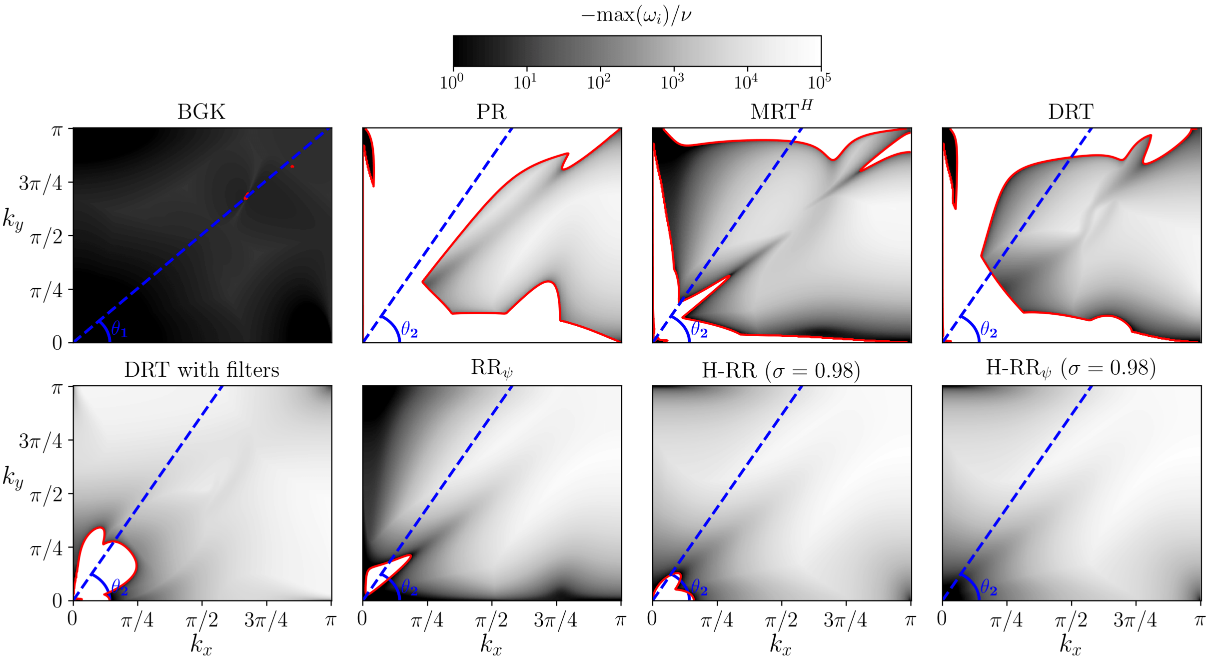

Figure 5.2 – *Maps of normalized maximal growth rate* $(\max(\omega_i)/\nu)$ *for several LB models. LSA are realized with a mean flow* $M_x = 0.2$ *and a viscosity* $\nu = 10^{-6}$. *The red solid isoline corresponds to the stability threshold* $(\max(\omega_i) = 0)$. *The dashed blue line corresponds to the position of the one dimensional cut showed on Fig. 5.3.* $\theta_1 = 45.3°, \theta_2 = 60°$.

It should also be noted that the use of selective filters with the DRT model, although it does not solve the problem of low wavenumber anti-dissipation, does filter out the high wavenumber instabilities induced by the SpuriousAc (□) mode. Additionally, regarding the low dissipation of the BGK model and its very localized instability appearing for high wavenumbers, one might want to associate it with the same kind of filtering (or the fractional propagation scheme introduced in Sec. 4.7) to stabilize it. However, the instability being very strong as shown in Tab. 5.1, the amount of filtering required would dissipate too much the physical waves. Moreover, even with a filter, the non-hydrodynamic modes are barely dissipated by this model even for $k \to 0$. Thus, it would not enable to realize proper simulations with non-uniform grids.

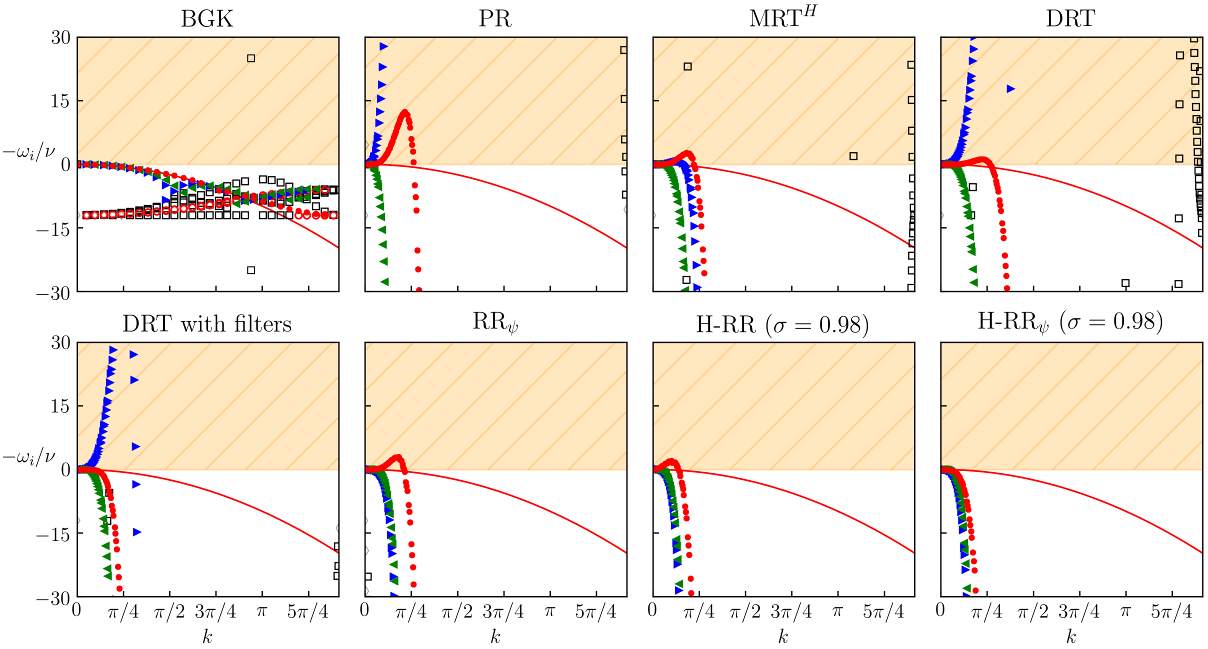

Figure 5.3 – *Dissipation curves extracted along a θ_i cut as described on Fig. 5.2 for several LB models. LSA are realized with a mean flow $M_x = 0.2$ and a dimensionless viscosity $\nu = 10^{-6}$. (▸): Ac+ mode, (◂) : Ac- mode, (●) : Shear mode, (○) : SpuriousS modes, (□) : SpuriousAc modes, (◊) : SpuriousG modes, (—) : Isothermal Navier-Stokes.*

More quantitatively, Table 5.1 provides the maximum value of the amplification rate visible on the maps of Fig. 5.2. It can be seen that the orders of magnitude of the mode amplifications that make the models unstable are very different from one model to another. A model with a high value of $\max(\omega_i)$ will diverge quickly. Conversely, a low value will require a very large number of iterations for the calculation to diverge. For all the models studied, very high amplification rates appear with the BGK, PR, MRT^H and DRT models with and without the use of selective filters. The RR$_\psi$ model has a very low antidissipation rate under these conditions. Therefore, in practice in a simulation performed with this model, the calculation will take a very long time to diverge. The only satisfactory model from the stability point of view is the H-RR$_\psi$ model which is not unstable for this Mach number and viscosity. As shown on Fig. 5.1, the latter is by far the most stable under low viscosity conditions.

Once the stability has been studied, let's investigate the accuracy of the models.

Model	BGK	PR	MRT^H	DRT	DRT with filters	RR	H-RR	H-RR$_\psi$
$\mathbf{max(\boldsymbol{\omega_i})}$	1506	20642	1231	2344	1173	5	6	0

Table 5.1 – *Maximum amplification rate for several LB models with* $M_x = 0.2$, $\nu = 10^{-6}$. *A positive value for* $\max(\omega_i)$ *means that the LB scheme is unstable.*

The H-RR in its uncorrected form without the ψ term will no longer be studied since the properties of this model are very close to those of the corrected model but with an instability that appears at low wavenumbers.

5.2 Accuracy of lattice Boltzmann models

Following the extended LSA methodology proposed in [148], it is possible to use the content of eigenvectors to access the quantity transported by a mode. It is thus possible to quantify its associated dissipation. Generally in CFD, the dissipation is characterized through the effective viscosity $\nu_e = -\omega_i / ||\boldsymbol{k}^2||$ of a solver. This effective viscosity includes the kinematic viscosity and the numerical viscosity induced by the numerical scheme, or any artifice used in complement, such as a turbulence model for example. Fig. 5.5 shows the effective viscosity per physical quantity transported (*ie.* Shear, Ac+ and Ac- modes respectively). These maps consider the dissipation of a given transported quantity and do not differentiate whether the wave carrying this quantity is physical or non-hydrodynamic. In practice, for low wavenumbers ($|\boldsymbol{k}| < \pi/2$), the least dissipated wave is always the one closest to the associated Navier-Stokes mode, which is therefore considered to be hydrodynamic so the analysis remains very relevant. First of all one can see that the BGK model has a very low numerical viscosity, which means that it dissipates weakly. Indeed, its effective viscosity is of the same order of magnitude as the kinematic viscosity ν. It can also be noted that no instability area is visible for the BGK model. This is because the instabilities, under these conditions, come from the eigenvalue collision of two SpuriousAc (□) modes (*cf.* Fig. 5.3) which are not represented here. Conversely, all the other models have a highly anisotropic and large dissipation compared to the kinematic viscosity. This anisotropy is essential to consider when evaluating a numerical scheme.

On this last point, it is actually worthwhile to come back to the conclusions of Marié *et al.* [143, 199] which compares the spectral properties of Navier-Stokes schemes with two LB models: the BGK and the MRT of d'Humières *et al.* [134]. It is mentioned that the precision of these LB schemes lies between a NS solver with second-order scheme in space and a third-step Runge-Kutta in time, and third-order scheme in space with a third-step Runge-Kutta algorithm for the time discretization. However, the study is carried out only for a **mean field and perturbations propagating in the x direction, for which an asymptotic behavior in dissipation for the acoustic modes is found** on Fig. 5.5.

In view of the anisotropy of the different advanced collision models studied here (including the PR, MRT^H, DRT which can directly be seen as MRT models [70, 173]), it would be interesting to come back to this type of comparative study by taking into account several possible angles for the mean flow and several directions of propagation for the perturbations. Moreover, it is also uncommon to find this kind of study in the NS community where schemes are generally studied and optimized for one-dimensional advection equations only [139, 140, 200–205], which does not guarantee at all the isotropy and stability of the scheme.

In brief, the question of the accuracy of a LB scheme is not simple since it is generally second-order accurate in time and space but has a precision that varies widely, notably due to their incorrect dissipation properties compared to the BGK scheme as shown on Fig. 5.2. It is currently quite difficult to conclude objectively on a comparison of the two approaches, given the uncertainty on the accuracy of LB schemes and the lack of background on the stability and isotropy of full NS schemes.

More pragmatically, if one is interested in comparisons made on aeroacoustics cases of landing gear, there are two recent papers [56,57] comparing NS and LB methods. The first one compares simulations performed with the same solver LAVA developed by the NASA [206] that embedded both methods. This solver includes in the same platform a sixth-order WENO spatial scheme with a fourth-order Runge-Kutta (RK4) time discretization for the Navier-Stokes part, and a D3Q27 lattice with an entropic collision model [207] for the LB part. Both methods use non-body fitted boundary conditions (which are obviously not identical) with an identical mesh size. The discrepancy in accuracy is quite striking as shown on Fig. 5.4 and if one quotes their paper: "*In general, the LB approach minimizes numerical dissipation while simultaneously retaining the robustness necessary for under-resolved engineering simulations at full-scale Reynolds numbers*". In this paper, they argue a 15 factor improvement in CPU performance in favor of LBM. However, this result is to be tempered because the impact of boundary conditions is very important on the production of turbulent structures. Moreover, WENO schemes, even if they are sixth-order, are widely used to capture shocks but are known to be not very accurate for this kind of turbulent flows [208]. Finally, they use an entropic MRT collision model [152,207] that we did not study, but which is simply a MRT with dynamic relaxation times for the high-order moments. This collision model varies between a BGK model and a PR one. An illustration of the "entropic stabilizer" is provided in Fig. 7 of [153], where it is apparent that the model never comes down into BGK in the sheared regions.

The second article is the one of Hou [57] produced with OpenFOAM [209] for the NS part, and a beta version of the LaBS/ProLB code including the H-RR collision model that we provided to Southampton University to carry out this study. Overall they find that both solvers have similar accuracy for the finest meshes but that LaBS/ProLB is faster and has a richer high-frequency content, which indicate that LaBS/ProLB is less dissipative. However, the conclusion of the superiority of one method over the other is not clear-cut. In view of these different observations, it is still too early to correctly situate LB methods compared to methods based on Navier-Stokes equations, even for low Mach numbers, where LBM is recognized as very efficient.

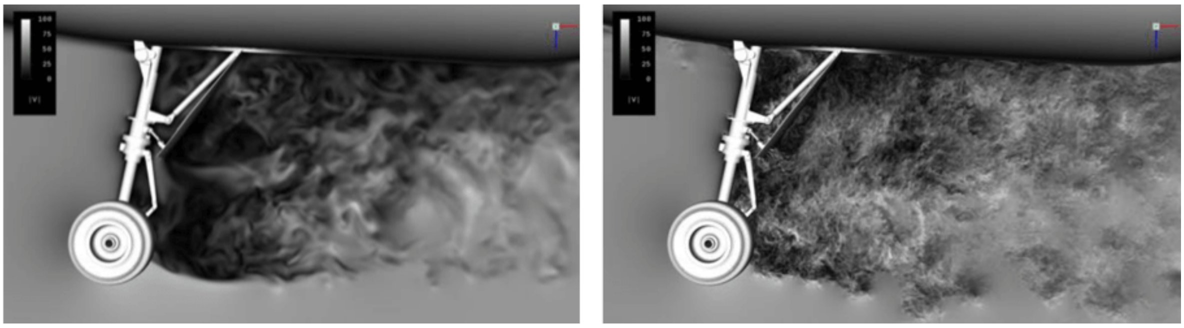

Figure 5.4 – *Comparison of velocity fields on the PDCC-NLG landing gear with the LAVA solver from NASA. Left: NS-WENO6-RK4,* $2.22.10^8$ *cells. Right: LBM-D3Q27,* $2.6.10^8$ *cells. Extracted from [56].*

Digression aside, if we go back to the comparisons of the different models presented on Fig. 5.2, it can be seen that all the models except the BGK dissipate strongly and in an anisotropic way. Additionally, the selective filtering used in LaBS/ProLB in addition to the DRT model allows to strongly reduce the areas of instability at high wavenumbers. However, it is not sufficient for low wavenumbers in the diagonal direction where instabilities persist. The RR_ψ model is strongly anisotropic on the dissipation of acoustic waves in particular. This can be seen very clearly if one compares the dissipation cuts performed at $\theta = 0°$ and $\theta = 60°$ shown on Fig. 4.1 and Fig. 5.3 respectively. This anisotropy is reduced with the H-RR_ψ model which no longer has this asymptotic behavior for acoustic modes propagating in the normal and tangential direction to the mean field.

So far it has been seen that the H-RR model, and in particular its corrected version, has attractive properties of stability and non-hydrodynamic mode filtering, without having a detrimental effect on the accuracy. In the next section, it is proposed to study the behavior of the model in the $\sigma = 0$ limit.

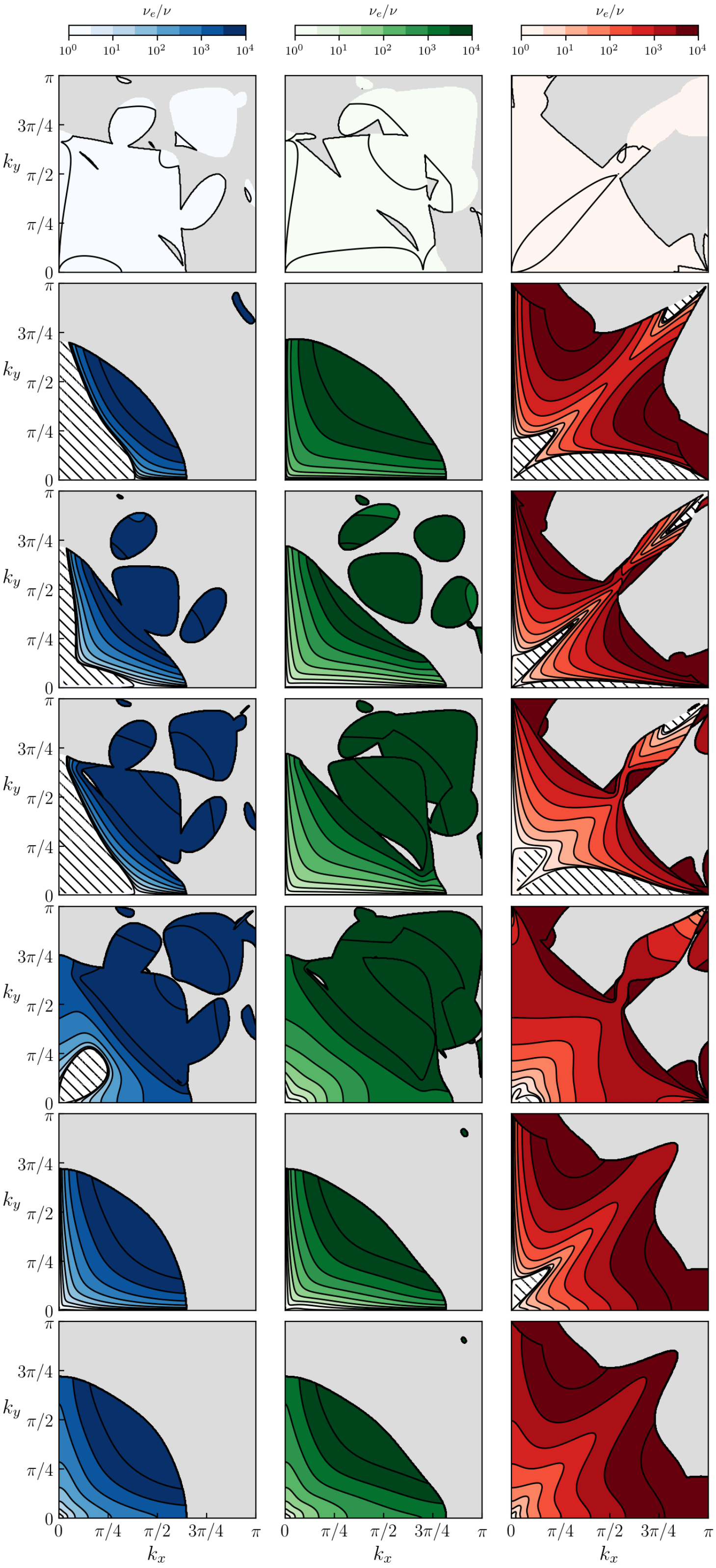

Figure 5.5 – *Maps of normalized effective viscosity* ν_e/ν *of the modes carrying physical waves for several LB models with* $\nu = 10^{-6}$, M_x*=0.2. From left to right: Ac+ mode, Ac- mode, Shear mode. From top to bottom: BGK, PR,* MRT^H, *DRT, DRT with filters,* RR_ψ, *H-*RR_ψ *(*$\sigma = 0.98$*). Grey color indicate zones where no physical wave are identified. Hatched areas indicate zones where models are unstable (*$\omega_i > 0$*).*

5.3 Stability and accuracy of the H-RR model in the $\sigma = 0$ limit

The analyses previously conducted concerning stability and accuracy are reiterated here, particularly for the specific case of $\sigma = 0$.

5.3.1 Stability domains

The stability domains for the three values of the hybridization parameter $\sigma = [0, 0.98, 1]$ which becomes equivalent to the RR scheme for $\sigma = 1$ are shown on Fig. 5.6. First of all, it can be observed that the H-RR ($\sigma = 0$) model is highly unstable if it does not include the ψ correction, whereas it is stable if it does, up to a Ma > 0.7 whatever the value of the dimensionless viscosity in the range of interest for aeronautic applications.

This result was not expected since it was originally developed without these correction terms [60], which were added in the high-subsonic and compressible version [120] where they are justified since Ma > 0.7 [114, 210]. Recently, Wissocq [149] studied the properties of a model close to the H-RR($\sigma = 0$): the AR model (for analytically regularized model). This model is a regularization with a complete reconstruction of the stress tensor by its expression involving the viscous stress rate tensor $S_{\alpha\beta}$

$$a^{(2),\mathrm{AR}}_{1,\alpha\beta} = -2\tau\rho c_s^2 S_{\alpha\beta} \tag{5.3.1}$$

This $a^{(2),\mathrm{AR}}_{1,\alpha\beta}$ term is then injected in Eq. (4.1.2), and Eq. (4.1.1). This model is thus close to the H-RR ($\sigma = 0$), with two noticeable differences: 1/ there is no recursive computation of the third-order non-equilibrium moments, 2/ $S_{\alpha\beta}$ is computed in an exact way in its spectral analysis, while we use second-order centered differences to compute $a^{(2),\mathrm{FD}}_{1,\alpha\beta}$ (Eq. (4.1.11)).

On Fig. 14 and 15 of Wissocq study [149], one can notice that this model is unstable with a D2Q9 lattice (with a partial fourh-order equilibrium) and stable with a D2V17 lattice (with a third-order equilibrium). The D2V17 lattice being a Q = 7 order quadrature, it allows to exactly recover the third-order moment of the equilibrium function. Thus, the retrieved LBM model no longer has a Mach error in the viscous stress tensor. In the same way, we observe with the corrected H-RR$_\psi$($\sigma = 0$) model, that while correcting the Mach error, this model is stable until Ma > 0.7. One can therefore presume that this error is at the origin of the instability observed when the viscous stress tensor is reconstructed from $S_{\alpha\beta}$.

The ceiling observed for Ma > 0.7 is in agreement with the results of Renard [210] who exhibits a limit of the H-RR$_\psi$($\sigma = 0$) for CFL = $(\mathrm{Ma} + 1)c_s = 1$ corresponding to Ma = 0.732. To get beyond this limitation, the CFL must be decreased by adjusting the reference temperature, which requires a suitable equilibrium function and additional correction terms [120, 121, 210].

In our simulation, the σ value is set to $\sigma = 0.98$ but can nevertheless be decreased in order to stabilize simulations that would require it. This hybridization parameter is

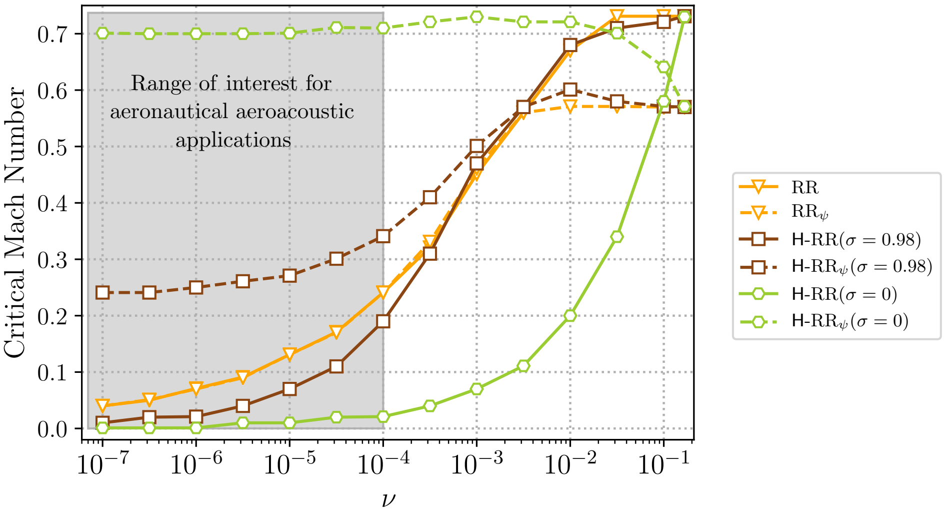

Figure 5.6 – *Critical Mach number reachable for a given dimensionless viscosity* ν *for three values of the hybridization parameter* σ *with and without cubic Mach correction terms* $\boldsymbol{\psi}$.

a very efficient way to stabilize the simulations at a lower cost. Indeed, this method remains local, using the nearest neighbors, compared to the use of selective filters for instance [162].

5.3.2 Nature of instabilities

A stability map with the same analysis parameters as in Sec. 5.1.2.b is presented in Fig. 5.7 for the H-RR and H-RR$_\psi$($\sigma = 0$) model. The H-RR exhibits an instability bubble for low wavenumbers ($k < \pi/8$) which disappears with the H-RR$_\psi$. This instability is illustrated on the dissipation curves of Fig. 5.7 where a clear anti-dissipation of the shear and acoustic modes appears for $k \to 0$. This might be considered as a first order error of the uncorrected scheme. This demonstrates the necessity of the ψ correction when reconstructing the viscous stress tensor from the stress rate tensor, even for low Mach numbers.

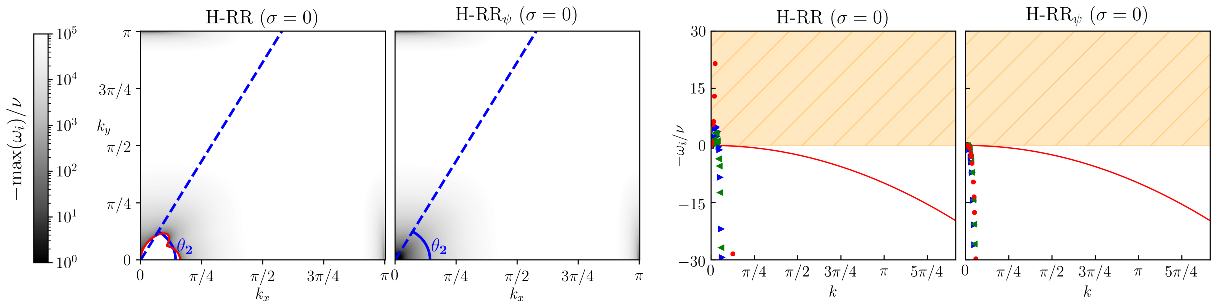

Figure 5.7 – *Left: Maps of normalized maximal growth rate* $(\max(\omega_i)/\nu)$. *The red solid isoline corresponds to the stability threshold* $(\max(\omega_i) = 0)$. *Right: Dissipation curves extracted along the* θ_2 *blue cut.* (▸)*: Ac+ mode,* (◂) *: Ac- mode,* (●) *: Shear mode,* (—) *: Isothermal Navier-Stokes. Mean flow* $M_x = 0.2$, $\nu = 10^{-6}$.

From now on, the H-RR model will no longer be studied without Mach correction terms.

5.3.3 Accuracy

The dissipation induced by the H-RR$_\psi$ ($\sigma = 0$) model is shown on Fig. 5.8. It can be seen that under these conditions ($M_x = 0.2$, $\nu = 10^{-6}$), the resulting dissipation is considerable. For example, for a physical wave propagating in the flow direction and discretized with height points per wavelength (ppw), the associated effective viscosity reaches $\nu_e/\nu \sim 10^4$ compared to $\nu_e/\nu \sim 10^2$ when $\sigma = 0.98$ (*cf.* Fig. 5.5). It is noteworthy that this dissipation does not come from the finite difference induced dissipation used to reconstruct the stress rate tensor. Indeed, Wissocq also observes a very important dissipation with the AR model, by computing the gradients in an exact way (spectrally) [149]. Thus, **increasing the order of the finite difference reconstruction will not improve the dissipation of this scheme**. The origin of this dissipation is currently unknown, but it is not surprising since all the models studied in this chapter except the BGK model present important dissipation errors. In any case, it is clear that the relaxation or reconstruction of third and fourth-order moments has a strong impact on the physical dissipation of LBM schemes.

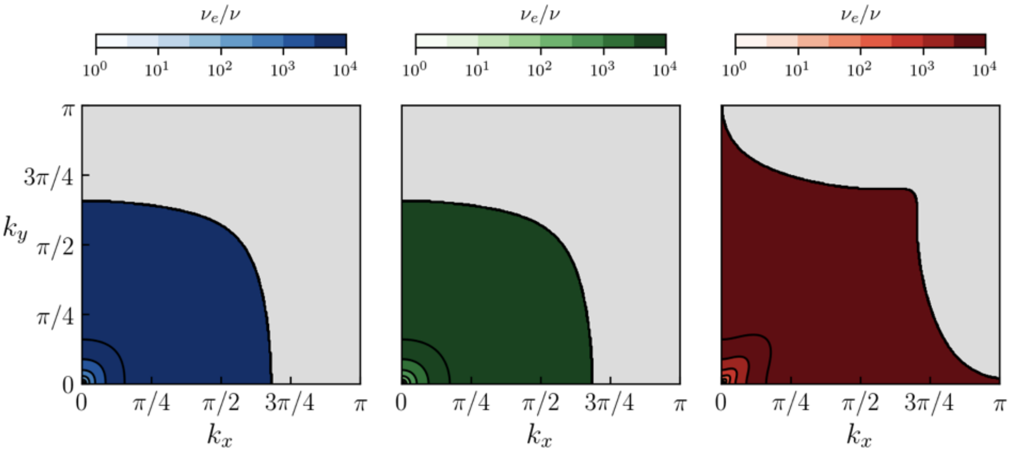

Figure 5.8 – *Maps of normalized effective viscosity ν_e/ν of the modes carrying physical waves for the H-RR$_\psi$ ($\sigma = 0$) collision model with $\nu = 10^{-6}$, M_x=0.2. From left to right: Ac+ mode, Ac- mode, Shear mode. Grey color indicate zones where no physical wave are identified.*

Finally, after having analyzed this model, the choice of $\sigma = 0.98$ appears to be a good compromise. Indeed, using a larger value of σ allows to tend towards the RR$_\psi$ model. However the latter is less stable, does not dissipate non-hydrodynamic modes and has a higher anisotropic dissipation, which is finally close to that of the H-RR$_\psi$ ($\sigma = 0.98$) for most of the possible propagation directions for the perturbations. Using a lower value of σ strongly increases the dissipation of physical waves, and, in practice, is not necessary for damping the non-hydrodynamic modes that are already dissipated with a value of $\sigma = 0.98$.

Now that the spectral properties of the different models have been evaluated for a D2Q9 lattice, numerical validations will be performed afterwards on a convected vortex and a two-dimensional acoustic pulse where an analytical solution exists. These validations will notably serve to anticipate the behavior of models based on a D3Q19 lattice that are of interest for industrial applications.

5.4 Numerical validations

The first test case studied is a vortex convected in a periodic box. This case will evaluate the stability and accuracy of the code for convecting vorticity quantity. Furthermore, at initialization, the vortex generates a weak acoustic emission due to discretization errors. This emission can also trigger acoustic instabilities which will be of interest to consider. In a second step, an acoustic pulse will be studied to evaluate the ability of the LBM to propagate acoustics. Both test cases are performed at a dimensionless viscosity $\nu = 10^{-6}$ with a D2Q9 lattice and a third-order Hermite equilibrium function. These test cases have been voluntarily considered with such a viscosity since it corresponds to real aeronautical conditions, and it is in line with the stability analyses presented previously. Consequently, when compared to the analytical Euler solutions, a small additional dissipation is expected in the simulations.

5.4.1 Convected vortex in a periodic box

A convected vortex is initialized at the center of a periodic square box of size [L,L] with L = 201 until 50 characteristic times $t_{conv} = \mathrm{L}/\mathrm{U}x$ are reached. The initialization is identical to the one described in Sec. 4.4.3. The radius has been doubled ($R_c = 20$) in order to reduce discretization errors. Fig. 5.9 shows the progress of the vortex after $50t_{conv}$ for models with a sufficient stability and Tab 5.2 summarizes their status.

Model	BGK	PR	MRT^H	DRT	DRT with filters	RR$_\psi$	H-RR$_\psi$
$\boldsymbol{t_{NaN}}(t_{conv})$	37	0.4	12	4	4	✓	✓

Table 5.2 – *Number of convective time until the simulation become unstable for several LB models for the periodic vortex case with* $M_x = 0.2$, $\nu = 10^{-6}$. ✓: *stable after* $50t_{conv}$

The only two models able to achieve $50t_{conv}$ are the RR$_\psi$ and the H-RR$_\psi$. This result was expected since the Tab. 5.1 indicates that the RR$_\psi$ have a very low (but still positive) amplification rate and only the H-RR$_\psi$ model was supposed to be stable in these conditions. The other models are all strongly unstable. The quickest being the PR allowing the vortex to do only $0.4t_{conv}$, as suggested by its larger amplification rate. The DRT and filtered DRT models then follow-up with instability caused by a low wavenumber acoustic wave propagating diagonally. Since this instability is not sufficiently attenuated by the

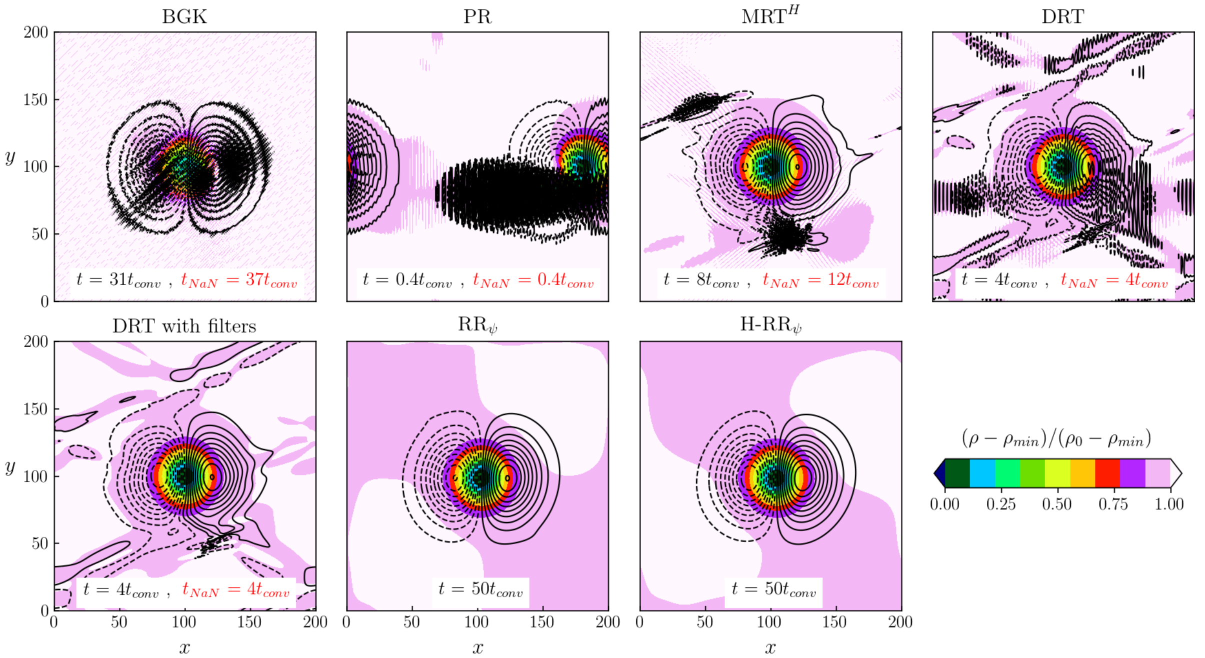

Figure 5.9 – *Periodic convected vortex for several collision models.* $M_x = 0.2$, $\nu = 10^{-6}$. *20 isocontours of the transverse velocity component* u_y*.* t*: time of the current fields.* t_{NaN}*: time where the simulation diverge.* t_{conv}*: The characteristic convected time for a box tour.*

filters, the latter do not improve the stability range of the model. Finally, the MRT^H model allows to triple the time during which this test case remains stable compare to the DRT. However, the calculation still diverges quickly.

It is nevertheless interesting to wonder how the version of LaBS/ProLB that uses a filtered DRT model has enabled aeronautical industrial simulations to be carried out at these flow conditions [36, 178] without being unstable. In this kind of simulation, the grid refinements (*cf.* App. B) as well as the turbulence model greatly help to stabilize the computation as shown on Fig. 5.10, where a Smagorinsky model [30] has been added with a Smagorinsky constant $C_s = 0.17$. One can notice that the calculation remains stable after $50t_{conv}$, but the obtained solution is strongly degraded. The use of selective filters is particularly useful when used in conjunction with a turbulence model.

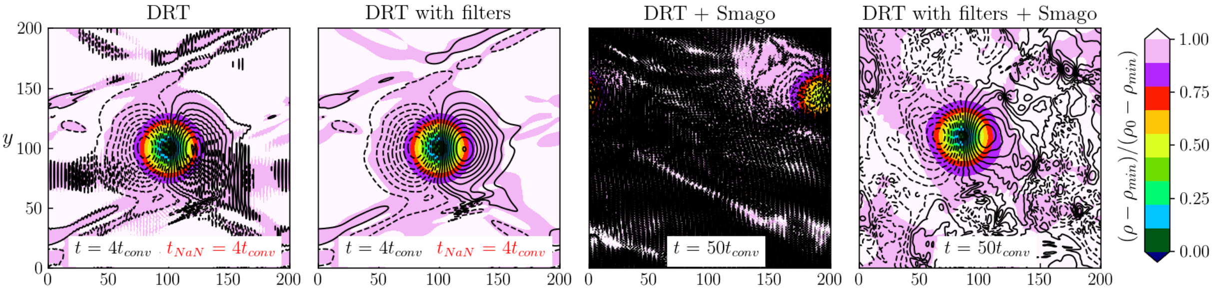

Figure 5.10 – *Periodic convected vortex for DRT and filtered DRT collision model with additional Smagorinsky turbulence model.* $M_x = 0.2$, $\nu = 10^{-6}$. *20 isocontours of the transverse velocity component* u_y. *t: time of the current fields.* t_{NaN}*: time where the simulation diverge.* t_{conv}*: The characteristic convected time for a box tour.*

Afterwards, the accuracy of the RR_ψ and $\mathrm{H\text{-}RR}_\psi$ models will be evaluated once the vortex has completed 50 turns ($t = 50t_{conv}$). The $\mathrm{H\text{-}RR}_\psi(\sigma = 0)$ model is also studied to assess its numerical dissipation. Fig. 5.11 shows the density and velocity profiles at the center of the vortex. It can be seen that the RR_ψ and $\mathrm{H\text{-}RR}_\psi$ ($\sigma = 0.98$) models allow to correctly convect this vortex. One can also note a dispersion that seems slightly lower for the model RR_ψ. The total reconstruction of $\boldsymbol{a}_1^{(2)}$ with by means of the stress rate tensor nevertheless adds a lot of numerical dissipation as previously illustrated on Fig. 5.8.

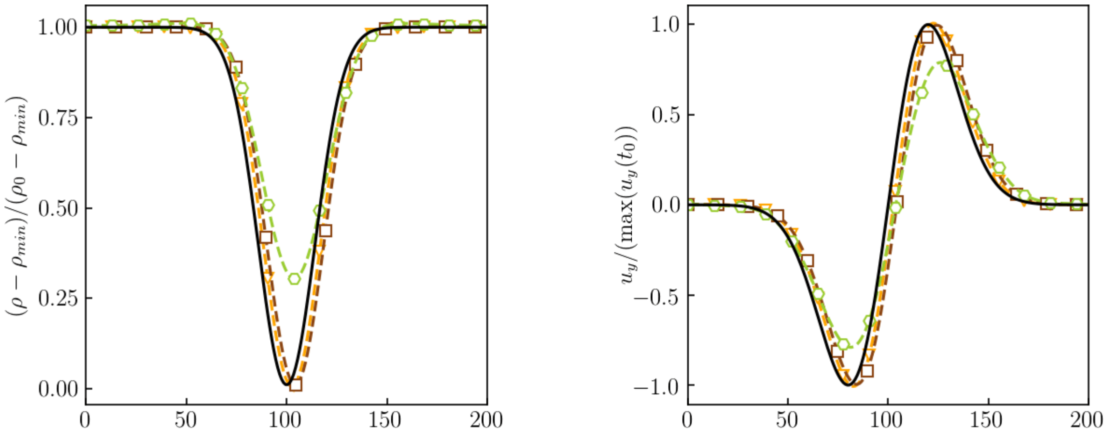

Figure 5.11 – *Density (left) and transversal component of the velocity* u_y *(right) profiles for the periodic convected vortex extracted along the x axis through each vortex center after 50 convected times.* RR_ψ: -▽-, $\mathrm{H\text{-}RR}_\psi$ ($\sigma = 0.98$): -□-, $\mathrm{H\text{-}RR}_\psi$ ($\sigma = 0$): -○-, —: *initial solution.* $M_x = 0.2$, $\nu = 10^{-6}$.

Another interesting point is to investigate the limits of these models for the vortex case, in terms of relative L^2 error, dissipation and dispersion for several Mach number and value of the hybridization parameter σ at $\nu = 10^{-6}$. The relative L^2 error is defined as

$$L^2_{err} = \sqrt{\frac{\sum_{x,y}\left[\rho(x,y,t_f) - \rho(x,y,t_0)\right]^2}{\sum_{x,y}\rho(x,y,t_0)^2}}. \tag{5.4.1}$$

In addition to the numerical scheme error, there is also an error related to the physical dissipation since the case has been chosen at $\nu = 10^{-6}$. However, this error is identical whatever the model. The Mach number is increased by step of 0.1 until $M_x = 0.7$ which is close to the stability limit of the H-RR$_\psi$ ($\sigma = 0$) model (*cf.* Fig. 5.6). The σ is increased from 0 to 1 by step of 0.1 and the $\sigma = 0.98$ has also been added. A total of 84 simulations are studied. Fig. 5.12 shows the L^2 error, the dissipation $\epsilon_{vortex} = \left[\min\left(\rho(t_f)\right) - \min\left(\rho(t_0)\right)\right] / \left[\rho_0 - \min\left(\rho(t_0)\right)\right]$, and the distance between the vortex center at initialization and the one obtained after $50t_{conv}$ (dc_{vortex}) which will qualify the dispersion. It is first of all important to note that the numerical errors are function of the number of iterations. Since this study is performed at a fixed number of characteristic time t_{conv}, it is expected that the error decreases as the Mach number increases. This does not necessarily mean that the models have better numerical properties as the Mach number increases.

Firstly, one can observe that whatever the Mach number studied, lowering the value of σ increases the dissipation. For instance, for a convective Mach number of 0.1, the amplitude loss on the vortex goes from 2%, to 53% for a σ ranging from $\sigma = 1$ to $\sigma = 0$. However, the dissipation gap between the two extreme σ values gets smaller as the Mach increases. This is an important statement because as reducing σ appears as an efficient way of stabilizing the collision scheme in high Mach while trying to limit the consequences on dissipation. One can also notice that the case becomes unstable for Mach approaching $M_x = 0.7$ when σ increases as confirmed by Fig. 5.6. For Mach numbers between 0.4 and 0.7, cases at $\sigma > 0.98$ are predicted unstable but instability does not appear yet after 50 turns. However, a strong increase in dispersion can be seen when $\sigma \to 1$ for $\mathrm{Ma} > 0.5$. This means that the vortex is deformed and that the simulation is about to diverge.

The same study was carried out in three dimensions with a D3Q19 lattice and the H-RR$_\psi$ model. Results are presented in App. A. Moreover, additional results have been added for diagonal vortex convection to complete the study. The results are almost identical when comparing D2Q9 and D3Q19 on this case. The diagonal convection cases show instabilities for both lattices when $\sigma = 1$, which is in agreement with the stability domains determined in Fig. 5.1.

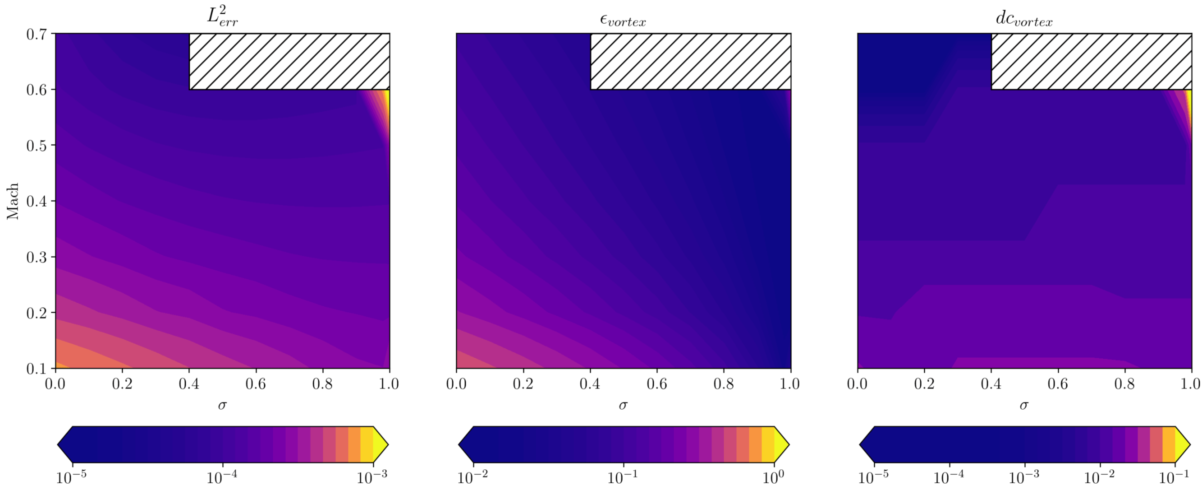

Figure 5.12 – *Maps of* L^2 *error* (L^2_{err}), *dissipation* $\epsilon_{vortex} = [\min(\rho(t_f)) - \min(\rho(t_0))] / [\rho_0 - \min(\rho(t_0))]$ *and dispersion* dc_{vortex} *for the periodic vortex test case after 50 convective time with the H-RR*$_\psi$ *model. Several convected Mach number and hybridization parameter* σ *are studied.* dc_{vortex} *is the distance between the vortex center at the initial and at the final state. The dimensionless viscosity is fixed to* $\nu = 10^{-6}$. *Hatched areas means unstable simulations.*

5.4.2 Convected two-dimensional Gaussian pulse

The test case of a Gaussian pulse is interesting to evaluate the capacity of a CFD solver to propagate acoustics. Moreover, this test case has an analytical solution [202] that will allow to assess the accuracy of the code. This analytical solution comes from the linearized Euler equations and can be considered as valid if viscosity effects are small. The pulse is advected under the same conditions as before in order to characterize the anisotropy.

The acoustic pulse is initialized in a [201,201] periodic domain as follows:

$$\begin{cases} \rho(x,y) = \rho_0\left(1 + A\exp\left(-\frac{(x-x_c)^2+(y-y_c)^2}{2R_c^2}\right)\right), \\ u_x(x,y) = U_x, \\ u_y(x,y) = 0, \end{cases} \tag{5.4.2}$$

with

$$\rho_0 = 1, \quad U_x = 0.2c_s, \quad A = 10^{-4}, \quad x_c = y_c = 100. \tag{5.4.3}$$

At first, the pulse is voluntarily under-discretized as in [70], in order to clearly identify numerical errors of the different models. For this purpose, a radius $R_c = 1$ is chosen. Fig. 5.13 shows the evolution of the pulse after $t = 120$ iterations for various models. An anisotropic density field can be observed whatever the model. The BGK in particular, reveals a very large number of spurious waves. These waves are non-hydrodynamic SpuriousAc (⧈) modes studied in Chap. 3and Chap. 4, and are not dissipated at all by the BGK model as confirmed by Fig. 3.2 and Fig. 5.3. Advanced collision models or the use of filters can reduce this phenomenon. Indeed, the filters used in addition to the DRT model allow to slightly reduce these unwanted high-frequencies. For dissipating this phenomena, the best performing models are the RR_ψ and $\mathrm{H\text{-}RR}_\psi$ where only spurious waves appear in the main directions. This is indeed confirmed by Fig. 4.1 and Fig. 5.3 for the RR_ψ model which shows that the SpuriousAc (⧈) wave is strongly dissipated out of the main directions of the mesh. The $\mathrm{H\text{-}RR}_\psi$ model allows to further reduce these spurious waves. From an isotropy and spurious wave filtering point of view, these two models are the most satisfactory for propagating acoustics. Additional results with the D3Q19 lattice on this test case are provided in App. A and shows exactly the same behavior compared to the D2Q9.

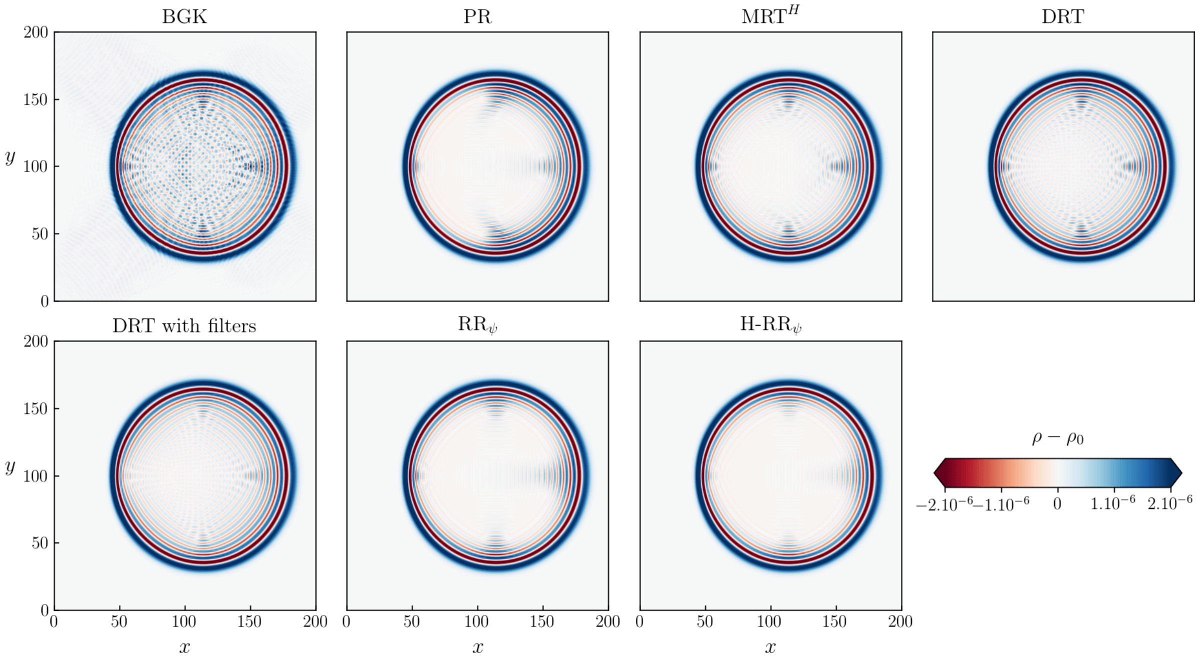

Figure 5.13 – *Relative density fields of a convected two-dimensional under resolved acoustic pulse for several LB models at* $t = 120$ *iterations.* $M_x = 0.2$, $\nu = 10^{-6}$.

It is however interesting to quantitatively evaluate the capacity of these models to propagate acoustics by comparing them to an analytical solution. The number of points in the radius for this purpose is increased up to $R_c = 5$.

Obviously, by increasing the radius of the Gaussian pulse with a fixed domain, the resolution of the peaks is enhanced and the numerical errors decrease for the prediction of the latter. Dispersion and dissipation effects are very clearly visible on Fig. 5.14 for $R_c = 3$. Dispersion errors are mostly visible for the acoustic wave moving in the flow direction.

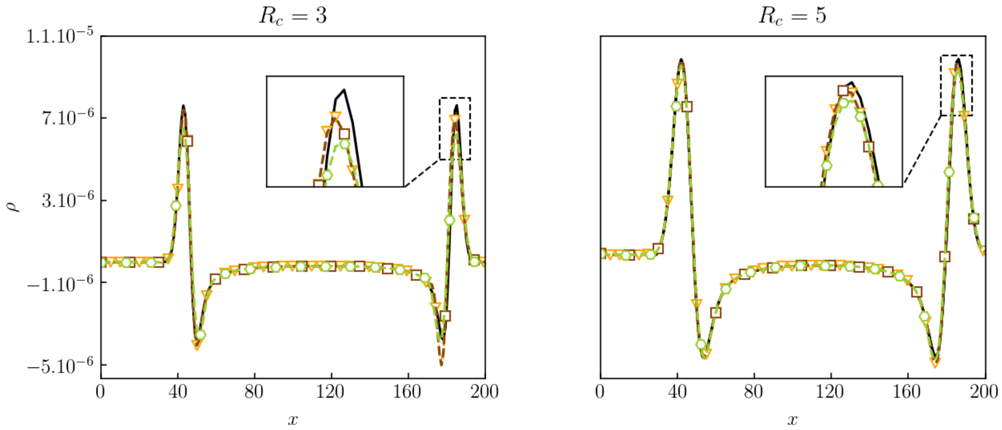

Figure 5.14 – *Density profiles of a convected two-dimensional acoustic pulse for several values of the hybridization parameter σ for the H-RR$_\psi$ collision model. Profiles are extracted for $y = 100$ at $t = 120$ iterations. $M_x = 0.2$, $\nu = 10^{-6}$. Left: $R_c = 3$, right: $R_c = 5$. RR$_\psi$: -▽-, H-RR$_\psi$ ($\sigma = 0.98$): -□-, H-RR$_\psi$ ($\sigma = 0$): -⬡-, —: analytical solution.*

For the latter, a low value of σ limits the dispersion of the wave. The wave is however strongly dissipated by the H-RR$_\psi$ ($\sigma = 0$) whereas the two other values give very similar results. The errors are very strongly reduced when the radius of the pulse increases to $R_c = 5$. For this value, the models corresponding to the three values of σ can accurately predict the propagation of the density pulse. These results are important to be known when one is interested in aeroacoustic simulations with direct noise propagation. In this kind of study, acoustics must be propagated without being degraded until it reaches the microphones, which may be far from the noise sources. In an airframe noise context, it may also be important to correctly propagate acoustic waves emitted by an installed landing gear to the wing overhanging this last where the waves can be reflected, refracted and diffracted. These phenomena can have a significant impact on acoustic predictions [13].

The choice of the H-RR$_\psi$ model with a value of $\sigma = 0.98$ seems satisfactory concerning the dissipation of non-hydrodynamic modes, as well as the good propagation of physical waves. Furthermore, this model extended to the D3Q19 lattice gives results very similar to those obtained in this section for the vortex and pulse test case. **This model is thus adopted as a reference in the rest of this thesis.**

5.5 Conclusion on the stability and accuracy of the LB methods

In this chapter, the stability and accuracy of the LB methods have been studied for several collision models used in the LB community. The stability defects of LB models were, once again, highlighted. For aeronautical applications at relatively low Mach number (Ma< 0.3), the outcome is that even at this moderate Mach number, few model can ensure a linear stability in the low-viscosity regime. In particular, one can mention that the BGK, PR, MRT^H and DRT models studied previously are essentially unstable. The RR model has a rather low stability in this chapter because the equilibrium function was chosen at the third-order so that the analysis is directly extensible to a D3Q19 lattice. However, a RR model with a fourth-order equilibrium would yield a much higher range of stability [136,149]. The standard H-RR model that was previously studied for its very good ability to dissipate non-hydrodynamic modes has been revealed to be unstable due to the stress rate tensor reconstruction part. This instability vanishes by adding the ψ cubic Mach correction terms. This last stabilizes the stress rate tensor reconstruction up to $\mathrm{Ma} \sim 0.7$ whatever the value of the viscosity. As a result, hybridization now greatly increases the stability of the H-RR_ψ hybrid model. As a side benefit for LaBS/ProLB, this model allows to get rid of the seven-points explicit filtering that was associated with the DRT model so far. Moreover, it has been shown that even with these filters, the DRT was not able to reach a sufficient linear stability for aeronautical applications. These results are nevertheless to be nuanced because the addition of a turbulence model (*cf.* Fig. 5.10), the change in resolution that filter out some wavenumbers and the use of sponge zones allow in practice to push back instabilities during industrial aeronautical simulations. Indeed, LaBS/ProLB has so far allowed to perform simulations of landing gears [36], cavities [178], rod-airfoil configuration [63] or even an axial fan [211] with this numerical scheme.

The accuracy of the LBM was then evaluated. It was determined that advanced collision models dissipate much more than the BGK one, and their dissipation is often anisotropic. This anisotropy is very important to characterize using the LSA or adapted test cases such as vortex or acoustic wave convection in directions deviating from the main axes of the mesh. This type of analysis is generally not performed in the NS literature where the schemes are characterized and optimized on a one-dimensional advection equation only. Proper comparisons between LB models and Navier-Stokes schemes are seriously missing in the literature and it is currently still difficult to draw a conclusion on the efficiency of LB methods with respect to their NS counterparts.

Anyway, the H-RR_ψ ($\sigma = 0.98$) model has, in addition to substantially improved stability, a precision that is not degraded compared to the filtered DRT model currently used in LaBS/ProLB v2.5 as shown on Fig. 5.5. Besides, the linear stability analyses of models have only been carried out with a D2Q9 lattice. However, numerical validations on vortex and acoustic pulse have shown a similar behavior between a D2Q9 and a D3Q19 lattice for the H-RR_ψ model (*cf* App. A).

The remaining step to perform accurate aeroacoustic simulation is to evaluate and improve the quality of grid coupling algorithm, which will be the purpose of the next chapter.

Chapter 6

Grid refinement for computational aeroacoustics on non-uniform meshes: a direct grid coupling approach

Contents

This chapter focuses on the accuracy of grid coupling algorithms for performing aeroacoustic simulations. A direct coupling cell-vertex algorithm, based on the work of Lagrava [212], is presented. This algorithm relies on conservation assumptions to build an equilibrium function consistent with both grids of different resolution. The proposed formulation is more accurate, easily handle arbitrary interfaces, and is directly usable in an industrial solver. Then, a method is proposed to preserve high-order interpolation schemes independently of the interface shape, which allows to improve the accuracy of non-aligned transitions. Finally, aeroacoustic validations are carried out with a pulse, a vortex and a turbulent flow around a cylinder, where a huge reduction of the spurious noise is achieved.

6.1 Introduction to LB grid refinement algorithms

Mesh refinement is a central concern for CFD solvers. For CPU cost reasons, it is essential being able to coarsen the mesh resolution beyond the areas of interest of a simulation. For instance, boundary layers, mixing layers or wakes must be accurately captured and require a significant number of points. On the other hand, a stationary and uniform flow close to an inlet boundary condition will not require the same resolution. Generally, Navier-Stokes solvers that are discretized with finite volume methods have flexible constraints and can progressively coarsened the mesh. On the contrary in LBM, with the associated discretization constraints, the refinement is inherently abrupt and requires an integer factor between two different mesh sizes (the integer factor can be greater than two for the multi-grid approach [157]). To give an idea of the CPU time saving when a mesh is coarsened by a factor of two in LBM, let us take the example of the grid presented on Fig. 6.1.

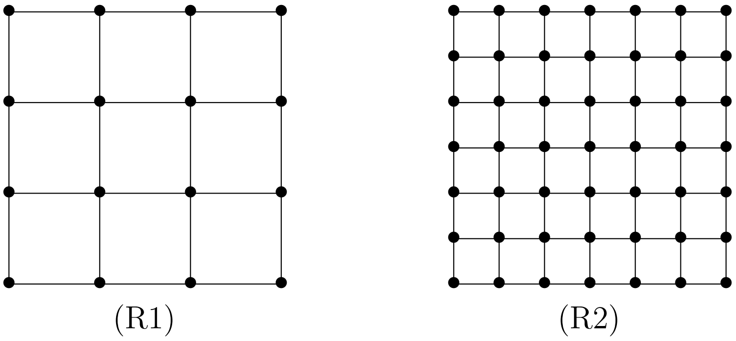
(R1) (R2)

Figure 6.1 – *Example of two different grid resolutions* $R1$ *(coarse) and* $R2$ *(fine) with a refinement factor of 2.*

The R2 grid is twice as fine as the R1. Thus, the R2 grid contains four times more cells than the R1 grid in two dimensions. Expanded in three dimensions the R2 grid would contain eight times more cells. Additionally, the acoustic scaling of the LBM imposes that the timestep is fixed by the mesh size. The latter is therefore doubled in the R1 grid (*cf.* Eq. (2.4.16)). The cost of the R2 grid for the same physical simulation time is consequently eight times higher in two dimensions and sixteen times higher in three dimensions. With this simple example, one quickly understands the absolute necessity to use algorithms that allow to couple two grids of different sizes. In the LBM literature, there are many algorithms for coupling grids. These algorithms, for those based on the classical collide & stream scheme that is a constraint for this thesis, can be expressed in two formalisms: cell-centered, where the distribution functions are stored at the center of the cells and cell-vertex where they are stored at corners as shown on Fig. 6.2.

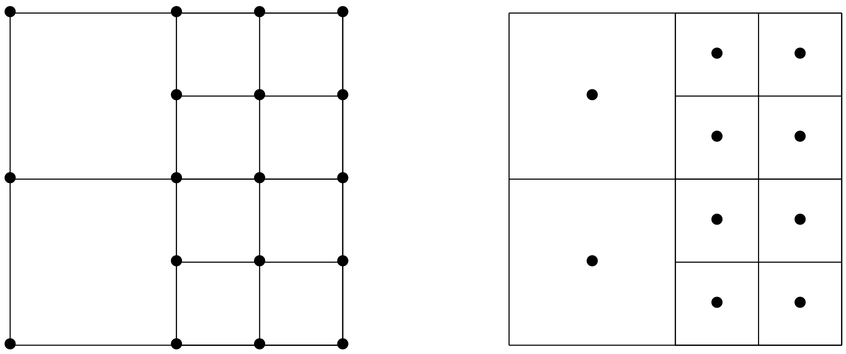

Figure 6.2 – *Cell-vertex formulation (left) and cell-centered formulation (right).*

These two data arrangements, although they do not have an influence on the LBM scheme in the fluid core, lead to significant differences in the grid coupling algorithms:

- Cell-centered: These algorithms share the particularity of having no co-located data, which prevents a direct transfer of information. They use two characteristic operations: the coalescence and explosion [159] to reconstruct the coarse and fine distribution respectively at the interface (*cf.* Fig. 6.3).

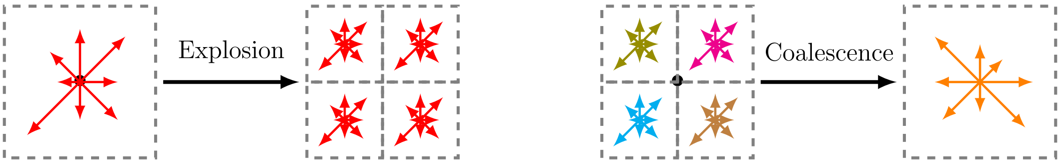

Figure 6.3 – *Explosion (left) and coalescence operations (right).*

This coalescence operation can be seen as a spatial filtering even if it is not explicitly mentioned [69]. The accuracy order used for these operations will greatly influence the precision of these grid coupling methods [213, 214]. These algorithms use an overlapping area between a fine and a coarse mesh and they are notably used in the commercial softwares PowerFLOW, Xflow or the open source code walBerla [133,213]. This data structure is not compatible with the one of LaBS/ProLB so we will not go this way. Yet, papers describing these algorithms can be found in [158, 159, 215–217]. Many peoples use these algorithms for aerodynamic applications [218–222]. Nevertheless, these studies do not require a very high accuracy of mesh interfaces. There are a couple of articles on aeroacoustic applications, mainly carried out with the PowerFLOW solver [177, 223–230] and one with the Xflow solver [37] that gives only near-field results. No details are given about the cell-centered refinement algorithm used. Besides, one can see on the Fig. 9 of [37] that even with the use of a large amount of bulk viscosity and a centered moment MRT model, spurious vorticity appears at mesh interfaces. Finally, Hasert's PhD thesis [84] also shows aeroacoustic results with a cell-centered algorithm. However, many disturbances are visible at the mesh interfaces. From our point of view, they are related to non-hydrodynamic modes on Fig. 9.6 rather than to the low order of interpolations used as proposed by the authors.

- Cell-vertex: These algorithms have the specificity of having co-located fine and coarse nodes at the grid interface. A direct transfer of the available distributions can thus be achieved by using a rescaling of the off-equilibrium distribution functions [156,157]. The non-coincident nodes are usually completed by means of spatial interpolations. The first articles used a multi-block strategy, where a fine mesh overlapped a coarse one [156, 157, 231]. Simultaneously, many authors have chosen a more efficient multi-domain approach, using an overlapping layer to connect the two grids while making available the missing distributions [160,161,232,233], rather than a complete superposition of both grids. These algorithms have been improved by the addition of a filtering procedure applied during the fine to coarse transfer, allowing to enhance the stability for turbulent flow simulations [59,83]. This formulation is used in the LaBS/ProLB v2.5 solver, as well as in OMNIS$^{\text{TM}}$/LB solver [234], based on the open source Palabos library [235]. Recently, the latter algorithm has been improved for aeroacoustic simulations by Gendre using a partial propagation method [70] (noded **PP**), this algorithm is evaluated in App. B.1. The same author, has also developed another algorithm based on a directional splitting method [69]. The latter, although more precise than the one currently used in LaBS/ProLB v2.5 [59], does not seem relevant for industrial purposes, since the author does not used the directional splitting algorithm for the industrial applications in its phD thesis with LaBS/ProLB. Another particularly interesting algorithm based on a concept of direct grid connection has been developed by Kuwata [236]. However, this algorithm is based on an incompressible equilibrium assumption [237] which prevents aeroacoustic applications. On a similar principle, Lagrava has developed in his thesis [212] a direct coupling algorithm, that is validated on a Poiseuille flow with a D2Q9 lattice and a second-order equilibrium function on a planar interface. Actually, the proposed implementation was not fully compliant with an industrial use, especially with the H-RR$_\psi$ collision model that requires a third-order equilibrium function and gradient computations.

The present chapter aims to improve this last algorithm (noted **DC** for Direct Coupling) in several ways and validate it in an aeroacoustic framework. The improvements include: (1) a simplification of the algorithm formulation and an efficient numerical resolution method for three-dimensional refinement interfaces of arbitrary shapes, and (2) a reconstruction of distribution functions more in line with the accuracy requirements of aeroacoustics applications. In this chapter we will compare the DC algorithm with the one used in LaBS/ProLB v2.5 [59], which will be noted **STD** for standard. Further comparisons are provided in App. B.1 with the Gendre's partial propagation (**PP**) algorithm [70] but will be limited to an academic configuration in our in-house two dimensional LBM python code developed for the needs of this thesis.

The chapter is organized as follows. First of all, the direct coupling (DC) grid refinement algorithms are described in Sec. 6.2. Secondly, the accuracy of spatial interpolations used for arbitrary interfaces will be discussed in Sec 6.3. Subsequently, in Sec. 6.4, numerical validations are performed on academic test cases: an acoustic pulse and a vortex convected across a grid interface. Both test cases are declined with plane and inclined transitions. Afterwards, a validation is performed on a highly turbulent flow around a cylinder with arbitrary grid refinement in Sec. 6.5.

6.2 Description of the direct coupling algorithm

All the notions concerning the rescaling of quantities when a change of resolution occurs have already been presented in Sec. 3.5.1 and will be kept in this chapter. The spatial and temporal interpolations presented in Sec. 3.5.2 will also be preserved hereafter, at least for a planar transition as discussed in Sec. 6.3. In addition, the rescaling specificities related to the adaptation of the H-RR$_\psi$ model to non-uniform meshes presented in Sec. 4.3 will be maintained.

Concerning this last point, the H-RR$_\psi$ model now integrates the ψ correction terms. These must also be rescaled when the resolution changes, in the same way as the strain rate tensor $S_{\alpha\beta}$.

$$\psi_i^f = \frac{\psi_i^c}{2}. \tag{6.2.1}$$

6.2.1 Algorithm description

The proposed grid coupling algorithm is introduced in this sub-section. In the standard collide & stream algorithm, some populations are missing at the grid interface due to the non-existence of neighboring nodes with a similar resolution. To reconstruct these populations, most of the existing algorithms use an overlapping area. This strategy is adopted both for the classical cell-centered [158, 159] or cell-vertex [156, 157] algorithms.

The present algorithm does not require any overlapping area to achieve the grid coupling. It only needs some particular treatments performed on two specific nodes (●, ○). Both of these nodes are displayed on Fig. 6.4. The first ones are co-located fine and coarse nodes. They are used to reconstruct the missing populations on both grids. The second ones are hanging fine nodes that do not have any counterpart in the coarse domain.

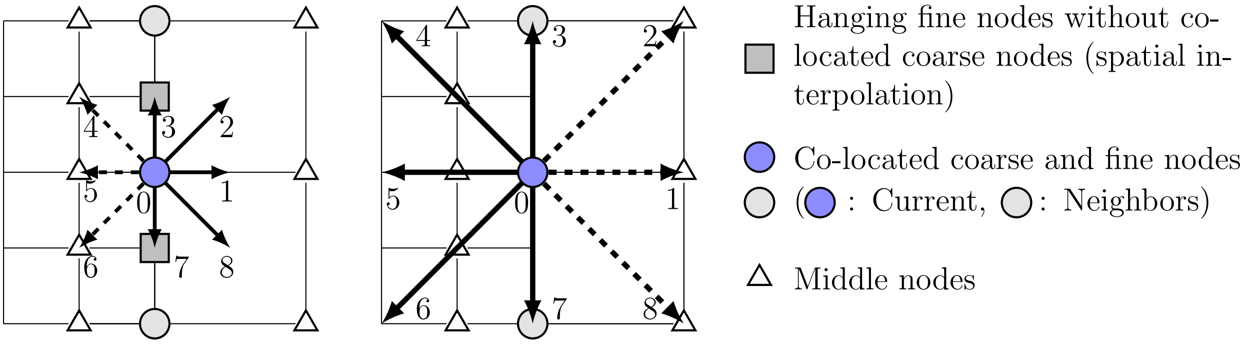

Figure 6.4 – *Two dimensional representation of a plane refinement interface.* (- - -►)*: Unknown distribution functions after a streaming step,* (⟶)*: known distribution functions. Left: fine domain, right: coarse domain.*

At the grid interface, several distribution functions are missing and cannot be streamed on (●) nodes (*cf.* Fig. 6.4). They have to be reconstructed after the streaming step. The present grid coupling algorithm aims at reconstructing the missing populations based on the following hypothesis ensuring mass and momentum conservation at (●) nodes

$$\sum_i \boldsymbol{\Phi}_i g_i^{(1),c} = \sum_i \boldsymbol{\Phi}_i g_i^{(1),f} = \mathbf{0}, \tag{6.2.2}$$

with $\boldsymbol{\Phi}_i = (1, e_{x,i}, e_{y,i}, e_{z,i})^{\mathrm{T}}$.

In practice, this equality cannot be satisfied straightforwardly since distributions with the same resolution are missing in each grid. Eq. (3.5.3) can be used to relate the off-equilibrium distributions of both grids. It is therefore possible to ensure Eq. (6.2.2) by mixing the off-equilibrium distribution functions belonging to one mesh with the other. Within the off-equilibrium part, g_i can be known since it corresponds to a post-collision function of an existing neighboring node. However, no $f_i^{(0)}$ is known since their computation involves unknown macroscopic quantities. It is with the objective of determining a consistent equilibrium function $f_i^{(0)}$ at (●) nodes that the system proposed by Eq. (6.2.2) must be solved.

Since fine cells are updated twice as often as coarse ones, the system will be solved in the fine mesh, *i.e.* only the right hand side part of Eq. (6.2.2) will be considered: $\sum_i \boldsymbol{\Phi}_i g_i^{(1),f} = \mathbf{0}$. Solving this system allows finding the macroscopic variables that are required to compute a local equilibrium on the (●) nodes. This equilibrium, in addition to the known distribution functions, will make it possible to reconstruct both missing fine and coarse distribution functions.

For the sake of generality, the set of indexes of fine and coarse missing populations will be respectively referred to as $\mathcal{M}^f$ and $\mathcal{M}^c$. The set of population indexes which are both known on the fine and coarse mesh after the streaming step will be referred to as $\mathscr{P}$, and the set of populations indexes that are only known on the fine mesh (resp. the coarse mesh) will be referred to as $\mathscr{Q}^f$ (resp. $\mathscr{Q}^c$). For instance, in the particular case of Fig. 6.4, one has $\mathscr{M}^f = \mathscr{Q}^c = \{4,5,6\}$, $\mathscr{M}^c = \mathscr{Q}^f = \{1,2,8\}$ and $\mathscr{P} = \{0,3,7\}$. With these notations, Eq. (6.2.2) can be re-written for the fine mesh, after replacing the missing fine populations by the rescaled coarse ones thanks to Eq. (3.5.3), as

$$\sum_{i\in\mathscr{Q}^f} \mathbf{\Phi}_i g_i^{(1),f} + \sum_{i\in\mathscr{M}^f} \mathrm{R}\cdot\mathbf{\Phi}_i g_i^{(1),c} + \sum_{i\in\mathscr{P}} \mathbf{\Phi}_i g_i^{(1),f} = \mathbf{0}. \tag{6.2.3}$$

Furthermore, it can be noticed that the last term of this equation, involving $\mathscr{P}$, can either be computed thanks to the fine populations $g_i^{(1),f}$ or their coarse counterpart $g_i^{(1),c}$ after a rescaling by $\mathrm{R} = 0.5\bar{\tau}_f/\bar{\tau}_c$. For this reason, and in order to generalize the resolution procedure, two parameters Γ_i and γ_i are introduced below, depending on the nature (*i.e.* fine or coarse) of the distribution functions that are taken into account in the system resolution. Eq. (6.2.3) can then be re-written as

$$\sum_i \Gamma_i\cdot\mathbf{\Phi}_i g_i^{(1),\gamma_i} = \mathbf{0}, \tag{6.2.4}$$

where

$$\begin{cases} \text{Fine distribution is used:} & \Gamma_i = 1, \qquad \gamma_i = f, \\ \text{Coarse distribution is used:} & \Gamma_i = \mathrm{R}, \qquad \gamma_i = c, \end{cases} \tag{6.2.5}$$

and where R is the rescaling factor to convert a coarse to a fine non-equilibrium distribution. The choice of the couple (Γ_i, γ_i) is not unique and will be further discussed in Sec. 6.2.2.

In Eq. (6.2.4), off-equilibrium distribution functions $g_i^{(1),\gamma_i} = g_i^{\gamma_i} - f_i^{(0)}(\mathbf{X})$ depend on a vector of macroscopic variables $\mathbf{X} = (\rho, u_x, u_y, u_z)$. This system of equations can be rewritten in the following manner:

$$\mathbf{F}(\mathbf{X}) = \sum_i \Gamma_i\cdot\mathbf{\Phi}_i\left(g_i^{\gamma_i} - f_i^{(0)}(\mathbf{X})\right) = \mathbf{0}. \tag{6.2.6}$$

In this system, all distribution functions $g_i^{\gamma_i}$ are known, while all equilibrium functions $f_i^{(0)}(\mathbf{X})$ are unknown. For three dimensional cases, this system contains four equations and four unknowns (ρ, u_x, u_y, u_z). Because of the quadratic, cubic or even higher-order powers in velocity arising in the adopted form of equilibrium function $f_i^{(0)}$, this system is genuinely non-linear. Furthermore, the non-equilibrium functions are multiplied by the Γ_i parameter, which takes as many values (1 or R) as the number of discrete velocities. For these reasons, the system can be very tough to solve for three dimensional cases and arbitrary grid refinement interfaces.

A general methodology of resolution is proposed here using an iterative Newton-Raphson method [238, 239]. This efficient method allows finding the roots of a given set of equations, here $\mathbf{F}(\mathbf{X}) = \mathbf{0}$.

Firstly, one can linearly evaluate, through a Jacobian matrix $\mathbf{J_F}(\mathbf{X_0}) = \mathrm{d}\mathbf{F}(\mathbf{X_0})/\mathrm{d}\mathbf{X}$, the value of $\mathbf{F}(\mathbf{X_0} + \delta\mathbf{X})$ that is the value of $\mathbf{F}(\mathbf{X_0})$ plus a small variation $\delta\mathbf{X}$ around a first estimation of the roots $\mathbf{X_0}$:

$$\mathbf{F}(\mathbf{X_0} + \delta\mathbf{X}) \simeq \mathbf{F}(\mathbf{X_0}) + \mathbf{J_F}(\mathbf{X_0}) \cdot \delta\mathbf{X}. \tag{6.2.7}$$

Subsequently, by assuming $\mathbf{F}(\mathbf{X_0}+\delta\mathbf{X}) = \mathbf{0}$, the roots $\mathbf{X_0}+\delta\mathbf{X}$ can be determined through a linear interpolation:

$$\delta\mathbf{X} = \mathbf{J_F}^{-1}(\mathbf{X_0})\,[\mathbf{F}(\mathbf{X_0} + \delta\mathbf{X}) - \mathbf{F}(\mathbf{X_0})] = -\mathbf{J_F}^{-1}(\mathbf{X_0})\mathbf{F}(\mathbf{X_0}). \tag{6.2.8}$$

The roots can be found from a given starting point $\mathbf{X_0}$ as

$$\mathbf{X_0} + \delta\mathbf{X} = \mathbf{X_0} - \mathbf{J_F}^{-1}(\mathbf{X_0})\mathbf{F}(\mathbf{X_0}). \tag{6.2.9}$$

Practically, the vector of macroscopic variable at the previous timestep is used to initialize the Newton-Raphson algorithm. Finally, since $\mathbf{F}$ is nonlinear, the macroscopic variables can be obtained iteratively in the following way:

$$\forall n \geq 0, \qquad \mathbf{X}_{n+1} = \mathbf{X}_n - \mathbf{J_F}^{-1}(\mathbf{X}_n) \cdot \mathbf{F}(\mathbf{X}_n). \tag{6.2.10}$$

The iterative method can be considered as converged when $||\delta\mathbf{X}|| < 10^{-12}$.

The analytical expression of the Jacobian matrix $\mathbf{J_F}$ is computed once and for all before it gets implemented by means of a free formal computation software, e.g. Maxima [240]. Then the inversion of the Jacobian matrix $\mathbf{J_F}^{-1}$ is directly computed in the LB solver, at each iteration of the Newton-Raphson algorithm, using LAPACK library [241]. It is also possible to compute analytically the inverse of the Jacobian matrix using an adequate mathematical tool. Nevertheless, in practice with such equilibrium in three dimensions, it is more efficient to inverse it directly in the code. In all the cases of Sec. 6.4-6.5, the Newton-Raphson algorithm takes less than three iterations to converge, which leads to very small overhead as compared to the substantial gain it brings.

Once the macroscopic variables at (●) nodes are updated, it is then possible to reconstruct the fine missing populations [156] using the new equilibrium distribution function $f_i^{(0)}$ determined with the updated macroscopic variables:

$$\forall i \in \mathscr{m}^f, \qquad g_i^f = f_i^{(0)} + \mathrm{R}\; g_i^{(1),c}. \tag{6.2.11}$$

Non-coincident nodes (○) are completed by means of spatial interpolations. Fourth-order one-dimensional interpolation schemes [83] are used to reconstruct their missing populations (*cf.* Eq. (3.5.8)). Spatial interpolations are a critical subject for the quality of grid coupling algorithms. It has been shown [83] that at least third-order spatial interpolations are required to ensure mass conservation. In the present work, the choice of one-dimensional interpolations is adopted for a sake of simplicity and to preserve the computational efficiency of the algorithm. A systematic use of three-dimensional interpolations that depend on the shape of the interface is indeed not conceivable. The one-dimensional interpolations have a significant impact on the quality of simulations, which will be quantified in Sec. 6.3 and Sec. 6.4.

Furthermore, as two fine iterations are performed during one coarse time step, a temporal interpolation of g_i^c is needed to reconstruct the missing populations g_i^f on (●^{f}) nodes. The interpolation described in Sec. 3.5.7 is used.

It is noteworthy that no spatial filtering is employed when transferring distributions from the fine mesh to the coarse one. Indeed, the algorithm being without overlapping layer, it is not possible to use an isotropic filtering as it is generally done in standard cell-vertex algorithms [59,83]. No particular needs for filtering have been observed in the numerical experiments of Sec. 6.4-6.5 and for industrial aeroacoustic applications.

In the following section, the choice of the Γ_i parameter is discussed. The latter depends on the choice of the distributions used in the DC algorithm which can be multiple.

6.2.2 Choice of the Γ_i parameter and distributions used in the DC algorithm

At the grid interface, several possibilities may exist to reconstruct the distribution functions. Populations for which $i \in \mathscr{P}$ are indeed known on both meshes. Other populations for which $i \in \mathscr{Q}^f$ (resp. $\mathscr{Q}^c$) are only known on the fine (resp. coarse) mesh.

This observation leads us to several reconstruction possibilities. Two of them are summarized in Table. 6.1. The first one, referred to as DC1, is a generalization of the reconstruction originally proposed by Lagrava [212]. The second one, referred to as DC2, is an improved reconstruction that is proposed in this study.

The distribution functions for the fine mesh reconstruction on (●)^f node and the associated value of Γ_i are summarized in Table 6.1.

Set of indexes	$\mathscr{P}$	$\mathscr{Q}^f$	$\mathscr{M}^f$
DC1	(1, f)	(1, f)	(R, c)
DC2	(R, c)	(1, f)	(R, c)

Table 6.1 – *Couples* (Γ_i, γ_i) *assigned on* (●) *nodes for the iterative resolution of Eq.* (*6.2.6*)*, according to the set of population indexes* i*.*

With regard to the reconstruction of the coarse distribution functions g_i^c on (●)^c nodes, in the same way as for the fine distribution reconstruction, many possibilities exist. However, a lack of consistency between reconstruction in the fine mesh and in the coarse one may lead to a non-conservation of mass and momentum in the collision step. It is therefore decided here to reconstruct all coarse functions using the previously completed fine ones, as

$$g_i^c = f_i^{(0)} + 1/\mathrm{R}\; g_i^{(1),f}. \tag{6.2.12}$$

In summary, the DC1 model reconstructs the fine distribution functions using as many informations coming from the fine mesh as possible. On the contrary, the DC2 model uses as many available coarse functions as possible. The DC2 formulation aims to reduce the reintroduction of interpolation errors occuring on (■) nodes in the reconstruction of the (●) nodes and to minimize aliasing effects.

If the interface is not planar as on Fig. 6.4, the only difference lies in the indexes associated with the sets $\mathscr{P}, \mathscr{Q}^f, \mathscr{M}^f$, and thus the values of associated couple (Γ_i, γ_i). The system (Eq. 6.2.6) being solved for discrete (Γ_i, γ_i) values, it is simply enough to substitute these values in the LB code, by the one corresponding to the given interface. App. B.2 provides some examples of sets $\mathscr{P}, \mathscr{Q}^f, \mathscr{M}^f$ for interfaces with corners in two dimensions.

6.2.3 Steps of the algorithm

The steps of the algorithm are summarized as follows:

1) **Reference state** → Fine grid t ; Coarse grid t
    a. All the distribution functions are known on both grids.
2) **Asynchronous iteration** → Fine grid $t + \Delta t^f$; Coarse grid $t + \Delta t^c$
    a. Propagation step towards fine and coarse middle nodes.
    b. Streaming of fine known populations towards (●) nodes.
    c. Streaming of coarse known populations towards (●) nodes.
    d. Temporal interpolation of previously streamed coarse populations g_i^c on (●^{f}) nodes using Eq. (3.5.7).
    e. Reconstruction of missing fine populations with parameter $\Gamma_i = \mathrm{R}$ with Eq. (6.2.11). $g_i^{(0)}$ is deduced from the macroscopic variables obtained thanks to the iterative scheme of Eq. (6.2.10).
    f. Estimation of the fine strain tensor $S_{\alpha\beta}^f$ and the cubic Mach corrective term ψ^f on (●^{f}) nodes using a second-order centered finite difference scheme following the methodology introduced in Sec. 4.3.
    g. Spatial interpolation of g_i^f, ψ^f and $S_{\alpha\beta}^f$ on (○) nodes.
    h. Collision of all fine nodes.
3) **Synchronous iteration** → Fine grid $t + \Delta t^c$; Coarse grid $t + \Delta t^c$
    a. Propagation step towards the fine middle nodes.
    b. Streaming of fine known populations towards (●^{f}) nodes

   c. Reconstruction of missing fine populations with parameter $\Gamma_i = \mathrm{R}$ with Eq. (6.2.11). The coarse populations used here are those streamed on step 2)c. $f_i^{(0)}$ is deduced from the macroscopic variables obtained thanks to the iterative scheme of Eq. (6.2.10).
   d. Estimation of the coarse strain tensor $S^c_{\alpha\beta}$ and the cubic Mach correction term ψ^c on (●^{c}) using second-order centered finite difference scheme scheme. On (●^{f}) nodes, transfer and conversion of $S^c_{\alpha\beta}$ and ψ^c to the fine scale using Eq. (4.3.1) and Eq. (6.2.1) respectively.
   e. Spatial interpolation of g_i^f, $S^f_{\alpha\beta}$ and ψ^f on (○) nodes.
   f. Reconstruction of coarse populations using Eq. (6.2.12).
   g. Collision of all nodes with Eq. (4.1.4).

4) **Repetition of steps 2) to 4) until the end of the simulation**.

For efficiency reasons, in the case of a regularized model, only the macroscopic variables $\rho, \boldsymbol{u}$ and the off-equilibrium moments can be interpolated instead of g_i. This grid refinement algorithm is made completely generic for any orientation of the interface and either two or three dimensional configurations. The only difficulty lies in the preliminary needs to use a formal computing tool to compute the Jacobian matrix used in the system to find the equilibrium function. Using a direct connection like this one allows reducing the number of duplicated points at grid interface compared to overlapping algorithms, which saves memory and improves code parallelization. Nevertheless, due to the Newton-Raphson iterative procedure, an extra-cost of 15% in the grid coupling algorithm is noticed for the DC compared to the STD in the simulations carried out afterwards. However, this cost remains very marginal considering the low number of interfacial nodes concerned by the algorithm. The overall cost of the grid refinements in the simulations performed in Sec. 6.4 and 6.5 is less than 1% of the total simulation time.

All the useful theoretical details the grid coupling algorithm being described, the validation of the DC algorithms are presented in the following sections.

6.3 Spatial interpolation schemes for arbitrary interfaces

6.3.1 Description of spatial interpolation schemes

Depending on the interface shape, several interpolation schemes can be adopted. One dimensional interpolations are generally used [83, 242] since the cost of three dimensional interpolation methods are prohibitive. To our knowledge, the topic of spatial interpolations used with cell-vertex algorithms for arbitrary interface in the fluid domain has never been addressed in the literature. Lagrava *et al.* [83] proposed three interpolations schemes that are used for plane interface with compatibility with domain borders. These interpolations are *a priori* mainly used by other authors. However, these last imply reducing the order and thus the precision for arbitrary transitions. This can be very inconvenient when using meshes with "layers" as it is usually done for industrial applications [61].

Hence a method (referred to as $\mathbf{I-3}$) is proposed here to keep an identical interpolation stencil whatever the shape of the grid interface in the fluid domain. Fig. 6.5 shows the possible configurations of a two-dimensional interface and the associated interpolation stencils for three interpolation methods. Using the node convention of Fig. 6.4 with the blue color that is associated with the current node it gives:

- Method $\mathbf{I-1}$: Only co-located fine nodes (○) are employed in the interpolation to reconstruct the hanging nodes (▣). Thus, second-order centered (Mesh A), upwind third-order (Mesh B) and fourth-order centered (Mesh C) spatial interpolation schemes are used depending on the shape of the interface.

- Method $\mathbf{I-2}$: Co-located (○) and middle fine nodes (△) are employed in the interpolation to reconstruct the hanging nodes (▣). Third-order upwind (Mesh A and B) and fourth-order centered (Mesh C) spatial interpolation schemes are used depending on the shape of the interface.

- Method $\mathbf{I-3}$: Both co-located fine nodes (○) and fine or coarse middle nodes (△) are utilized. Therefore, fourth-order centered scheme are used whatever the interface shape.

The interpolation schemes for a quantity h are detailed in the case of an interface with a tangential vector $e_y(0,1,0)$. Given in coarse unit for the $\mathbf{I-1}$ method which involves three different stencils it gives:

- Second-order centered spatial interpolation scheme (Mesh A)

$$h\,(\square, t) = \frac{1}{2}\Big(h\big(\bigcirc - e_y/2, t\big) + h\big(\bigcirc + e_y/2, t\big)\Big). \tag{6.3.1}$$

- Third-order upwind spatial interpolation scheme (Mesh B)

$$h\,(\square, t) = \frac{3}{8}h\big(\bigcirc - e_y/2, t\big) + \frac{3}{4}h\big(\bigcirc + e_y/2, t\big) - \frac{1}{8}h\big(\bigcirc + 3e_y/2, t\big). \tag{6.3.2}$$

- Fourth-order centered spatial interpolation scheme (Mesh C)

$$h\,(\square, t) = \frac{9}{16}\Big(h\big(\bigcirc + e_y/2, t\big) + h\big(\bigcirc - e_y/2, t\big)\Big) - \frac{1}{16}\Big(h\big(\bigcirc + 3e_y/2, t\big) + h\big(\bigcirc - 3e_y/2, t\big)\Big). \tag{6.3.3}$$

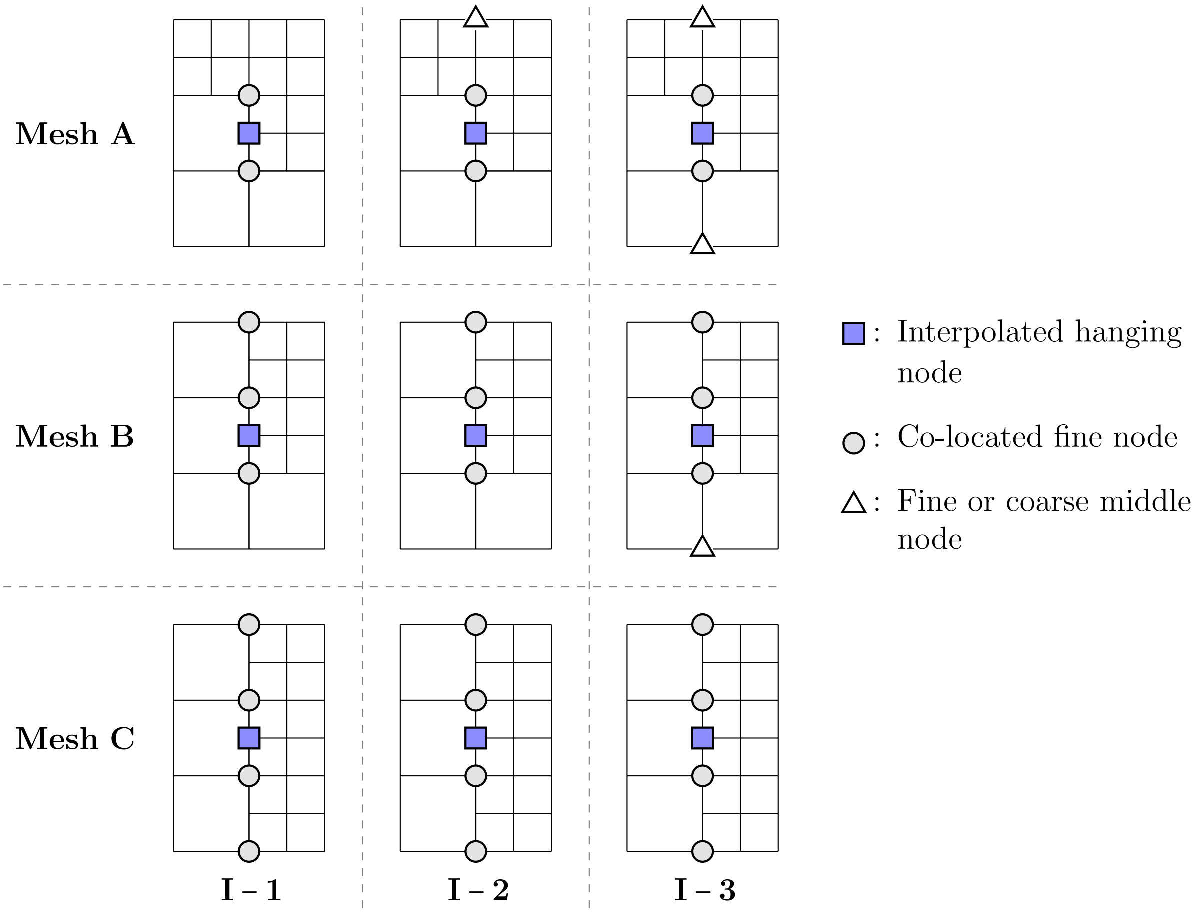

Figure 6.5 – *Stencils used for the three interpolation methods* (**I − 1** *to* **I − 3**) *for the different mesh configurations that can be encountered in two dimensions.*

The **I − 3** method constantly uses fourth-order interpolation schemes (Eq. (6.3.3)) except at boundaries. For this purpose, nodes employed for the interpolation can no longer be restricted to the interface. **A specificity thus appears when a middle coarse node (△) is used**. **A temporal interpolation is necessary at odd timestep** (Eq. (3.5.7)) **as well as a rescaling of the off-equilibrium distribution functions** (Eq. (6.2.12)). This method is more accurate but also more expensive for parallel purposes since nodes must be accessible outside the interface and even within the coarse mesh.

In the next section, the three interpolation methods that have been implemented in LaBS/ProLB will be compared on a convected vortex that crosses an inclined refinement interface. The STD cell-vertex algorithm that is described in [59, 87] and used in LaBS/ProLB v2.5 will be adopted for this comparison before it will be compared to the DC algorithms.

6.3.2 Comparison of interpolation methods on a convected vortex that crosses an inclined grid interface

This section aims to compare the accuracy and the spurious noise emitted by a vortex crossing an oblique transition depending on the interpolation method used. This test case is typical of an aeroacoustic application and it is used in the two previous studies dealing with aeroacoustics with non-uniform meshes [69, 87]. For this test case, a reference to our previous article [87] or to Chap. 4 is of paramount importance to get rid of the non-hydrodynamic modes present in the vortex, which can drastically increase the spurious emission. Like in the previous study, these modes are here filtered out by the use of the H-RR$_\psi$ collision model.

The case of a vortex crossing an interface with thirty degrees of inclination is chosen since it allows to find the two cases (Mesh A & B) of interface described on Fig. 6.5. The third case (Mesh C) being identical for both three interpolation methods, it is not studied here.

The barotropic vortex [183] that is solution of the isothermal Euler equations is initialized in the fine mesh as follow:

$$
\begin{aligned}
\rho\left(x,y,z\right) &= \rho_0 \exp\left[-\frac{\epsilon^2}{2(r_g T_0)^2}\exp\left(-\frac{(x-x_c)^2+(y-y_c)^2}{R_c^2}\right)\right],\\
u_x\left(x,y,z\right) &= U_x - \epsilon\left(\frac{y-y_c}{R_c}\right)\exp\left(-\frac{(x-x_c)^2+(y-y_c)^2}{2R_c^2}\right),\\
u_y\left(x,y,z\right) &= \epsilon\left(\frac{x-x_c}{R_c}\right)\exp\left(-\frac{(x-x_c)^2+(y-y_c)^2}{2R_c^2}\right),\\
u_z\left(x,y,z\right) &= 0,
\end{aligned}
\tag{6.3.4}
$$

with

$$
\begin{gathered}
\rho_0 = 1.17621 \text{ kg.m}^{-3}, \quad U_x = 0.1c_0, \quad r_g = 287.15 \text{ J.kg}^{-1}\text{.m}^{-1},\\
\epsilon = 0.15c_0, \quad \Delta x^f = 0.01 \text{ m}, \quad R_c = 0.06 \text{ m}, \quad (x_c, y_c) = (-6R_c, 0).
\end{gathered}
$$

Contrary to what has been done so far, all simulations will be presented with dimensioned values. The dimensionless values were useful to assess the numerical properties of the LBM. However, the dimensioned values are more suitable for the remaining applications. All the simulations of the present chapter are carried out with a kinematic viscosity of $\nu = 1.49.10^{-5}$ m^2.s^{-1}, a speed of sound of $c_0 = 347.3$ m.s^{-1}, a reference temperature of $T_0 = 300$K and a hybridization parameter $\sigma = 0.98$.

The simulation domain is described on Fig. 6.6. In order to avoid any reflection of spurious acoustic, explicit absorbing layers [79] are added at the domain boundaries, as previously done in Chap. 4. In order to record the emitted spurious acoustics, 36 pressure probes are located in a circle at a distance of 1.5m from the domain center.

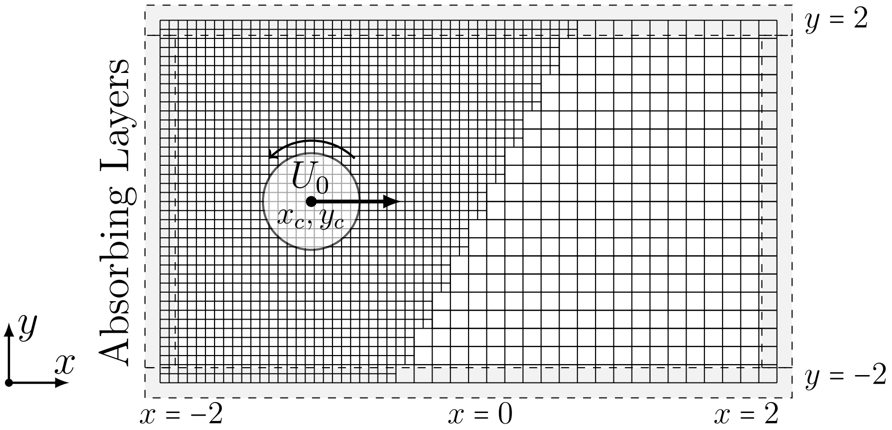

Figure 6.6 – *Sketch of the simulation domain for the vortex convected across a* 30°-*inclined grid interface. Absorbing layers map the domain boundaries to avoid reflection of spurious acoustic emission.*

The relative pressure field is compared for the three interpolation methods on Fig. 6.7 when the vortex has almost crossed the interface. A significant reduction of the noise emitted by the vortex at the interface can be observed with the $\mathbf{I-3}$ method compared to $\mathbf{I-1}$, as well as an improvement of the vortex continuity. This last point is crucial since any discontinuity in the transfer of the vortex will generate a huge acoustic emission. The $\mathbf{I-2}$ method is restricted to third-order upwind scheme for this test-case. It is significantly better than $\mathbf{I-1}$ but less accurate than $\mathbf{I-3}$ that uses fourth-order.

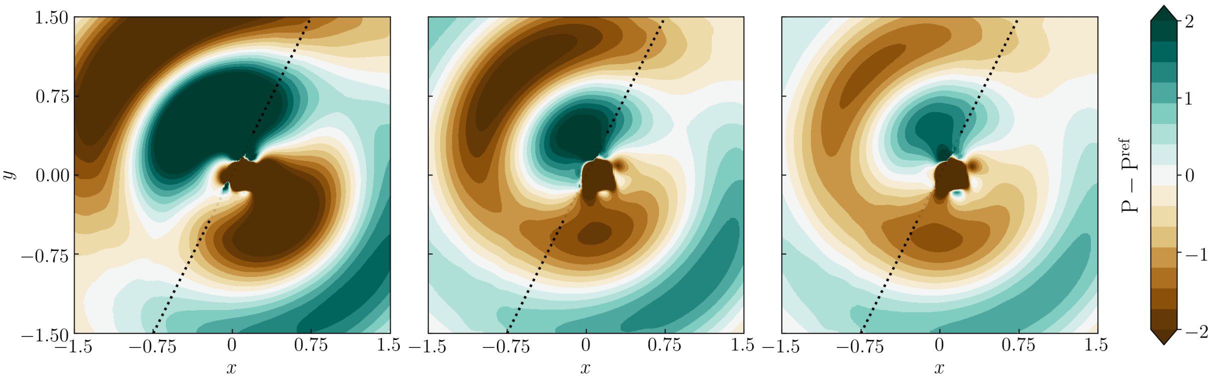

Figure 6.7 – *Relative pressure field* $(\mathrm{P}-\mathrm{P}^{\mathrm{ref}})$ *of the vortex convected across an inclined refinement interface at* $t = 1100 \cdot \Delta t^{f}$. *Left:* $\mathbf{I-1}$, *middle:* $\mathbf{I-2}$, *right:* $\mathbf{I-3}$. $(\cdots\cdots)$*: grid refinement interface.*

With microphones located in the far-field region, forming an arc around the spurious source, it is possible to compare OASPLs (Overall Sound Pressure Level) of spurious noise so as to quantify the intensity and directivity of emission. There is no reference here, since, theoretically, no acoustic noise is expected by the convection of a single vortex in a homogeneous flow. Thus, the whole recorded noise is spurious. As can be clearly identified on Fig. 6.8, a large reduction of the spurious noise is obtained whatever the direction with the **I − 3** method. The azimuthal averaged acoustic emission is then reduced for more than 6dB compared to the **I − 1** one. As a recall, a reduction of 3dB corresponds in dividing the sound intensity by a factor of 2.

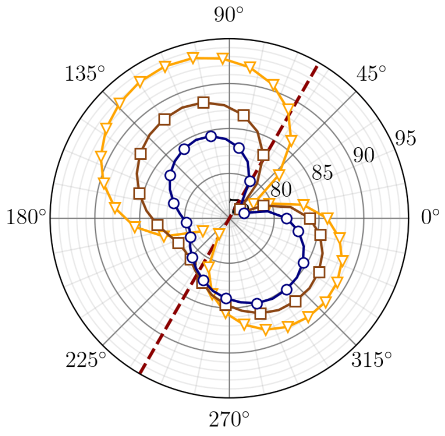

	I-1	**I-2**	**I-3**
maximum OASPL(dB)	**93.4**	**88.4**	**85.1**
mean OASPL(dB)	**88.7**	**85.1**	**82.6**

Figure 6.8 – *Left: Pressure OASPL of the spurious acoustic measured in the far-field for the convected vortex test case that crosses an inclined refinement interface with the STD algorithm.* -▽-*:* **I − 1***,* -□-*:* **I − 2***,* -○-*:* **I − 3***. Right: Table of maximum and average OASPL over the 36 microphones.* (- - -)*: grid refinement interface.*

The **I − 1** method generates a very strong dipole radiated noise [243, 244], especially in the direction of the fine mesh. A very large reduction of this noise is achieved in most propagation directions, and particularly in the fine grid, as can also be seen on Fig. 6.7.

These results obtained for an oblique interface allow to conclude that keeping fourth-order centered interpolations for all interface shapes that are likely to occur in the fluid core is really beneficial for aeroacoustic applications. It is therefore the **I − 3** interpolations that will be used later on to compare several grid refinement algorithms on academical test cases.

6.4 Numerical validation and comparison with an existing grid refinement algorithm on academic test cases

In this section, numerical validations and comparisons of the DC algorithms with the STD one that is used in LaBS/ProLB v2.5 will be performed [59].

Firstly, a two-dimensional acoustic pulse is considered over a plane and a circular interface to highlight anisotropy effect induced by the spatial interpolations. Secondly, a convected vortex through a plane and an inclined grid refinement interface is investigated.

6.4.1 Acoustic Pulse

A pseudo-2D acoustic pulse is considered in this section. This is a purely acoustic test case. The acoustic pulse is initialized in the fine grid as follows:

$$\begin{aligned} &\rho\left(x,y,z\right) = \rho_0\left(1 + A\exp\left(-\frac{(x+y)^2}{2R_c^2}\right)\right), \\ &\mathbf{u}\left(x,y,z\right) = \mathbf{0}, \end{aligned} \tag{6.4.1}$$

with

$$\rho_0 = 1.17621\text{kg.m}^{-3}\ , \quad A = 10^{-2}, \quad R_c = 0.06\ \text{m}.$$

Distribution functions are initialized at their equilibrium values computed with these macroscopic quantities. The simulated domain is a pseudo 2D periodic box of size $[L,L,\Delta x^c]$ with L = 3m and $\Delta x^c = 2\Delta x^f$ = 0.02m. The pulse is initialized at the center of the domain.

6.4.1.a Acoustic pulse across a plane refinement interface

In this section, propagation of the acoustic pulse across a plane interface is considered. The grid interfaces are located at $x = -0.75$m and $x = 0.75$m. The computational domain is sketched on Fig. 6.9.

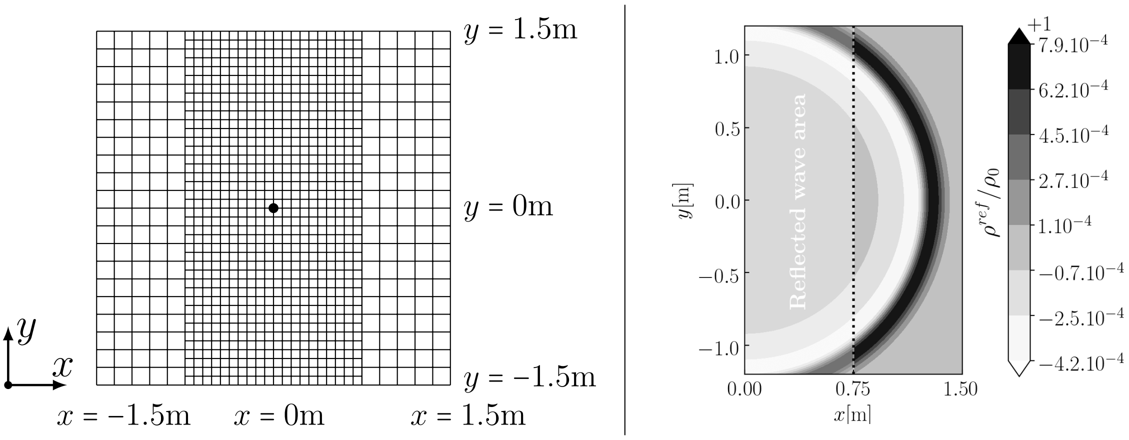

Figure 6.9 – *Left: Left: Sketch of the simulation domain for the acoustic pulse test case with plane mesh refinement interfaces. Right: density field for the pulse with a uniform fine mesh used as a reference* (ρ^{ref}) *for the non-uniform simulations.* (⋯⋯)*: refinement interface.*

In this test case, the acoustic reflection induced by the mesh interface is investigated. This spurious reflection can be attributed to three phenomena.

- A sudden variation in dispersion properties between a fine mesh and a coarse mesh, as evidenced in our last study [87] (*cf.* Fig. 3.4). This phenomenon is independent of the considered grid refinement algorithm.
- An aliasing effect. A wave resolved with less than four points per wavelength in a fine mesh has no counterpart in a coarse one. A spectral aliasing might thus take place, which results in a reflected acoustic wave. This phenomenon can be attenuated thanks to a filtering step when rescaling information from the fine mesh to the coarse one. However, no noticeable improvement has been obtained with the add of a filtering step on this test case.
- The precision of the grid coupling algorithm. A slight discontinuity in the transfer between grids may lead to an acoustic reflection.

Reflection rates exhibited with the relative density, obtained with the three grid refinement algorithms (STD, DC1 and DC2), are compared on Fig. 6.10 for this test case. Result from the simulation based on the uniform fine grid is displayed on Fig. 6.9. It will be considered as the reference result.

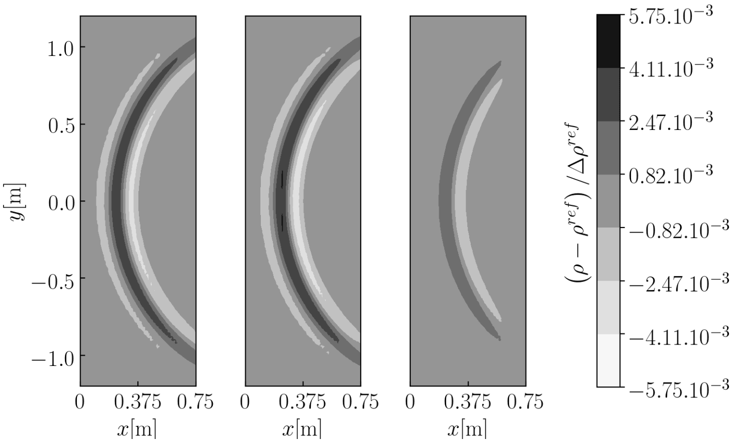

Figure 6.10 – *Relative density field of the reflected wave for the pulse test across a plane mesh refinement at* $t = 220\cdot\Delta t^f$. *The uniform fine simulation is taken as reference* (ρ^{ref}) *and* $\Delta\rho^{ref} = \rho^{ref}_{max}(t) - \rho^{ref}_{min}(t)$. *Left: STD, middle: DC1, right: DC2.*

Whatever the grid refinement algorithm considered, an acoustic reflection can be highlighted in non-uniform simulations, due to a combination of the three above-mentioned reasons. With the DC2 algorithm, the amplitude of the spurious reflected wave is significantly reduced compared to that obtained with the DC1 algorithm. This seems to be caused by the fact that in the DC1 algorithm, the reconstruction of the distribution functions is carried out keeping as many fine distribution functions as possible. This leads to a higher aliasing effect, inducing a larger acoustic reflection.

6.4.1.b Acoustic pulse across a circular refinement interface

In this section, a 1m-radius circular transition is located around the initial position of the acoustic pulse. This type of transition is chosen since it makes it possible to study a wide variety of interface shapes. A sketch of the computational domain is diplayed on Fig. 6.11.

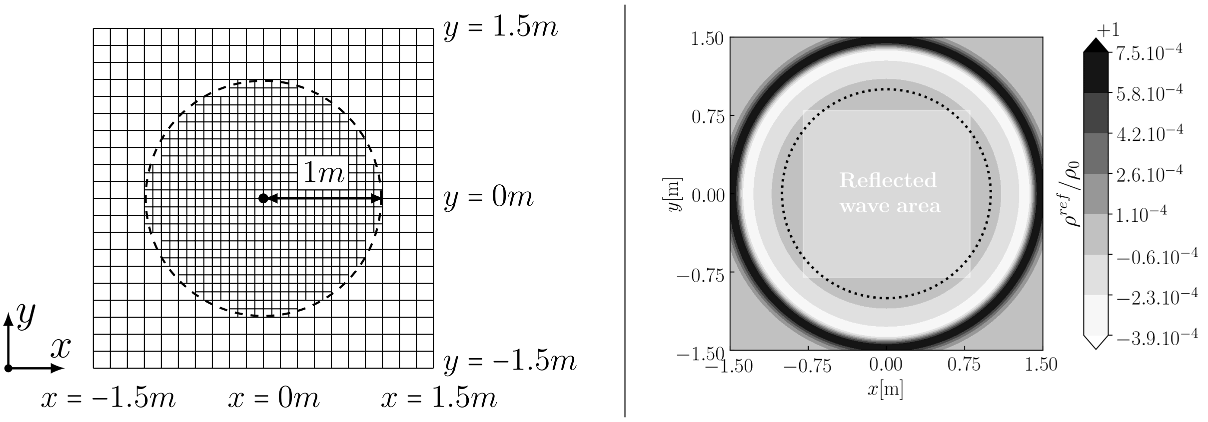

Figure 6.11 – *Left: sketch of the simulation domain for the acoustic pulse test case with a circular mesh refinement interface. Right: density field of the pulse with a uniform fine mesh used as reference for the non-uniform simulations.* (·····)*: refinement interface.*

This test case is relevant since it can evidence the anisotropy of the acoustic reflection, especially induced by the spatial interpolation. Even though fourth-order schemes are used regardless the shape of the interface, these interpolations remain one-dimensional. Thus, two non-coincident nodes, although very close to each other, can use interpolation stencils with different normal directions. Therefore, very different interpolation nodes can be used and lead to an anisotropy of the acoustic reflection.

Here, the acoustic pulse will expand and cross the interface. The reflected spurious wave is shown on Fig. 6.12. The reference used for these simulations is identical to the one used in the previous section since the latter is performed on an uniform mesh (Fig. 6.11).

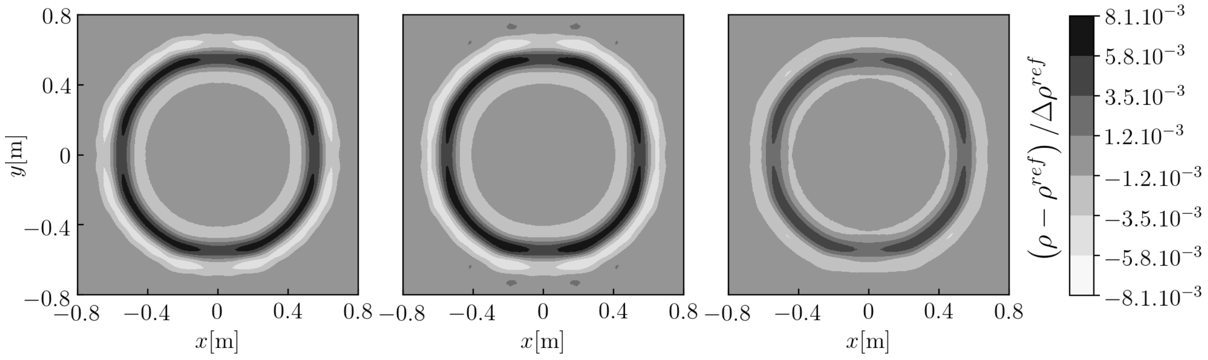

Figure 6.12 – *Relative density field of the reflected wave for the pulse test case across a cylindrical mesh refinement at* $t = 250 \cdot \Delta t^f$*. The uniform fine simulation is taken as reference* (ρ^{ref}) *and* $\Delta\rho^{ref} = \rho^{ref}_{max}(t) - \rho^{ref}_{min}(t)$*. Left: STD, middle: DC1, right: DC2.*

The three simulations highlight an anisotropy of the acoustic reflection, which may be caused by the one-dimensional spatial interpolations. The minimal reflection appears along the x- and y-axes. Along these axes, the cylindrical refinement interface is tangent to the Cartesian mesh, which makes it quasi-planar as schematically displayed on Fig. 6.11. The treatment of the non-coincident nodes is therefore optimal because neighboring non-coincident nodes use the same normal direction for interpolations.

Then, comparing the transition algorithms, it can be observed that the reflected wave with the lowest intensity is produced by the DC2 algorithm whatever the shape of the interface. As previously noticed in the plane transition case, the largest reflection is induced by the DC1 algorithm.

The conclusion retained from these two purely acoustic test cases is that the DC2 algorithm turns out to be the most accurate one for propagating an acoustic perturbation from a fine mesh to a coarse one. The opposite transfer from a coarse to a fine mesh has also been investigated and provides similar conclusions on the algorithm quality.

6.4.2 Convected vortex

The vortex convection across grid interface of various shape is studied in this section. First, a plane interface is considered, then a 30-degrees inclined will be discussed.

6.4.2.a Vortex convection across a vertical refinement interface

The vortex initialization characteristics are given in Sec. 6.3.2. The simulation domain is displayed on Fig. 6.13. A vertical refinement interface is located at $x = 0$ m. The vortex is initialized in the fine grid and is convected from the fine to the coarse one. This first case with a plane interface allows getting rid of issues related to interpolation and anisotropic treatment of the interface.

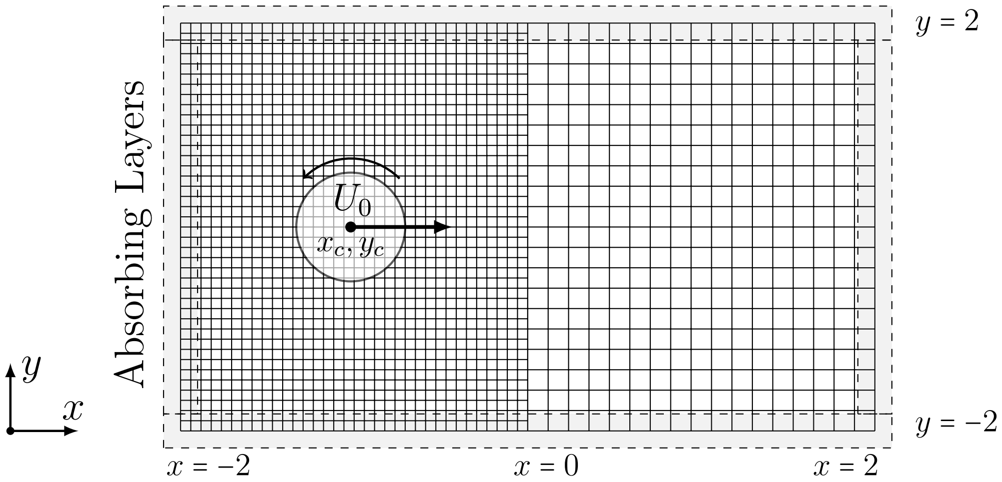

Figure 6.13 – *Sketch of the simulation domain for the vortex convected across a plane refinement interface. Absorbing layers map the domain boundaries to avoid reflection of spurious acoustic emission.*

The spurious noise emitted by the vortex is evidenced on Fig. 6.14 where the relative pressure fields are shown. A very strong attenuation of the parasitic noise is obtained with the two DC algorithms compared to the STD one. This is partly explained by the continuity of the vortex pressure and velocity, ensured by the DC algorithms in this case.

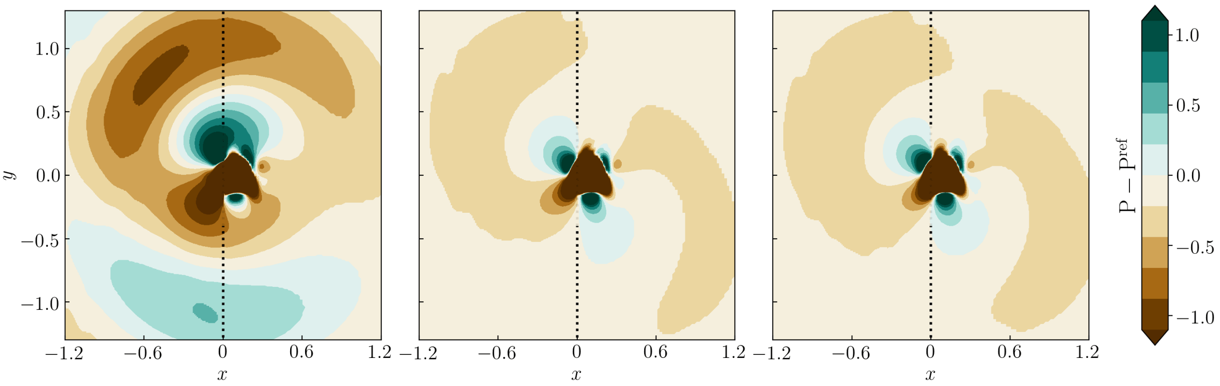

Figure 6.14 – *Relative pressure field* $(\mathrm{P}-\mathrm{P}^{\mathrm{ref}})$ *of the vortex convected across a plane refinement interface at* $t = 920 \cdot \Delta t^f$. *Left: STD, middle: DC1, right: DC2.* (·····)*: grid refinement interface.*

As previously, a more quantitative criteria can be considered in terms of the integrated spurious noise over the 36 the microphones located in the farfield region. As can be clearly identified on Fig. 6.15, a large reduction of the parasitic noise is obtained whatever the emitted direction with the DC algorithms. The averaged acoustic emission is then reduced for more than 10dB compared to the STD one. Both DC1 and DC2 formulations lead to very close emissions, even though the DC1 algorithm turns out to be slightly better on this case (0.9dB of average reduction).

However, as shown in App. B.1 focusing on the stability and accuracy of the interface, a strong dissipation of the vortex is induced by the DC1 algorithm, especially when the Mach number increases (*cf.* Fig. B.4). The dissipation is higher than for its DC2 counterpart, and even higher than for the STD algorithm when the Mach number is greater than 0.2.

The DC algorithms have proven to be very relevant for the case of the vortex advected across a vertical interface. In the following section, a similar vortex is convected across an oblique refinement interface.

6.4.2.b Vortex convected across an inclined refinement interface

The exactly same data setting as introduced in Sec. 6.3.2 is reproduced in this section. This case allows assessing the accuracy of the different grid refinement algorithms whatever the local shape of the transition (planar or stepped configuration). This time, spatial interpolations are expected to play a major role.

Spurious acoustics emitted by the vortex convection across this interface is displayed on Fig. 6.16 for the three grid refinement algorithms. This time, every algorithm qualita-

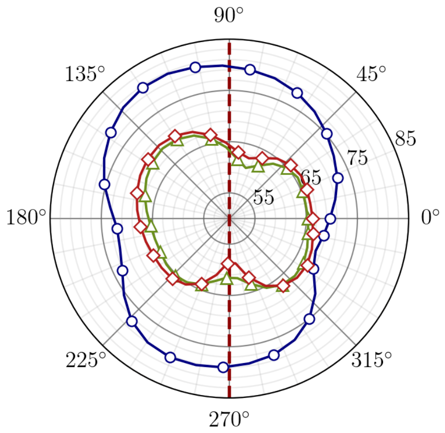

	STD	DC1	DC2
maximum OASPL(dB)	**80.7**	**68.9**	**69.8**
mean OASPL(dB)	**77.0**	**65.6**	**66.5**

Figure 6.15 – *Left: pressure OASPL of the spurious acoustics measured in the farfield for the vortex convected across a vertical refinement interface. -○-: STD, -△-: DC1, -◇-: DC2. Right: table of maximal and average OASPL over the 36 microphones.*

tively emits spurious acoustics in a similar intensity, and much larger than that obtained with a plane transition, even if better results are, again, obtained with the DC algorithms. In addition, there is a slight discontinuity of the vortex pressure field with the three algorithms, which may be responsible for this emission. This discontinuity can be attributed to the one-dimensional spatial interpolations used, resulting in an anisotropic treatment of non-coincident nodes.

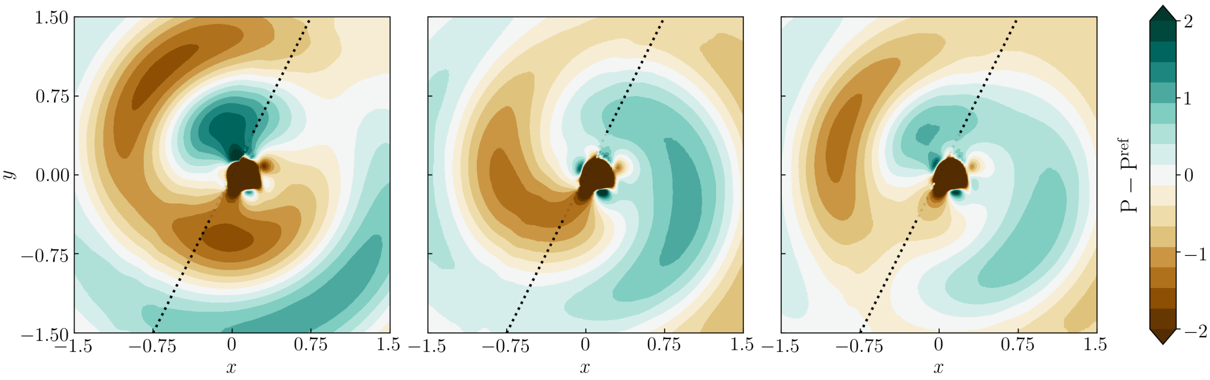

Figure 6.16 – *Relative pressure field* $(\mathrm{P}-\mathrm{P}^{\mathrm{ref}})$ *of the vortex convected across an inclined plane refinement interface at* $t = 1100 \cdot \Delta t^f$. *Left: STD, middle: DC1, right: DC2.* (·····)*: grid refinement interface.*

Quantitatively speaking, pressure OASPLs, displayed on Fig. 6.17, indicate that the emission of the three algorithms (STD, DC1, DC2) are, indeed, of the same order of magnitude. Averaged OASPLs are well above those obtained for a plane interface with an increase of 6, 15 and 13 dB respectively. Thus, the DC1 algorithm is the most degraded one by the use of oblique transitions. For this one, a very intense wave (up to 84.5dB) is observed in the coarse mesh, whereas the maximal acoustic amplitude produced in the fine mesh is 4dB less intense. This is all the more problematic as for aeroacoustic applications, microphones are generally located in the farfield region, *i.e.* in the direction of the coarse mesh. They would therefore be subject to a more intense spurious emission. This time, the DC2 algorithm is the most relevant one on this test case, although the benefit compared to the STD one is reduced on this inclined interface. Furthermore, the emission is better distributed between both grids with the DC2 algorithm.

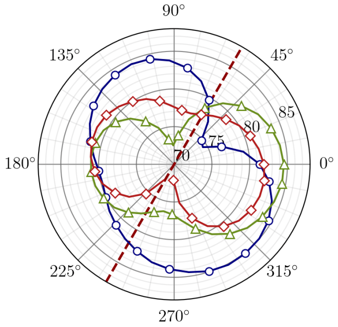

	STD	DC1	DC2
maximum OASPL(dB)	**85.1**	**84.5**	**82.1**
mean OASPL(dB)	**82.6**	**80.9**	**79.6**

Figure 6.17 – *Left: Pressure OASPL of the spurious acoustic measured in the farfield for the convected vortex test case that crosses an inclined plane refinement interface.* -○-*: STD,* -△-*: DC1,* -◇-*: DC2. Right: Table of maximum and average OASPL over the 36 microphones.* (- - -)*: grid refinement interface.*

From these academic test cases, the following conclusions can be drawn *whatever the shape of the interface.*

- The DC2 algorithm is the most relevant one to deal with pure acoustics.
- DC algorithms are much more accurate than the STD one to convect a vortex from a given mesh resolution to another. However, the benefits of these algorithms are strongly degraded by the quality of interpolations in the presence of arbitrary inclined transition. In that case, a slightly better behavior has been observed with the DC2 algorithm, especially when focusing on the acoustics propagated towards the coarse mesh. This is more critical for aeroacoustic applications, as microphones are generally positioned in that direction.

The last remark is of paramount importance: when using this type of interpolation, one should keep in mind that vortices convected across inclined interfaces are likely to generate more spurious noise. This specificity must be taken into account in the mesh design for aeroacoustic applications with complex geometries. For example, arbitrary layers of cells can be used close to the walls and plane grid interfaces should be preferred in the wake region, where many intense vortices are expected.

In the next section, algorithm comparisons will be performed on a turbulent case of a cylinder at high Reynolds number, under typical conditions of an industrial aeroacoustic application.

6.5 Numerical validation and comparison with an existing grid refinement algorithm on a turbulent test case

The purpose of this section is to evaluate the accuracy and stability of the grid refinement algorithms with arbitrary transitions in the presence of turbulent flows. A turbulent cylinder wake is chosen with a Reynolds number set in the super-critical flow regime [245, 246], that is representative of typical aeronautical applications. A comprehensive study of the flow physics will not be performed here, since it mainly depends on the parietal modeling, which is not the subject of this study. The aim is to simulate a low-viscosity turbulent flow across refinement interfaces minimizing the generation of spurious noise.

The ability of the H-RR$_\psi$ collision model to eliminate spurious vorticity, which is likely to appear at mesh transitions with other collision models, has been shown in a Sec. 4.5. Comparisons are therefore carried out with a flow that is free from spurious vorticity in the fluid core. Moreover, mesh refinement interfaces will be located far away from the cylinder so that their influence on the wake physics can be considered as weak.

Hence, the global noise emitted in this simulation is a superposition of the dipole noise emitted by the cylinder [247], and the spurious noise attributed to mesh transitions. Considering that the dipole noise sources are located near the cylinder wall, and the transitions are far from the latter boundary condition, it can be inferred that physical noise sources are identical whatever the transition algorithm used. Consequently, any additional noise is considered as spurious and will be quantified in this study as such.

In this section, the test case is firstly declined using box-shaped transitions to minimize interpolation errors. In a second step, mesh layers surrounding the cylinder are considered instead of the first cubic box resolution. This second case makes it more representative of industrial meshes where one would like to better capture the physics related to the boundary layers.

6.5.1 Simulation of the turbulent cylinder with box-shaped grid interfaces

A sketch of the simulation domain is shown on Fig. 6.18. Three resolution domains (RD) are placed around the cylinder, on which a wall law taking into account adverse pressure gradients and curvature effects is applied [66,78]. These boxes are placed in such a way that the mesh in the wake is fine enough to ensure the development of turbulent structures before crossing the interfaces. 36 Probes are placed on a 1.5m-radius circle centered around the cylinder to record acoustic directivity.

The simulation parameters are

$$\mathrm{M}_\infty = 0.1, \quad \rho_\infty = 1.17621\ kg.m^{-3}, \quad \Delta \mathrm{x}^{\mathrm{f}} = 0.001m,$$
$$\mathrm{D} = 0.3m, \quad \nu = 1.49.10^{-5} m^2.s^{-1}, \quad \mathrm{T} = 0.5s,$$

where M_∞ is the free stream Mach number imposed at the inlet, D is the diameter of the cylinder, ν is the kinematic viscosity and T the overall simulation time.

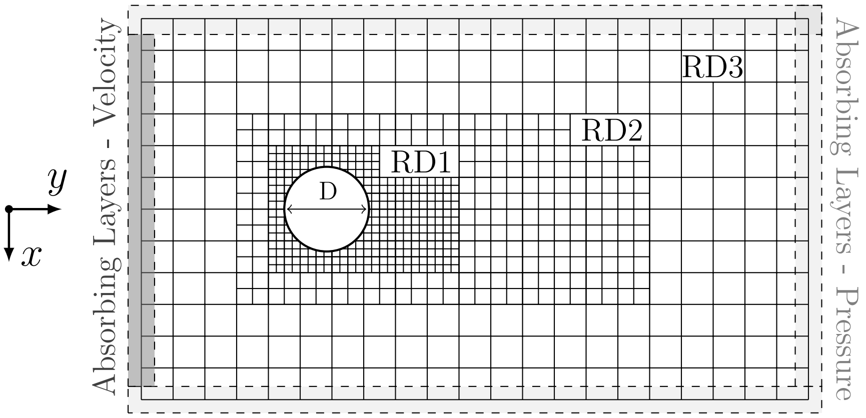

Figure 6.18 – *Sketch of the simulation domain for the cylinder test case. Three refinement domains (RD) are used. Absorbing layers map the domain boundaries to avoid any acoustic reflection.*

A Dirichlet velocity boundary condition is imposed at the inlet and a Dirichlet density boundary condition at the outlets. Both conditions are implemented using a full reconstruction of distribution functions estimated with finite differences as in [80–82]. A thickness of 1.6D is chosen in the third dimension (z axis) in order to allow the three-dimensional turbulence to be fully developed. Furthermore, absorbing layers [79] map the domain boundaries to avoid acoustic reflections and reduce the spurious noise that may be caused by the impact of the turbulent wake on the outlet Dirichlet condition.

Velocity dilatation fields are displayed on Fig. 6.19, where colormaps are tightened to highlight acoustic wave fronts. A huge decrease in the spurious noise can be observed with the DC algorithms, as expected from the results obtained with the convected vortex of Sec. 6.4.2. Both sources, from RD1 and RD2, are highly attenuated. Finally, it can be noted that no harmful numerical artifacts or parasitic vorticity can be observed at the transitions despite this very tight colormap, whatever the algorithm. This is explained by the use of the H-RR$_\psi$ algorithm which damps non-hydrodynamic modes that generate spurious noise sources at the refinement interface [87].

Pressure OASPLs are displayed on Fig. 6.20. A significant reduction of the spurious noise, of about 20dB, is obtained between the STD and the DC algorithms, whatever the directivity. The DC2 algorithm is the one generating fewest parasitic acoustics (on average 2.2dB less than the DC1 algorithm). These results were not expected with regards to

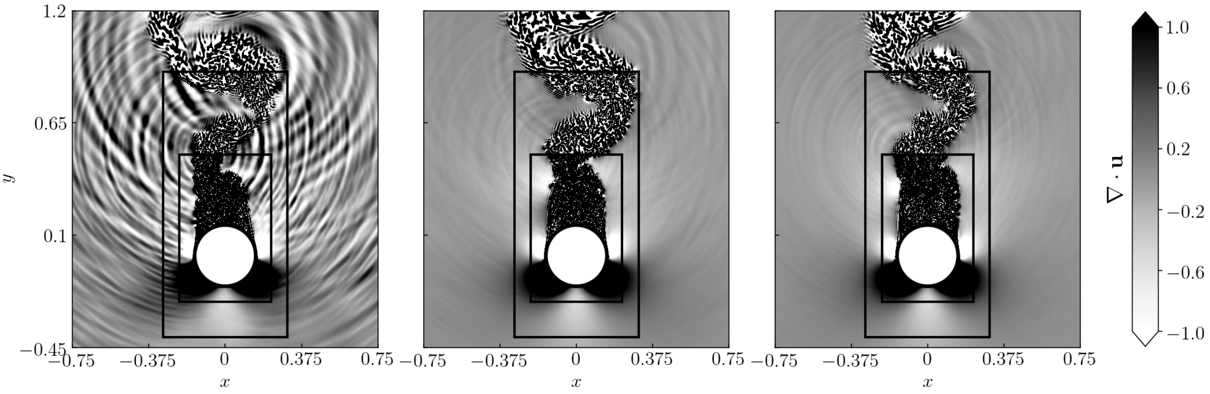

Figure 6.19 – *Velocity dilatation field* $(\nabla \cdot \mathbf{u})$ *of the turbulent flow around a cylinder with box-shaped grid interfaces. Left: STD, middle: DC1, right: DC2.*

the test case of the convected vortex crossing a plane interface, where the DC1 algorithm seemed to emit less parasitic acoustics than the DC2 algorithm (0.9 dB less in that case).

However, all the simulations performed on turbulent test cases led to the same conclusions: the DC2 algorithm is more accurate in the handling of turbulent flows. This may be explained by the fact that using coarse distribution functions in the reconstruction of g_i acts as a partial filtering step. Fine distribution functions have indeed a richer spectral content thanks to the ability of the fine mesh to resolve smaller structures. If this spectral content is directly transferred to the coarse mesh, an aliasing effect may occur, since high frequency waves of the fine mesh does not have any counterpart in the coarse one. Ideally, all fine functions used during the fine to coarse transfer should be filtered [59, 83]. However, common isotropic filter cannot be used on transition nodes of non-overlapping algorithms, for which some distributions are unknown on the coarse side. Hence, reconstructing distributions with as many coarse distributions as possible minimizes the aliasing phenomenon. This can explain the minimal noise recorded on OASPLs with the DC2 algorithm.

In the following section, additional simulations of the same flow configuration are carried out with a cylindrical RD1 resolution domain.

6.5.2 Simulation of the turbulent cylinder with mixed layers and box-shaped grid interfaces

Offset mesh layers are widely used in industrial simulations, as shown for example in recent LB studies [57, 74, 222]. They make it possible to refine the grid close to the walls, and thus to capture the physics of boundary layers that drive much of the flow physics on realistic geometries.

The adopted mesh is shown on Fig. 6.21, where a layer of 75 cells is considered in RD1. This very large distance between the first refinement interface and the solid wall allows better visualizing the flow and the numerical artifacts that might occur. This

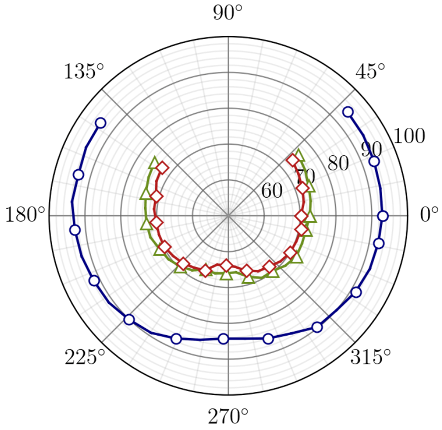

	STD	**DC1**	**DC2**
maximum OASPL(dB)	**94.1**	**75.8**	**73.7**
mean OASPL(dB)	**91.7**	**72.2**	**70.0**

Figure 6.20 – *Left: Pressure OASPL measured in the farfield of the turbulent cylinder with box-shaped grid interfaces. -○-: STD, -△-: DC1, -◇-: DC2. Right: table of maximal and average OASPL over the microphones.*

choice is not adopted for a physically optimized simulation, where generally layers of 6 to 7 cells are designed close to the walls.

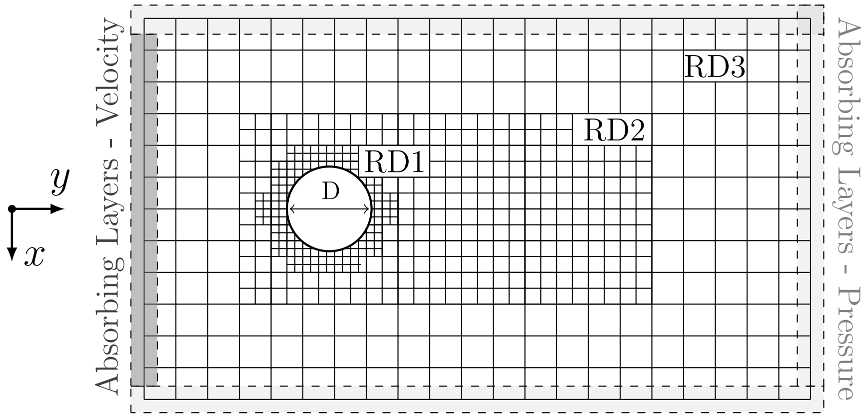

Figure 6.21 – *Sketch of the simulation domain for the cylinder test case. Three refinement domains (RD) are used, the first one being cylindrical. Absorbing layers map the domain boundaries to avoid reflection of spurious acoustic emission.*

Velocity divergence fields are shown on Fig. 6.19. Like in the previous section, a very strong reduction of the spurious noise is observed with the DC algorithms. No numerical artifacts, except parasitic acoustics, appear on the cylindrical transitions whatever the algorithm. The acoustic source generated by the RD1 one is less intense than that observed on Fig. 6.19. This may be attributed to the position of the interface that is closer to the cylinder. Turbulent structures that are convected across it are then smaller and less intense. These structures therefore produce less acoustic noise, even though the quality of the algorithm may be degraded by spatial interpolations as discussed in

Sec. 6.4.

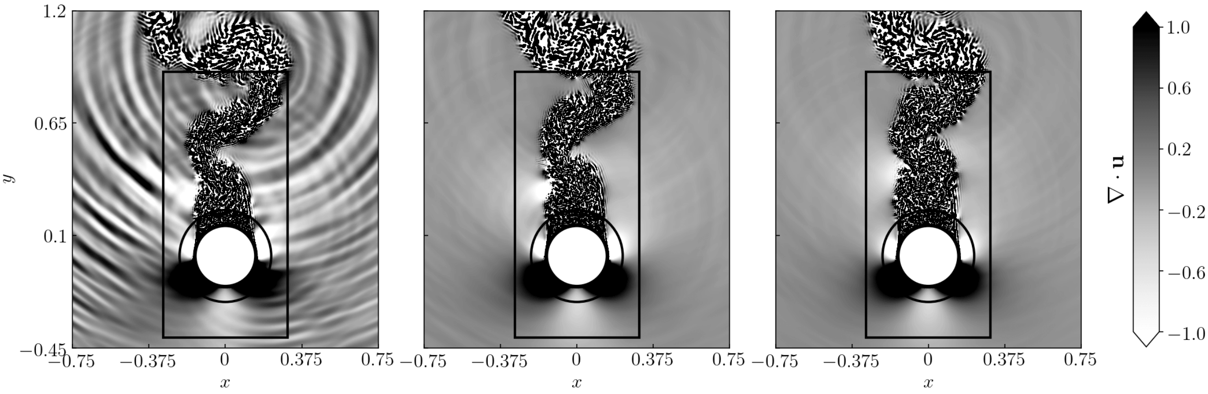

Figure 6.22 – *Velocity dilatation field* ($\nabla \cdot \mathbf{u}$) *of the turbulent cylinder with a mixed of layers and box-shaped grid interface. Left: STD, middle: DC1, right: DC2.*

Quantitatively speaking, it can be seen on the OASPLs (Fig. 6.23) that a significant decrease in spurious noise is again observed with the DC algorithms, with notably 21dB reduction between STD and DC2 algorithms. The simulation with the DC1 algorithm is the only one where the average noise has been increased by the use of cylindrical transitions. The difference with the DC2 algorithm is thus increased from 2.2dB to 2.6dB. This result was expected, since Sec. 6.4.2.b highlighted that the DC1 algorithm could emit significantly more noise to the far field than the DC2 one with a non-planar interface.

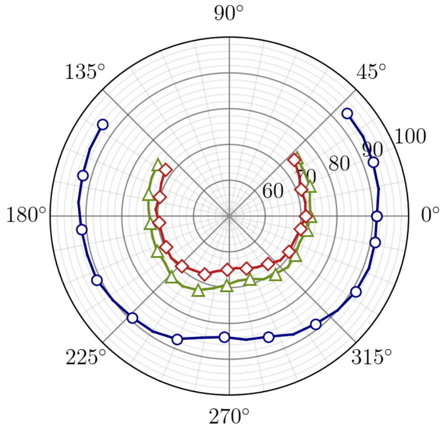

	STD	DC1	DC2
maximum OASPL(dB)	**93.7**	**75.0**	**73.9**
mean OASPL(dB)	**90.9**	**72.5**	**69.9**

Figure 6.23 – *Left: Pressure OASPL measured in the farfield of the turbulent cylinder with a combination of cylindrical and box-shaped grid interfaces.* -○-*: STD,* -△-*: DC1,* -◇-*: DC2. Right: Table of maximal and average OASPL over the microphones.*

These turbulent test cases allowed for validating the DC algorithms under realistic conditions, typical of industrial aeroacoustic applications. These algorithms do not present any stability issue and offer a very important gain in accuracy. A stability study is carried out in App. B.3 to corroborate these statements. They are key elements in addition to the H-RR$_\psi$ collision model (or any model filtering out non hydrodynamic modes) to perform aeroacoustic simulations that are not polluted by spurious noise. More specifically, the DC2 algorithm is more relevant for dealing with turbulent flows than the DC1. This might be attributed to the use of coarse distribution functions in the reconstruction, which reduces aliasing effects. Furthermore, since this formulation is more accurate when using transitions of any shape, as well as to transmit acoustic waves, the DC2 algorithm should be preferred for aeroacoustic simulations.

6.6 Conclusion

In this study, a new family of algorithms has been proposed to cope with the abrupt resolution transitions of lattice-Boltzmann non-uniform grids. Based on a direct grid coupling formulation, these types of algorithms distinguish from commonly used methods, where overlapped grid areas are generally considered. The proposed algorithms derived from the Lagrava's work [212] are based on the use of a unique and consistent equilibrium distribution function at the mesh interface, which complies with the conservation of mass and momentum through a local iterative procedure. This equilibrium function has been used to reconstruct the missing distribution functions at both coarse and fine mesh sides, as well as in the collision step. The way missing distributions are reconstructed is not unique since some of them are known in both meshes: one can either conserve fine, as it was originally done in [**?**] or coarse populations. This choice has a significant influence on the accuracy of the algorithm. In this study, two possible reconstructions have been addressed and compared. Validations and comparisons on academic cases have been carried out for arbitrary transitions. First of all, the DC2 algorithm proved to be the most accurate for a purely acoustic pulse crossing a mesh transition. Then, a vortex convected across a transition has been studied. For this case, the spurious noise generated by the DC1 algorithm was slightly lower than that generated by the DC2 algorithm for plane transitions. It was especially much lower than the STD algorithm, on which a discontinuity of the vortex is observed. However, the accuracy of the uni-directional interpolation schemes, commonly used in the literature, strongly alters the accuracy of the algorithm for arbitrary transitions and, in the end, the DC2 algorithm proves to be globally more accurate.

In view of the prohibitive cost of complex three-dimensional high-order interpolations, the choice of uni-directional interpolation schemes remains wise for cell-vertex algorithms. Meanwhile, we have studied the effect of the order of interpolation schemes on the accuracy of the grid coupling. A new method has been proposed (I-3), allowing to keep fourth-order interpolations everywhere in the fluid core. This improvement allowed, in addition to the DC algorithms, to greatly improve the accuracy of the refinement interfaces in LaBS/ProLB. However, meshes must be designed carefully, especially when well-developed wakes cross refinement interfaces: the use of plane transitions away from solid boundaries remains to be preferred.

Globally, it is shown that DC algorithms remain stable for high Reynolds number flows and greatly improve the accuracy of the grid interface. Moreover, the DC2 algorithm turns out to be the most accurate one for the realistic case of a turbulent cylinder wake flow. These last results may be due to reduced aliasing effects, which are all the more important as turbulent structures are under-resolved. Moreover, it has been evidenced in App. B.3 that the accuracy of the DC1 algorithm strongly deteriorates when the Mach number increases.

Furthermore, results obtained with the H-RR$_\psi$ model on the vortex convection as well as on the cylinder wake flow, confirm the generic nature of our first study in Chap. 4, in which the STD algorithm was used. No harmful contribution of non-hydrodynamic modes at mesh transitions is noticeable with the DC algorithms. On the vortex case, neither spurious vorticity, nor any striations on the pressure field are indeed visible in the vicinity of the vortex. On the turbulent cylinder case, no high-frequency waves are observed.

Finally, the marginal cost of the grid coupling algorithm ($< 1\%$ of the total computational cost on all the test cases performed), makes the use of the DC algorithms quite acceptable for an industrial use. A combination of the H-RR$_\psi$ collision model, and the DC2 algorithm seems to be a suitable choice for industrial aeroacoustic studies. The combination of these models will be assessed on industrial aeronautical applications in the next chapters.

Chapter 7

Aeroacoustic study of the LAGOON 1 landing gear

Contents

This chapter is devoted to the study of the LAGOON 1 landing gear. Following a bibliographic review of previous studies, and an introduction to the CFD/CAA coupling methods, it is chosen to compare both solid and permeable FW-H formulations. Three grids of increasing resolution are investigated. First, steady and unsteady aerodynamic results are presented with the aim of validating the ability of LaBS/ProLB to capture such flow and to locate noise sources. Then, the contributions of the H-RR$_\psi$ *model, as well as of the DC grid coupling algorithm are quantitatively assessed for aeroacoustics. The limitations of the solid FW-H formulation are discussed for the prediction of landing gear noise. Finally, far-field results are provided with narrow band PSDs and directivity curves.*

7.1 Introduction

The LAGOON project (for **LA**nding **G**ear n**O**ise database for CAA validati**ON**) is a project supported by Airbus [248, 249], which involves ONERA, DLR and Southampton University. The objective is to provide a reliable and highly instrumented experimental database for the validation of coupled CFD/CAA methods on landing gears of increasing complexity. To this end, three configurations have been studied in dedicated experimental campaigns, taking into account components that are getting increasingly close to a realistic landing gear.

The three mock-ups are shown on Fig. 7.1. These mock-ups share a common basis, the LAGOON 1, then extra components are added.

- LAGOON 1: The simplest configuration used as a baseline. It is composed of a lower leg, an upper leg and an axle that connects two wheels.
- LAGOON 2: The lights, the steering actuator and the tow bar are added to the baseline.
- LAGOON 3: The torque link is included. Inner and outer rim periphery caps are removed.

These mock-ups correspond approximately to a 1:2.5 scaled nose landing gear of an Airbus A320 aircraft. The wheel diameter is D = 0.3m resulting in a Reynolds number based on this last of 1.564×10^6. In these conditions, the flow is expected to be completely turbulent, at least on wheels. The test campaigns, as well as the various numerical simulations carried out on these configurations are summarized in the following sections.

7.1.1 Overview of LAGOON experimental campaigns

The LAGOON project was divided into two experimental campaigns. The first one [248], was conducted in 2008 in the closed wind tunnel F2 from ONERA (*cf.* Fig. 7.2).

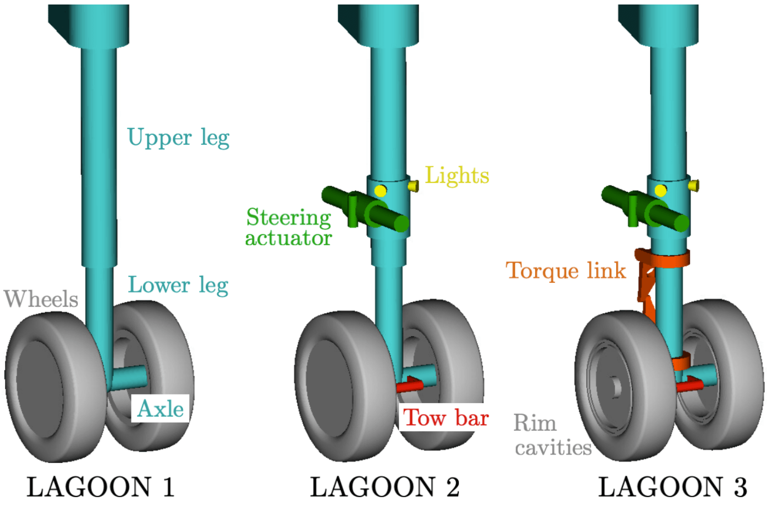

Figure 7.1 – *The three* LAGOON *mock-ups.*

The aim of this campaign was to study the stationary and unsteady flow generated by a landing gear. For this purpose, several measurements were recorded with a dedicated instrumentation including:

- For the mean quantities: 2D PIV planes (Particle Image Velocimetry [250]), LDV (Laser Doppler Velocimetry [251]), and static pressure taps at several strategic locations of the LG.
- For the unsteady quantities: LDV, hot-wire [252], and unsteady pressure sensors (kulites) for wall pressure measurements.

Specifically, kulites will be very useful to study turbulent separation on wheels. The second campaign [249] was carried out one year later by the same research laboratory in the anechoic open jet CEPRA19 wind tunnel (*cf.* Fig. 7.2), allowing acoustic measurements. The acoustic recordings were realized by means of two arcs containing 12 microphones: a flyover arc located in the symmetry plane of the LG and a sideline arc with an angle of 56° as shown on Fig. 7.21. These microphones are located at a distance of six meters from the model center. In this second campaign, aerodynamic measurements have also been carried out in order to compare the results with those obtained in the F2 wind tunnel [249].

In these experiments, the three mock-ups of increasing complexity were considered for different Reynolds numbers and LG positions. The only condition that will be studied is the one simulated by many actors of the CFD community and which corresponds to a Mach number of 0.23 and a Reynolds number based on the wheel diameter of 1.564×10^6. Experimental results will be described progressively as CFD results will be introduced.

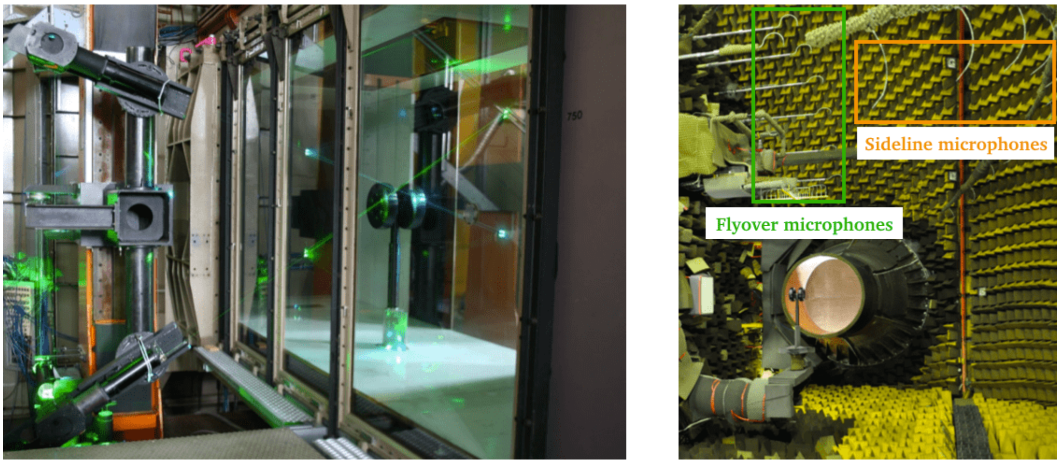

Figure 7.2 – LAGOON *experiments performed at:* F2 *closed-section wind tunnel (left),* CEPRA19 *open-jet wind tunnel (right). Courtesy of ONERA.*

7.1.2 CFD/CAA coupling strategies

In the CEPRA19 wind tunnel (*cf.* Fig. 7.21), as in many others, the microphones can be located at a large distance from the landing gear. This is equally common in flight tests where microphones can be placed on the ground (*cf.* Fig. 1.5). With CFD methods, propagating the acoustics without deteriorating it over such a distance is often very expensive, even unrealistic because of the dissipation and dispersion induced by the numerical schemes (*cf.* Chap. 5). On the other hand, there are integral methods allowing to propagate acoustics over large distances at low cost. In the following, the Lighthill analogy will be briefly introduced, as well as the Ffowcs-Williams and Hawkings (FW-H) one, allowing among other things to extend the Lighthill analogy to the consideration of solid surfaces. The CFD/CAA coupling between the FW-H method and a CFD solver is widely used for the prediction of landing gear noise [75]. For a detailed description of the acoustic analogies that are used in this thesis, the interested reader can refer to the PhD thesis of Gloerfelt [253].

7.1.2.a The Lighthill analogy

The theory of aerodynamic noise proposed by Lighthill in 1951 [254, 255] consists in establishing an analogy between a problem governed by the general fluid mechanics equations and the classical theory of acoustics. By rearranging the fluid mechanics governing equations in the form of an inhomogeneous wave equation where the terms on the right hand side represent the noise sources, of a quadrupole nature:

$$\frac{\partial^2 \rho}{\partial t^2} - c_0^2 \Delta \rho = \frac{T_{ij}}{\partial x_i \partial x_j}. \qquad (7.1.1)$$

This nonlinear source term is known as the Lighthill tensor T_{ij} and is defined as

$$T_{ij} = \rho u_i u_j + \left(p - c_0^2 \rho\right) \delta_{ij} - \tau_{ij}, \tag{7.1.2}$$

with c_0 the speed of sound of the undisturbed medium surrounding the source region and δ_{ij} the Kronecker operator. This term includes the fluctuations of the Reynolds stresses $\rho u_i u_j$ due to the vorticity which generally prevails, the viscous stresses τ_{ij}, and an entropy term $(p - c_0^2 \rho)$ which is small if there are no strong density inhomogeneities in the source region.

This equation is exact since it is a combination of the fluid mechanics equations without any assumptions. Eq. (7.1.1), governing the density fluctuations in a real fluid, can be compared to that ruling a uniform acoustic medium at rest. Actually, in such a medium of density ρ_∞, the Lighthill tensor is null and the density fluctuations $\rho_a = \rho - \rho_\infty$ satisfy a homogeneous wave equation:

$$\frac{\partial^2 \rho_a}{\partial t^2} - c_0^2 \Delta \rho_a = 0. \tag{7.1.3}$$

This equation may also be expressed in terms of pressure by considering $p_a = c_0^2 \rho_a$. The Lighthill's equation does not have an analytical solution because it involves one equation for five unknown variables. The brilliant idea is to consider two distinct media: a uniform and resting **observer medium** dominated by a linear propagation phenomenon, and a well localized **source region**, where the flow generates the sound in a complex and non linear way. Therefore, Lighthill considers that the density fluctuations are independent in each medium if the source region is correctly defined. The term on the left hand side contains the acoustic fluctuations ρ_a and the one on the right hand side includes both acoustic and hydrodynamic fluctuations.

It should be noticed that this independence assumption implies that the fluctuations of ρ_a do not disturb the density fluctuations of the source medium, i.e. there is no acoustic feedback phenomenon from the observer zone on the source zone. This situation can occur in the case of reflections from a surface. In this case, the source domain must be enlarged to include all the interaction phenomena. Concerning the right hand side, it introduces a second-order spatial derivative which represents a distribution of quadrupoles in the classical theory of acoustics.

The resolution of this equation is achieved by means of the Green's function formalism which allows the solution of an inhomogeneous wave equation to be expressed as an integral equation involving a volume integral over the source volume. Several formalisms of Green's functions can be used (spatial, temporal, spectral), as well as different points of view can be adopted, either with respect to the observer or to the source. All these alternatives are detailed in the PhD thesis of Gloerfelt [253]. For example, the space derivative expression with respect to the observer of the Lighthill equation for the sound pressure p'_a at an observation point $\boldsymbol{x}$ and at time t reads (see Fig. 7.3 for the notations):

$$4\pi p'_a(\boldsymbol{x}, t) = \int_{V_s} \frac{1}{r} \frac{\partial^2 T_{ij}}{\partial x_i x_j} \left(\boldsymbol{y}, t - \frac{r}{c_0}\right) d\boldsymbol{y}. \tag{7.1.4}$$

The pressure is thus the sum of the contributions emitted by the source volume V_s but radiated at different times since the propagation distance r depends on each source point. This is troublesome from a numerical implementation standpoint and is commonly referred to as the *retarded time* method. Moreover, the use of the Lighthill analogy requires the knowledge of the set of second derivatives of T_{ij} in the volume V_s. The latter can be obtained analytically, experimentally [256], or numerically via a CFD computation [257, 258]. The temporal storage of a whole volume remains nevertheless challenging to achieve.

Besides the practical aspect, the Lighthill analogy has other limitations. Specifically, the observer's medium is considered at rest and this formulation does not take into account solid boundaries, which is obviously not suitable for landing gear simulation. The first constraint can be overcome by taking into account a mean field [254, 259]. The second can be achieved with the Curle formulation [260], based on the Kirchhoff's formula (1883) taking into account the noise generated by solid surfaces. This formulation is convenient to use, but only considers dipole sources, so it is not appropriate for many applications such as jet noise and probably landing gear noise (*cf.* Sec. 7.4.2). The Ffowcs-Williams and Hawkings formulation [261] generalizes the Ligthill equation to the case of a flow involving any moving surface, it will be used in this thesis and presented subsequently.

7.1.2.b The Ffowcs-Williams and Hawkings analogy (FW-H)

The Ffowcs-Williams and Hawkings acoustic analogy [261] enables the consideration of both stationary and moving solid surfaces. In this analogy, one considers a surface Σ partly included in the source region as shown in Fig. 7.3.

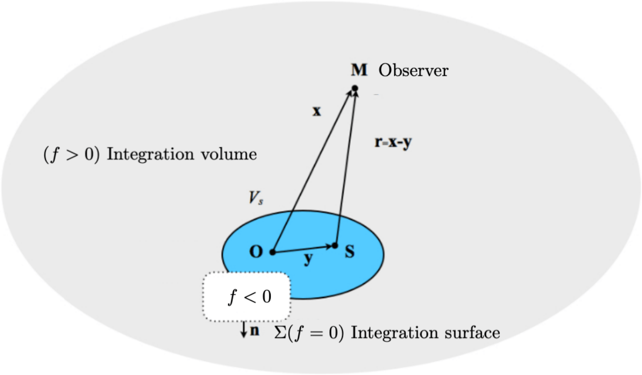

Figure 7.3 – *Space representation according to the analogy of Ffowcs-Williams and Hawkings [261] extracted from [253]: The source region of volume V_s is coloured in blue, the propagation region in which the observer M is located corresponds to the shaded area, the surface Σ of normal $\boldsymbol{n}$, defined by the function $f = 0$, is partially included in the source region.*

The Σ surface moves at the velocity $\boldsymbol{u}^{\Sigma}$. Its position is indicated by the function

$f(\boldsymbol{x},t)$ which is null for the points belonging to the surface Σ, negative for those inside and positive for those outside. The Heaviside function $H(f)$ is also introduced as

$$\begin{cases} H(f) &= 0 \quad \text{if} \quad f < 0, \\ H(f) &= 1 \quad \text{if} \quad f \geq 0. \end{cases} \tag{7.1.5}$$

The normalized normal $\boldsymbol{n}$ of the surface is directed outward. Multiplying the conservation of mass and momentum equations by $H(f)$ and combining them gives the Ffowcs-Williams and Hawkings equation

$$\left\{\frac{\partial^2}{\partial t^2} - c_0^2 \Delta\right\} \left[\rho_a H(f)\right] = \frac{\partial^2}{\partial x_i \partial x_j} \left[T_{ij} H(f)\right] - \frac{\partial}{\partial x_i} \left[L_i \delta(f)\right] + \frac{\partial}{\partial t} \left[Q \delta(f)\right], \tag{7.1.6}$$

with T_{ij} previously defined in Eq. (7.1.2) and

$$L_i = \left[\rho u_i \left(u_j - u_j^\Sigma\right) + P_{ij}\right] n_j, \tag{7.1.7}$$

$$Q = \left[\rho \left(u_j - u_j^\Sigma\right) + \rho_\infty u_j^\Sigma\right] n_j, \tag{7.1.8}$$

where $P_{ij} = (p - p_\infty)\,\delta_{ij} - \tau_{ij}$. An inhomogeneous wave equation for the fluctuations ρ_a is thus derived. It can be noticed that in the absence of surface Σ, the Lighthill equation is recovered. The presence of Σ induces two additional terms: a dipole term L_i and a monopole one Q. It should also be noted that if the Ffowcs-Williams and Hawkings analogy makes surface sources appear, this remains a purely mathematical consequence of the analogy. Indeed, the acoustic sources are physically located in the fluid, and the dipole acoustic sources at the solid surface represent mathematically the phenomenon of diffraction of volume sources by the solid surface.

In the same way as above for the Lighthill equation, one can use the Green's function formalism to find a solution of Eq. (7.1.6). For example, the expression in spatial derivative with respect to the observer of the FW-H equation [253] reads:

$$\begin{aligned} 4\pi H(f) p'(\boldsymbol{x},t) = &\frac{\partial^2}{\partial x_i \partial x_j} \int_{f>0} \frac{1}{r\left|1 - M_r^\Sigma\right|} T_{ij}\left(\boldsymbol{y}, t - \frac{r}{c_0}\right) d\boldsymbol{y} \\ &+ \frac{\partial}{\partial x_i} \int_{f=0} \frac{1}{r\left|1 - M_r^\Sigma\right|} L_i\left(\boldsymbol{y}, t - \frac{r}{c_0}\right) d\Sigma \\ &+ \frac{\partial}{\partial t} \int_{f=0} \frac{1}{r\left|1 - M_r^\Sigma\right|} Q_i\left(\boldsymbol{y}, t - \frac{r}{c_0}\right) d\Sigma, \end{aligned} \tag{7.1.9}$$

with M_r the Mach number relative to the surface normal defined by $M_r^\Sigma = (r_i u_i^\Sigma)/(r c_0)$. The $|1 - M_r^\Sigma|$ term accounts for the *Doppler effect*.

One can notice in Eq. (7.1.9) that the quadrupole term cancels if all acoustic sources are contained in the Σ surface. In this particular case, it is referred to as a wave extrapolation method based on the FW-H equation [253], or **permeable FW-H formulation** [262, 263]. The effect of the quadrupole sources is transferred to the surface sources of the vibrating surface. This technique is very convenient to operate when coupling the FW-H analogy with a CFD solver, since it requires only the data recording on a surface.

The particular case of an impermeable, non-vibrating and immobile surface ($u_i n_i = u_i^\Sigma n_i = M_r^\Sigma = 0$) is also interesting to consider, since Eq. (7.1.9) reduces to the expression proposed by Curle [260]

$$4\pi H(f)p'(\boldsymbol{x},t) = \frac{\partial^2}{\partial x_i \partial x_j} \int_{f>0} T_{ij}\left(\boldsymbol{y}, t - \frac{r}{c_0}\right)\frac{d\boldsymbol{y}}{r} + \frac{\partial}{\partial x_i}\int_{f=0} P_{ij}\left(\boldsymbol{y}, t-\frac{r}{c_0}\right) n_j \frac{d\Sigma}{r}. \quad (7.1.10)$$

Lighthill [254] and Curle [260] show that the acoustic intensity I of quadrupole and dipole sources varies with respect to $I_\mathrm{Q} \propto Ma^8$ and $I_\mathrm{D} \propto Ma^6$ respectively. Thus, for low Mach numbers the volume integral in Eq. (7.1.10) might be neglected. This formulation will be referred to as **solid FW-H** in the following, and is mostly used for landing gear noise prediction [75].

For practical purposes, the spatial formulation expressed in terms of derivatives with respect to the observer is not convenient. Indeed, in a CFD code the data are collected at the source, it is therefore more appropriate to express the derivatives with respect to the source as proposed by Farassat [264, 265] and then Brentner [266]. This formulation is usually referred to as 1A. Finally, the different formulations presented above express the sound pressure at time t from the various contributions of the sources expressed at delayed times. However, these retarded times do not coincide with the data extraction times of a CFD computation and require a costly interpolation. To remedy this, Casalino has proposed an *advanced time* method that takes the source time as reference [267]. The latter is much more time efficient and allows for co-processing, thereby limiting disk storage. The 1A method with advanced times available in the KIM FW-H solver [268,269] developed by ONERA will be used in the following.

7.1.3 Literature review on LAGOON 1 numerical studies

The LAGOON 1 case has been of great interest to the scientific community and has been used as a benchmark for airframe noise computations in the NASA BANC-II and -III workshops. These workshops are dedicated to the evaluation of numerical methods for the simulation of unsteady flows and the noise generated by these latter. During these workshops, many CFD solvers were compared. A first summary of these different simulations can be found in the comparison paper of Manoha and Caruelle [75]. Nevertheless, others studies have been published since 2015 and will also been described in the following.

The main physical phenomena to be captured are:

- The cavity modes resulting from an interaction between wheel cavities, widely studied by Ribeiro, Casalino *et al.* [51, 52], Giret [9], De la Puente Cerezo [270].

- The laminar-to-turbulent transition on the wheels that can be assessed with the help of kulites.
- The turbulent wake estimated by means of PIVs.
- The recirculation regions downstream of the wheels characterized by the PIVs and LDVs planes.
- The location of the detachment points on the axle and leg, determined by kulites.

A wide variety of numerical methods have been applied onto the LAGOON 1 configuration, leading to a vast amount of publications. The following paragraphs intend to sort them out and identify their strengths, weaknesses, and findings

7.1.3.a Solvers using block-structured meshes

This meshing strategy makes it easier to increase the numerical scheme order, and to obtain better isotropic meshes. However, mesh generation is very tedious and not very adapted to complex geometries often leading to low quality meshes in the most important regions.

ZDES using elsA solver
The first aeroacoustic simulation was performed by Sanders *et al.* [43] using ZDES mode 1 [41] modeling (for Zonal Detached Eddy Simulation). This type of method requires hand-setting the RANS and LES zones, and therefore requires prior knowledge of the flow. As described in the article, the generation of such a mesh with conformal blocks was very challenging and the same authors used a Chimera technique, which consists in coupling non-coincident blocks for the LAGOON 2 simulation [45]. The results obtained are good for stationary aerodynamics, and globally good for unsteady ones. However, the cut-off frequency operates as early as 2kHz for kulites and even earlier for probes placed in the wake. The aeroacoustic results are very satisfactory coupled with a solid FW-H method. The use of a permeable FW-H formulation however overestimates the noise levels, especially for downstream microphones. This problem is investigated in another paper [44] with a lower free stream Mach number. The reflection of acoustic waves on the ceiling, which is not present in the wind tunnel, is an advanced explanation, in addition to over-estimation caused by downstream hydrodynamic perturbations.

DES using high-order SotonCAA solver
Liu *et al.* [46, 47] have carried out simulations with the SotonCAA code using high-order schemes with rather coarse grids (3M and 15M cells). They use a compact fourth-order finite difference scheme [271] for the spatial discretization. The y^+ being in some areas above 1, they sometimes used a wall model [272]. Their aerodynamic results are correct but quite large deviations appear on the PIV sections in the wake [75]. Relatively few kulites are shown and they exhibit a cut-off frequency around 2kHz. Concerning the aeroacoustic results with a solid FW-H formulation, these are consistent in the 700Hz to

2kHz range upstream, but significant under-predictions are noticed downstream. They were the first to indicate the influence on the far field of the various LG components (although the accuracy of this practice is controversial [273]). They highlighted that most of the noise came from the wheels, then from the leg. In their papers, they also made an iso-grid comparison on their coarse grid with the FLUENT solver and highlight a much lower dissipation using high-order schemes.

7.1.3.b Solvers using unstructured meshes

This meshing method makes it easier to take into account complex geometries.

ZDES using CEDRE solver
ZDES simulations were performed with the CEDRE solver by De la Puente Cerezo *et al.* [48] using a low-order scheme (first-order in time and a second-order Roe type in space). Their mesh consists of 61 millions elements with prism layers at the wall. Another study was published three years later by the same authors [49, 270] with an improved mesh, numerical scheme and turbulence modeling. The recent results obtained are good on both stationary and unsteady aerodynamics, as well as on far-field acoustics. However, some discrepancies appear for microphones positioned at the extremities. This point will be discussed in Sec. 7.4.2. They also compared the solid and permeable FW-H formulation and concluded (unfortunately only with the 2014's setup), as Sanders [44] that the solid formulation is more accurate for this kind of flow. However, turbulent structures cross their permeable surface located very close to the LG, resulting in a significant overestimations of the far-field acoustics, especially for flyover microphones.

Under-resolved LES with the AVBP solver
A sub-resolved LES with the AVBP solver using a TTG4A scheme [274] of fourth-order in time and third-order in space has been realized by Giret *et al.* [9, 32]. The average y^+ used in the most refined simulation is about 30 for CPU cost reasons, which is well above the recommendations of $y^+ = 1$ for solving a boundary layer without wall-modeling [22]. The results obtained are globally satisfactory concerning the aerodynamics, with however a separation occurring too early on the wheels. The aeroacoustic results are very convincing. In addition, an extensive study of cavity modes using Dynamic Mode Decomposition (DMD) [275, 276] and a Helmholtz solver [277] has been performed and is available in [9]. A comparison with a logarithmic wall law (WL), theoretically better suited for this range of y^+ has been conducted. The WL gives better results in the wake but generates a very strong overestimation of the far-field noise originating from the leg. This led to Zhang's thesis for solving these issues and for employing more advanced wall-laws, whose efficiency has been shown on LAGOON 1 by Sengissen et al. [36].

Wall-modeled LES (WMLES) with the AVBP solver
Zhang, in his PhD thesis [21] has pursued the work of Giret [9] with the AVBP solver, but this time focusing on a wall-law modeling, theoretically more appropriate to the y^+ ranges encountered by Giret. For these simulations, the same mesh is used, called LA-

GOON1_FINE in [32]. A comparison is made between a Dirichlet condition, a classical logarithmic wall-law, the Afzal law [78] taking into account an adverse pressure gradient, and the Afzal law with a turbulence transition sensor [278] developed by the same author. This sensor allows, depending on the turbulent viscosity, to compute the wall shear stress with its laminar definition, or the one provided by Afzal's law in turbulent regions. The results obtained on the LAGOON 1 are globally satisfactory concerning the aerodynamics. However a transition to turbulence occurs very early, as soon as the K1 kulite positioned on the upstream part of the wheel perimeter for simulations involving a wall-law. Results in the far field are satisfactory, and comparable to those obtained by Giret, with a cut-off frequency that is pushed back towards high-frequencies.

Wall-modeled LES with the weakly compressible OpenFOAM solver

Hou *et al.* [34] carried out simulations comparing an incompressible solver with a weakly compressible formulation in the OpenFOAM opensource solver. This strategy significantly reduces the computational cost compared to a fully compressible solver. A rather coarse mesh was used (22M cells) with a mean $y^+ = 100$ on wheels, hence the use of the Afzal wall law [78] has been chosen to realize this WMLES. Results obtained with the incompressible solver are satisfactory only for the mean aerodynamic and RMS quantities. However the cavity resonances are not detected and the broadband noise is strongly under-predicted. Conversely, the weakly compressible solver seems to correctly predict steady and unsteady aerodynamics (but few kulites are shown). Acoustic results are also satisfying but with a relatively high over-prediction obtained in the 800-3kHz range for microphone 3, placed upstream, and a significant underestimation downstream.

7.1.3.c LBM solvers based on Cartesian octree grids

This meshing strategy, coupled with specific boundary conditions (immersed boundaries, cut-cell approach, ...) allows a quasi-automatic meshing of very complex geometry.

V-LES with the PowerFLOW solver

The first LBM study on LAGOON was performed by Ribeiro, Casalino *et al.* [51, 52] with the commercial PowerFLOW solver. A Cartesian octree mesh is used with a D3Q19 lattice. A turbulence modeling called "V-LES" for very-large eddy simulation is used, by adjusting the LBM relaxation time $\bar{\tau}$ by a value corresponding to a turbulent viscosity [64] based on a variant of the RNG $k-\epsilon$ model [279]. It is conceptually similar to the DES family of turbulence models, for which the small structures attached to the wall are modeled in RANS, whereas the larger ones in separated regions and wakes are resolved [38]. A wall law is also applied, taking into account adverse pressure gradient and roughness effects. The results obtained are good for both aerodynamics and far-field acoustics. However, discrepancies with the experiments appear for the microphones placed at the extremities. These deviations will be discussed in Sec. 7.4.2. Additionally, an interesting study of cavity modes has been carried out. This last reveals a pressure node in the LG symmetry plane, preventing the emergence of tonal peaks for the flyover microphones.

Wall-Modeled LES with the LaBS/ProLB solver

Two years later, Sengissen *et al.* also achieved this study with the LaBS/ProLB solver [36]. The version used included the filtered DRT collision model presented in Sec. 4.7, a SISM turbulence model [77], and the mesh refinement algorithm noted STD in Chap. 6. In this article, a comparison is made with the LES of Giret *et al.* [32]. The aerodynamic results are very satisfactory, especially the PIV fields and the LDV slices which are comparable to the AVBP results with a strongly reduced cost. Kulites on the wheels exhibit a correct boundary layer transition. The effect of the turbulence model and parietal modeling are also investigated. In addition, preliminary results on the LAGOON 2 and LAGOON 3 configurations are provided, showing the influence of the tow bar and wheel outer flank. However, far-field acoustic results are not available. Obviously, in view of the spurious acoustics shown in introduction in Sec. 1.4.2, the far field acoustic results could not be satisfactory in 2015, hence the initiation of this thesis.

7.1.3.d Discussions about numerical studies

As shown during previous subsection, many numerical methods, sometimes very different, were compared on this test case coupled with a FW-H solver. From an industrial point of view, three criteria are driving the downselection of the most promising method for such simulation [36] in a very pragmatic manner :

1. High accuracy in simulating noise generating and propagating mechanisms up to the far-field.
2. Ability to handle seamlessly very complex geometries of realistic configurations.
3. Turnover time of the whole simulation chain in terms of human and CPU time.

The first criterium is broadly met by most studies. Even codes using second-order schemes (OpenFOAM, CEDRE, elsA, CFL3D) may fairly well predict acoustics. Generally, the lack of the mesh resolution may be considered to be the source of discrepancies, and can be overcome by increasing such resolution.

The second point, however, prevents block-structured codes, even using chimera techniques, from being used in an industrial framework for LG simulations. Unstructured solvers make it much easier to take into account complex geometries. Yet the meshing process remains tedious or sometimes even impossible for industrial configurations. Conversely, the LBM, based on a Cartesian octree grid, allow to mesh very easily complex geometries by embedding quasi-automatic meshers directly within industrial solvers. This technology is not restricted to LBM solvers, but only a handful of Navier-Stokes based solvers include an octree Cartesian discretization such as the NASA LAVA code [56].

The third point is broken down into a pre-processing stage, whose time spent depends mainly on the mesh generation mentioned earlier, and the computation phase itself.

The computing time is strongly dependent on several numerical ingredients, one can mention:

- The numerical scheme: The amount of operations involved in the numerical scheme will strongly influence efficiency. High-order schemes are more expensive but more accurate, they allow in principle to reduce the mesh density needed for reaching an equivalent accuracy. On this topic, the LBM scheme seems to be the fastest by roughly one order of magnitude if one compares the CPU/element/iteration of the Tab. 2 in [75]. This is notably due to the adaptive temporality inherent to LBM schemes, allowing to compute the coarse meshes every $2^{N_{\mathrm{RD}}}$ timesteps with N_{RD} the index of the resolution domain. LaBS and PowerFLOW each use 10 levels of refinements. Note that this data structure is not restricted to LBM [56,280].

- The turbulence model: Turbulence handling takes a significant part in the computation time. Firstly, turbulence models have a significant cost as they may require additional equations to be solved, as is the case with DES models. Explicit LES turbulence models using sub-grid scale viscosity are less expensive. However, DES mesh constraints are much more flexible in the RANS zones and allow very high stretching rates in directions transverse to the current lines [22]. Thus, for this type of application, in case of resolved boundary layer, a DES is cheaper due to mesh constraints.

- Parietal modeling: The use of wall-law makes it possible to strongly increase the first near-wall cell sizes and therefore to reduce the number of mesh elements. Moreover, for solvers with explicit temporal resolution such as AVBP, or LBM solvers, increasing the size of the smallest element has a direct impact on the time step and thus on the computational cost. This is less straightforward for solvers with implicit time schemes (OpenFOAM, CEDRE, elsA, CFL3D), as they do not need to set their time step in relation to the smallest cell size of the domain. The latter is fixed on the physics of interest, which can increase performance [281,282].

In view of all these criteria it is very difficult to compare these methods on pure CPU performance, because the different numerical ingredients have a cost which is to be highlighted with the parallelization capacity and the associated meshing strategy. Nonetheless, the LBM solvers, with a complete chain going from the quasi-automatic mesh generation to the simulation itself, meet all these criteria necessary for an industrialist. Moreover, on the performance summary tables available for this test case in [34,75], LBM solvers have a much lower restitution time than other solvers with an at least equivalent result quality, which places them as very promising for landing gear applications.

These benchmarks also allowed to compare the solid and permeable FW-H formulation. This last formulation requires to correctly propagate the acoustics outside the areas of the flow interest, and therefore requires a higher computational cost. The two solvers that have performed acoustic propagation using a permeable formulation are elsA and CEDRE. Their conclusions are identical, the permeable formulation brings nothing more than the solid one for this type of application, and even their results were deteriorated.

However, a recent study conducted by Hajczak, Sanders *et al.* [283] on an isolated LAGOON wheel performed a comparison of both formulations with a proper acoustic propagation and convergence studies on the position of the permeable surface. This study revealed the existence of high-frequency quadrupole sources emanating from the landing gear wake that are not taken into account by the solid formulation and that could contribute to broadband noise as shown on Fig. 7.4. These recent and more precise results are in contrast to their first study, which led to an opposite conclusion [284]. In their last study, they have also performed a source localization maps using the beamforming method [14–16] to corroborate this observation. This could explain why all solvers underestimate the high-frequency acoustics for downstream microphones in [75], even those using a permeable FW-H formulation, due to the poor resolution that might mask this phenomenon.

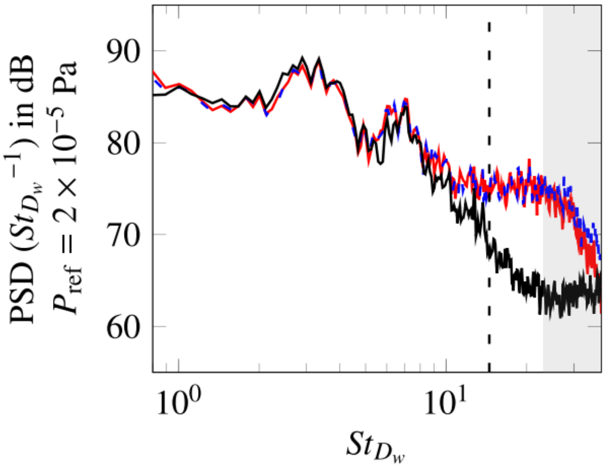

Figure 7.4 – *Near-field pressure PSD obtained with* (---)*: permeable approach,* (—)*: solid approach,* (—)*: Direct noise computation at* $(x/D, y/D, z/D) = (2.8, 0, 1.2)$*. Gray area: CFD cut-off. Extracted from [283].*

Furthermore, Spalart highlighted since 2013 [273, 285] the limitations of solid FW-H formulation for such aeronautical applications. This topic will be extensively discussed in Sec. 7.4.2.

Under the light of these articles, it was chosen in this study to similarly compare the two formulations. This is facilitated in LBM by the temporal method, allowing to strongly reduce the cost of the grid extension necessary for such acoustic propagation, which will not be updated every time step.

7.2 Numerical setup

The physical parameters of the simulation match the conditions of the CEPRA19 wind tunnel. The pressure is set to $P_{ref} = 99447$Pa, the temperature to $T_{ref} = 298$K and the velocity to $U_{ref} = 78.99\mathrm{m.s}^{-1}$, which corresponds to a Mach number of Ma = 0.23. The Reynolds number based on the diameter is $Re_\mathrm{D} = 1.564 \times 10^6$.

The computational domain as well as the mesh have been modified compared to the previous LaBS study by Sengissen *et al.* [36]. A ceiling considered as a sliding wall has been added to hold the landing gear. This reduces the shear layer generated at the base of the profile on which the landing gear is mounted. In addition, an absorbing area [79] is placed on this ceiling to avoid acoustic reflections generated by the landing gear, that are not encountered in the wind tunnel tests. For the remainder, a very large computational domain box was simulated with a velocity Dirichlet boundary condition at the inlet, and a pressure imposed on the other boundaries. Absorbing layers wrap all the domain boundaries to damp outgoing acoustics. Finally, a wall-law accounting for adverse pressure gradient and curvature effect is applied on the LG.

Three grids of different resolution have been dimensioned. These three meshes are however restricted by the same constraint: the ability to correctly propagate the acoustics to the permeable surface used by the FW-H solver. Our LBM scheme with the H-RR$_\psi$ collision model requires at least 8ppw (points per wavelength) to propagate the acoustics correctly over such a distance without dispersing/dissipating it too much (*cf.* Fig. 4.3 & Chap. 5). If a cut-off frequency of 10kHz is targeted, as it is generally chosen in the various previous studies, cells with a maximum size of 4mm are required in the extended propagation zone up to the permeable surface. The construction of the three grids is thus fixed by this criterion, and therefore the choice is made to coarsen the mesh only by removing areas of near-wall resolution as shown on Fig. 7.5.

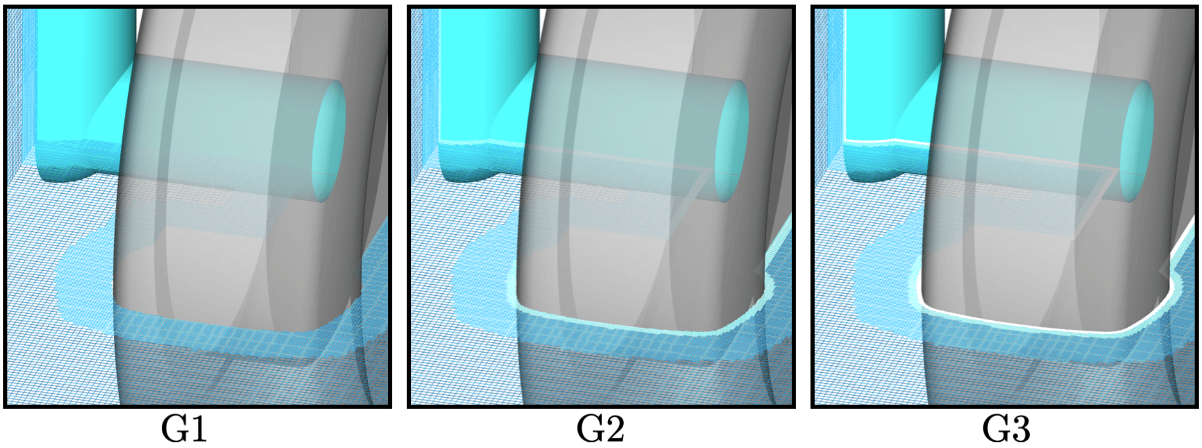

Figure 7.5 – *Three grids used for the convergence study. LAGOON rear view.*

In Tab. 7.1, the three grids are described. The fine equivalent column represents the equivalent in number of cells updated every iteration due to the adaptive time step. This column, together with the time step one, is very indicative of the computing cost.

The Tab. 7.2 summarizes the performance of the code for the various grids. Some precisions are however necessary. The column CPU/element/iterations and CPU/element/1ms of physical time is calculated with respect to the total number of cells, and not all cells are

Mesh	**Number of cells** (10^6)	**Equivalent fine** (10^6)	Δx_{min} (mm)	D/Δx_{min}	Δt_{min} (s)	**Resolution Domains**
G1	112	37	1	300	$1.68 \cdot 10^{-6}$s	10
G2	130	38	0.5	600	$8.42 \cdot 10^{-7}$s	11
G3	235	112	0.25	1200	$4.21 \cdot 10^{-7}$s	12

Table 7.1 – *Three grids used with associated parameters.*

updated every time step. In addition, the version used is a development version which has degraded performance compared to the commercial version. Finally, the computations are carried out with double precision, which increases the computation time by 30%. It will be interesting, for an industrial use, to investigate the effect of the simple precision on the results.

Mesh	**Total CPU time (h)**	**Total clock time (h)**	**CPU cores**	**CPU/elem/it** (10^{-6}(s))	**CPU/elem/1ms** (10^{-3}(s))
G1	2750	17	160	0.45	0.26
G2	8300	16	512	0.54	0.65
G3	28000	55	512	0.76	1.84

Table 7.2 – *Computation time informations.*

The refinement domain for propagating the acoustics to the permeable surface is shown on Fig. 7.6. The latter imposes a uniform mesh size of 4mm, which is finer than the mesh used in [283] that is converged. This resolution area represents $50 \cdot 10^6$ cells. They are updated every $6.74 \cdot 10^{-6}$s and are therefore updated every 4, 8 and 16 iterations for the G1, G2 and G3 meshes respectively. The cost of such refinement domain, when reduced to the number of cells updated per time step (equivalent fine nodes) is 11·, 6· and $3 \cdot 10^6$ respectively. The relative cost of such propagation becomes weak in our case when the near wall resolution is increased (30, 16, 3% of the equivalent fine nodes respectively for the G1, G2 and G3 grids).

The simulation time is 0.34ms, with the last 0.17ms being kept in the presented results. This corresponds to 45 convective times based on the wheel diameter. The PSDs are realized with the Welch method [286] using 15 blocks, 50% of overlap and a Hanning window. The sample frequency for unsteady signals is 75kHz.

In the wind tunnel tests, tripping devices were added to trigger the boundary layer transition on the wheels, axle and leg. In the simulation, cylinder layers have been incorporated to trigger this laminar to turbulent transition. These are visible on Fig. 7.7.

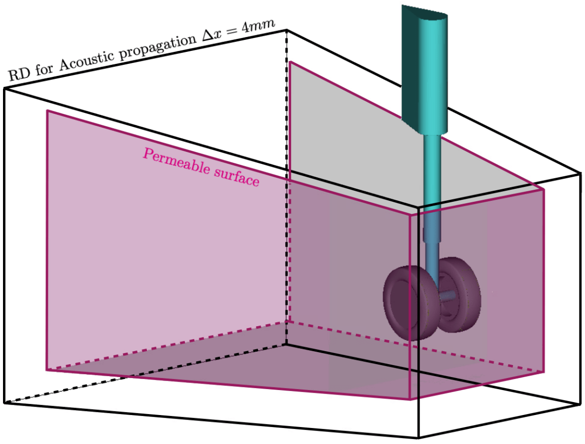

Figure 7.6 – *Position of the permeable surface used for the FW-H propagation.*

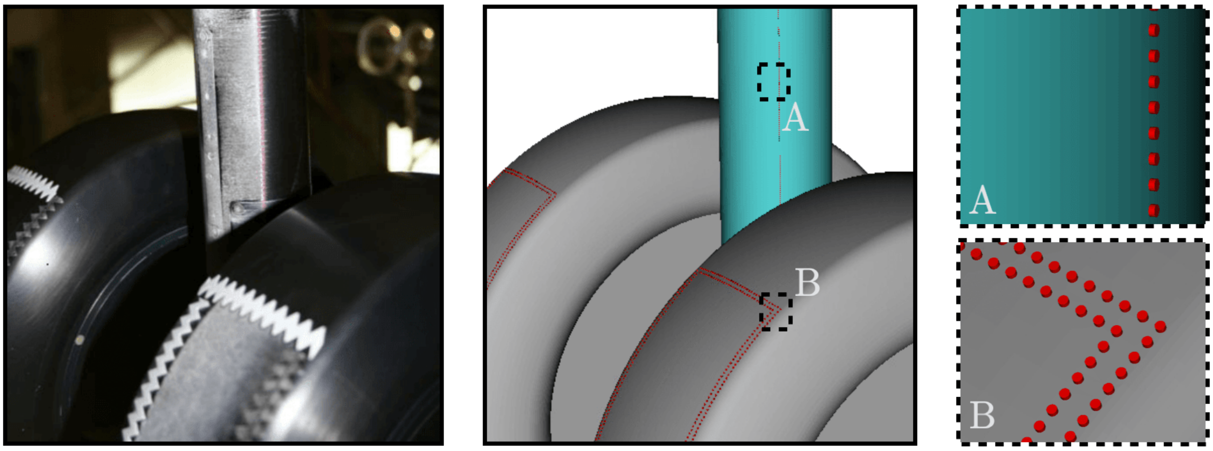

Figure 7.7 – *Tripping devices have been added on the wheels, leg and axle as in the experiments.*

7.3 Aerodynamic results

The results presented in this section are obtained with the H-RR$_\psi$ collision model and the DC grid coupling algorithm.

7.3.1 Mean coefficients at walls

7.3.1.a Wheel perimeter

The wall-pressure coefficients are compared on the left wheel circumference, with the 37 pressure taps placed in the experiments. Fig. 7.8 shows the Cp and CpRMS along an azimuthal cut made in the center of the wheel. The blockage effect caused by the leg that generates a higher acceleration on the upper part of the wheel (90°) than on the lower part (−90°) is well recovered with the three meshes. Indeed, the Cp profiles are asymmetrical with a higher depression for the positive angles. The three meshes are in agreement with experiments as well as most codes [75]. Pressure oscillations can be noticed on the Cp profiles. These oscillations come from parietal treatment and will disappear very soon with the new numerical ingredients that are not yet implemented in the LaBS/ProLB version we used [67, 68].

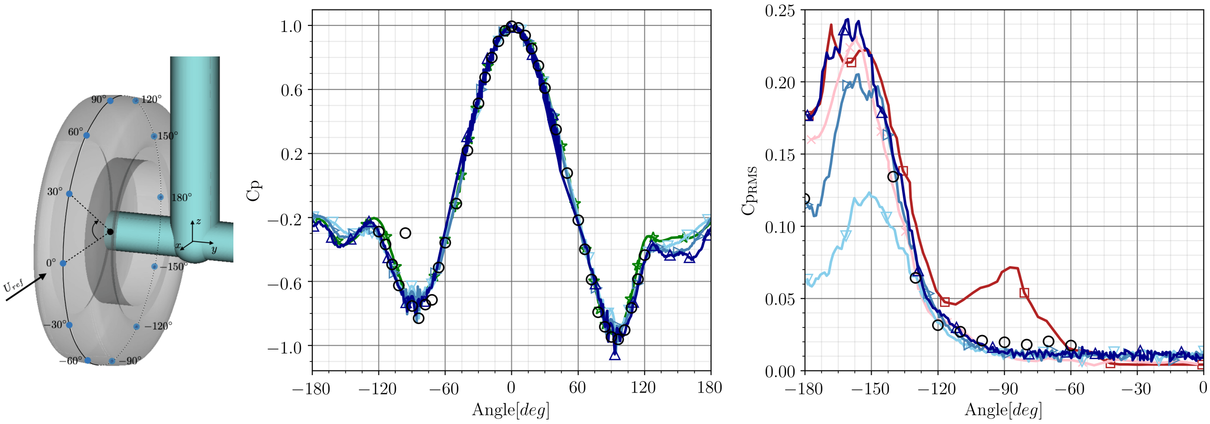

Figure 7.8 – *Mean (left) and RMS (right) static pressure coefficients distribution along a cut extracted on the left wheel perimeter.* (—▽—)*: G1 grid,* (—▷—)*: G2 grid,* (—△—)*: G3 grid,* (—☆—)*: Ribeiro,* (—⊟—)*: Zhang-LAF,* (—×—)*: De la Puente Cerezo ,* (○)*: Experiments.*

Pressure fluctuations are very well captured by refining the mesh. This means that the turbulent boundary layer development is going right, as will be confirmed by the kulite analysis in Sec. 7.3.5. As can be seen on Fig. 7.9, the boundary layer does not show vortices until the tripping strips, then the transition occurs and the boundary layer becomes increasingly turbulent. The flow physics is very complex around the wheels, with a significant influence of the flows coming from the internal and external cavities. These secondary flows gather downstream of the wheels and help the detachment by absorbing the developed boundary layer. To our knowledge, only two previous studies report the Cp_{RMS}. That of De la Puente Cerezo [49], with whom the results are located in between our G2 and G3 mesh, and are in very good agreement with experiments, and that of Zhang [21], with various wall laws. The reference reported on Fig. 7.8 is the one using the most advanced wall law (referred as LAF in [21]). However, the Afzal law used by the same author, as well as the results reported here, gives Cp_{RMS} with levels much too high from the upstream part of the wheel compared to our simulations. This is a sign of a too fast development of the turbulent boundary layer.

7.3.1.b Leg and axle

Fig. 7.10 shows the static pressure distribution on an azimuthal slice located on the leg and on the axle. These two parts are composed of cylinders with diameters of 55 and 44mm respectively. The Reynolds number based on these is $2.9 \cdot 10^5$ and $2.3 \cdot 10^5$ respectively. These Reynolds numbers are in the critical regime [287]. The finest mesh (G3) is the only one allowing to capture correctly the Cp after the detachment point on

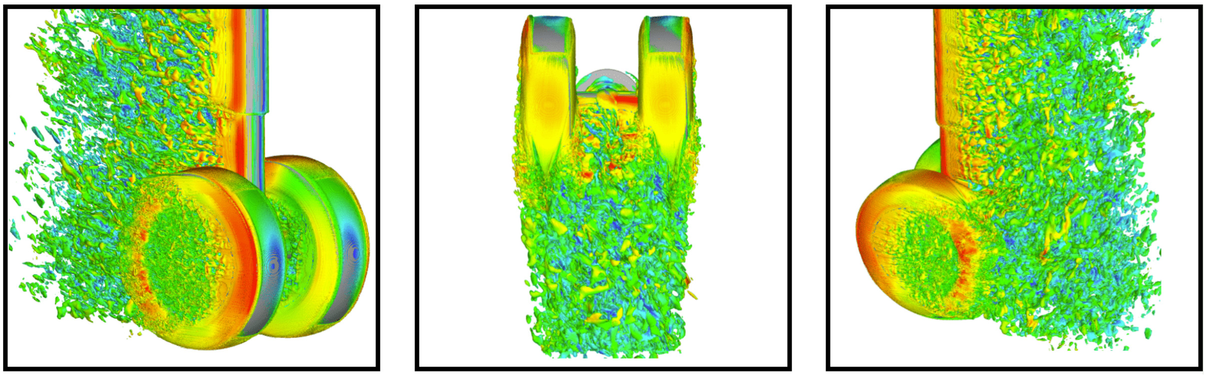

Figure 7.9 – *Iso-surface of* Q-criterion = $2 \cdot 10^7$ *colored by the velocity magnitude for several views of the* LAGOON 1 *with the G3 mesh.*

the leg. The pressure distribution around the axle is not symmetrical due to the blocking effect induced by the leg, which is well captured by all three meshes. Experimental measurements are unfortunately lacking to have a reliable idea of the pressure distribution on the axle.

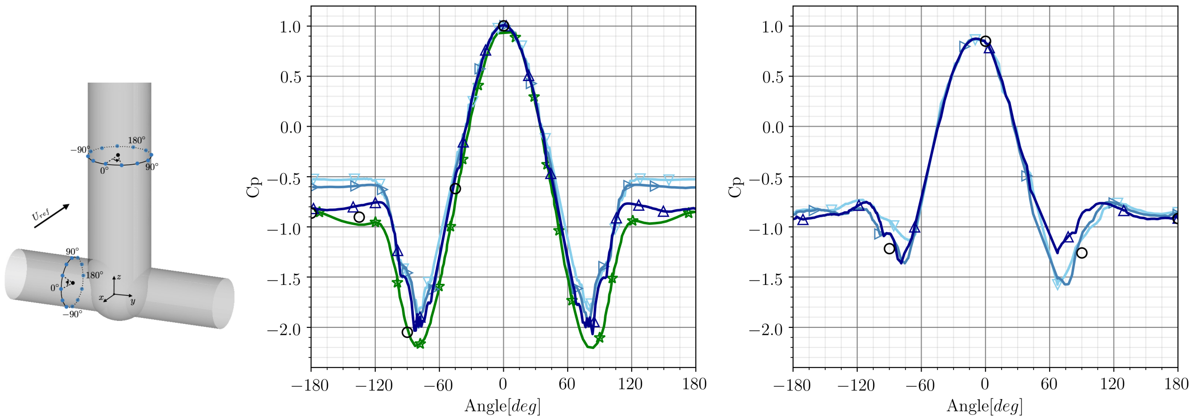

Figure 7.10 – *Leg (left) and axle (right) mean static pressure coefficients distribution.* (–▽–)*: G1 grid,* (–▷–)*: G2 grid,* (–△–)*: G3 grid,* (–☆–)*: Ribeiro,* (○)*: Experiments.*

7.3.2 Mean velocity profiles

Velocity profiles were measured in the experiments using LDV2D. Fig. 7.11 compares the velocity profiles of the Ux and Uz components along a line located at −90° underneath the wheel. For the Ux velocity, the coarse mesh (G1) thickens the boundary layer. However, the G2 & G3 meshes have a good agreement with experiments. The boundary layer obtained with PowerFLOW is also too thick with a maximum speed under-predicted. This is probably due to the low resolution of the mesh used around the wheel, which is in-between our G1 and G2 resolution. The Uz speed profile is underestimated compared to the experiments for every grids. Nevertheless, this is the general trend for all the codes that have performed the BANC benchmark, except CEDRE [75] at that time. Although the latest more precise simulations of De la Puente Cerezo [49] with CEDRE also exhibit this velocity deficit.

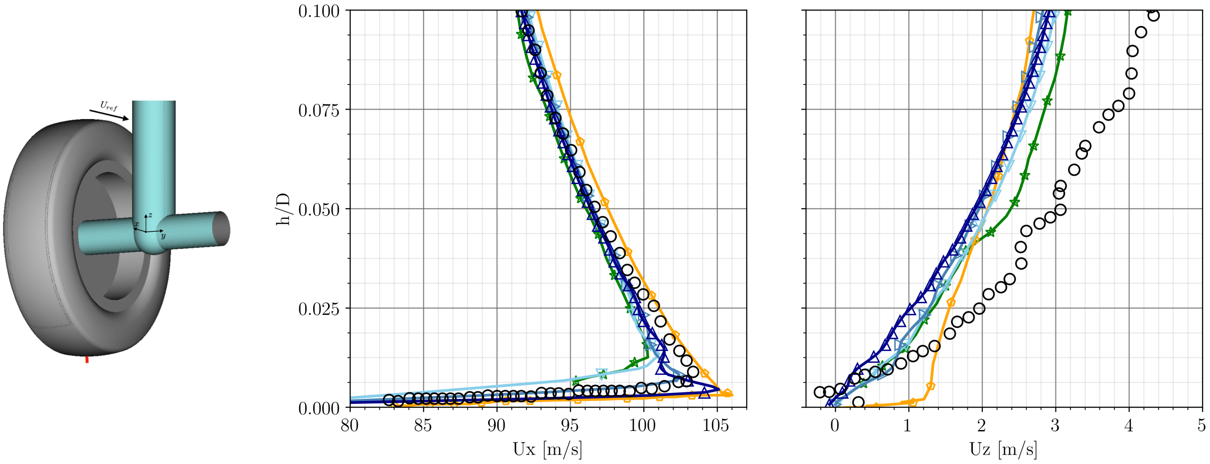

Figure 7.11 – *Velocity profile underneath the left wheel. Left: longitudinal velocity* Ux*, right: vertical velocity* Uz*.* (−▽−)*: G1 grid,* (−▷−)*: G2 grid,* (−△−)*: G3 grid,* (−☆−)*: Ribeiro,* (−⬠−)*: Giret,* (○)*: Experiments.*

7.3.3 PIV and LDV profiles in the wheels' wake

The flow downstream of the landing gear wheels is visualized in the $z = 0$m plane on Fig. 7.12. Only the streamwise and crosswise velocity components were obtained through PIV measurements, while the vertical velocity was measured on a reduced window and is not shown here. In this plane, the flow is composed of the recirculation area behind the two wheels, visible on the streamwise velocity, and the wake generated by the axle and the leg that accelerates in between the tires. The accuracy on the resolution of these last two components greatly influences the flow downstream of the wheels. Indeed, these wakes generate a suction zone in the $z = 0$m and $y = 0$m plane for the axle and the leg respectively. This phenomenon, in the case of the leg is visible on the crosswise component of the velocity where the leg wake tends to aspirate towards the middle the wakes coming from the wheels and to gather them. This is visualized with a crosswise flow, going from the respective wake of the wheels towards the symmetry axis of the LG. A significant increase in velocity fluctuations in this mixing zone is thus produced. These effects are very well captured with the three meshes. However, the coarse mesh (G1) under-predicts fluctuations downstream of the axle and the leg, which reduces the intensity of these mixing layers and delayed this effect. Another effect that is captured only by refining the grid is the intensity of velocity fluctuations in the recirculation zone for the two wheels. These fluctuations are strongly underestimated for the G1 mesh.

An interesting point to notice is that these three meshes are identical as soon as the distance from the wall is greater than 0.005m, which corresponds to the whole PIV plane measured in the experiments. However, the fluctuations are very different downstream, which shows that the physics to be captured is fine and very strongly dependent on the boundary layers and upstream separation points.

Velocity profiles were extracted using LDV in the experiments, in the same way as the extraction of velocity profiles under the wheel in Sec. 7.3.2. The profile positions, located

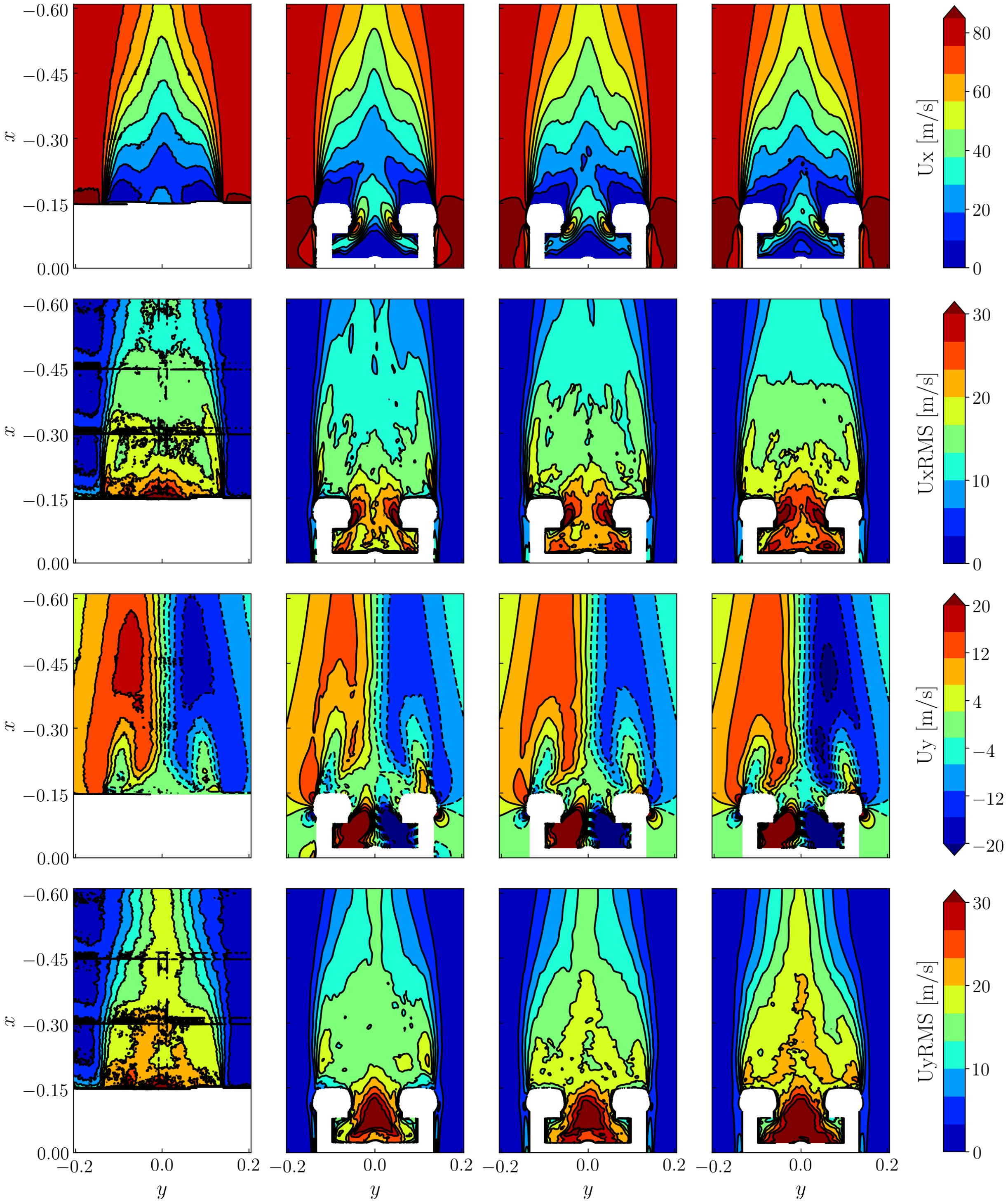

Figure 7.12 – *Comparison with PIV measurements for the* $z = 0$m *plane. From top to bottom:* Ux, UxRMS, Uz, UzRMS. *From left to right: Experiment, G1, G2, G3.*

in the $z = 0$m plane, are given on Fig. 7.13. Three profiles are located for a value of x set at an increasing distance downstream of the landing gear, and one profile is located in the left wheel wake. This time, only the x and z components of the velocity are available in the experiments. Fig. 7.13 shows the velocity profile at $y = -0.115$m. In the immediate vicinity of the wheel, the recirculation zone is well retrieved. The velocity fluctuations in this zone are very well captured by refining the mesh, as confirmed by the PIV planes on Fig. 7.12. Except in the immediate vicinity of the wheel, the three meshes are in good agreement with each other and with the experiments.

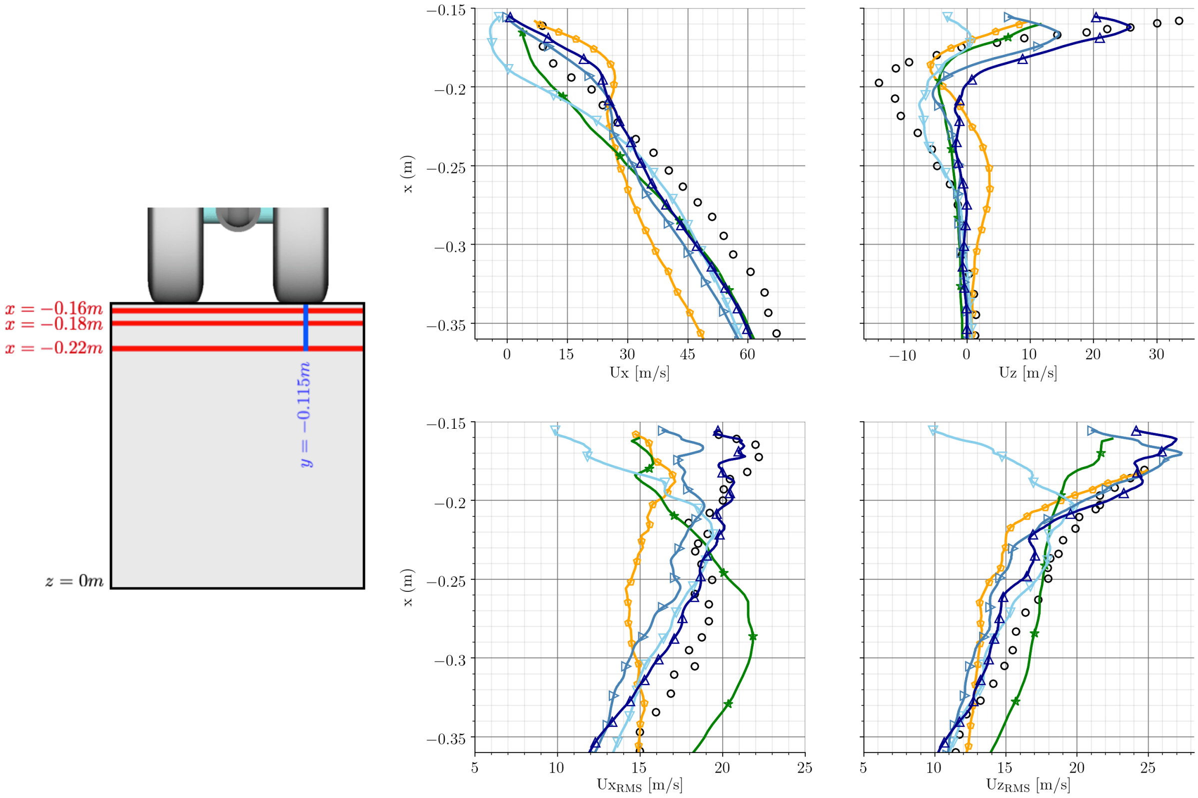

Figure 7.13 – *Mean (top) and RMS (bottom) axial (left) and vertical (right) velocity components in the cutting line $y = -0.115m, z = 0m$.* (–▽–): *G1 grid,* (–▷–): *G2 grid,* (–△–): *G3 grid,* (–☆–): *Ribeiro,* (–⬠–): *Giret,* (○): *Experiments.*

The velocity profiles along the x axis are shown on Fig. 7.14. The furthest upstream cut ($x = -0.16$m), presents, for the Ux component, two near-zero speed plateaus appearing behind the wheels. Conversely, strong variations of the vertical velocity Uz are encountered, which are not symmetrical due to the presence of the leg. A longitudinal velocity acceleration zone is present between the wheels, for $-0.06\mathrm{m} < y < 0.06\mathrm{m}$. This acceleration results from the downstream flow of the axle and the leg, which interacts and accelerates between the tires, a phenomenon that is very well captured by the meshes G2 and G3. Then the profiles are spread out and homogenized for downstream cuts. The streamwise velocity fluctuations present strong gradients in these mixing layers. The finer the resolution, the closer the results come to the experiments but the fluctuation levels are slightly underestimated near the symmetry axis. For the velocity fluctuations in the vertical direction, the G2 and G3 grids matches the experimental results, while the G1 mesh is really too under-resolved to capture this complex physics, very strongly dependent on the wheels separation points.

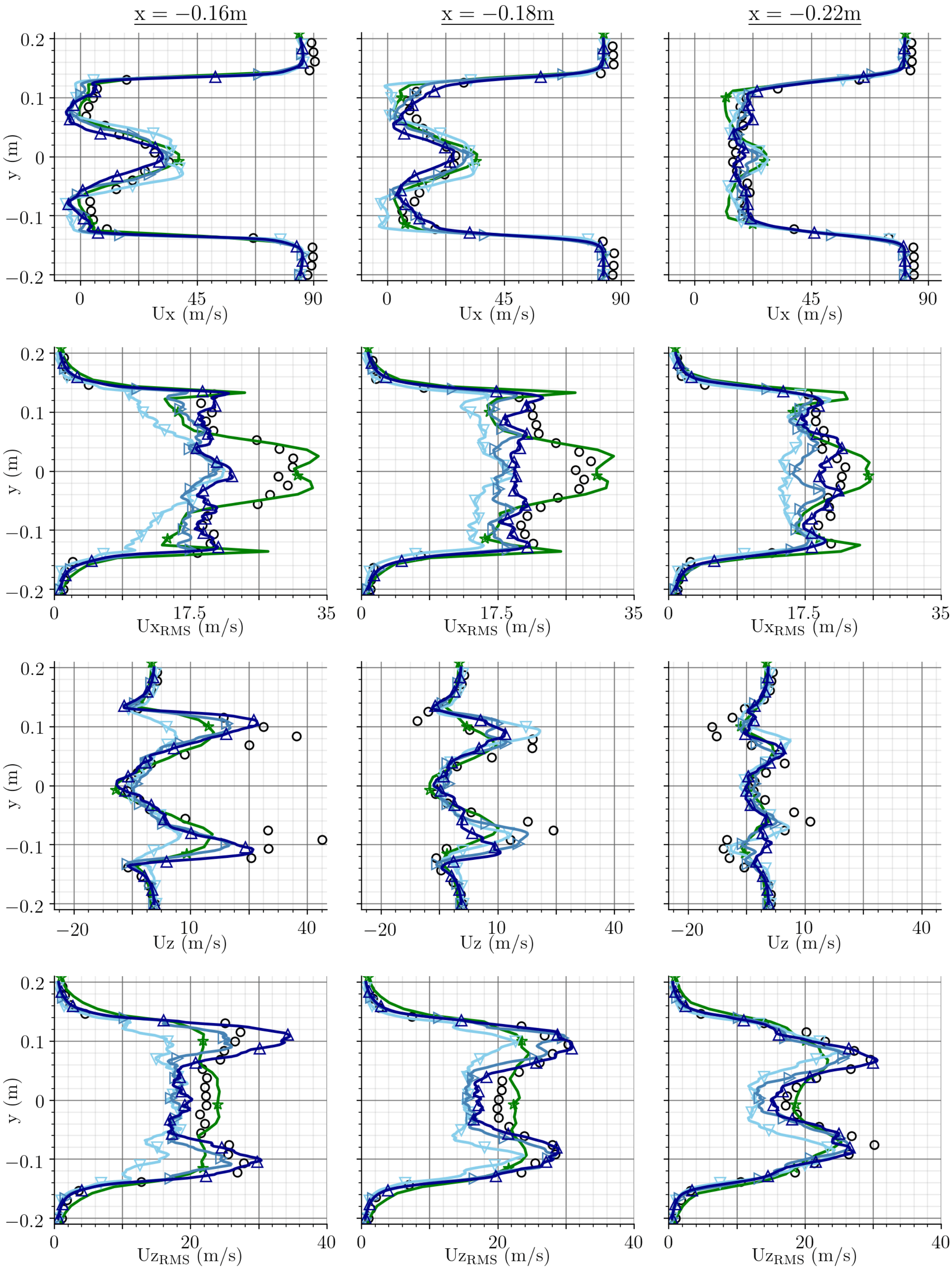

Figure 7.14 – *Velocity profiles at increasing distance downstream the wheels in the* $z = 0$m *plane. Left:* $x = -0.16$m*, middle:* $x = -0.18$m*, right:* $x = -0.22$m*. From top to bottom:* Ux, UxRMS, Uz, UzRMS. (−▽−)*: G1 grid,* (−▷−)*: G2 grid,* (−△−)*: G3 grid,* (−☆−)*: Ribeiro,* (○)*: Experiments.*

7.3.4 Velocity spectra

In the F2 wind tunnel facility, velocity spectra have been extracted from the LDV measurements. These data are particularly useful to evaluate the dissipation of turbulent structures in the wheels wake. The Fig. 7.15 presents the results for the three meshes.

All the three curves are almost superposed, and have the same cut-off frequency. This is because of the identical mesh size for the various grids in this region. Moreover, the measurements are performed at 0.3D downstream of the wheel. At this location, the deviations on the velocity fluctuation profiles for the various grids are reduced (*cf.* Fig. 7.13). It can be noticed that the cut-off frequency occurs around ~ 2.5kHz against 1kHz for Giret with AVBP [32] and 6kHz for Ribeiro and Casalino with PowerFLOW [51, 52]. This result is quite unexpected given that the mesh size used in our calculation is 2mm in this region against 2.4mm with PowerFLOW. Nevertheless, on Fig. 7.13, one can see that our results obtained for $\mathbf{U}_{\mathrm{RMS}}$ are more consistent with experiments than those obtained with PowerFLOW, although high frequencies contribute little to $\mathrm{U}_{\mathrm{RMS}}$. Anyway, the agreement on the spectral content is quite good.

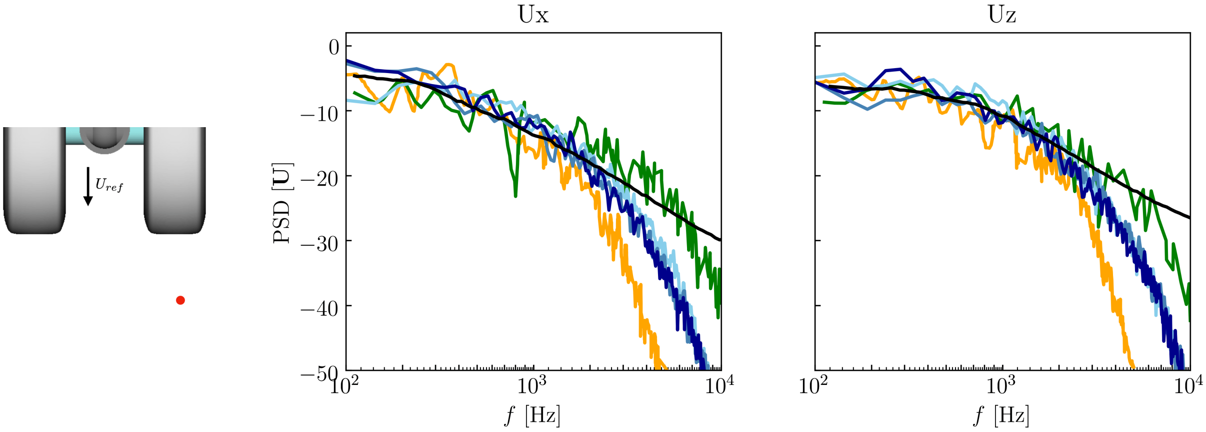

Figure 7.15 – *Power spectral density of streamwise (left) and vertical (right) velocity components at position* $(x, y, z) = (-0.24, -0.115, 0)$m. (—)*: G1 grid,* (—)*: G2 grid,* (—)*: G3 grid,* (—)*: Ribeiro,* (—)*: Giret,* (—)*: Experiments.*

7.3.5 Wall-pressure spectra

Unsteady pressure probes (kulites) were instrumented on the landing gear: on the wheels, axle and leg. These kulites provide an estimation of the near-field spectral content, which is a very good indicator of turbulent intensity and of separation points location. This knowledge is very useful for estimating near-field acoustic sources.

Probes K1 to K9 are located in the mid-span plane of the right wheel, with K1 positioned at −60° and K9 at −140° downstream as shown on Fig. 7.17. The results are presented for the three meshes on the same Figure, as well as the V-LES LBM simulation of Ribeiro, Casalino *et al.* [51, 52] and the LES of Giret [9]. It is important to remember that tripping bands allowing to force the boundary layer transition have been placed in the experiments, at +/−55°. Therefore, the spectral content of the boundary layer is very rich at high frequencies. Our simulations as well as all codes that have performed simulations on this configuration are not able to reproduce faithfully these high-frequencies except the LaBS calculations performed by Sengissen *et al.* [36]. Indeed, these simulations were performed with the filtered DRT collision operator presented in Sec. 4.7 which does not filter the non-hydrodynamic SpuriousS modes carrying shear. As illustrated on Fig. 7.16, where a simulation is performed with the filtered DRT model using LaBS/ProLB v2.5 and compared to the currently used H-RR$_\psi$ one, spurious vorticity is strongly present in the DRT simulation. It appears at the various resolution transitions, even upstream, without any disturbance of the flow. This phenomenon has been widely studied in Sec. 4.5 with the RR collision model, but the principle is similar here. The parasitic vorticity enriches the spectral content of the boundary layer, in an uncontrolled way. Filtering these waves, as the H-RR$_\psi$ collision model does very well, therefore degrades the PSD found on kulites K1 to K6 but for legitimate reasons and our results are in agreement with other CFD codes. The effect of trippings is noticeable on the vorticity fields where the boundary layer thickens at +/ − 55°.

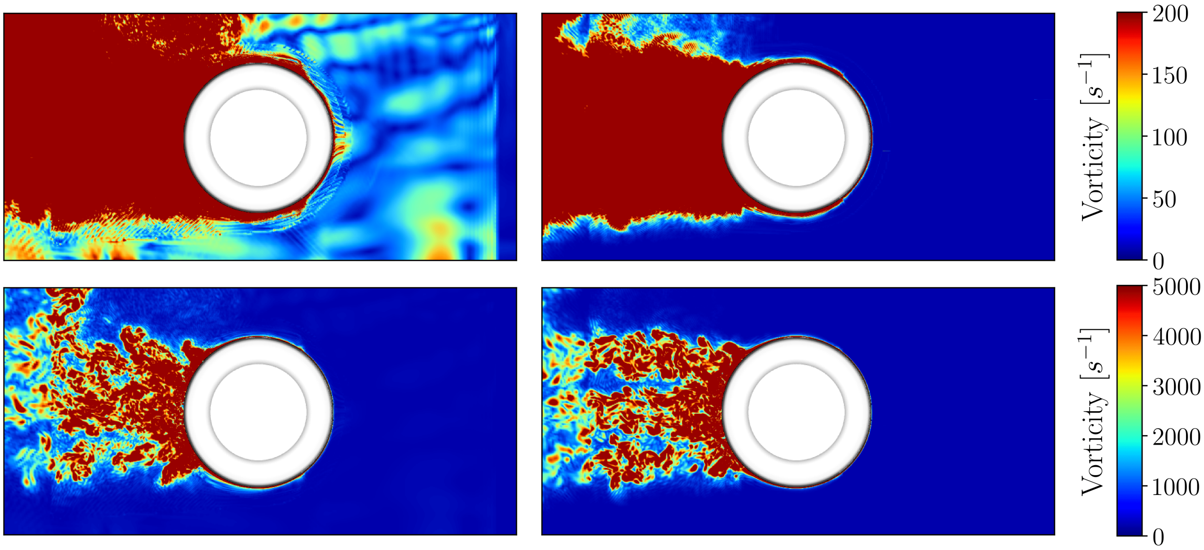

Figure 7.16 – *Vorticity fields obtained with the G2 grid on a plane through the middle of the left wheel for two collision models and two colormaps with different color dynamics. Left: Filtered DRT collision model, right: H-RR$_\psi$ collision model.*

From kulite K1 to K6, the turbulent content of the boundary layer grows, leading to increased levels of pressure fluctuations. Two tonal peaks are apparent, at 1kHz and 1.5kHz, corresponding to acoustic cavity modes [9, 51, 52, 270]. These are gradually drowned out by the noise related to the turbulent fluctuations of the boundary layer. These two modes are very well recovered. Then, the boundary layer separates, around K7 (−120°), and the levels are much closer to the experiments for high frequencies. In the separated region, the grid resolution greatly influences the noise levels. The fine mesh G3 is the closest to the experiments. The results are in agreement with those obtained by Ribeiro and Casalino *et al.* with PowerFLOW [51, 52, 75]. Those obtained with AVBP predict a boundary layer separation occurring too early. Improving wall modeling, with advanced wall laws as in Zhang's thesis [21] leads to the same observation. Surprisingly, the Afzal wall law used in his thesis (referred as AF [21]) predicts a separation starting from K1 (−60°), while a similar law behaves correctly in our simulations.

The results of the kulites arranged on the inner side of the right wheel are also depicted on Fig. 7.17. From K13 to K15, on the upstream inner edge of the tire, the boundary layers are well attached as in the experiments. Noise levels are low, which allows the two tonal peaks related to the cavities modes to appear. Inside the cavity and downstream of this last, the noise levels are very high. These areas are major acoustic sources [9]. Noise levels are slightly underestimated inside the cavity and overestimated downstream on the K20 probe. The agreement remains very good with both PowerFLOW and the experiments.

For the outer edge of the right tire the spectra are given on Fig. 7.18. This time, the K10 to K12 probes located upstream present a transient regime towards turbulence requiring a high spatial resolution. Moreover, in the experiments, important discrepancies appear on these kulites between experiments carried out in the F2 wind tunnel and CEPRA19 [75], which is a clear indication of a phenomenon very sensitive to external conditions. The simulated levels get closer and closer to the experiments as they move away from the upstream flank of the tire, and the noise level increases sharply between K12 and K10. On these probes, a very strong dispersion appears between CFD codes. The K18 probe downstream presents very good agreements regardless of the mesh size. Probe K19, located at the rear of the tire, in the recirculation zone, indicates a high level of pressure fluctuation. This level is under-estimated for the G1 mesh and over-estimated with the G3. The agreement is satisfactory with experiments for kulites located in the downstream part of the wheel. The latter have the highest fluctuation levels, which means that their importance as an acoustic source should be more significant.

Finally, the remaining kulites studied are located around the leg, and one on the axle at 90°. The kulite located on the axle (K23) shows correct relative levels but too low in absolute terms. The levels are improved by refining the mesh but are underestimated by 10dB. The axle is probably a major source of noise in the low frequency range for flyover microphones [9, 21] as well as the leg for the sideline arc. The probes around the leg show very good agreement upstream (K24 & K25) where the boundary layers are attached, but the separation before 120° (K26) is not correctly retrieved. Downstream, in the recirculation zone, the kulite K27 presents correct fluctuation levels for the finest mesh. The PowerFLOW wall model or its DES turbulence modeling seems more adequate to capture high Reynolds number flows around such cylinders, even with lower spatial resolution. Recent works on DES with LaBS/ProLB will be very relevant to assess in this case.

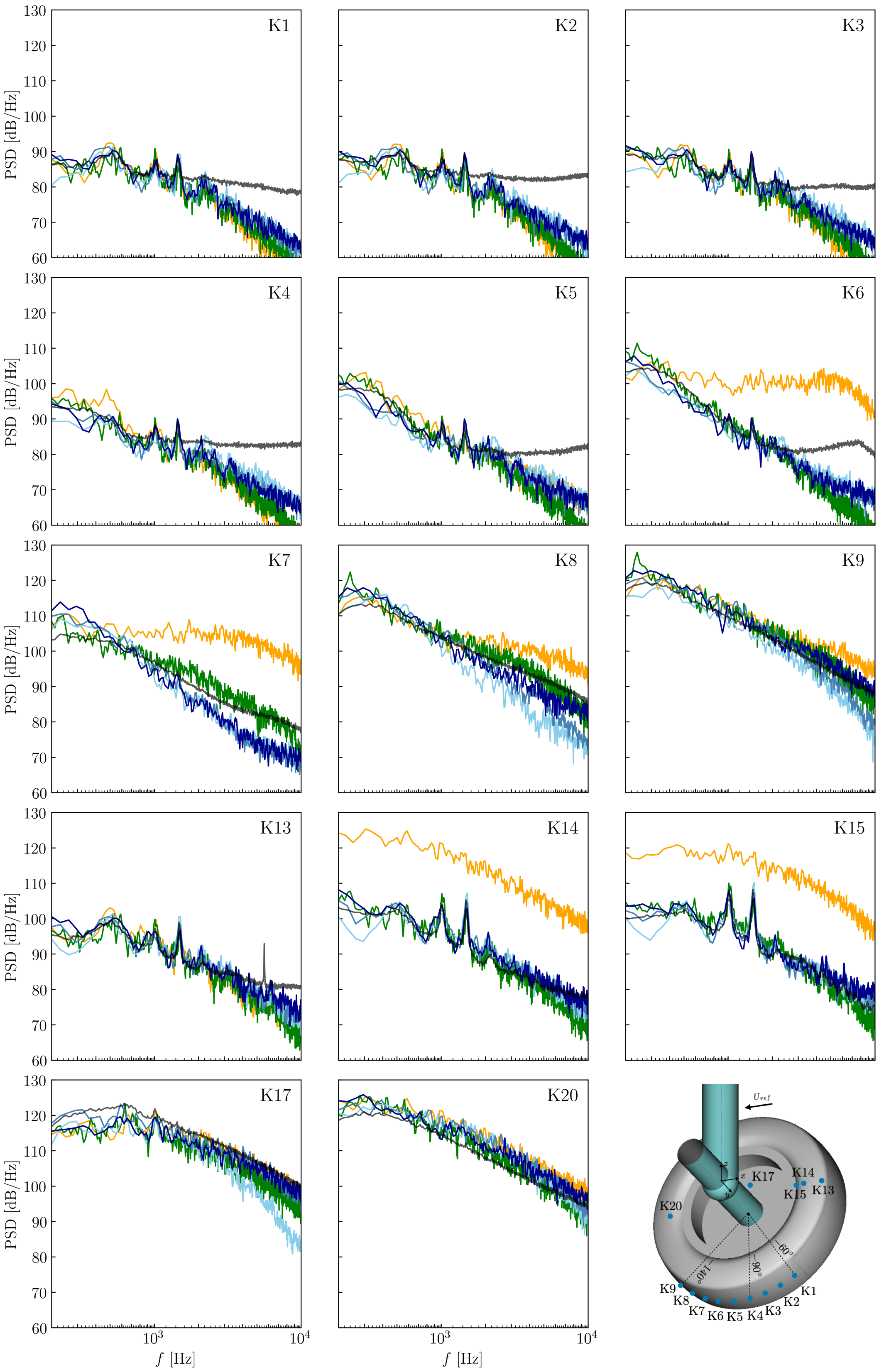

Figure 7.17 – *Wall pressure PSD along the wheel centerline and in the inner flank of the right wheel tire. Comparison with kulites measurements. (—): G1 grid, (—): G2 grid, (—): G3 grid, (—): Ribeiro, (—): Giret, (—): Experiments.*

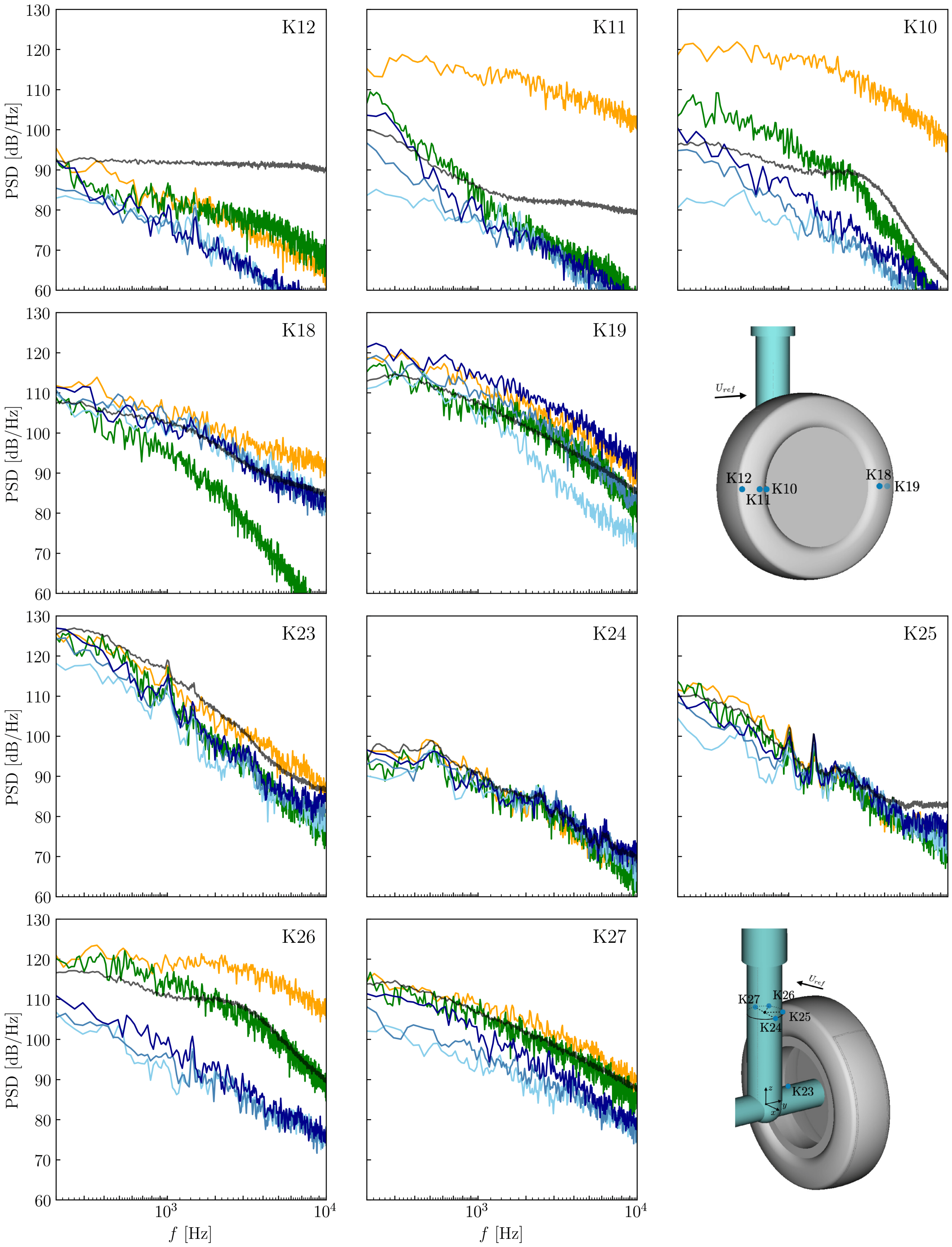

Figure 7.18 – *Wall pressure PSD in the outer flank of the right wheel tire and along the axle and leg. Comparison with kulites measurements.* (——): *G1 grid,* (——): *G2 grid,* (——): *G3 grid,* (——): *Ribeiro,* (——): *Giret,* (——): *Experiments.*

7.4 Aeroacoustic results

This section is dedicated to the acoustic predictions obtained in the far-field for the LAGOON1 gear. First, the benefits obtained with the use of the H-RR$_\psi$ collision model, as well as with the developed DC grid coupling algorithm will be presented. Subsequently, both solid and permeable FW-H formulations for CFD/CAA coupling will be evaluated and compared to a direct noise calculation. The defects of the solid formulation will be emphasized for such aeronautical application. Finally, far-field acoustic results will be discussed along with noise directivity.

7.4.1 Enhancements brought by the improved LB modeling

The Fig. 7.19 illustrates sound pressure fields obtained with the G2 mesh for three versions of LaBS/ProLB:

- The standard LaBS/ProLB v2.5 version using the filtered DRT collision model, which is very close to the one used by Sengissen [36] during the first study performed on the LAGOON gear. In the thesis introduction, in Sec. 1.4.2, the acoustic and vorticity fields were presented with the setup used by Sengissen [36] that does not use any ceiling and with a different grid. Spurious acoustic waves generated by grid refinements were visible, as well as non-hydrodynamic modes studied in Chap. 3. & 4. In Fig. 7.19, the noise emanating from wake vortices that cross refinement interfaces is always very noticeable. In addition, strong non-hydrodynamic disturbances appear in the refinement area used to propagate the acoustics to the FW-H permeable surface, making any FW-H coupling using this formulation illusory.

- A version using the H-RR$_\psi$ collision model and a grid coupling algorithm identical to the LaBS/ProLB v2.5 version, named STD in Chap. 6. This time, only spurious acoustic emissions emanate from the refinement interfaces. No more non-hydrodynamic perturbations are noticeable, especially in the RD used to propagate the acoustics to the FW-H coupling surface. The noise emanating from the grid interfaces is still visible but is reduced.

- The latest version uses the H-RR$_\psi$ collision model, as well as the DC grid coupling algorithm, developed in Chap. 6. The latter allows to considerably attenuate the spurious acoustic sources emanating from the grid interfaces, that are almost no longer visible and the main source comes very clearly from the landing gear.

Quantitatively speaking, pressure probes (P1,P2,P3) were positioned under the landing gear at $x = (0, -0.2, -0.4)$m, $y = (0.0, 0)$m, $z = (-0.5, -0.5, -0.5)$m respectively. The latter allow, to quantify the spurious acoustics generated by the grid interfaces on Fig. 7.20. Several phenomena can be seen there. First of all, the v2.5 version using the filtered DRT collision model generates hydrodynamic fluctuations, of non-hydrodynamic origin, which predominate over the spectra for low frequencies. If a permeable FW-H surface were placed at this location, these over-estimates would be directly retrieved to

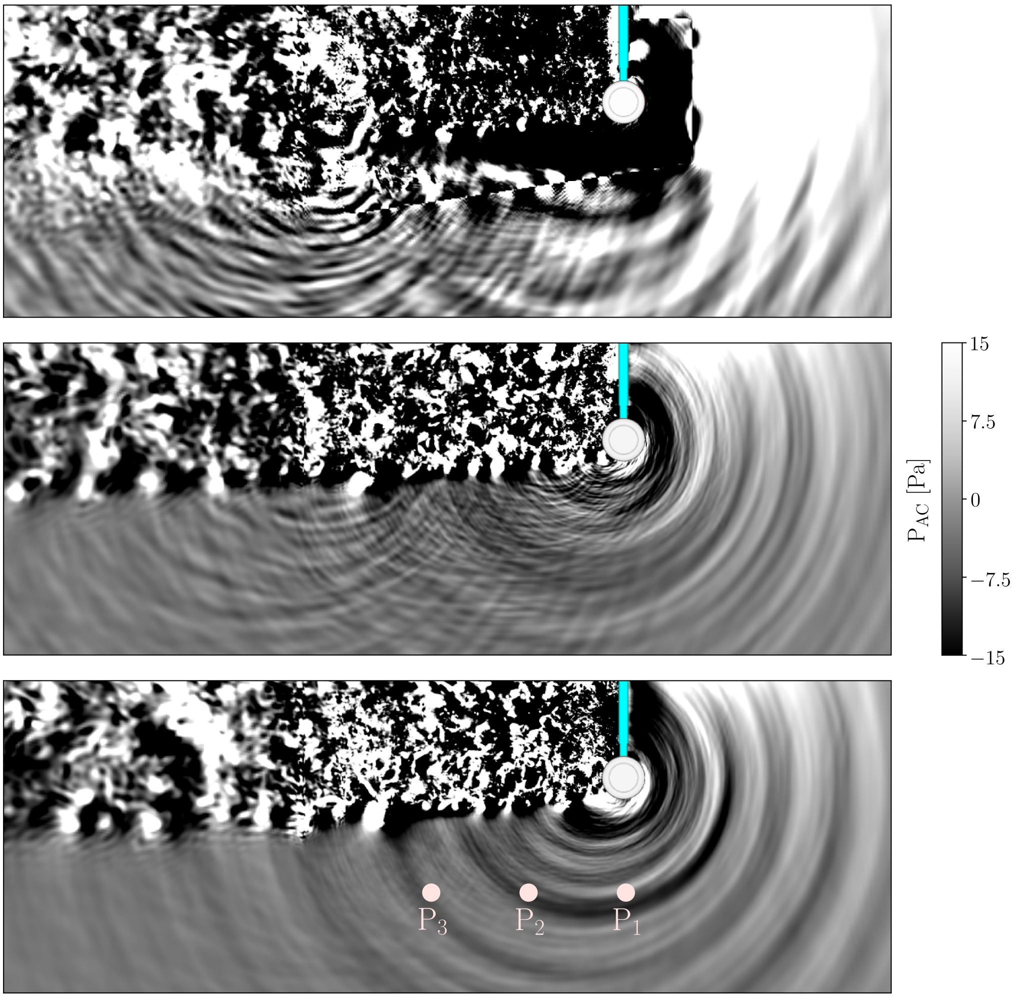

Figure 7.19 – *Acoustic pressure field* ($P_{AC} = p - p_{AVG}$) *for three associations of collision model / grid refinement algorithm with the G2 grid. Top: (LaBS/ProLB v2.5) filtered DRT / STD, Middle: H-RR*$_\psi$ */ STD, Bottom: H-RR*$_\psi$ */ DC.*

the noise levels obtained in the far-field, which is obviously not acceptable. At high frequencies an overestimation of about 3 to 5dB is visible compared to the H-RR$_\psi$ version using the same STD grid refinement algorithm. This discrepancy is attributed to the lack of non-hydrodynamic mode filtering in the wake with the filtered STD model which incorrectly increases wake turbulence. This effect has been discussed in Sec. 4.5 and is visualized more clearly in Fig. 4.18. With the H-RR$_\psi$ model, there is still a lot of noise when using the STD algorithm compared to DC. This spurious noise largely predominates over the physical noise generated by the gear over a wide frequency range (> 1kHz). This noise is more and more predominant downstream and when moving away from the source of the landing gear, and does not allow correct acoustic prediction. The DC algorithm reduces it by more than 10dB. This result was expectable given the reduction obtained on the turbulent cylinder in Sec. 6.5.

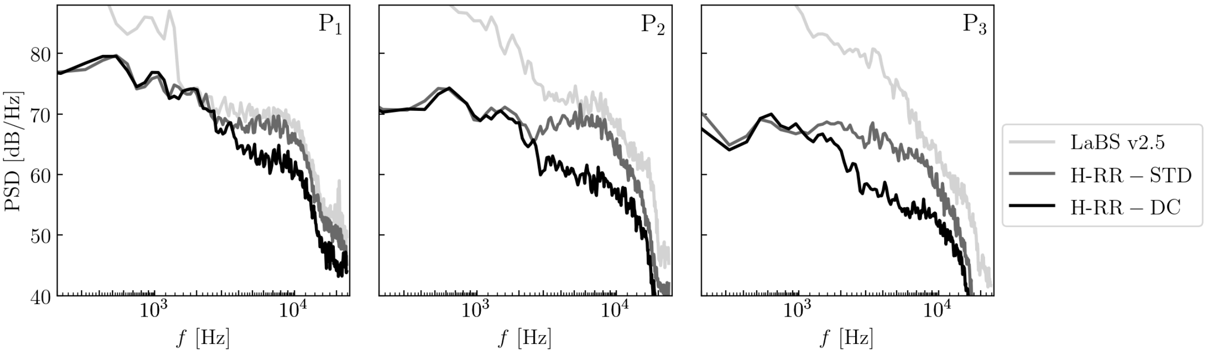

Figure 7.20 – *Noise recorded on the three pressure probes displayed on Fig. 7.19. The increase in noise compared to H-RR$_\psi$ – DC is assumed to be spurious.*

These noise measurements allow us to compare models with each other, but do not allow to quantify if the remaining spurious noise from the H-RR$_\psi$ / DC combination can affect the acoustic predictions. Besides, spurious acoustic waves of low amplitudes are always visible on Fig. 7.19. Therefore, comparisons to experiments are carried out in the following section, where the microphones location in CEPRA19 experiment is given on Fig. 7.21.

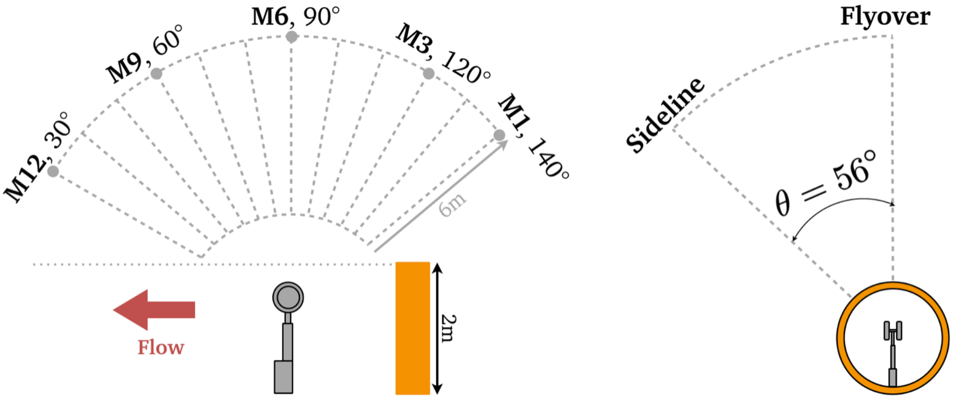

Figure 7.21 – *Positions of microphones in the CEPRA19 wind tunnel.*

7.4.2 Issues of the solid FW-H formulation for landing gear noise prediction

Section 7.1.2.b has introduced the theoretical concepts of acoustic integral methods, and more specifically the Ffowcs-Williams and Hawkings approach. The present section aims at identifying in a quite pragmatic way the potential issues encountered when applying the FW-H analogy for landing gear noise predictions.

The FW-H analogy is now widely used to extract acoustic sources from a CFD solver and propagate them to the far-field. It is so to say the only method used on all previous

LAGOON studies, and a scientific consensus is shared by the airframe noise community for such usage. In practice, this method is mainly used under two formulations, the first one being a specific case of the second (*cf.* Sec. 7.1.2):

- The solid formulation (S): It allows to estimate the dipole sources on a solid surface. This formulation is very simple, as it only requires the knowledge of the unsteady pressure p or density ρ on the solid surface. It is also very useful, since it is not necessary, during a CFD computation, to propagate the acoustics to a permeable surface, which greatly reduces the simulations cost. Furthermore, it is sometimes used to propagate acoustic sources from several surfaces individually in order to estimate the contributions of each components. In practice, this use is quite imprecise because, in addition to the solid formulation issues that we will discuss later on, it does not take into account the shielding effects of components among themselves [74, 273]. Additionally, it is necessary to consider the cross-correlations between the separate components to account for acoustic interferences that potentially affect noise levels [288].

- The permeable formulation (P): It consists in positioning in the simulation domain a permeable and considered vibrating surface which encompasses the sources. The latter allows to capture, in addition to the dipole sources generated by the solid surface, the quadrupole sources related to the turbulence in the fluid. However, it requires the storage of $\rho, \rho u, \rho v, \rho w, p$ and its placement is trickier: the coupling surface must be positioned as much as possible outside of hydrodynamic disturbances. Indeed outgoing eddies (quadrupoles) might be interpreted by the FW-H analogy as spurious acoustic sources (dipoles) when crossing the coupling surface. Many articles deal with the issue and propose several corrections to take into account the wake crossing [289–291]. These corrections help to avoid over-estimating low frequencies. In our study, it did not appear useful to close the surface and use flux correction terms, since the comparison of the two formulations in Fig. 7.22 shows identical results at low frequencies. So far in the studies carried out on the LAGOON gear, this method has always given less satisfactory results than the solid one. However, it might be caused by spurious sources and by the dissipation/dispersion between the sources and the permeable surface.

The solid formulation is equivalent to Curle's theory [260] according to which the pressure variation of dipole sources ($p'_{\mathrm{D}} = p_{\mathrm{D}} - P_{ref}$) would be proportional to $p'_{\mathrm{D}} \propto Ma^3$, while quadrupole sources would vary in $p'_{\mathrm{Q}} \propto Ma^4$ according to Lighthill [254, 255]. Therefore, the sound intensity ratio of the two sources $I_{\mathrm{Q}}/I_{\mathrm{D}} = O(Ma^2)$ would be of second order and neglecting the quadrupole sources for low Mach would be an acceptable approximation. However, Spalart refuted this assumption in 2013 [285]. It is based on the simple observation that if one can decompose

$$p'(t) = p'_{\mathrm{D}}(t) + p'_{\mathrm{Q}}(t), \tag{7.4.1}$$

as it is done in acoustic analogies [260, 261], then

$$p'^2 = p'^2_{\mathrm{D}} + p'^2_{\mathrm{Q}} + 2p'_{\mathrm{D}}p'_{\mathrm{Q}}. \tag{7.4.2}$$

A $2p'_{\mathrm{D}}p'_{\mathrm{Q}}$ cross term of order Ma^7 appears in the pressure square which is directly contained in the sound intensity ($I/I_0 = p'^2/p_0^2$) with I_0 and p_0 the reference sound intensity and pressure levels. The approximation $I_{\mathrm{Q}}/I_{\mathrm{D}} = O(Ma)$ is actually of the first-order when dipole and quadrupole sources coexist in the same simulation.

Before addressing the influence of this term, let's first compare the solid and permeable FW-H formulation with a direct propagation computation carried out up to microphones placed at 1.2m under the gear but with the same angles. These results are presented with the G2 mesh, and the direct propagation computation benefits from an extension of the acoustic propagation RD (*cf.* Fig. 7.6) up to these microphones, with a uniform mesh size of 4mm. For obvious CPU cost reasons, direct propagation was only performed for flyover microphones. Noise attenuation inversely proportional to the distance square was simply applied to these signals for comparisons with WTT microphones. For convenience purposes, the effect of the mean field on propagation between the microphone positions in the direct simulation and in the wind tunnel tests was not taken into account.

The far-field propagation is carried out with the FW-H solver KIM from ONERA [268, 269]. The results obtained are compared to recent studies on the LAGOON landing gear using a solid FW-H formulation. These studies were chosen because they all offer excellent aerodynamic results and very good agreement on parietal kulites. Moreover, as can be seen in Fig. 7.22, these three studies give very similar aeroacoustic results and with similar deviations from experiments. The trend is always the same, for the upstream microphone (M3) the noise is overestimated from St = 4 (St = $U_{ref} * f/\mathrm{D}$). The one at 90° (M6) is correctly predicted, and the noise on the M9 downstream microphone is underestimated for St > 7. The same tendency is found for the LaBS results obtained with the solid formulation (LaBS-S). For the latter, the high frequencies are slightly higher than for the other three CFD codes as discussed later on. Nevertheless, the same trend is observed with a little more uncertainty on absolute levels. The results obtained with the permeable FW-H formulation and the direct propagation calculation give results that match, up to the cut-off frequency, over a large portion of the spectrum. The results are much more accurate at the upstream end, where the experimental results are correctly retrieved, unlike all the other codes presented which use a solid F-WH approach. However, an over-estimation is to be noted at the downstream end for St > 20, which might be attributed to remaining grid refinement spurious noise. The solid formulation underestimates the downstream levels, which Hajczak [283] attributes (in our opinion rightly) to neglected quadrupole sources.

Thereafter, an original spectral decomposition of p'^2 is proposed for the various pressure terms given in Eq. (7.4.2). This decomposition will provide a better insight into the gaps observed between the two formulations. Beforehand, the method and recent results proposed by Spalart [273] to decompose in time these terms will be discussed. Spalart proposes to separate the $p'_{\mathrm{D}}(t)$ component coming from the solid FW-H formulation from

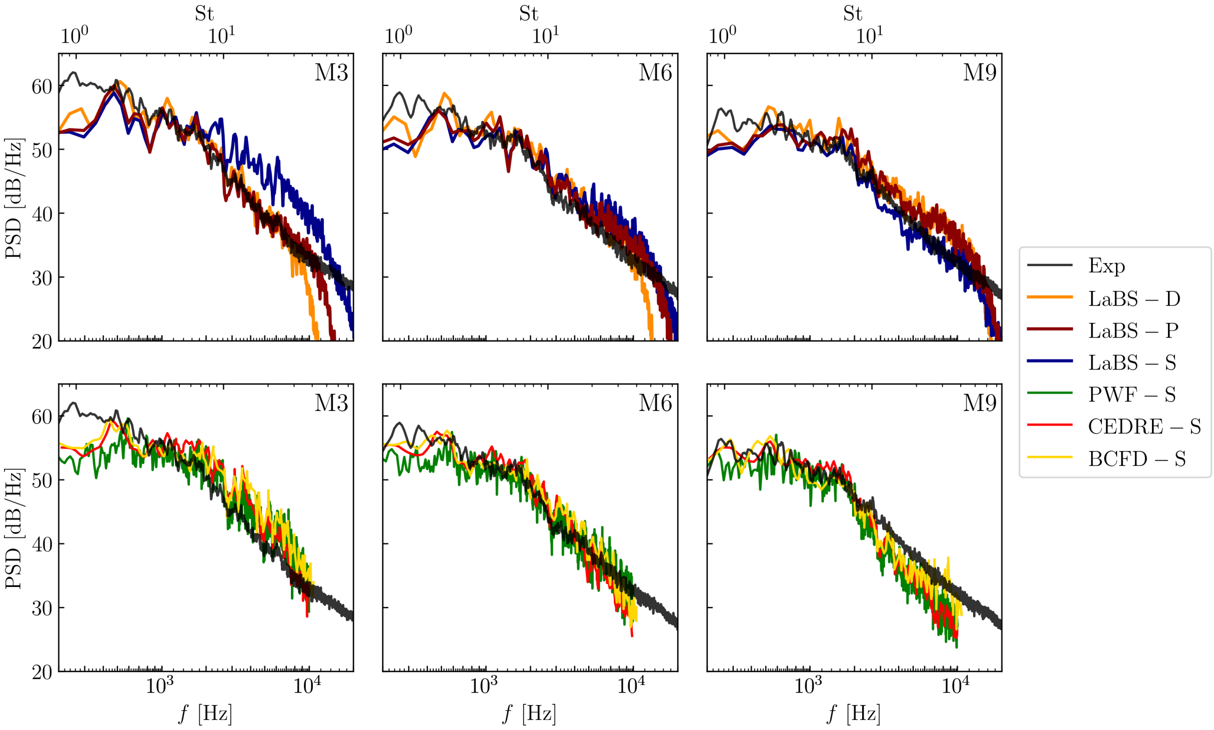

Figure 7.22 – *Power spectral density of far field noise for M3, M6 and M9 microphones located on the flyover arc. Top: LaBS/ProLB simulations with the G2 grid for D: Direct propagation, P: permeable FW-H, S: solid FW-H. Bottom: Others CFD solvers that use a solid FW-H formulation. PWF [51, 52], CEDRE [49], BCFD [50].*

$p'(t)$ obtained with the permeable one. Thus, $p'_{\mathrm{Q}}(t)$ can easily be deduced. In his study, the author is interested in turbulent flows beneath an aircraft fuselage at Ma = 0.25. Whether with a cavity, or a bluff body, the same phenomenon is observed with the solid FW-H formulation: a significant overestimation of the upstream acoustics, and a significant underestimation of the downstream one. He thus plots the temporal evolution of the different components of Eq. (7.4.2) and obtains a very convincing result. In the Tab. 7.3, the ratio of the mean values (referred as $\langle\ \rangle$) of the various components are calculated with regards to $\langle p'^2\rangle$. The result is staggering:

- Upstream: the dipole component is slightly dominant compared to the quadrupolar, which is not easily intuitive. Moreover, the components $\langle p'^2_{\mathrm{D}}\rangle$ and $\langle p'^2_{\mathrm{Q}}\rangle$ are much higher than $\langle p'^2\rangle$ and the cross term is highly negative. In this case, using a solid formulation (that implies $\langle p'^2\rangle = \langle p'^2_{\mathrm{D}}\rangle$) overestimates the noise by 10.45dB.

- Downstream: Quadrupole sources are weakly predominant and the cross term is significantly weaker. Nevertheless, using the solid formulation would underestimate the noise level by 2.6dB.

	$\langle p_{\mathrm{D}}'^2\rangle/\langle p'^2\rangle$	$\langle p_{\mathrm{Q}}'^2\rangle/\langle p'^2\rangle$	$\langle 2p_{\mathrm{D}}'p_{\mathrm{Q}}'\rangle/\langle p'^2\rangle$
Upstream	11.1	8.7	-18.8
Downstream	0.55	1	-0.55

Table 7.3 – *Ratio of the average p'^2 components for a turbulent flow of a bluff body under a fuselage at* $\mathrm{Ma} = 0.25$. *Calculated from [273].*

It is however possible to go further, by decomposing these terms in the frequency domain. Referring to the notions introduced in App. C, one notes $\mathrm{P}(f)$, $\mathrm{P_D}(f)$ and $\mathrm{P_Q}(f)$ the Fourier transform of $p'(t), p_{\mathrm{D}}'(t)$ and $p_{\mathrm{Q}}'(t)$ respectively and * their conjugate values. According to Eq. (7.4.1), the power spectral density of $p'(t)$ reads

$$
\begin{aligned}
|\mathrm{P}(f)|^2 &= \mathrm{P}(f)\mathrm{P}^*(f) \\
&= \big(\mathrm{P_D}(f) + \mathrm{P_Q}(f)\big)\big(\mathrm{P_D}^*(f) + \mathrm{P_Q}^*(f)\big) \\
&= \underbrace{\mathrm{P_D}(f)\mathrm{P_D}^*(f)}_{|\mathrm{P_D}(f)|^2} + \underbrace{\mathrm{P_Q}(f)\mathrm{P_Q}^*(f)}_{|\mathrm{P_Q}(f)|^2} + \underbrace{\mathrm{P_D}(f)\mathrm{P_Q}^*(f) + \mathrm{P_D}^*(f)\mathrm{P_Q}(f)}_{\mathrm{X_{2P_DP_Q}}},
\end{aligned}
\tag{7.4.3}
$$

where the contributions of $p_{\mathrm{D}}'(t)$ and $p_{\mathrm{Q}}'(t)$ appear in the PSD of $p'(t)$ along with two cross spectral densities that account for the $2p_{\mathrm{D}}'p_{\mathrm{Q}}'$ contribution in Eq. (7.4.2). This cross term will be referred as $\mathrm{X_{2P_DP_Q}}$ hereafter.

The decomposition is presented in Fig. 7.23, along with the coherence function. This function is zero if the dipole and quadrupole sources are uncorrelated, and equal to one if they are perfectly correlated. The green curve ($10\log\left(-\mathrm{X_{2P_DP_Q}}/|\mathrm{P}|^2\right)$) directly represents the effect of the cross term $\mathrm{X_{2P_DP_Q}}$ on the red curve of the noise taking into account all contributions $|\mathrm{P}|^2$. The $\mathrm{X_{2P_DP_Q}}$ term is always negative, that's why it is plotted with a minus sign, and causes a decrease of the noise level. Concretely, if the green curve is positive, the $\mathrm{X_{2P_DP_Q}}$ term removes energy from the red one. If it is negative or zero, it can be interpreted as having no noticeable effect.

Upstream, in the same way as in [273], it is observed that quadrupolar sources contribute as much as dipole sources for $\mathrm{St} > 10$, which would result in an additional increase of 3dB compared to the solid FW-H results. However, the $\mathrm{X_{2P_DP_Q}}$ cross term leads to a reduction of 10dB in this Strouhal range and thus allows to recover the experimental results. Upstream, the sources are highly correlated, with a coherence value higher than 0.8 for $\mathrm{St} > 10$. This curve illustrates very well the limitations of the solid FW-H method to correctly predict the noise of a landing gear. For the M6 microphone, the quadrupole sources become dominant at high frequencies, and the $\mathrm{X_{2P_DP_Q}}$ term, as well as the coherence decrease. In this configuration, the solid formulation seems reasonably satisfactory compared to experiments (*cf.* Fig. 7.22). However, it seems that this result is fortuitous with the $\mathrm{X_{2P_DP_Q}}$ term that compensate $|\mathrm{P_Q}(f)|^2$. In this situation neglecting quadrupole sources would give similar results. Finally downstream, the noise is mostly due to quadrupolar, and the sources are poorly correlated. In this situation, neglecting the quadrupole sources would lead to an underestimation of the noise levels, as can be seen with PowerFLOW, CEDRE and BCFD on Fig. 7.22. This result consolidates the recent statements of Hajczak [283] that claims the presence of quadrupole sources in the wake that they have identified using beamforming methods.

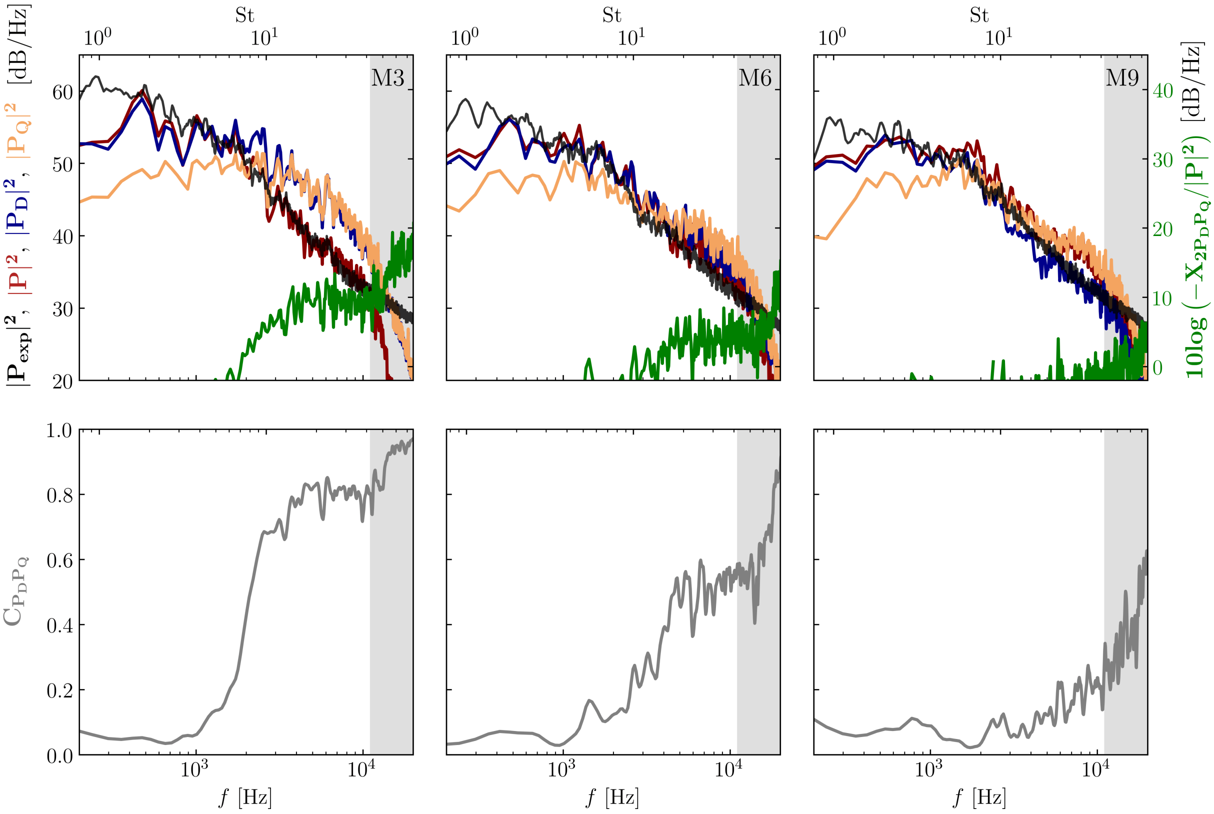

Figure 7.23 – *Top: Separate contributions of dipole and quadrupole sources on the far field noise obtained for M3, M6 and M9 microphones located in the flyover arc.* $|\mathrm{P}|^2$*: total contribution from all sources,* $|\mathrm{P_D}|^2$*: dipole contribution,* $|\mathrm{P_Q}|^2$*: quadrupole contribution,* $10\log\left(\mathrm{X}_{2\mathrm{P_D P_Q}}/|\mathrm{P}|^2\right)$*: influence of the dipole/quadrupole cross term on the total contribution* $|\mathrm{P}|^2$*. Bottom: Coherence function* $C_{\mathrm{P_D P_Q}} = \frac{|\mathrm{P_D P_Q}|^2}{|\mathrm{P_D}|^2 * |\mathrm{P_Q}|^2}$*. Gray area: frequencies above the mesh cut-off.*

However, these results need to be nuanced. Indeed, for this decomposition to be accurate, the CFD calculation would have to be ideal. However, some spurious noise remains downstream which could certainly be attributed to resolution transitions for St > 20, and this is not captured in the same way with the two FW-H methods. The energy of a spurious source related to a wake transition enclosed in the permeable surface will be significantly greater than that of the reflection of a fraction of this spurious source on the gear wall. Similarly, wall pressure extrapolation concerns may affect the solid FW-H but will have no effect on the permeable one. The extrapolation is likely what causes the overestimates of solid FW-H results with LaBS/ProLB compared to the other codes in Fig. 7.22. Indeed, the wall normal in LaBS/ProLB is not considered for extrapolating the pressure. This information is however required in the integration of the wall surface loads by the FW-H solver (*cf.* Eq. (7.1.10)). An inconsistency may occur between the

LaBS/ProLB outputs and the FW-H solver. Caution should therefore be exercised in the analysis of these results at least on absolute levels, as spurious sources may disturb this decomposition. Nevertheless, the conclusions are in perfect agreement with the results of Spalart [273] and Hajczak [283], and the results obtained with other CFD codes using a solid formulation also support our statements.

More generally, the latter conclusion is corroborated by a very recent paper by Ricciardi [292] dating from March 2021, which compares both solid and permeable methods on a complex landing gear, with significant resolution in the wake. Their Figure 24 exhibits exactly the issues of the solid formulation that we highlight here with an overestimation of levels upstream and an underestimation downstream. This provides further evidence of the issues encountered with the solid formulation.

As computing resources grow, and CFD solvers become more and more accurate, performing clean FW-H permeable propagations will become increasingly affordable. This should allow to re-evaluate the conclusions on permeable FW-H for landing gear noise prediction. It would also be very interesting to compare this decomposition with other solvers in the coming years.

7.4.3 Far-field acoustic results

The acoustic results obtained in the far-field with the FW-H permeable method are presented for the various grids in Fig. 7.24. First, it can be noticed that increasing the parietal resolution allows to better capture low frequencies ($f < 800Hz$). According to [9, 21], the axle and the leg contribute mostly in this frequency range for flyover and sideline microphones respectively. This will be further corroborated by analyzing the wall pressure maps filtered by frequency bands in Sec. 7.4.4. These elements are of small dimensions with Reynolds numbers of $2.9 \cdot 10^5$ and $2.3 \cdot 10^5$ for the leg and the axle respectively. According to the grids, their resolutions are ~ 50, ~ 100 and ~ 200 cells per diameter for the G1, G2 and G3 grids. These resolutions are rather low to capture the flow around a turbulent cylinder in critical regime. The G3 mesh offers much better results on these components (*cf.* Fig. 7.10 and 7.18), and more generally on all microphones. Finally, the cavity tonal peak at 1kHz is well captured whatever the mesh size for sideline microphones, as predicted by the kulite analysis in Sec. 7.3.5. This peak does not appear on flyover microphones since they are located on the $y = 0$m plane which is a pressure node for this cavity mode [32, 51, 52].

Downstream, spurious transition noise is visible for $f > 5$kHz. Nevertheless, noise levels in these frequency ranges are low and weakly contribute to the OASPL (Overall Sound Pressure Level). For lower frequencies, the predicted noise is physical and the underestimates related to the solid FW-H formulation visible for other CFD codes on Fig. 7.22 do not appear here anymore. This reinforces the thesis of the predominance of downstream quadrupole sources for $f > 2$kHz.

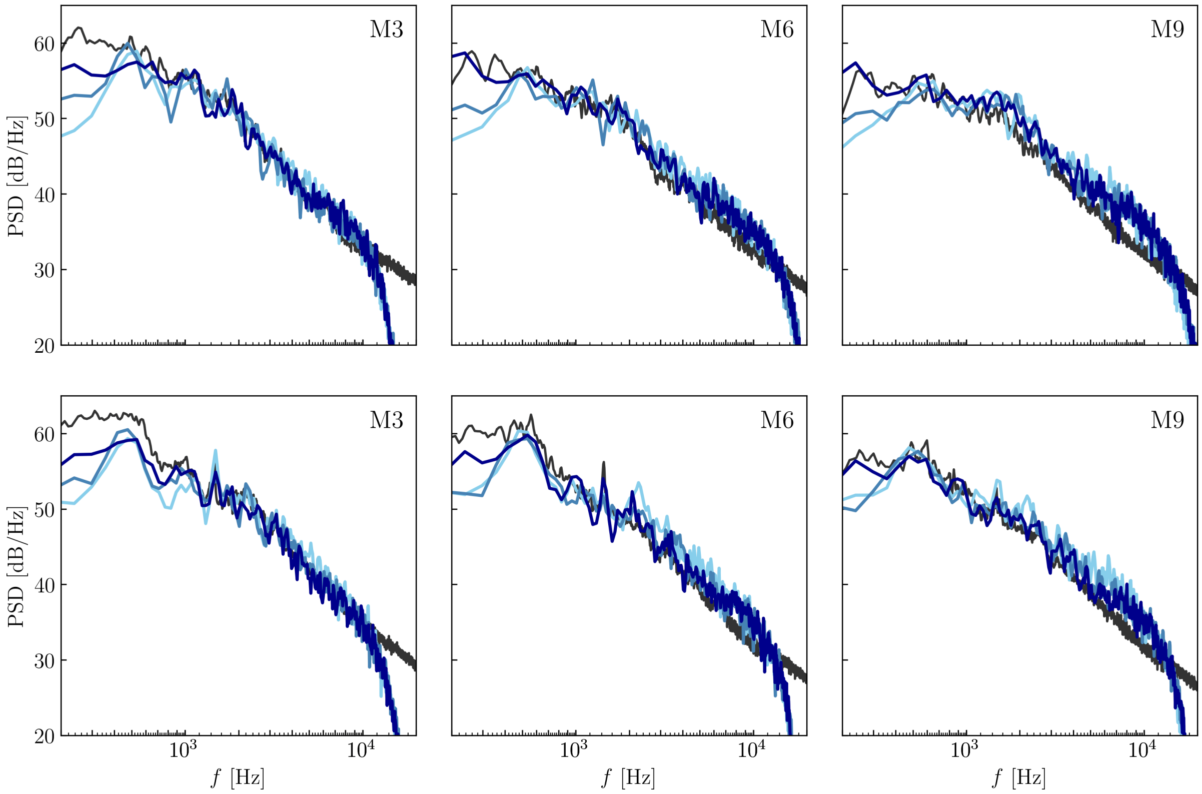

Figure 7.24 – *Power spectral density of far field noise for M3, M6 and M9 microphones obtained with the permeable FW-H formulation. Top: Flyover arc, bottom: Sideline arc.* (—): *G1 grid,* (—): *G2 grid,* (—): *G3 grid,* (—): *Experiments.*

The values of the integrated OASPL on the 200Hz to 10kHz frequency band are shown in Fig. 7.25. The angles do not correspond exactly to those presented in Fig. 7.21 since they take into account the refraction correction related to the shear layer in the experiments. In addition, the M7 flyover microphone has a higher level than its neighbors. This is simply because it is located at a smaller distance from the landing gear than others microphones.

Directivity is well captured with much higher noise levels upstream than downstream for both microphone arcs. The G3 fine mesh is the most accurate with a maximum deviation of 2dB upstream. This deficit comes from the lack of axle and leg resolution. Finally, the M12 microphone (30°) is not presented since it is almost tangent to the wake. Therefore, the open permeable surface used for the FW-H coupling does not allow to capture all the acoustics for this angle and the levels obtained are too low which is not physical.

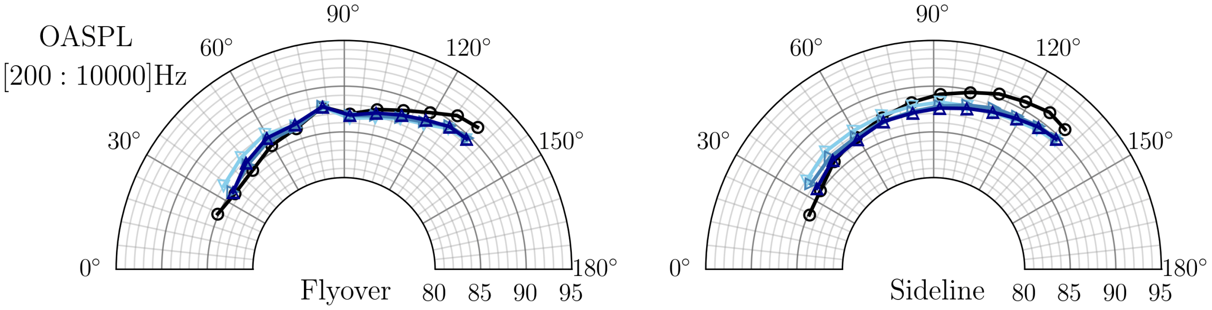

Figure 7.25 – *OASPL integrated in the 200Hz to 10kHz frequency bands. Left: Flyover arc, Right: Sideline arc. (▽): G1 grid, (▷): G2 grid, (△): G3 grid, (○): Experiments.*

7.4.4 Frequency band filtered pressure maps

Frequency band filtered unsteady pressure maps are of great interest for locating dipole wall acoustic sources. In particular, they allow to highlight areas of boundary layers separation or vortex impingement.

However, this method applied to the landing gear skin has several limitations that should be kept in mind:

- It does not allows to locate quadrupole sources, nor their interactions with dipole ones.
- It does not take into account constructive or destructive interferences that occur while propagating to the far-field.
- Acoustic reflecting surfaces can be confused with actual sources (as it was for instance the case of kulites K13, K14, K15 located in the upstream part of the wheel inner flank where two tonal peaks appeared coming from the cavity mode).

In Giret's PhD thesis, third-octave integration bands are provided [9]. In view of the broadband character, only three bands of integration are chosen here: [100-800]Hz, [800-2000]Hz and [2000-10000]Hz. Results are given in Figs. 7.26 to 7.28.

These maps indicate that:

- The noise is broadband in nature and comes from flow separation on the leg, the axle, the inner and outer flanks of the tires, as well as the rear part of the tires which is heavily sheared.
- The impingement of the vortex shedding on the inner downstream flank of the wheel is a major source of noise.
- The spatial resolution greatly influences the separation areas.

This last point is the one we are interested in to shed light on the visible gaps in the spectra between the three grids (*cf.* Fig. 7.24). According to Giret [9] and Zhang [21], the axle and the leg are mainly responsible for the noise emitted at low frequencies ($f < 500Hz$). However, it is clearly seen that the levels of pressure fluctuations in this frequency range for these components increase sharply when refining the mesh, which may explain the improvements obtained with the G3 mesh. Another interesting point is the position of the flow separation on the outer flank of the wheels. The latter is moving towards the upstream part by refining the mesh. This results is in agreement with the oil-test of Rego [293] at Mach 0.1 and the simulations of Giret [9] and De la Puente [270]. Moreover, broadband noise in the frequency range [500-10000]Hz is dominated by wheels [9, 21]. For all three grids, the levels of pressure fluctuations are similar in the downstream inner flank of the tires. These fluctuations result from vortex shedding impingements that are generated upstream of the tire flank and of the axle. This could explain why even the G1 coarse mesh is partly able to predict the broadband noise on this simple landing gear.

However, the direct link between these pressure maps and far-field noise cannot be directly established. It could be very useful to use beamforming methods [14–16] to corroborate these observations.

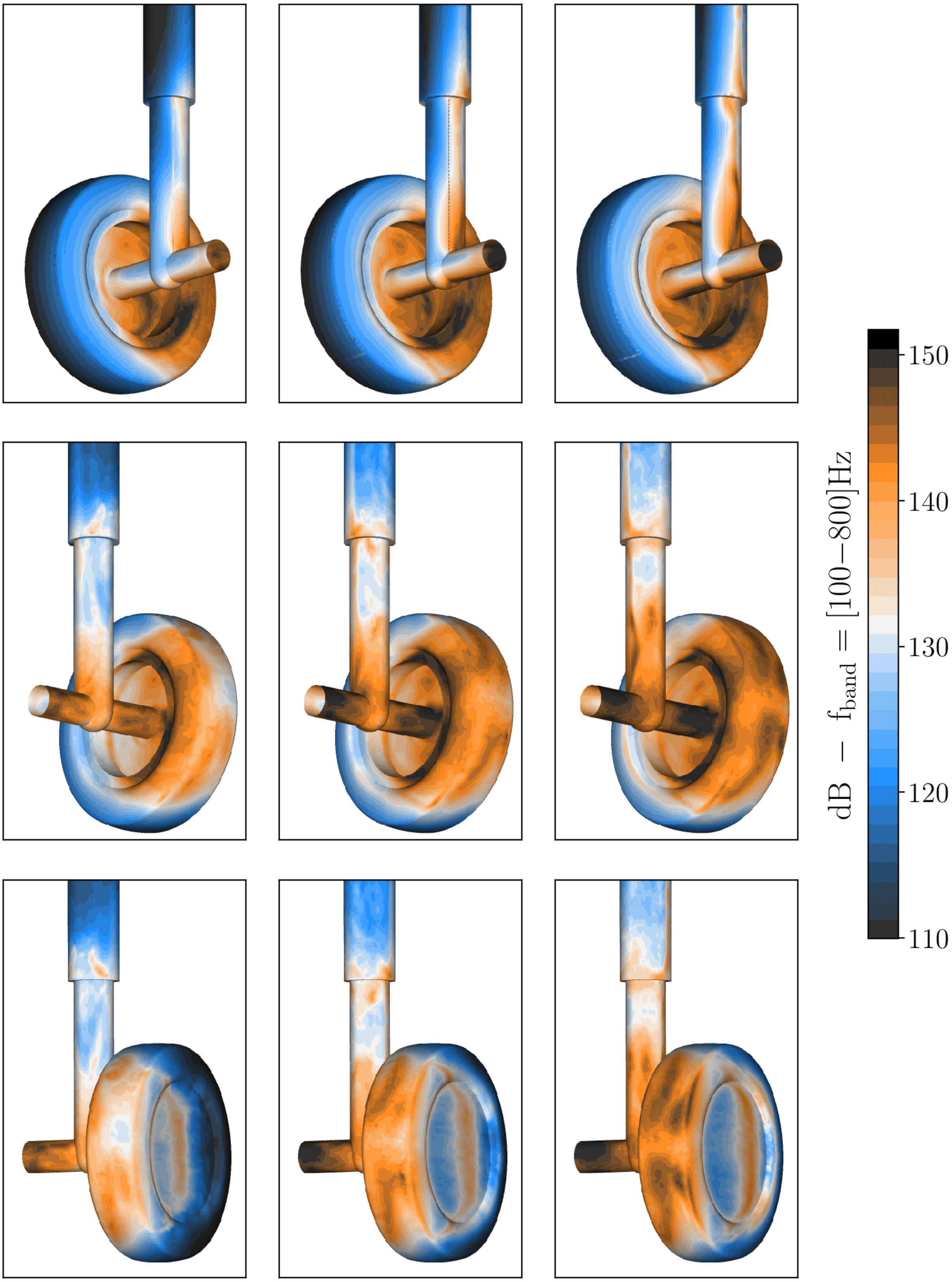

Figure 7.26 – *Wall pressure band map ranging from 100 to 800Hz. From top to bottom: Inboard front view, inboard rear view, outboard rear view. From left to right: G1, G2, G3 grid.*

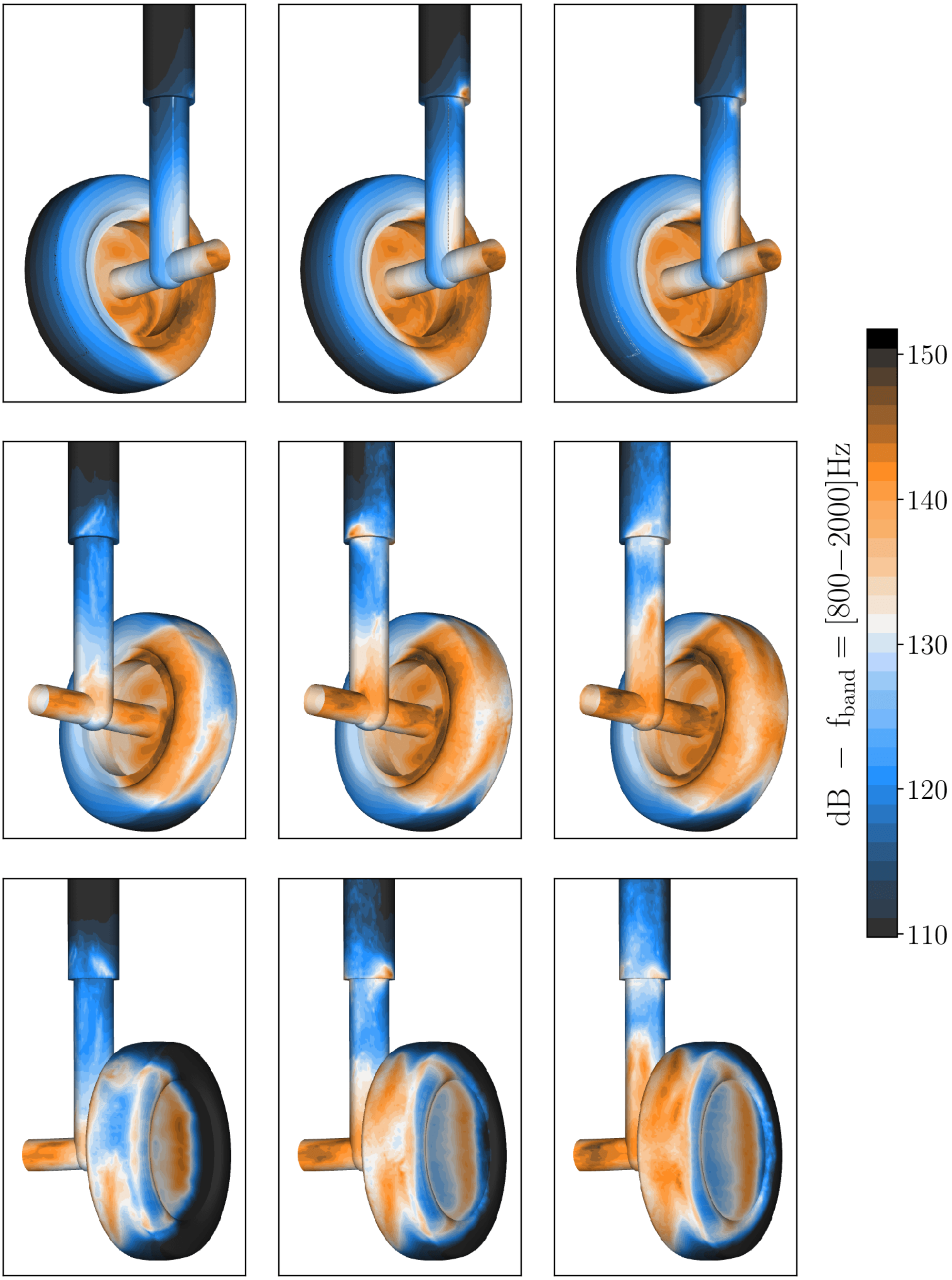

Figure 7.27 – *Wall pressure band map ranging from 800 to 2000Hz. From top to bottom: Inboard front view, inboard rear view, outboard rear view. From left to right: G1, G2, G3 grid.*

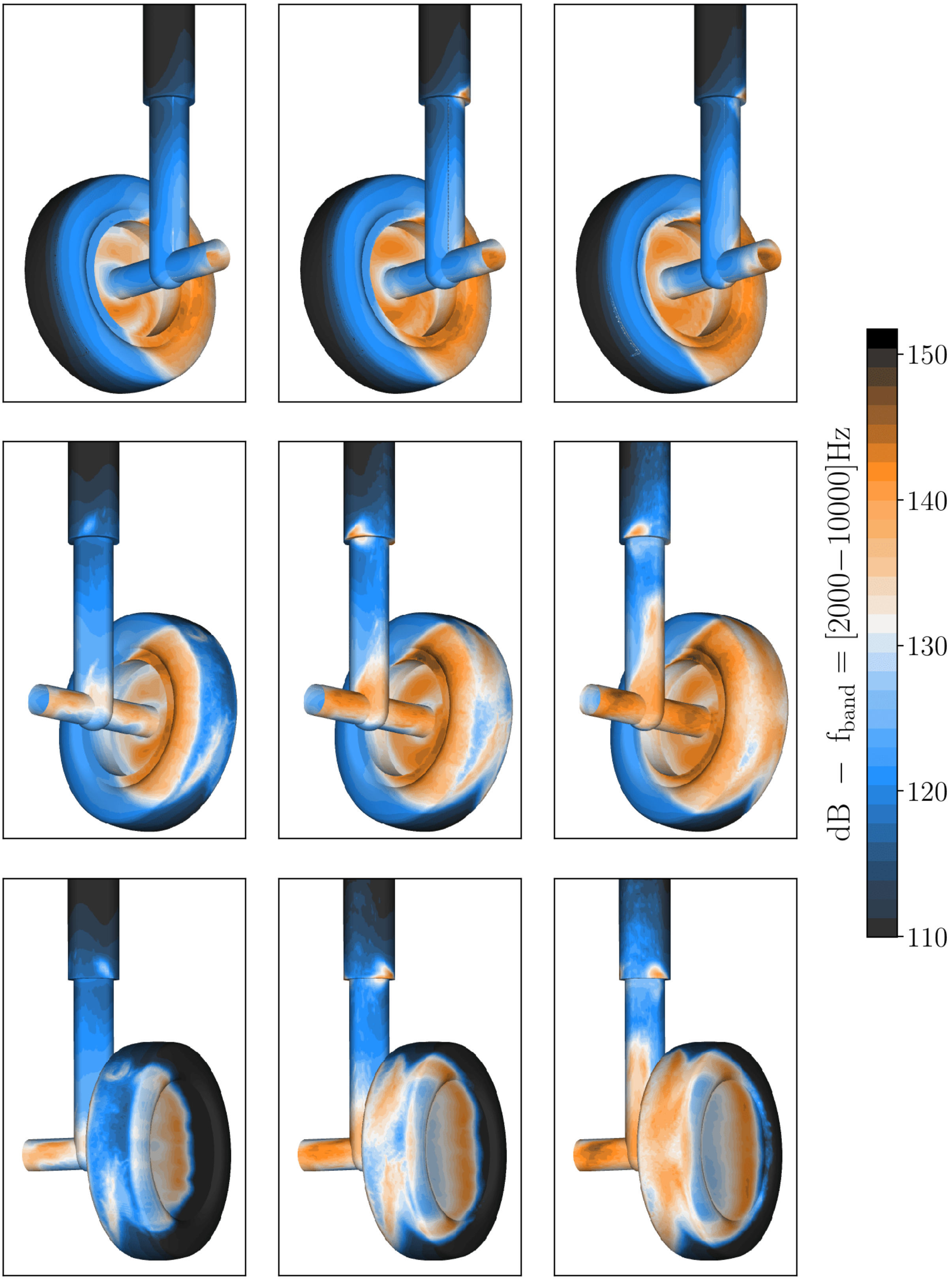

Figure 7.28 – *Wall pressure band map ranging from 2 to 10kHz. From top to bottom: Inboard front view, inboard rear view, outboard rear view. From left to right: G1, G2, G3 grid.*

7.5 Conclusion of the LAGOON 1 study

This chapter aims at validating the new LBM ingredients adapted to the landing gear aeroacoustic framework that have been investigated in this manuscript.

For this purpose, an aerodynamic study was first carried out for three grids of increasing resolution. By analyzing the unsteady kulites, it came out that the development of the turbulent boundary layer on the wheels is very well retrieved by refining the mesh, as well as the two tonal peaks at 1kHz and 1.5kHz corresponding to cavity modes. The only downside identified is the prediction of separation points on the axle and the leg which are in critical flow regime and require a high resolution. In the wheels wake, the PIV planes, as well as the average and fluctuating velocity profiles obtained by LDV in the experiments are very well recovered. Moreover, the spectral behavior extracted on a 0.3D probe downstream of the left wheel shows velocity fluctuations in accordance with the experiment. Finally, the spurious vorticity observed with the filtered DRT scheme completely vanished when using the H-RR$_\psi$ collision model.

Subsequently, the focus shifted to aeroacoustic predictions. The latter are much more sensitive from a numerical point of view in LBM, since in addition to being prone to spurious vorticity problems influencing aerodynamics, they are very exposed to parasitic noise sources that can disrupt the predictions. We have thus quantified the contribution of the H-RR$_\psi$ model and DC resolution transitions compared to the filtered DRT model coupled with STD grid coupling algorithm. As expected, the H-RR$_\psi$ model completely eliminated the non-hydrodynamic modes responsible for spurious vorticity and parasitic acoustic sources. In addition, unwanted acoustic sources originating from eddies passing through the wake resolution interfaces have been reduced thanks to the suppression of non-physical turbulence caused by SpuriousS waves (*cf.* Chap. 4). Finally, the H-RR$_\psi$ model coupled with the DC algorithm allowed a huge reduction of spurious sources, by more than 10dB on a pressure probe positioned downstream of the landing gear.

As direct acoustic propagation to the wind tunnel microphones was not considered for the LAGOON gear due to the large propagation distance. As all the previous studies on this case, an acoustic propagation solver based on the FW-H analogy was used. It was demonstrated that the solid formulation, mostly used for the prediction of landing gear noise was not valid in this context. Indeed, neglecting quadrupole sources in such a simulation is responsible for a strong over-estimation of noise levels upstream, and under-estimation of levels downstream over a wide range of frequencies. This has been illustrated based on the recent work of Spalart [273, 285], and by proposing a spectral decomposition of the different noise contributions.

This result reinforces the need to use numerical ingredients that minimize spurious effects. Indeed, a permeable surface should ideally be placed outside of hydrodynamic fluctuations, and necessarily includes resolution transitions in the wake. Moreover, it requires a precise numerical scheme to correctly propagate the acoustics from the source to the surface. This formulation is much more complex to implement and previous attempts on LAGOON [43, 48] have not shown any benefits from this formulation as opposed to our results.

We obtained a deviation from experiments of less than 1.5dB on OASPLs. This discrepancy is most probably due to the lack of resolution of the axle and the leg. A slight overestimation of the noise levels is however to be deplored at high frequencies for the downstream microphones, which could be attributed to grid refinement noise.

Finally, a growing number of recent references show the attractiveness of quadrupole sources for landing gear noise prediction [273,283]. Even experimentally, the recent study by Rego *et al.* [293] observed for p'^2 a noise scaling as a function of Mach number ranging from 6 at low frequencies, to 8 at high frequencies on Fig. 17. It could be very interesting to reproduce this study with CFD solvers in the coming years.

Chapter 8

Aeroacoustic study of the LAGOON 2 and LAGOON 3 landing gears: component effects

Contents

This chapter evaluates the ability of LaBS/ProLB to capture the effect of extra components to the LAGOON 1 gear. For this purpose, the LAGOON 2 and LAGOON 3 configurations are considered. These configurations allow to progressively come closer to a realistic landing gear. As in the previous chapter, an aerodynamic study followed by an aeroacoustic one is carried out. The interaction phenomenon between the tow-bar and the leg will be particularly discussed, since it is at the origin of a tonal peak which will be especially complex to capture.

In this chapter, numerical simulations of the LAGOON 2 (L2) and LAGOON 3 (L3) configurations are carried out, in order to validate the effects of the additional components. These configurations have been less studied than LAGOON 1 because of confidentiality purposes. The only available studies on LAGOON 2 are that of Sanders [45] with elsA, and a confidential part of the Giret's thesis [9] that deals with both L2 and L3 carried out with the AVBP solver.

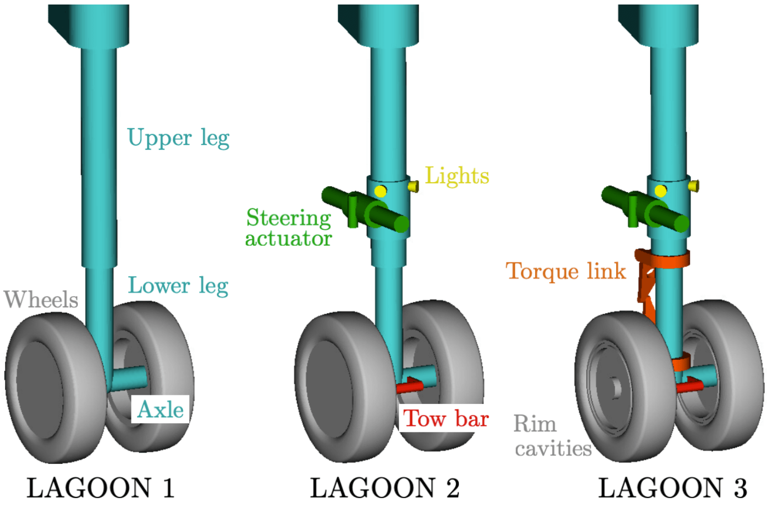

Figure 8.1 – *The three* LAGOON *mock-ups.*

8.1 Numerical setup

The simulation conditions are identical to those of the previous chapter. Only one grid is studied, based on the G3 fine mesh. Additional meshing specifications are introduced to take into account extra components:

- Tow-bar: cylinder of small dimensions (D_{tb} = 0.02m) with a Reynolds number $\mathrm{Re}_{\mathrm{D}_{\mathrm{tb}}}$ = 106000. This component is at the origin of a tonal noise at 1100Hz resulting from the interaction between the tow-bar vortex shedding and the lower leg [45]. Given its small size, this element requires to decrease the minimum mesh size, and thus strongly increases the computation cost. A mesh size of Δx_{min} = 0.0625mm is chosen, corresponding to $\mathrm{D}_{tb}/\Delta x_{min}$ = 320. Moreover, the wake of the tow-bar is finely resolved hoping to capture the interaction with the leg.

- Steering actuator and lights: These components probably do not require very high resolution, since the detachment locations are imposed by the geometry (*cf.* Fig. 8.4). Moreover, according to Sanders [45], these components are expected to contribute very little to the far field noise. $\Delta x_{min} = 0.25$mm will be imposed, as on the whole gear.

- Torque-link: This component is located downstream of the leg and the interaction between these two components is of importance for noise prediction. A refinement zone of constant size $\Delta x = 1$mm is therefore added to capture this interaction. The torque-link itself is solved with the same mesh size as the whole landing gear.

- Rim cavities: These cavities enforce a well-localized geometric detachment. The turbulent structures produced must be sufficiently resolved until the downstream end of the wheel to capture the vortex impingements. A maximum mesh size of $\Delta x = 1$mm in the cavity is chosen for this purpose.

The grid used is displayed on the Fig. 8.2.

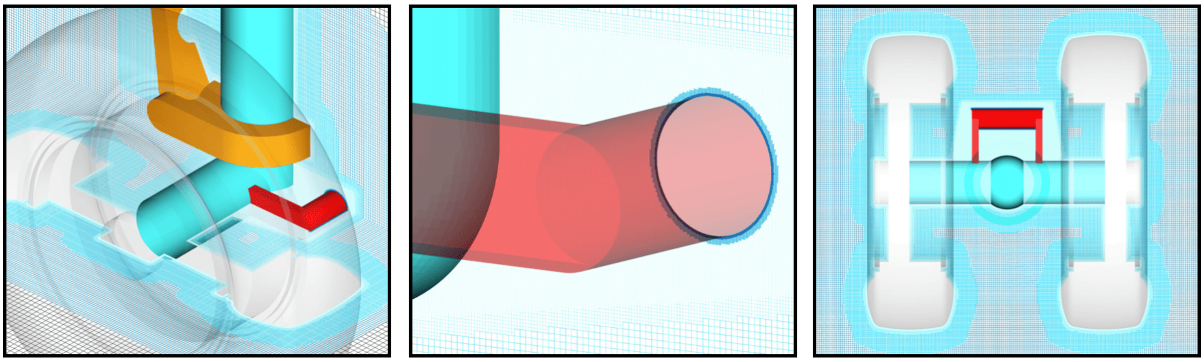

Figure 8.2 – *Mesh used for the* LAGOON 3 *study. The* LAGOON 2 *grid is identical except for the shared components.*

The Tab. 8.1 gives details on the volume grids used. The total number of cells has been increased by about 50%. This extra cost is mainly attributed to the tow-bar and its wake. Moreover, it can be seen that the addition of the torque-link and inner and outer rim cavities only slightly increases the volume of the mesh between L2 and L3 (15M cells). We are conscious that the tow-bar mesh and its wake are not optimal and that many cells could be saved in future studies. More generally, the mesh is constructed to avoid intersections of transition with the walls. Indeed, these intersections still generate some spurious acoustics that we want to avoid. Promising work has been started during the thesis on this issue but has not reached a sufficient level of maturity to be used in the present simulations. Finally, the number of fine equivalent nodes for both L2 and L3 is significantly lower than in the L1 case, since only the tow-bar is included in RD1, unlike the entire LG.

Tab. 8.2 summarizes the performance of the solver for these various simulations. The extra cost, mainly attributed to the tow-bar, is about a factor of three on the computational cost. Further ongoing works on the scalability of the solver are expected to decrease

Mesh	Number of cells ($\cdot 10^6$)	Equivalent fine ($\cdot 10^6$)	Δx_{min} (mm)	Δt_{min} ($\cdot 10^{-7}$ s)
L1	235	112	0.25	4.21
L2	346	39	0.0625	1.05
L3	361	42	0.0625	1.05

Table 8.1 – *Grids used for the L2 and L3 gears with associated numerical parameters. The L1 is added as a reference.*

this factor. In any case, this extra cost is substantial, and one can already imagine that simulating a complex landing gear where one wants to finely capture the effect of the dressings proves to be a major challenge.

Conf.	Total CPU time (h)	Total clock time (h)	CPU cores	CPU/elem/it (10^{-6}(s))	CPU/elem/1ms (10^{-3}(s))
L1	28000	55	512	0.76	1.84
L2	96300	120	800	0.32	3.05
L3	105300	131	800	0.33	3.14

Table 8.2 – *Computation time informations. The* L1 *is added as a reference.*

Similar procedure as used in Chap. 7 will be followed : First, an aerodynamic study will be carried out with the investigation of PIV planes located downstream of the add-on components, and the study of the wall kulites. Then, the far-field acoustics will be considered in terms of PSD and integrated overall sound pressure level directivity.

8.2 Aerodynamic results

8.2.1 PIV planes

PIV planes have been positioned in the wake of the additional components (*cf.* Fig. 8.3). For the LAGOON 2 configuration, they are located downstream of the steering actuator and lights, and for the LAGOON 3, at several sections along the torque-link. Moreover, a common plane is available in $z = 0$m as previously studied for the LAGOON 1.

8.2.1.a PIV planes of the LAGOON 2 configuration

The streamwise and crosswise velocity fields and their associated fluctuations for the LAGOON 2 are shown on Fig. 8.5 and Fig. 8.6. The three components effects considered are:

- The tow-bar: the flow in the $z = 0$m plane is only affected by the inclusion of the tow-bar. Compared to LAGOON 1 (*cf.* Fig. 7.12), relatively few differences are noticeable in this plane regarding the mean velocities, except a slight acceleration of the flow in the symmetry plane of the gear that is well captured by the simulation.

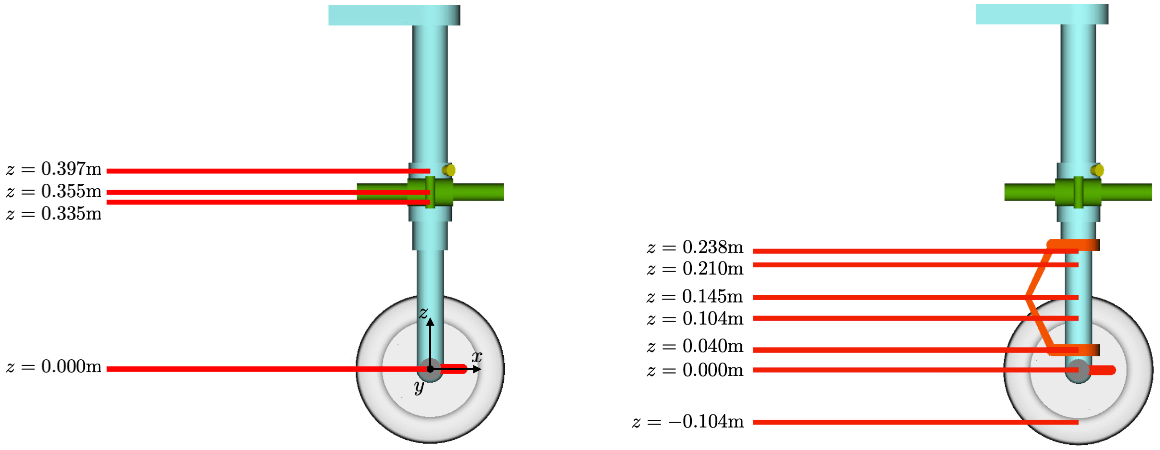

Figure 8.3 – *PIV plane positions for the* LAGOON 2 *(left) and* LAGOON 3 *(right).*

The velocity fluctuations are strongly reduced downstream of the axle. This is explained by a slowdown of the flow caused by the tow-bar, which is well recovered.

- The steering actuator: the $z = 0.335$m and $z = 0.355$m planes are located at two positions downstream of this element. The latter generates a massive detachment illustrated on Fig. 8.4 which is rather well captured in the simulation. The obtained fluctuation levels are slightly underestimated for the crosswise velocity, that can probably be attributed to the insufficient resolution of the steering actuator wake.

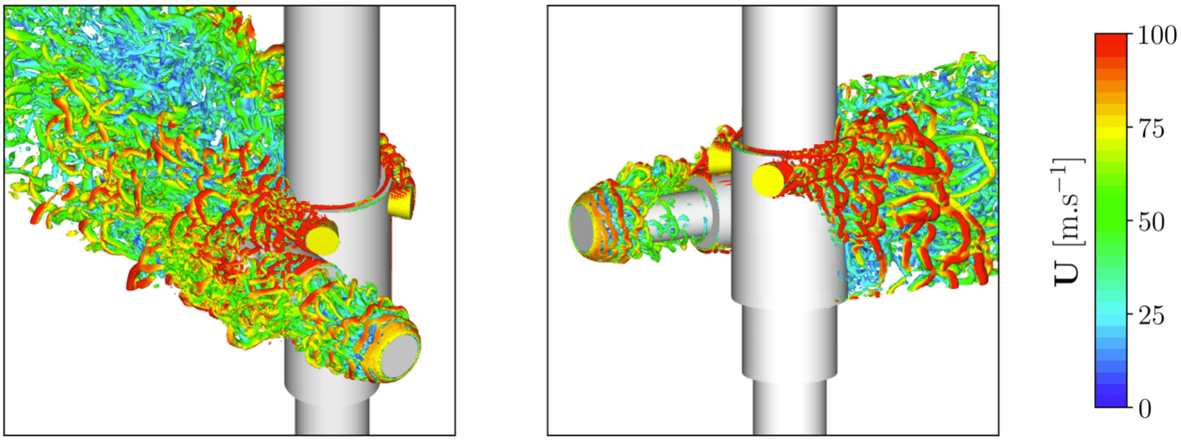

Figure 8.4 – *Iso-surface of* Q-criterion = $2 \cdot 10^7$ *colored by the velocity magnitude around the steering actuator and the lights.*

- The lights: the $z = 0.397$m plane depicts the flow downstream of the lights. The latter imposes a sharp geometrical separation as shown on Fig. 8.4. The flow presents a dissymmetry caused by the steering actuator which is particularly visible on the crosswise velocity component. The mean values show good agreement, however, with a slightly over-extended recirculation region. A deficit in velocity fluctuation is observed on the crosswise velocity, that can probably be attributed to the low resolution of the lights wake.

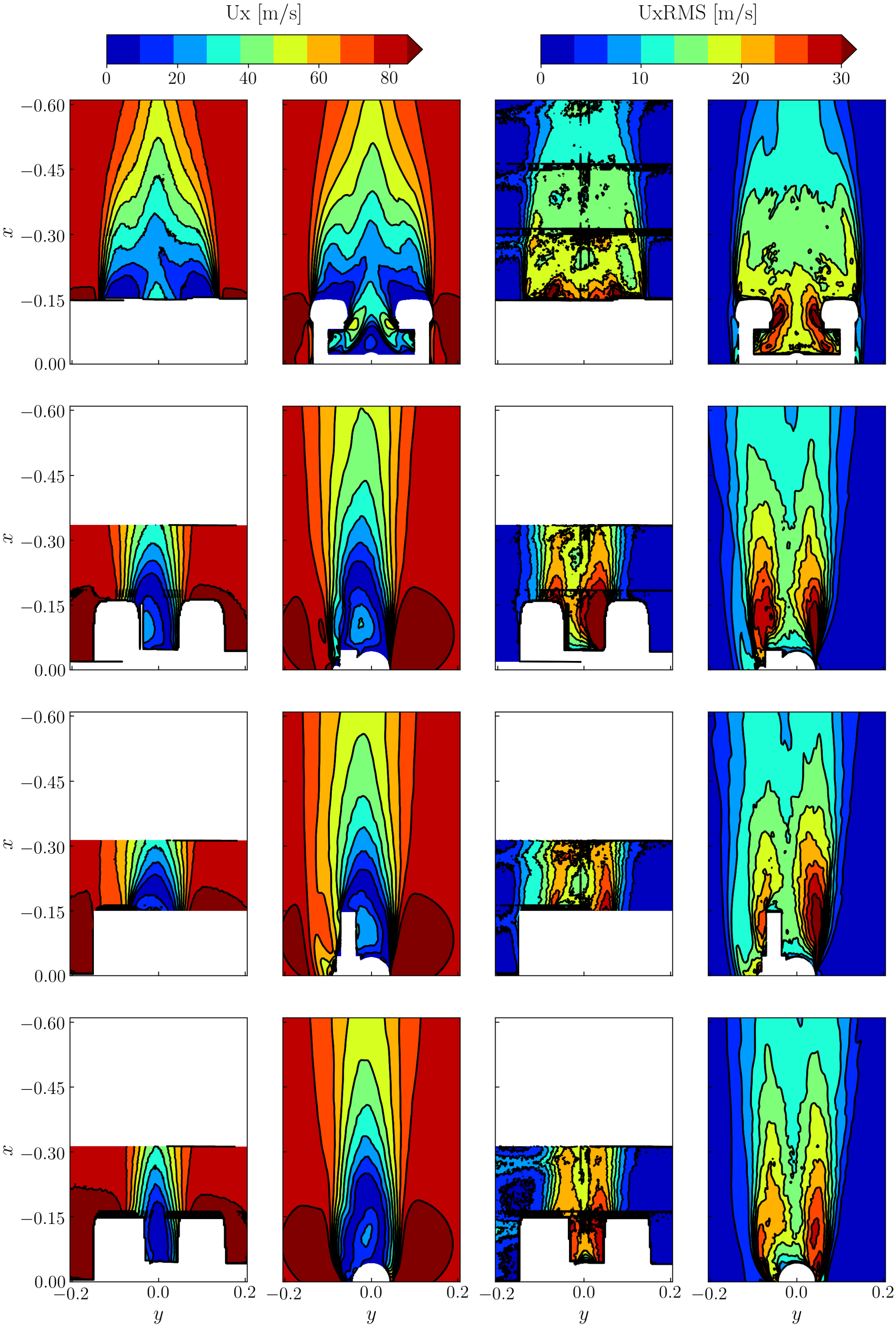

Figure 8.5 – *Comparison with PIV measurements for the streamwise velocity component of the LAGOON 2 configuration. From top to bottom:* $z = 0$m, $z = 0.335$m, $z = 0.355$m, $z = 0.398$m. *Left: Experiments, Right: LaBS/ProLB.*

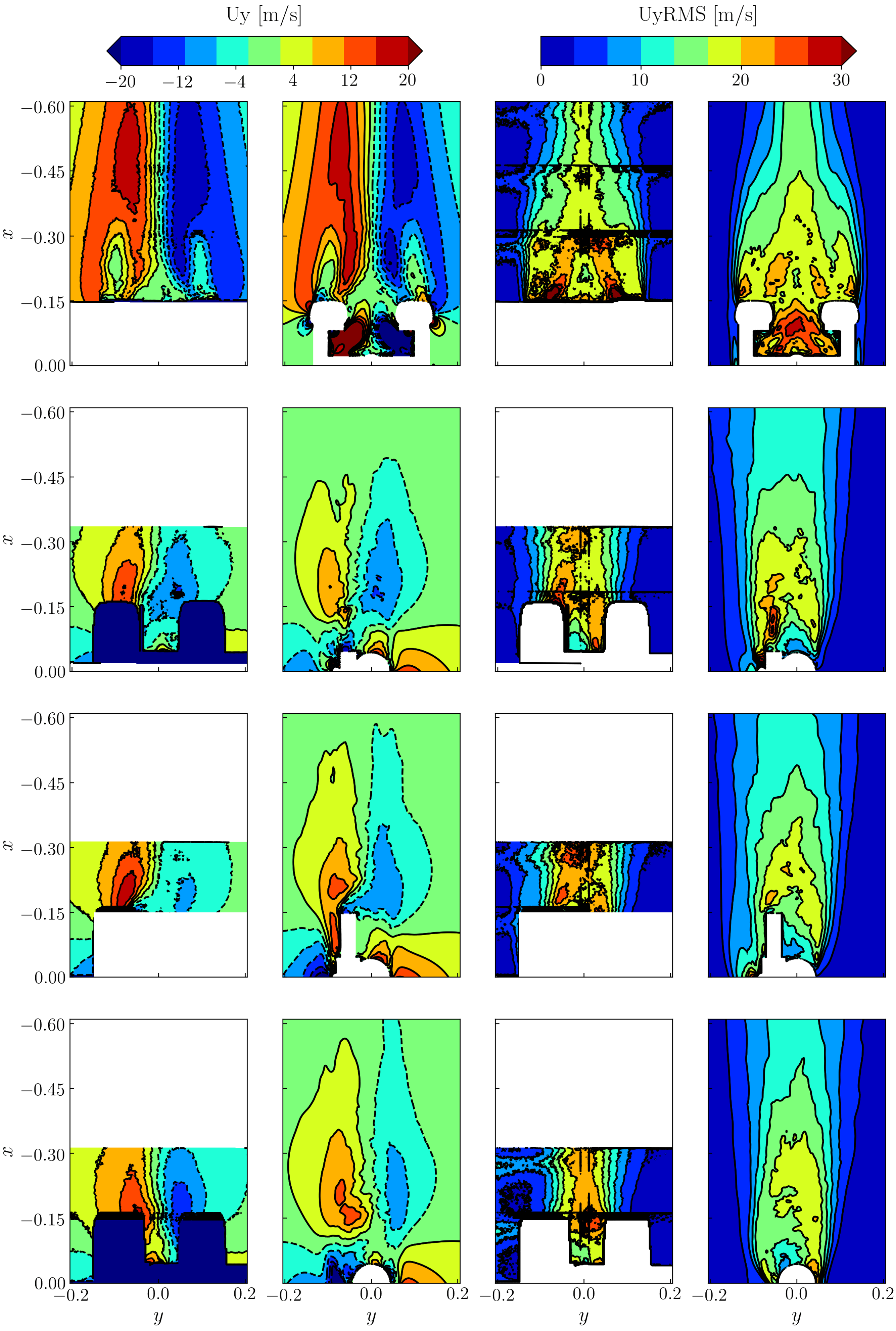

Figure 8.6 – *Comparison with PIV measurements for the crosswise velocity component of the LAGOON 2 configuration. From top to bottom:* $z = 0\text{m}$, $z = 0.335\text{m}$, $z = 0.355\text{m}$, $z = 0.398\text{m}$. *Left: Experiments, Right: LaBS/ProLB.*

The comparisons with the PIV planes are overall quite satisfactory with regard to the LAGOON 2 configuration. The torque-link and rim cavity effects are investigated in the next section for the LAGOON 3 configuration.

8.2.1.b PIV planes of the LAGOON 3 configuration

The PIV planes for several sections of the LAGOON 3 configuration are displayed from Fig. 8.9 to Fig. 8.12. Unfortunately, the PIV of velocity fluctuations are highly noisy in the experiments. The two components effects studied are the rim cavities effect where the caps have been removed, and the torque-link effect.

- Rim cavity: This effect is visible on the $z = 0$m plane and on Fig. 8.7, where the open cavity is compared to a sealed one as on L2. There is a clear thickening of the wake downstream of the tires. This is caused by a late and partial re-attachment of the flow at the downstream portion of the rear tire. Most of the separated flow does not re-attach to the rear wheel as it did when the cavities were sealed. Therefore, the streamwise and crosswise velocity fluctuations which were very low, strongly increase in this area, which is affected by higher vortex impingements. The suction effect of the flow towards the landing gear symmetry axis that is induced by the leg is intensified. This is visible on the crosswise component of the velocity which presents a higher magnitude as well as more intense fluctuations near the symmetry axis. These phenomena are perfectly captured by the simulations. Finally, the effect of the inner cavity covers that have been removed does not seem to be noticeable in the simulation. This cannot be confirmed by the PIV which are shielded in this area.

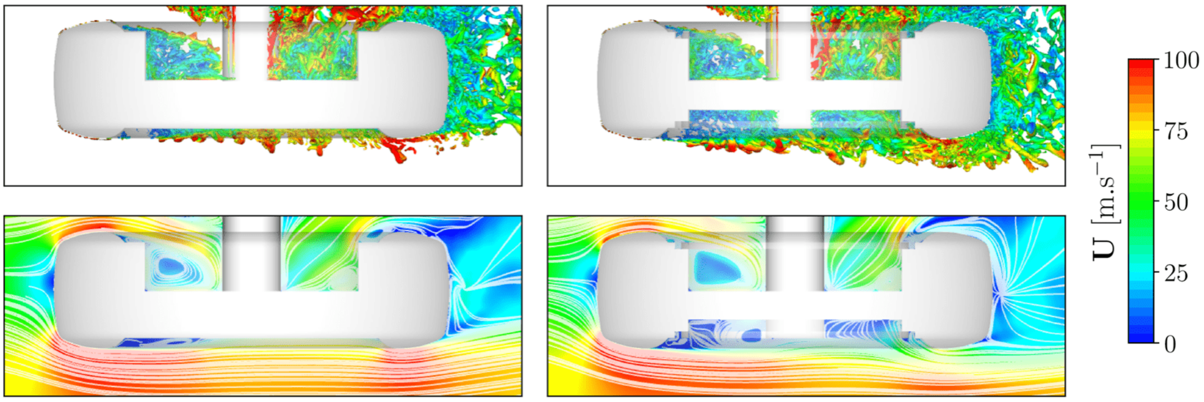

Figure 8.7 – *Top: Iso-surface of* Q-criterion $= 2 \cdot 10^7$ *colored by the velocity magnitude around the right wheel. Bottom: Mean velocity fields and associated streamlines. Left: LAGOON 2, Right: LAGOON 3.*

- Torque-link: This effect is visible on the sections from $z = 0.04$m to $z = 0.238$m. This component undergoes a strong interaction with the vortex shedding that comes from the upstream leg, as illustrated on Fig. 8.8. This interaction results in high velocity fluctuations on the sections located from $z = 0.104$m to $z = 0.210$m. A good agreement with experiments is achieved for this component, both on the average and fluctuating velocities.

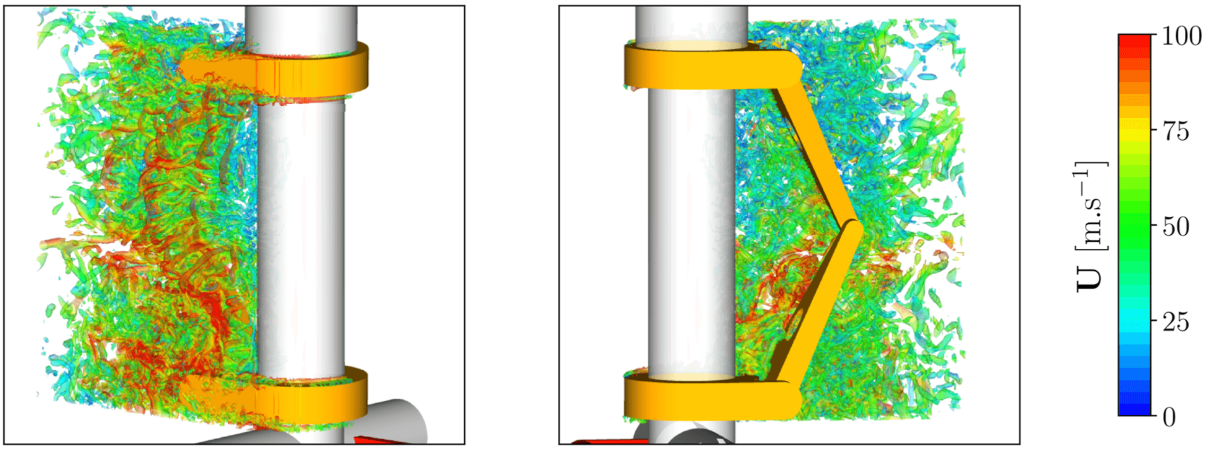

Figure 8.8 – *Iso-surface of* Q-criterion = $2 \cdot 10^7$ *Iso-surface of* Q-criterion = $2 \cdot 10^7$ *colored by the velocity magnitude around the torque-link.*

The last PIV plane available in the experiments is located at $z = -0.104$m. This plane does not exhibit any component effect and the flow is, *a fortiori*, almost identical for the three configurations. The flow is strongly sheared with the mixture of the streams coming from the outside of the wheels merging with the one going through the inside which is accelerated. The agreement with the experiments is excellent.

The comparisons of the PIV planes for the LAGOON 3 configuration show a very good agreement with the experiments. The rim cavities and the torque-link are two elements that are subject to significant vortex impingements and are likely to be significant acoustic sources.

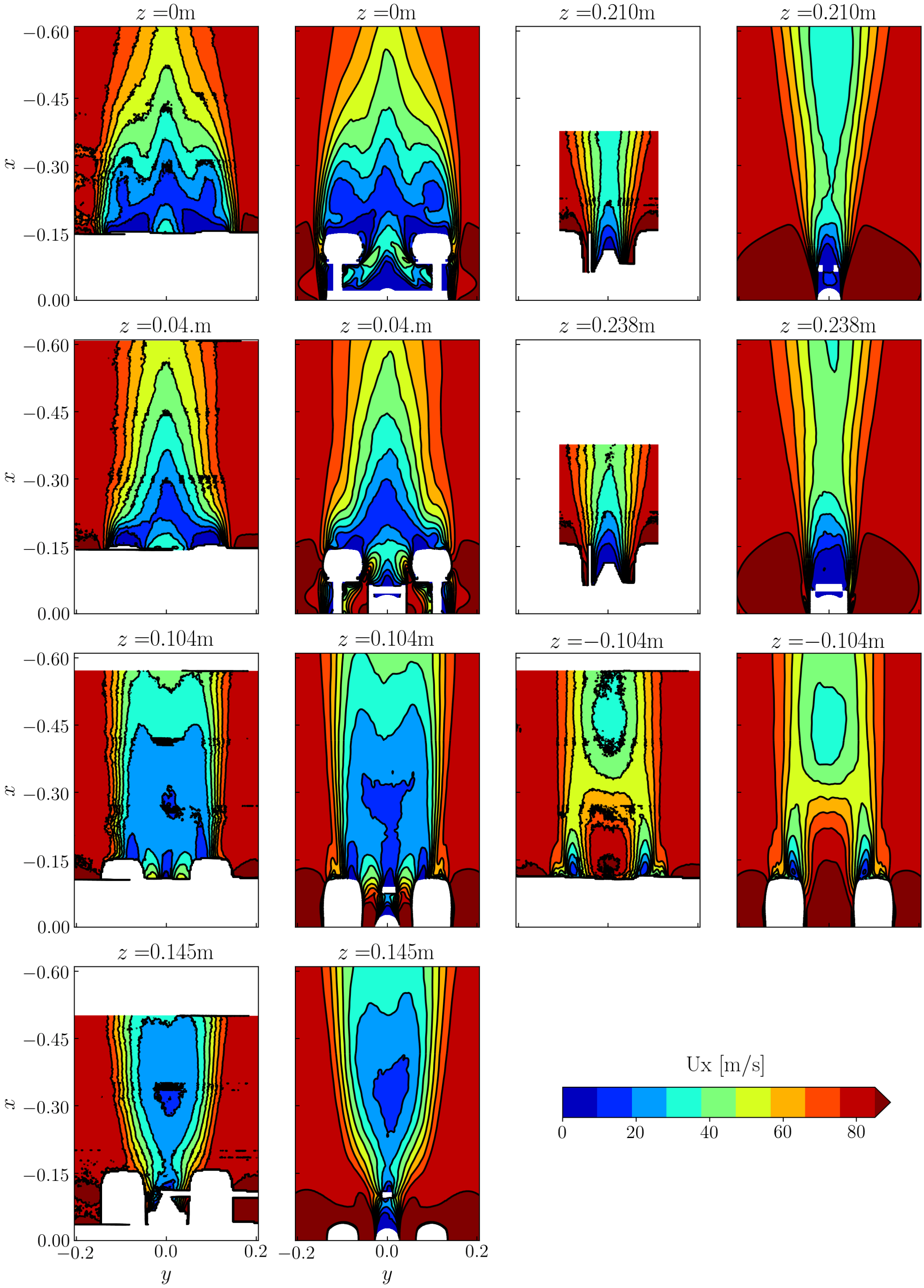

Figure 8.9 – *Comparison with PIV measurements for the streamwise velocity component of the LAGOON 3 configuration. For each z−position : Left: Experiments, Right: LaBS/ProLB.*

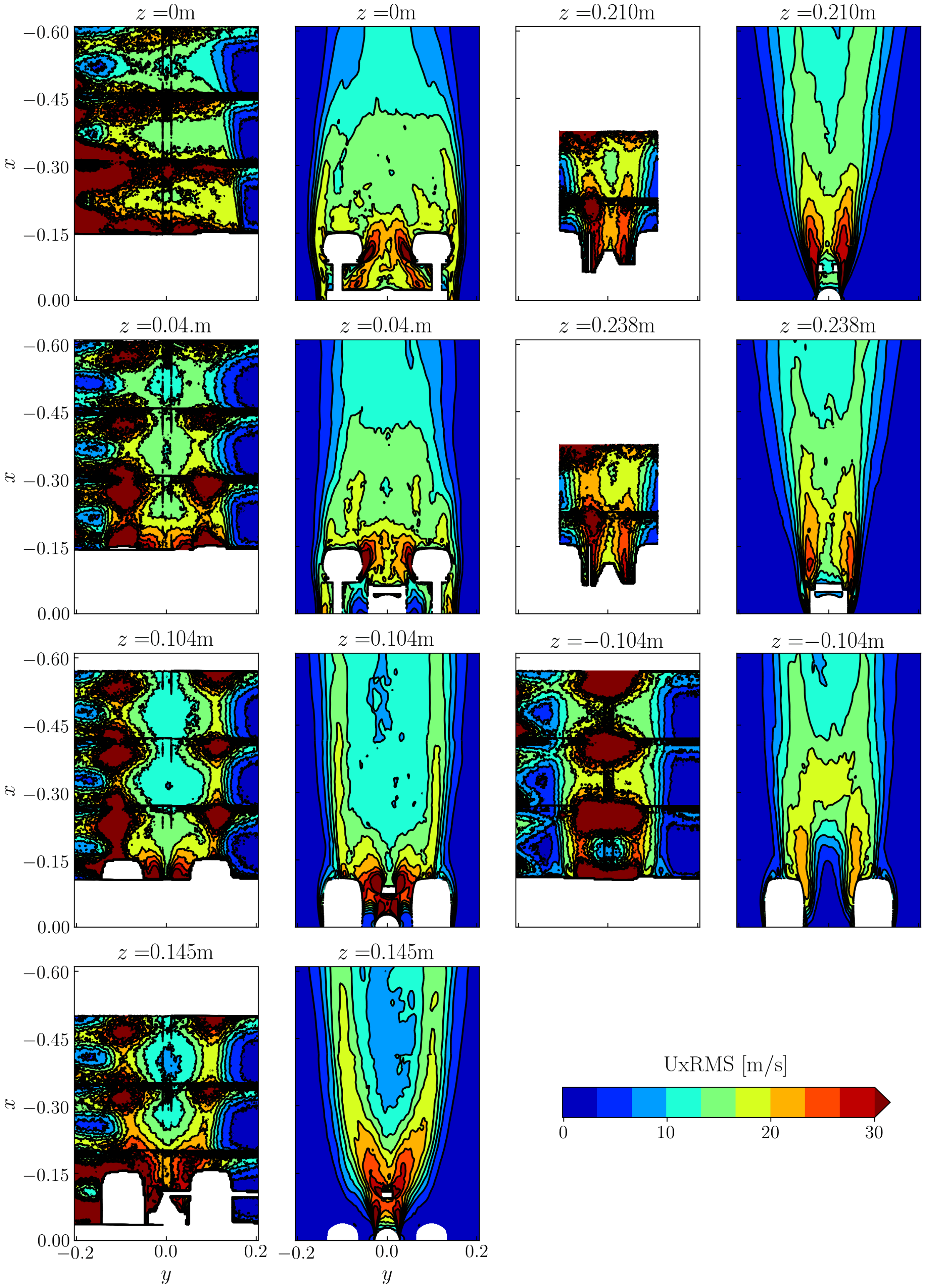

Figure 8.10 – *Comparison with PIV measurements for the streamwise velocity fluctuations of the LAGOON 3 configuration. For each z−position : Left: Experiments, Right: LaBS/ProLB.*

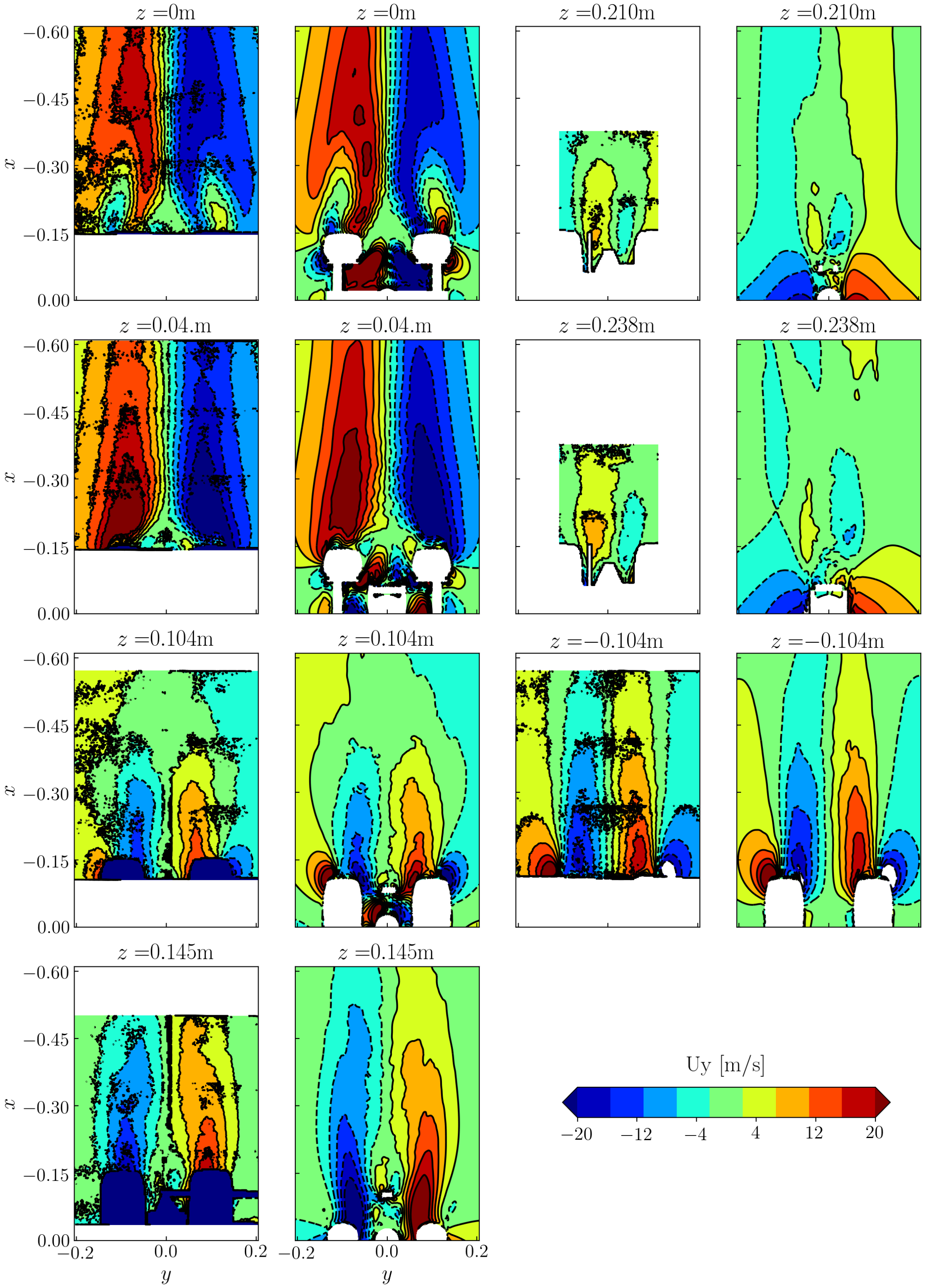

Figure 8.11 – *Comparison with PIV measurements for the crosswise velocity component of the LAGOON 3 configuration. For each z−position : Left: Experiments, Right: LaBS/ProLB.*

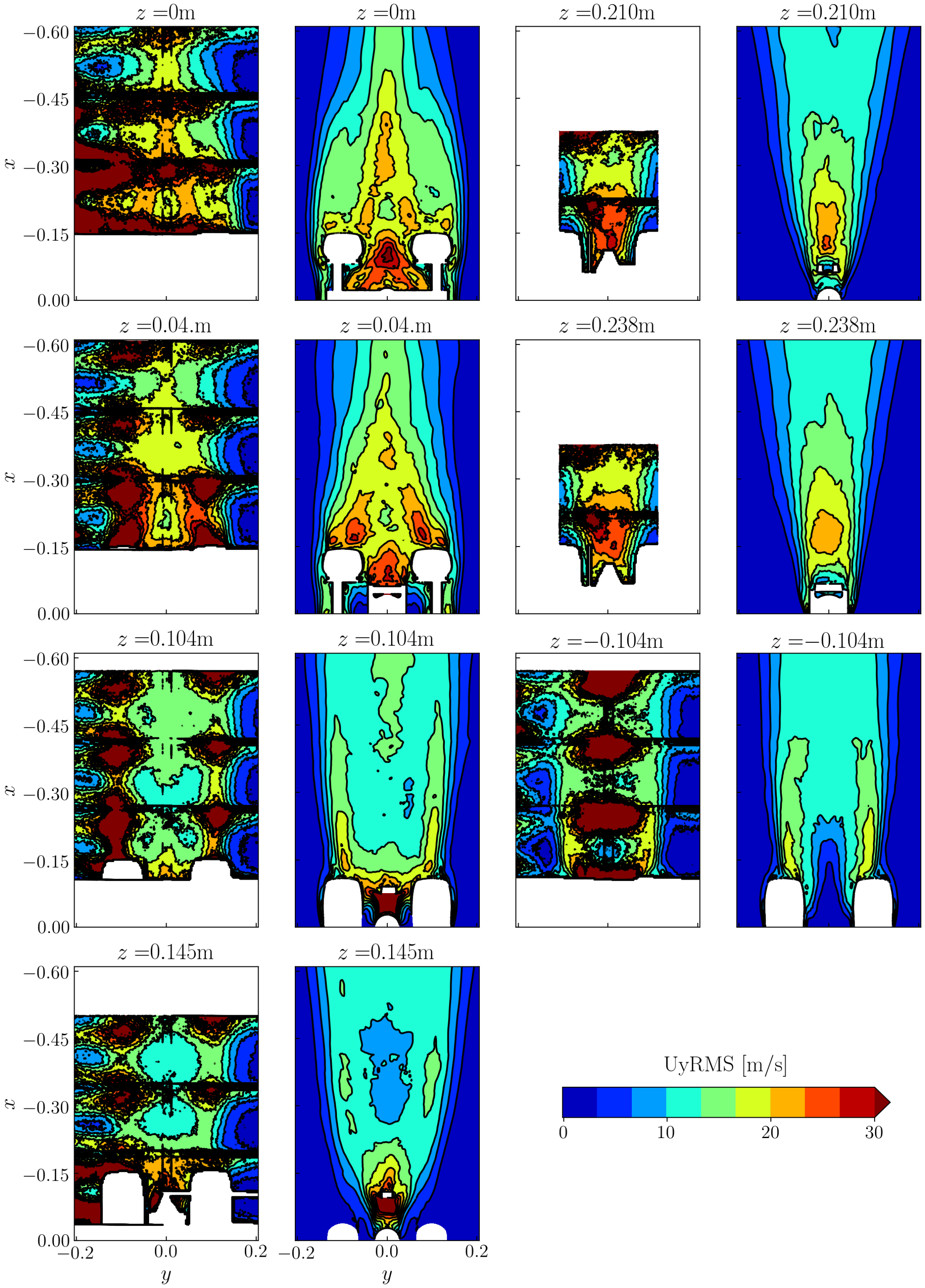

Figure 8.12 – *Comparison with PIV measurements for the crosswise velocity fluctuations of the LAGOON 3 configuration. For each z−position : Left: Experiments, Right: LaBS/ProLB.*

8.2.2 Wall-pressure spectra

Cross-comparisons of parietal pressure spectra for the L2 and L3 configurations are compared to pressure kulites on Fig. 8.14 and Fig. 8.15. The probes positions are identical to those in the previous chapter, and only some of them will exhibit a distinct effect. To help visualizing the changes in pressure fluctuations, Fig. 8.13 shows the RMS pressure levels on the gear surface. A very strong increase of the levels can be noticed on the lower part of the leg, and on the outer downstream part of the wheels, where the cavity covers have been removed. Additionally, the torque-link which receives a turbulent flow from the leg shows high levels.

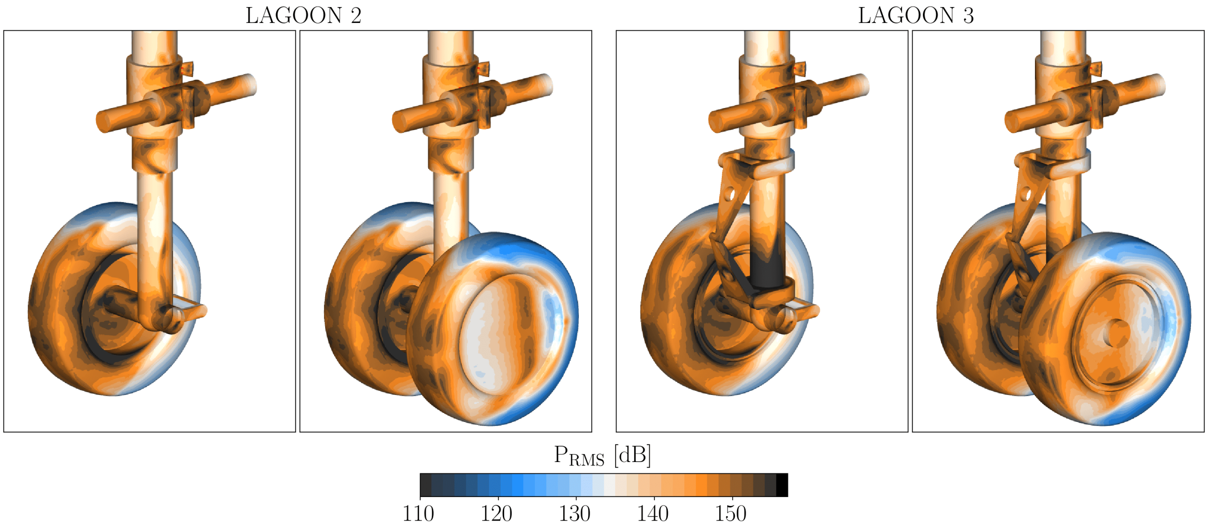

Figure 8.13 – *Two views of the wall RMS pressure fields. Left: L2, Right: L3.*

The kulites analysis indicates:

- Probes K1 to K9 around the wheel perimeter show an additional peak at 1.1kHz. This peak is attributed to the tow-bar [45] and emerges only weakly in the L2 simulation at 1.25kHz, and is not visible for the L3 one. This will be discussed in Sec. 8.2.3. Furthermore, at high frequencies the spectral behavior of the experiments is significantly richer than that of the simulation up to K6. This is due to tripping and none of the other CFD codes (except LaBS/ProLB v2.5 as discussed in Sec. 7.3.5) fail to capture these high frequencies. Except for these effects, the development of the turbulent boundary layer up to K9 is in very good agreement with the experiments, and the flow dynamic on the wheel perimeter is similar for both configurations.

- The K13 to K15 probes on the inner side of the wheel confirm a laminar boundary layer with low noise levels. For the high frequencies, slightly higher levels are obtained for the L3 configuration compared to L2 on these kulites, which in the experiment is found only for K14.

- The K20 probe shows slightly lower levels for the L3 configuration. This is the small contribution of the inner cavity covers. This relative underestimation is well recovered by the simulations. However, the absolute levels are slightly overestimated.

- Probes K10 to K12 do not recover the right fluctuations levels at all, as was already experienced with the L1 configuration.

- Probe K18 exhibits the effect of the outer rim cavity. This probe is exposed to significant vortex impingements originating from upstream for the L3 configuration, whereas the boundary layer is attached for the L2 as shown on Fig. 8.7. The fluctuation levels are increased by 10dB, and this effect is well recovered by the simulation.

- The K19 probe is located directly downstream of the tire. No difference is detected in the simulation and the levels are overestimated by 10dB compared to the experiments.

- The K23 probe is located on the axle, just beneath the low torque-link mounting. The torque-link generates a substantial increase of high frequency levels, up to 25dB. In the simulation, the maximum reached is 17dB, with a correct distribution of the fluctuations according to the frequency.

- Probes K24 to K27 are located on the leg at mid-height of the torque-link. The increase of the fluctuation levels are well captured in the simulation. Only the K26 probe gives too low levels which indicates a wrong position of the separation point.

In conclusion, the kulites analysis indicates that the effect of the torque-link add-on and of the rim cavities that are no longer sealed are very well captured by the simulations. However, the tonal noise induced by the interaction of the tow-bar vortex shedding on the leg does not appear for the L3 configuration and only weakly for the L2 one. Finally, the kulites which were not well recovered for the L1 configuration are logically not retrieved here either.

In the next section, the effect of the tow-bar will be further investigated, to understand why this component does not show a tonal peak for the L3 configuration in the simulation, when it should.

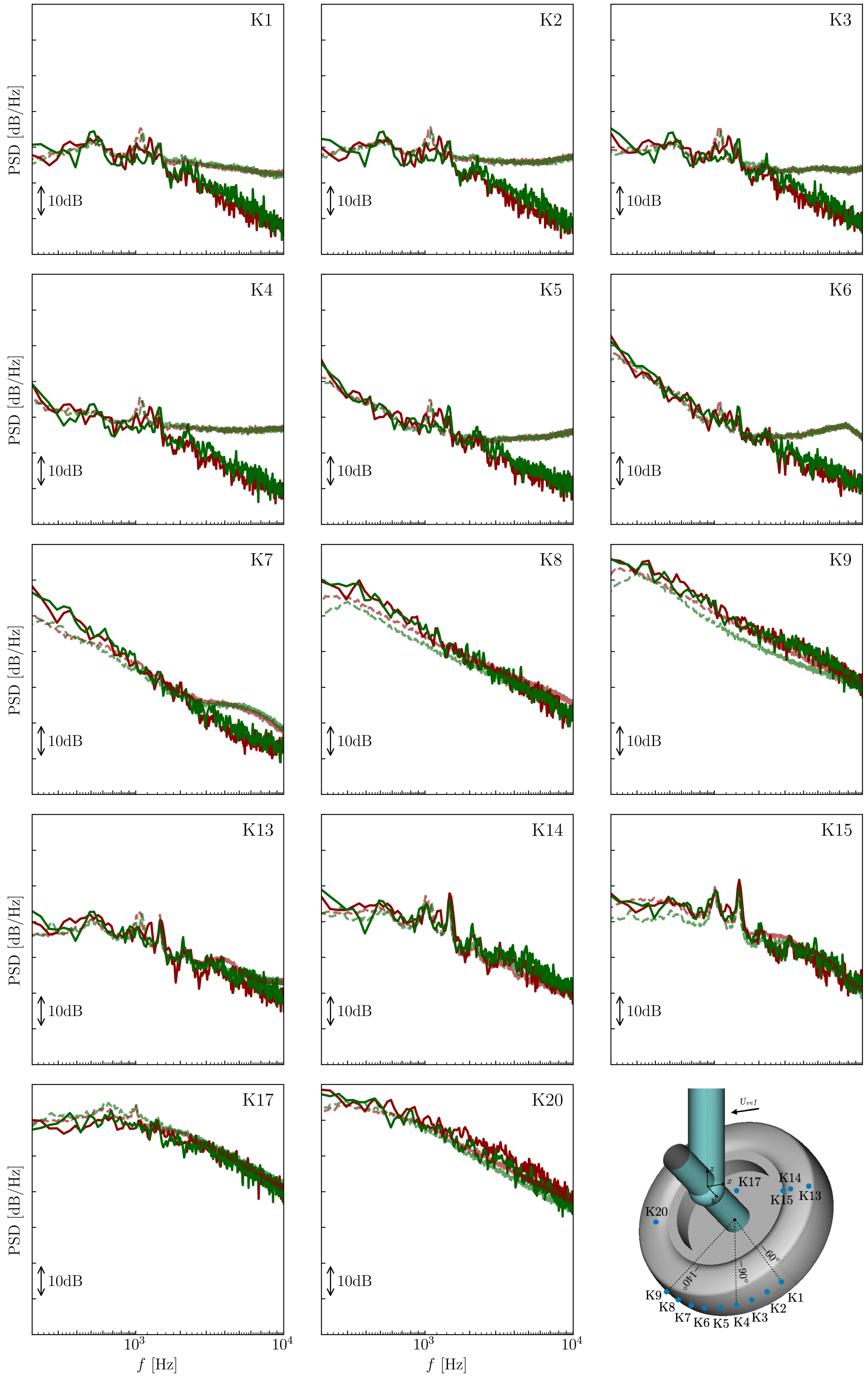

Figure 8.14 – *Wall pressure PSD along the wheel centerline and in the inner flank of the right wheel tire. Comparison with kulites measurements (the extra components are hidden in the picture giving the kulites location.).* (——)*: L2,* (——)*: L3,* (- - -)*: L2-Exp,* (- - -)*: L3-Exp.*

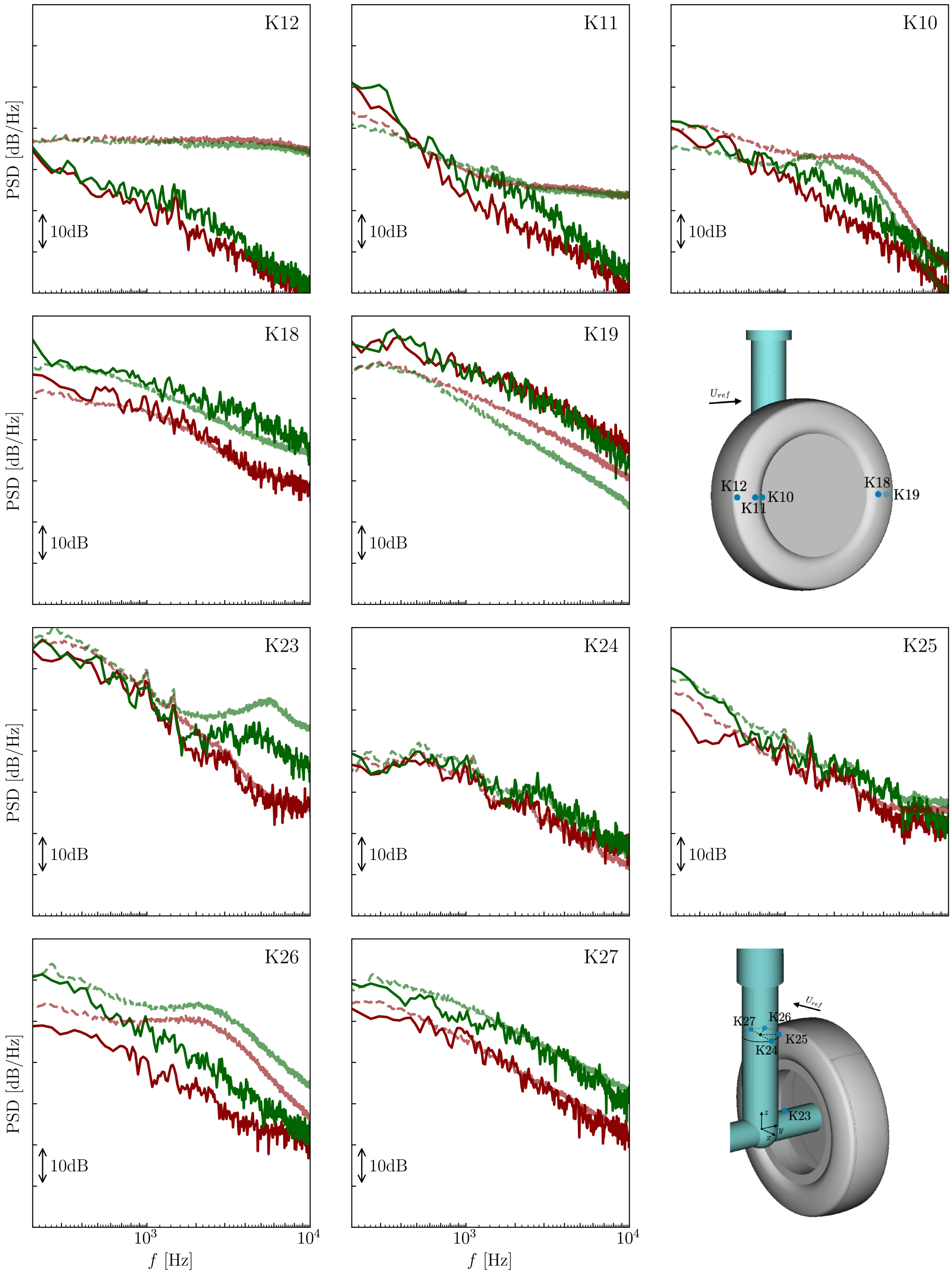

Figure 8.15 – *Wall pressure PSD in the outer flank of the right wheel tire and along the axle and leg. Comparison with kulites measurements (the extra components are hidden in the picture giving the kulites location). (—): L2, (—): L3, (- - -): L2-Exp, (- - -): L3-Exp.*

8.2.3 Investigation of the flow near the tow-bar

The tow-bar, being a small cylinder, produces a vortex shedding at a frequency of about 1100Hz in the experiments. The interaction of the tow-bar wake with the axle and the leg should generate a tonal peak of significant amplitude. However, this peak appears at 1250Hz in the L2 simulation and does not appear in the L3 one. Fig. 8.16 shows the flow around the tow-bar, and its interaction with the leg and the axle. One can see on the streamlines, that the lower torque-link fixation deflects the flow downwards (and accelerates it due to the reduction of the cross-section). This phenomenon delayed the position of the upper separation point of the tow-bar and the flow of the L3 is deflected downwards. Thus no strong pressure fluctuation induced by the tow-bar is observed for the L3 in the vicinity of the axle and leg, while high fluctuations are visible for the L2 in this area. This phenomenon is extremely sensitive to capture, since it requires to exactly predict the separation points on a cylinder in the critical regime, and the interaction with the torque-link in the case of L3. Besides, in the experiments, the tonal peak frequency seems to increase slightly by some hertz for the L3 and its intensity remains similar.

In 2015, Sengissen had shown very encouraging preliminary results for K1 and K2 of the L2 configuration [36]. The tonal peak emerged at 1250Hz for the “FINE” grid with $\mathrm{D}_{tb}/\Delta x_{min} = 50$. As this resolution is rather low to correctly capture a flow around a cylinder in such regime (*cf.* axle and leg in Chap. 7), the choice here is a much finer mesh with $\mathrm{D}_{tb}/\Delta x_{min} = 320$. However, no significant improvement are observed for the kulites results.

So far, it has been observed that the effects of the added components were well captured, except for the interaction noise induced by the tow-bar. This last point could be improved in the future with the use of tripping to enforce the separation point. The next section is dedicated to the far-field aeroacoustic study of L2 and L3.

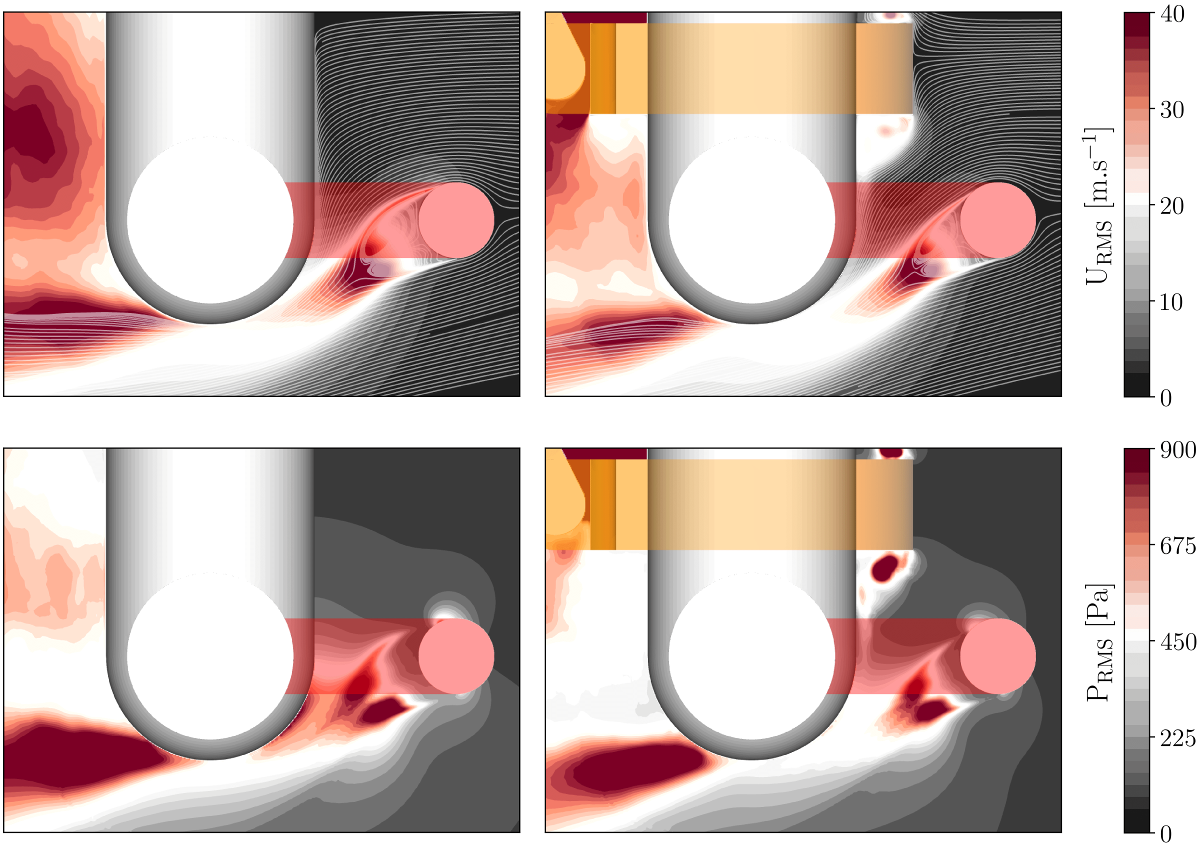

Figure 8.16 – *Flow near the tow-bar. Top: Velocity fluctuations with streamlines, Bottom: Pressure fluctuations. Left: L2, Right: L3.*

8.3 Far-field aeroacoustic results

The acoustic results obtained in the far-field with the FW-H permeable method are presented on Fig. 8.17. First of all, in the experiments the tow-bar peak emerges strongly from the broadband noise at 1.1kHz on both the flyover and sideline microphone arcs. This peak is retrieved on the flyover arc by the L2 simulation only, at a frequency of 1.25kHz. For the sideline arc, the peak emerges only for the downstream microphone M9. No peak is detected for the L3 simulation, as expected from the kulite analysis in Sec. 8.2.2 and the flow investigation in Sec. 8.2.3. At low frequencies (f < 800Hz), the experimental L2 and L3 plots are superposed, then a significant increase in broadband noise levels appears for L3, attributed to the torque-link and rim cavities. The relative increase in broadband noise is very well captured by the simulation. A very good agreement is obtained for the upstream microphone M3. However, an overestimation of the levels for the microphones M6 and M9 is observed for f > 5kHz. This over-estimation could be attributed to the resolution transitions, even if it looks like this spurious noise becomes dominant only from f > 7kHz, where the L2 and L3 curves almost overlap.

The values of the integrated OASPL on the 200Hz to 10kHz frequency bands are shown

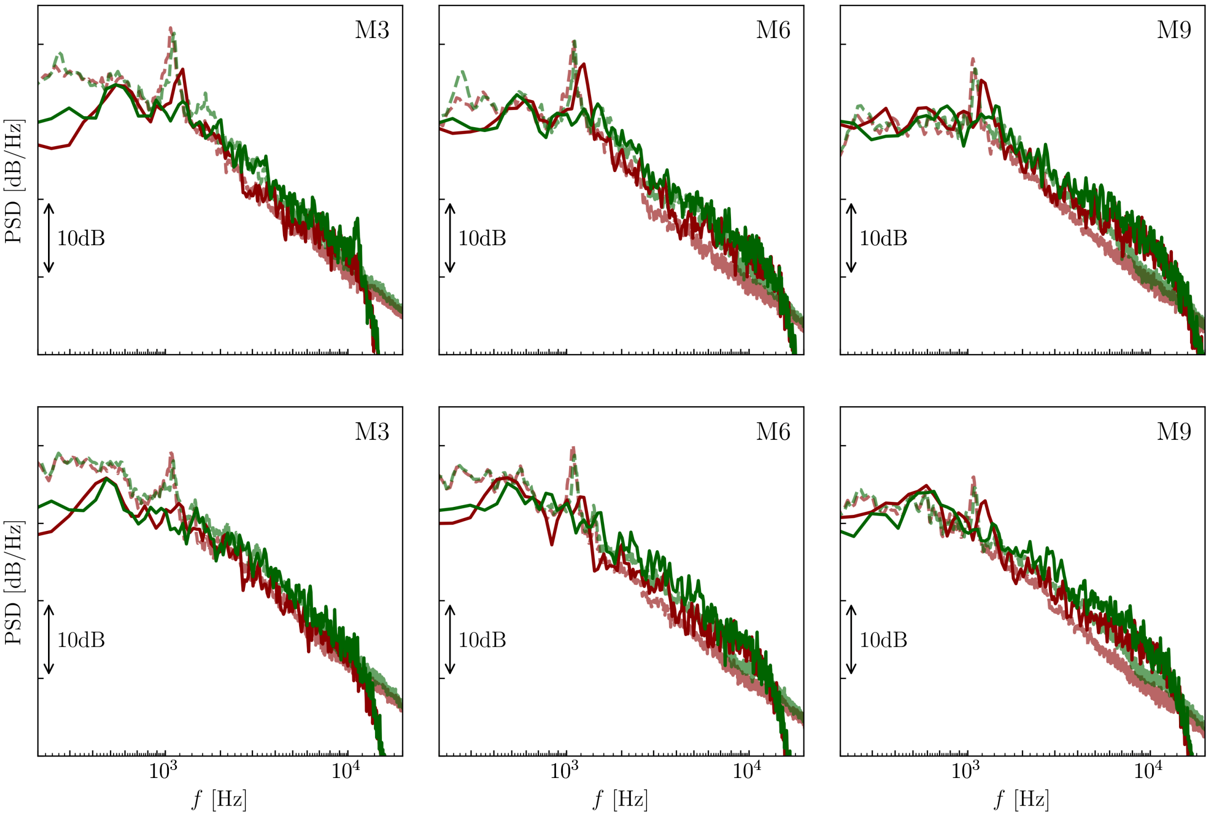

Figure 8.17 – *Power spectral density of far field noise for M3, M6 and M9 microphones obtained with the permeable FW-H formulation. Top: Flyover arc, bottom: Sideline arc.* (—): *L2,* (—): *L3,* (- - -): *L2-Exp,* (- - -): *L3-Exp.*

on Fig. 8.18. A noise deficit for low frequencies is observed upstream (> 90°) as in the L1 case shown on Fig. 7.25. This gap is mainly the result of the imperfect prediction of the detachment points on the axle and leg for the flyover and sideline arcs respectively (*cf.* Chap. 7). Downstream (< 60°), an overestimation of 1dB is probably caused by the resolution transitions. If the L2 and L3 simulations are compared to each other, the relative OASPL between the two configurations is comparable to that obtained in the experiments for all angles and microphone arcs.

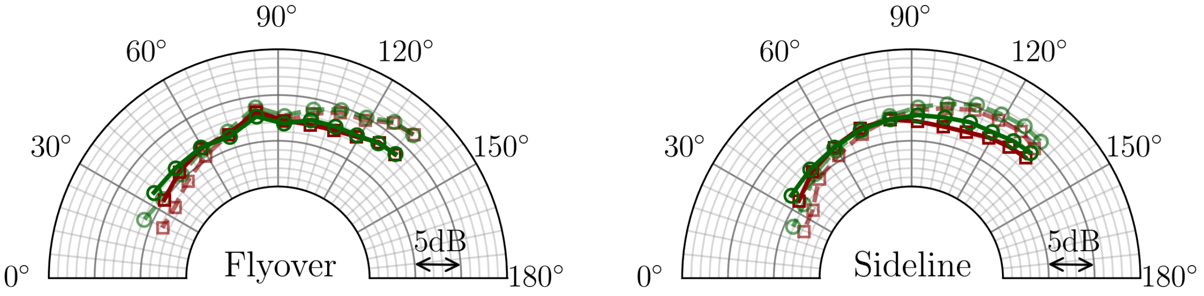

Figure 8.18 – *OASPL integrated in the 200Hz to 10kHz frequency bands. Left: Flyover arc, Right: Sideline arc.* (-□-): *L2,* (-○-): *L3,* (-□-): *L2-Exp,* (-○-): *L3-Exp.*

Apart from the tow-bar effect, the other components are well captured by the simulations.

8.4 Conclusion of the LAGOON 2 and 3 study

Following the promising results achieved for the LAGOON 1 configuration in Chap. 7, where a grid convergence study was performed, the addition of extra components has been studied in this chapter. The aerodynamic results were quite satisfying with an excellent correlation for the PIV planes. The kulites study has allowed to verify that the effect of the extra components as possible acoustic sources were well captured. It was checked that the torque-link and the rim cavities were responsible for a significant increase in the parietal pressure fluctuation levels. However, the interaction phenomenon between the tow-bar vortex shedding and the axle and leg, expected to generate a significant far-field tonal peak, does not occur for the L3 simulation. It has been noticed that the torque-link's fixation deflects the tow-bar wake below the leg thus avoiding the interaction. Since a tonal peak does emerge in the experiments, this suggests a too late upper flow separation for the tow-bar in the L3 simulation. To improve this point, tripping could be added on the tow-bar to enforce the separation point.

Regarding the far-field acoustic results, the relative level increase between the L2 and L3 configurations is well captured. The torque-link and rim-cavities generate a significant increase in levels for $f > 1400\text{Hz}$. However, the frequency of the tow-bar tonal peak is increased by 150Hz in the L2 simulation, and only appears downstream for the sideline microphone arc. Moreover, an overestimation of noise levels is noticed for downstream microphones for $f > 5\text{kHz}$, which is probably induced by remaining spurious grid transition noise. Possible ways to improve these predictions could be 1/ to increase the resolution of the axle and the leg as for the LAGOON 1, 2/ to add tripping on the tow-bar.

This study is a starting point towards the noise prediction of a realistic landing gear. It will be worthwhile in the future to increase the geometrical complexity, with in particular the analysis of the partially dressed cavity-closed landing gear (PDCC) [294]. This study has already been carried out with LaBS/ProLB by Hou in 2019 [57] but the contribution of the DC grid coupling algorithm, as well as the FW-H coupling with a permeable formulation will be worth quantifying.

Finally, the study of a realistic landing gear will notably involve the dressings (*cf.* Fig. 1.4), which are typically cylinders of very small dimensions that can produce significant interaction noises. These components will require a considerable increase in spatial resolution, and thus in the density of the volume mesh. Therefore, substantial CPU performance will be needed and the use of LBM to predict the noise of such realistic landing gears will be more and more justified.

Chapter 9

Conclusion and perspectives

Predicting landing gear noise is a major challenge for an aerospace manufacturer, since it accounts for about 40% of the total aircraft noise during approach phases. In-flight and wind tunnel tests have helped to understand the mechanisms that generate noise, and enable noise reduction devices to be designed. However, these experiments are a long and costly process. The CFD is therefore an essential complement to its experimental approaches. In view of the significant unsteadiness of the flow and the broadband nature of landing gear noise, it is necessary to turn towards methods such as large eddy simulations to predict acoustic sources. Thus, the LBM which has recently shown a strong potential for this type of simulation has been adopted for this thesis. The available LBM solver: LaBS/ProLB v2.5, however, did not reach the level of accuracy required for such simulations. Indeed, the stability was insufficient at high velocities and non physical acoustic and vorticity waves severely polluted simulations. It was shown in this thesis that these waves were closely related to resolution transitions, but came from two distinct origins:

- **A non-hydrodynamic origin inherent to the LBM scheme and deleterious at mesh interfaces:** In Chap. 3, we have seen that non-hydrodynamic modes coexisted with physical ones in an LBM simulation, and could carry a macroscopic quantity. Due to their particular pulsation ω_r, these modes invert at each iteration and produce a discontinuity at the interface caused by the asynchronous evolution of the two grids. This discontinuity generates a very high amplification of these waves and is responsible for vorticity and unwanted acoustics that pollute simulations. The proposed solution was therefore to dissipate these modes in the fluid core, something we have achieved in Chap. 4. By means of spectral analysis, we have selected a collision model that allows to fulfill this goal: the H-RR. Indeed, thanks to a partial reconstruction of the viscous stress tensor thanks to a finite difference estimation of the stress rate tensor, these modes are highly dissipated. This has allowed the suppression of spurious vorticity, which can appear even beyond hydrodynamic fluctuations, as well as a reduction of the spurious noise emitted by eddies passing through mesh interfaces.

- **An insufficient accuracy of the grid coupling algorithm:** In Chap. 6 we pointed out that the algorithm used in v2.5 version of LaBS/ProLB led to a discontinuity of vortices crossing the mesh interfaces. This discontinuity is responsible for important spurious acoustic emission. To overcome this problem, we have proposed an algorithm based on a direct grid coupling, which extends the work of Lagrava [212]. This algorithm solves a non-linear system to find an equilibrium function that strengthens the link between two meshes of different resolution based on conservation assumptions. It has enabled a significant reduction of spurious noise at interfaces crossed by turbulent flows. Finally, improved spatial interpolations have also been proposed and validated to improve the accuracy of non-planar interfaces.

These two parasitic sources were thus drastically reduced via 1/ a global solution applying to the whole fluid, 2/ a local solution only applied at the interface. The combination of the two is therefore required to get rid of the spurious behaviors.

Subsequently, the ability of the H-RR model to be stable and accurate under the low viscosity and moderate Mach number conditions of interest was assessed. It was found that **this model requires cubic Mach correction terms to be stable for non-zero Mach numbers**, which was not expected. It has been pointed out that this corrected model (H-RR$_\psi$) proves to be much more stable than many models in the literature, for an equilibrium function at the third-order compatible with a D3Q19 lattice.

Regarding the accuracy, the strong anisotropy in dissipation of advanced LBM schemes was highlighted, which was already known for regularized models [149]. Actually, the advanced models turn out to dissipate much more than the basic BGK and the "*very low-dissipative properties of the LBM*" should be taken with caution as it varies a lot from one collision scheme to the other. Nevertheless, a proper comparison of the Navier-Stokes and LBM properties for different flow angles and possible propagation directions for the perturbations is still sorely missing in the literature for comparison. Hence, we have only compared LBM models with each other, and the H-RR$_\psi$ proves to be quite satisfactory (*cf.* Fig. 5.5).

Once these different models were evaluated and implemented in the LaBS/ProLB solver, simulations were carried out on the LAGOON landing gears of increasing complexity. Three grids of various resolution were assessed. The aerodynamic results obtained are very satisfactory and are notably in agreement with those obtained with the PowerFLOW solver which is the current reference in LBM for aeroacoustics. Concerning the aeroacoustic results, the combination of the H-RR$_\psi$ collision model and the DC grid coupling algorithm allows a huge reduction of the spurious acoustics. Nevertheless, a small amount of spurious noise is still observed on the PSD for St> 20.

We pointed out that the solid FW-H formulation, mostly used for landing gear noise, was not appropriate in this context. Indeed, following the methodology of Spalart [273] and thanks to a dedicated spectral decomposition, we have highlighted that **neglecting quadrupole sources is not a valid hypothesis** for two reasons:

- **Quadrupole sources do not seem to be negligible** for any direction of propagation. **Downstream, these sources apparently appear to be predominant**.

The most accurate studies using the solid FW-H formulation all have a downstream noise deficit.

- **Neglecting the quadrupole sources in FW-H leads to the cancellation of a cross-correlation term between dipole and quadrupole sources which is not negligible**. Many recent studies thus show an over-estimation of the **upstream noise** for St > 5. Indeed, this cross term leads, for middle to high frequencies, to a noise reduction of up to 10dB **upstream** for the LAGOON landing gear.

Hence, with the permeable FW-H formulation, very convincing results were obtained for the LAGOON 1 configuration, with however a slight overestimation of the downstream spectra due to some remaining mesh transition noise.

The LAGOON 2 and 3 configurations were further investigated to evaluate the effect of extra components. The PIV analysis showed a very good agreement with the experiments for these components. Moreover, the kulites have enabled verifying that the effect of the torque-link add-on and of the rim cavities on the L3 configuration are well captured. However, the interaction noise between the tow-bar and the leg is not correctly retrieved, especially in the L3 case where it does not appear at all. A future study, with the addition of tripping on the tow-bar to enforce the separation point could improve this matter. Finally, the acoustic results show a good agreement of the extra components, if the L2 and L3 simulations are compared to each other. However, a lack of resolution on the axle and leg leads to a noise deficit at low frequencies for upstream microphones, which is reflected on the OASPLs, as was also observed for the L1 configuration. Besides, noise overestimates for high frequencies are observed on the downstream microphones, which may likely be attributed to resolution transitions.

Finally, the H-RR$_\psi$ model has been integrated into the v3 commercial version of LaBS/ProLB. Furthermore, the DC grid coupling algorithm, as well as the improved spatial interpolations (I-3 in Sec. 6.3.1) have been integrated in a candidate version, and will likely be used in the commercial version in a near future.

Perspectives

From a numerical point of view, three important aspects remain to be addressed at grid interfaces:

- The intersections between boundary conditions and mesh transitions: the current intersections generate a lot of spurious noise, and can detach boundary layers. Thus, local refinements at the wall have to be avoided, which has strongly increased the cost of our simulations. Work has been started during this thesis, and will be continued after the PhD to improve these intersections.

- Turbulence handling at mesh interfaces: a large jump in turbulent viscosity is produced by the Smagorinsky model at the interface. It has been observed (but not presented in this manuscript) that the noise generated by a vortex crossing a transition (*cf.* Fig. 6.14 and 6.15) is increased by 3dB on the OASPL when the Smagorinsky model is activated. The LES assumptions where the variation of the mesh size is generally neglected are no longer valid in this case [295], and additional terms have to be taken into account.

- Spatial interpolations for arbitrary transitions: Although the I-3 method proposed in Sec. 6.3.1 improves the handling of arbitrary interfaces, they remain much less accurate than plane interfaces. More compact and isotropic interpolations might improve this point [296] but are not very suitable for cell-vertex structures.

From an industrial point of view of landing gear noise, two aspects should be carried out:

- The first step is to investigate more realistic landing gear geometries, especially including four wheels and a bogie. Such configuration will lead to more complex phenomenology that LBM is quite capable of capturing.

- The next step is to focus on the noise prediction of high-lift devices to be able to predict the noise of landing gears installed under the wings. The installation effect is important to consider, which is the reason why we worked on the confidential ARTEM configuration during this thesis. This configuration integrates a complete landing gear installed under a wing in high-lift configuration. However, the current level of accuracy regarding the aeroacoustic of the high-lift devices is insufficient. For that purpose, DES models appear as a relevant option [27, 297]. In addition, recent improvements to the walls [67, 68] must be integrated in the same version to address these issues.

Finally, from a physical analysis point of view, further work is required on the methodologies to identify landing gear noise root causes and to achieve the best possible low noise designs, while mitigating other integration constraints. A project such as INVENTOR will follow that path.

Scientific publications

- **T. Astoul**, G. Wissocq, J.-F. Boussuge, A. Sengissen, P. Sagaut, Analysis and reduction of spurious noise generated at grid refinement interfaces with the lattice Boltzmann method, *Journal of Computational Physics*, 2020.
- **T. Astoul**, G. Wissocq, J.-F. Boussuge, A. Sengissen, P. Sagaut, Lattice Boltzmann method for computational aeroacoustics on non-uniform meshes: a direct grid coupling approach, *Revision for Journal of Computational Physics* since May 2020.

Conferences

- **T. Astoul**, G. Wissocq, J.-F. Boussuge, Alois Sengissen, P. Sagaut, Analysis and reduction of spurious noise generated at grid refinement interfaces with the lattice Boltzmann method. 28th International Conference on Discrete Simulation of Fluid Dynamics, 2020, Bengalore India.

Online course – Trainings

- Small private online course (SPOC): Fundamentals of Lattice Boltzmann Method
- Instructor-led training session at CERFACS: https://cerfacs.fr/en/event/basic-lattice-boltzmann-methods/
- Practicals about the lattice Boltzmann method, at ISAE-Suparo (graduate school of aeronautical engineering).

Appendix A

Additional results for the numerical validation of the D3Q19 H-RR$_\psi$

The aim of this appendix is to provide additional results on the vortex and pulse convection test cases. In addition, a comparison between lattices D2Q9 and D3Q19 completes the study to validate the tri-dimmensional model implemented in LaBS. Indeed, the stability analyses were performed only for the D2Q9 lattice and only a numerical validation is performed for the D3Q19 one.

A.1 Results on a convected vortex in a periodic box

The case of a convected vortex previously studied in Sec. 5.4 is carried out with the two lattices D2Q9 and D3Q19. Then the mean field will be inclined in the diagonal direction of the lattice in the (x, y) plane and finally in the diagonal of the cube for the D3Q19 lattice in order to study empirically the limits of the model.

Fig. A.1 shows the relative L^2 error, dissipation and dispersion of the vortex after 50 box laps for both lattices. One can see that the results are almost identical for $x-$aligned direction. Afterwards, the Fig. A.2 gives the comparisons for an average field inclined at $(\theta = 45°)$ in the plane (x, y). This time, slight deviations are to be noted. For small values of σ the errors are almost identical. However, when $\sigma \rightarrow 1$, the lattice D3Q19 does not diverge while D2Q9 does. Nevertheless, the increase in dispersion (dc_{vortex}) is a sign that the computation will ultimately diverge.

It can therefore be considered that the two lattices behave in almost the same way for two-dimensional test cases. The study was also carried out for the D3Q19 lattice with a mean field oriented in the diagonal of the cube to evaluate if major stability problems appear. Fig. A.3 shows that the stability is not deteriorated in this direction compared to cases of inclined flow at $(\theta = 45°)$. In any case, lowering slightly the value of σ allows to be stable for aeronautical simulations in subsonic regime.

A.2 Results on a convected Gaussian pulse

The case of the under-resolved advected pulse $(R_c = 1)$ is also performed with the D3Q19 lattice since it is the case with the most important numerical errors. Fig. A.4 compares the two lattices on this case. The behavior can be considered as identical whatever the value of σ. The spectral properties evaluated in two dimensions thus seem to be valid for the lattice D3Q19.

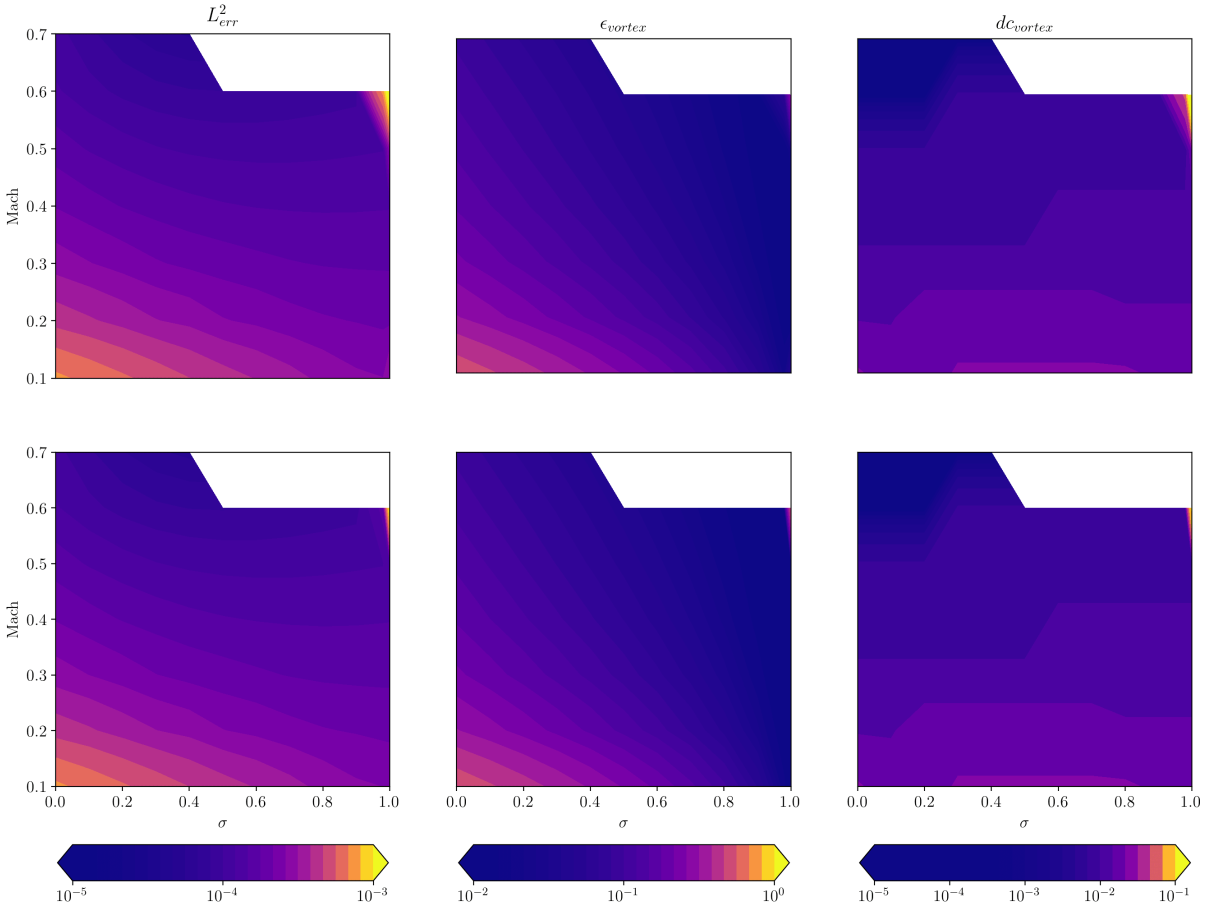

Figure A.1 – *Maps of* L^2 *error* (L^2_{err}), *dissipation* $\epsilon_{vortex} = [\min(\rho(t_f)) - \min(\rho(t_0))] / [\rho_0 - \min(\rho(t_0))]$ *and dispersion* dc_{vortex} *for the periodic vortex test case after 50 convective time* t_f *with the H-RR*$_\psi$ *model.* ***The mean flow is horizontal*** ($\theta = 0°$) ***in the*** x ***direction****. Several convected Mach number and hybridization parameter* σ *are studied.* dc_{vortex} *is the distance between the vortex center at the initial and at the final state. The dimensionless viscosity is fixed to* $\nu = 10^{-6}$. *White areas means unstable simulations. Top: D2Q9 lattice, bottom: D3Q19 lattice.*

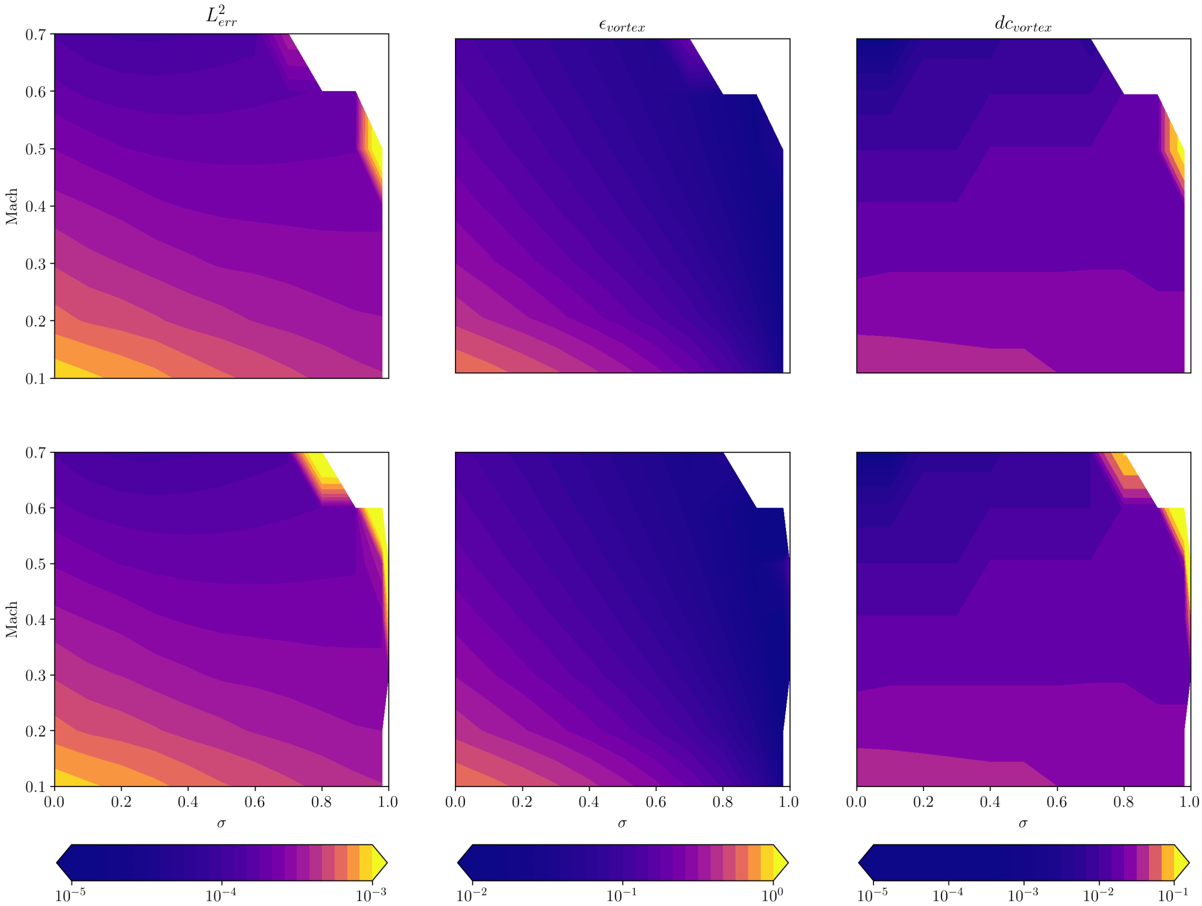

Figure A.2 – *Maps of L^2 error (L^2_{err}), dissipation $\epsilon_{vortex} = [\min(\rho(t_f)) - \min(\rho(t_0))] / [\rho_0 - \min(\rho(t_0))]$ and dispersion dc_{vortex} for the periodic vortex test case after 50 convective time t_f with the H-RR$_\psi$ model.* ***The mean flow is inclined*** $(\theta = 45°)$ ***in the*** (x, y) ***plane****. Several convected Mach number and hybridization parameter σ are studied. dc_{vortex} is the distance between the vortex center at the initial and at the final state. The dimensionless viscosity is fixed to $\nu = 10^{-6}$. White areas means unstable simulations. Top: D2Q9 lattice, bottom: D3Q19 lattice.*

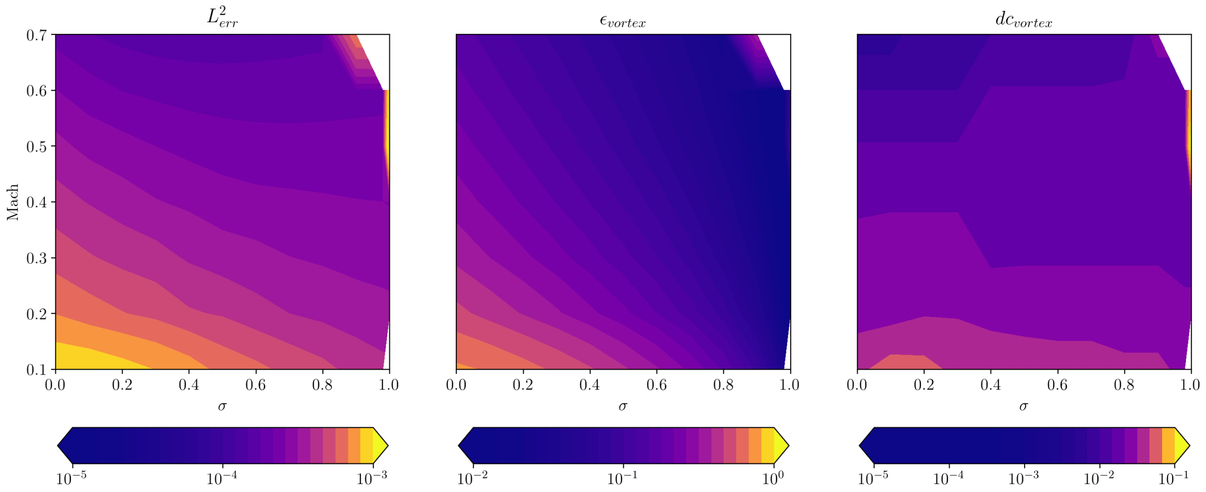

Figure A.3 – *Maps of* L^2 *error* (L^2_{err}), *dissipation* $\epsilon_{vortex} = [\min(\rho(t_f)) - \min(\rho(t_0))] / [\rho_0 - \min(\rho(t_0))]$ *and dispersion* dc_{vortex} *for the periodic vortex test case after 50 convective time* t_f *with the H-RR*$_\psi$ *model and the* ***D3Q19 lattice***. ***The mean flow is inclined*** ($\theta = 45°$) ***in the cube diagonal***. *Several convected Mach number and hybridization parameter* σ *are studied.* dc_{vortex} *is the distance between the vortex center at the initial and at the final state. The dimensionless viscosity is fixed to* $\nu = 10^{-6}$. *White areas means unstable simulations.*

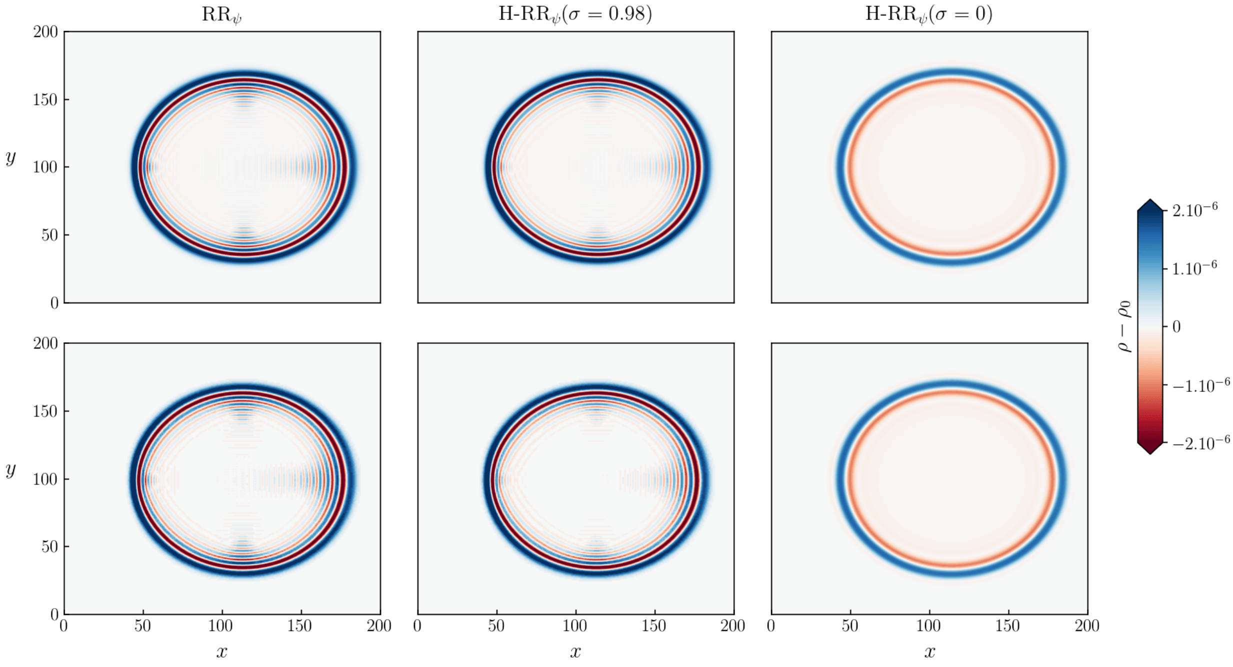

Figure A.4 – *Relative density fields of a convected two-dimensional acoustic pulse for the D2Q9 lattice (top) and the D3Q19 lattice (bottom) at* $t = 120$ *iterations.* $M_x = 0.2$, $\nu = 10^{-6}$.

Appendix B

Additional results with the Direct Coupling algorithm

B.1 Comparison of several grid refinement algorithms on a convected vortex

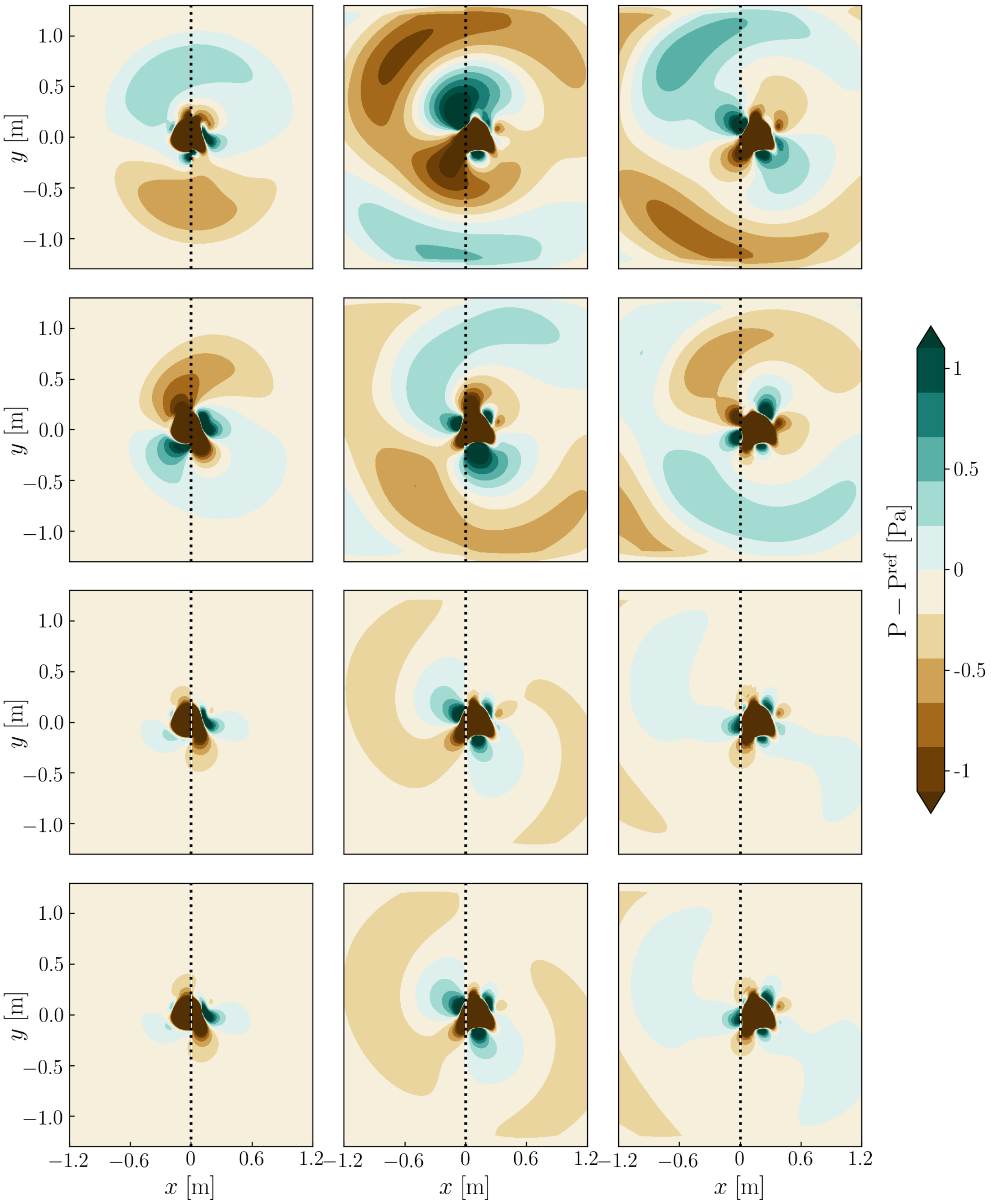

Figure B.1 – *Relative pressure field* $(\text{P} - \text{P}^{\text{ref}})$ *of the vortex convected across a plane refinement interface at* $t = 810 \cdot \Delta t^f$ *(left)* $t = 920 \cdot \Delta t^f$ *(middle)* $t = 980 \cdot \Delta t^f$ *(right) obtained in an in-house 2D LBM solver. From top to bottom: STD, PP, DC1, DC2.* $(\cdots\cdots)$*: grid refinement interface.*

B.2 Examples of two-dimensional refinement interface with corners with the DC algorithm

In this appendix, the particular example of a plane refinement interface illustrated in Fig. 6.4 is extended to interfaces with concave and convex corners. With the formalism described in the paper, the only difference between a plane interface and corners lies in the value of the velocity indexes which are associated with the sets $\mathscr{P}, \mathscr{Q}^f, \mathscr{M}^f$. These sets determine the allowable values of the parameters Γ_i and γ_i as described in Table 6.1.

The configuration of planar, concave and convex interfaces are the only three ones that can locally be found with Cartesian meshes in two dimensions. An extension to the three-dimensional case is straightforward by further distinghishing edges and corners. Anyway, the computation of the Jacobian matrix involved in Eq. (6.2.6) is done only once in advance and considers any possible shape for the interface. The choice of sets $\mathscr{P}$, $\mathscr{Q}^f$, $\mathscr{M}^f$ is directly substituted in the LBM code.

A concave corner is displayed on Fig. B.2. In this situation, the sets $\mathscr{P}$, $\mathscr{Q}^f$, $\mathscr{M}^f$ take the following values: $\mathscr{P} = \{0, 1, 3\}$, $\mathscr{Q}^f = \{2\}$ and $\mathscr{M}^f = \{4, 5, 6, 7, 8\}$.

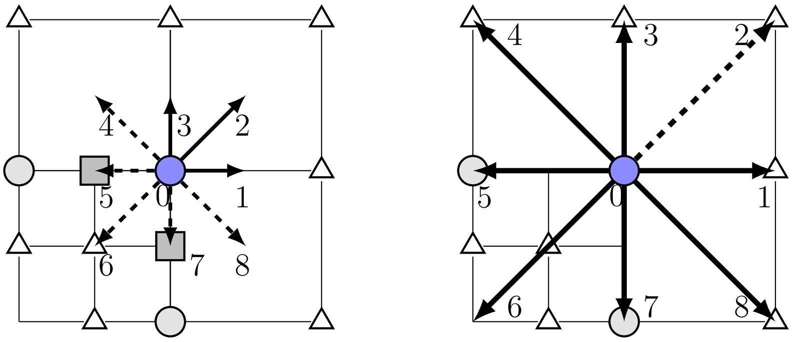

Figure B.2 – *Two dimensional representation of a concave corner refinement interface. (- - -►): Unknown distribution functions after a streaming step, (——►): known distribution functions. Left: fine domain, right: coarse domain.*

A convex corner is displayed on Fig. B.3. This time, the sets $\mathscr{P}$, $\mathscr{Q}^f$, $\mathscr{M}^f$ take the following values: $\mathscr{P} = \{0, 5, 7\}$, $\mathscr{Q}^f = \{1, 2, 3, 4, 8\}$ and $\mathscr{M}^f = \{6\}$.

Coarse distributions function are all reconstructed with Eq. (3.5.5) whatever the shape of the interface.

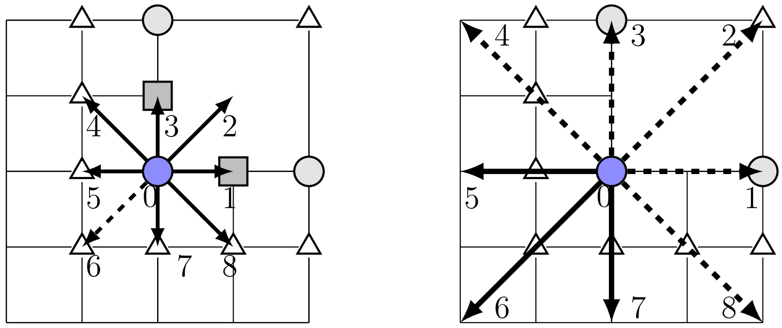

Figure B.3 – *Two dimensional representation of a convex corner refinement interface. (- - -►): Unknown distribution functions after a streaming step, (——►): known distribution functions. Left: fine domain, right: coarse domain.*

B.3 Stability limits in the presence of mesh refinement

This complementary study aims at evaluating the gap in stability between a coarse uniform, a fine uniform and a non-uniform simulation. To this end, numerical experiments are performed with the same vortex case as the one presented in Sec. 6.3.2, with an increased convection Mach number ranging from 0.1 to 0.6. The vortex is initialized at the center of a $[1\text{m}, 1\text{m}]$ periodic box and is advected to the right until 100 characteristic times $t_c = L/U_x$ are reached.

Such validation is widely used to estimate the numerical method stability and accuracy. Usually, numerical error analysis is done considering two criteria:

- Dissipation properties: by quantifying the amplitude lost by the vortex at $t = 100t_c$.
- Dispersion properties: considering the deformation of the vortex and its location mismatch with respect to the domain center at $t = 100t_c$.

The focus here is only put on numerical stability, so these errors will not be quantified. Pressure maps of the convected vortex at $t = 100t_c$ are presented in Fig. B.5. Note that in presence of mesh refinement, the vortex has been affected by 200 passages across the interface. It turns out that simulations performed with non-uniform grids are more stable than those with uniform ones for this test case. This is justified by the fact that the unstable modes of a LB scheme are altered by the mesh transition at each passage, so that they do not have enough time to grow and make the simulation diverge [149]. The energy of the latter, when passing through a transition, is re-distributed to the other modes (*cf.* Fig. 3.4 and 3.5). It is important to underline that the obtained results are only relevant for the H-RR$_p$*si* model, which partially filters out non-hydrodynamic modes at the fluid core. As it was shown in Fig. 5.1, this model is linearly unstable for $Ma > 0.25$ in these conditions.

Qualitatively discussing the global accuracy, dispersion is mainly related to the convection time spent in each grid. However, it is worth mentioning that since the simulations are performed at iso laps number, those with a low Mach number require more iterations and therefore will accumulate more numerical errors. Moreover, coarse grid calculations require half as many iterations as fine ones, which also minimizes the effects of dispersion and stability.

With these facts in mind, one can argue that propagation in the fine mesh is very little dispersive and the vortex remains close to the center of the domain and very slightly deformed at $t = 100t_c$. Conversely, the propagation on the coarse mesh is more dispersive, the vortex distorts and drifts away from the center, even though it has gone through half as many iterations. Regarding non-uniform simulations, the vortex is less distorted with the DC2 algorithm than with both DC1 and STD one.

More quantitatively, Fig. B.4 shows, for these various simulations, the maximum of vorticity over time. This quantity is a useful indicator of the numerical dissipation generated by the numerical scheme to propagate a source of vorticity. First, it can be observed that for Mach = 0.6 the two uniform meshes have a non-linear behavior showing a probable instability of the numerical scheme in the fluid core. The coarse mesh consistently dissipates the vortex more than the fine one. For non-uniform simulations, the DC1 algorithm shows a strong degradation of its accuracy as the Mach number increases. The DC2 algorithm is the most accurate, up to Mach = 0.6 where the dissipation induced by the STD model is similar. This study reinforces the choice of the DC2 algorithm within the framework of aero-acoustic simulation.

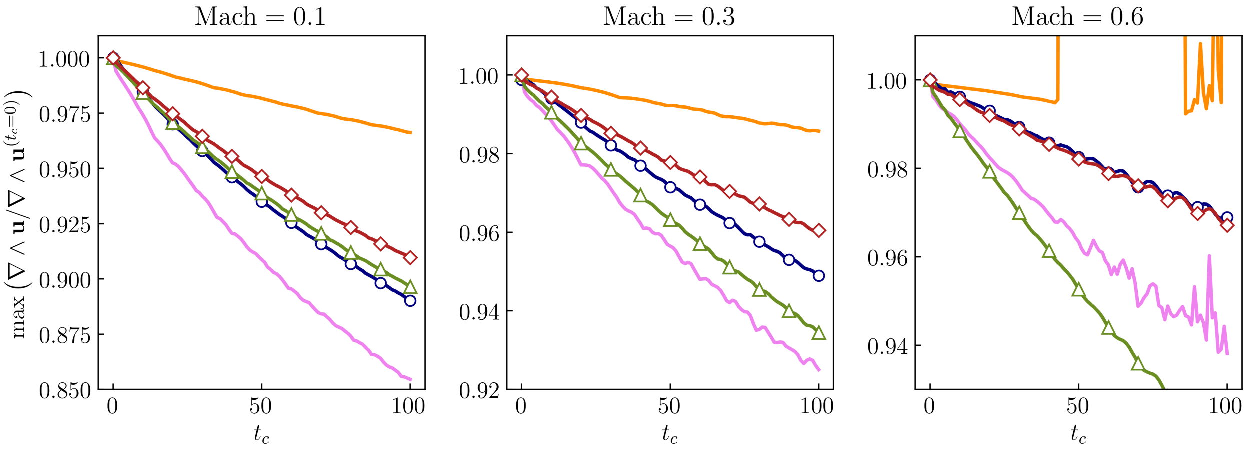

Figure B.4 – *Comparison of the maximum of vorticity as a function of the convective time t_c for increasing Mach numbers. -○-: STD, -△-: DC1, -◇-: DC2, —: Coarse uniform, —: Fine uniform.*

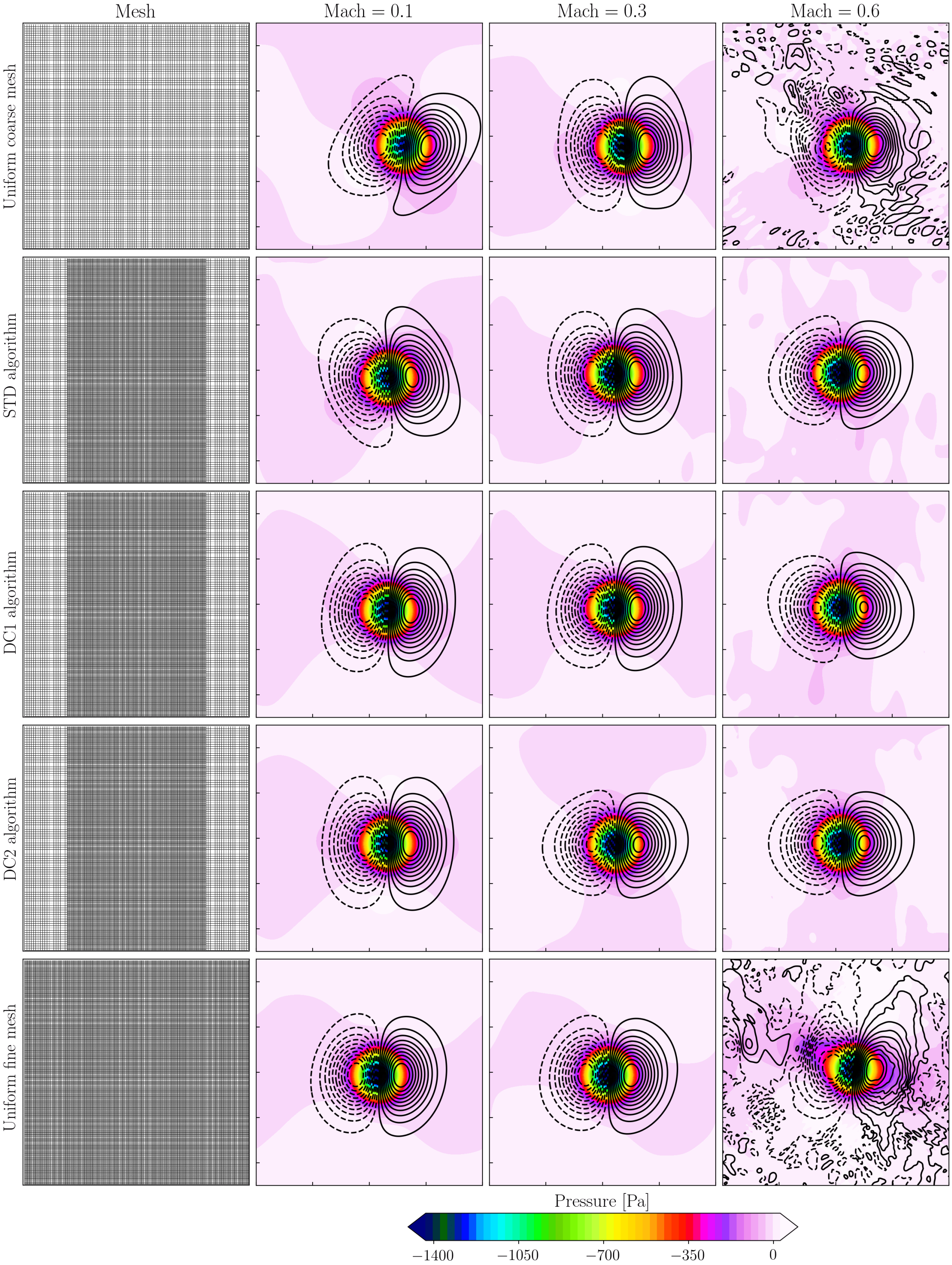

Figure B.5 – *Convected vortex ($R_c = 0.1m$) $t = 100t_c$ in a square-periodic box of $1m$ for increasing Mach numbers. $\Delta x^c = 2\Delta x^f = 0.01m$. Pressure field and 20 isocontours of the transverse velocity component u_y are displayed, with a viscosity $\nu = 1.49.10^{-5} m.s^{-1}$. From top to bottom: Coarse uniform, non-uniform with STD algorithm, non-uniform with DC1 algorithm, non-uniform with DC2 algorithm, fine uniform.*

Appendix C

Definition and properties of Power and Cross spectral densities

Power and cross spectral densities are a widely used tool in signal analysis. These functions are defined as the Fourier transform of correlation functions. Correlation functions indicate the similarity of processes as a function of time, whereas spectral densities find them as a function of frequency.

Auto- and cross- correlation functions

For two time signals $x(t)$ and $y(t)$ with finite energy, the auto-correlation functions R_{xx} (noted R_x for simplicity) with $i \in [x, y]$ and cross-correlation functions R_{xy} are defined as

$$\mathrm{R}_x(\tau) = \int_{-\infty}^{\infty} x(t)x^*(t-\tau)dt, \tag{C.0.1}$$

and

$$\mathrm{R}_{xy}(\tau) = \int_{-\infty}^{\infty} x(t)y^*(t-\tau)dt, \tag{C.0.2}$$

with τ a time delay between both signals and the superscript $(^*)$ stands for the conjugate. By hermitian symmetry, these functions have the property $\mathrm{R}_{xx}(\tau) = \mathrm{R}^*_{xx}(-\tau)$ and $\mathrm{R}_{xy}(\tau) = \mathrm{R}^*_{yx}(-\tau)$.

These correlation functions can also be written according to the convolution product $< * >$.

$$\mathrm{R}_x(\tau) = x(\tau) * x^*(-\tau) \qquad , \qquad \mathrm{R}_{xy}(\tau) = x(\tau) * y^*(-\tau). \tag{C.0.3}$$

Power- and cross- spectral densities

The power spectral density S_x and the cross spectral density S_{xy} are defined as the Fourier transform $\mathcal{F}$ of the auto- and cross-correlation functions respectively.

$$\mathrm{S}_x(f) = \int_{-\infty}^{\infty} \mathrm{R}_x(\tau)e^{-j2\pi f\tau}d\tau, \tag{C.0.4}$$

and

$$\mathrm{S}_{xy}(f) = \int_{-\infty}^{\infty} \mathrm{R}_{xy}(\tau)e^{-j2\pi f\tau}d\tau \tag{C.0.5}$$

Alternatively, they can be obtained from the convolution product:

$$\begin{aligned} \mathrm{S}_x(f) &= \mathcal{F}\left\{x(\tau) * x^*(-\tau)\right\}, \\ &= \mathcal{F}\left\{x(\tau)\right\} * \mathcal{F}\left\{x^*(-\tau)\right\}, \\ &= X(f)X^*(f), \\ &= |X(f)|^2 \end{aligned} \tag{C.0.6}$$

and

$$\begin{aligned}
\mathrm{S}_{xy}(f) &= \mathcal{F}\left\{x(\tau) * y^*(-\tau)\right\}, \\
&= \mathcal{F}\left\{x(\tau)\right\} * \mathcal{F}\left\{y^*(-\tau)\right\}, \\
&= X(f)Y^*(f)
\end{aligned} \tag{C.0.7}$$

In the same way, one can write

$$\mathrm{S}_{yx}(f) = Y(f)X^*(f) = S^*_{xy}(f). \tag{C.0.8}$$

These tools will be very useful to analyze and decompose the signals corresponding to dipole and quadrupole sources and their correlations in Sec. 7.4.2.

Coherence function

Finally, the last notion to be introduced that will be useful is the coherence function $\mathrm{C_{xy}}$.

$$\mathrm{C}_{xy} = \frac{|S_{xy}(f)|^2}{S_{xx}(f)S_{yy}(f)} \quad , \qquad 0 \leq \mathrm{C}_{xy} \leq 1. \tag{C.0.9}$$

The $x(t)$ and $y(t)$ signals are considered incoherent at the frequency f_0 if $\mathrm{C}_{xy}(f_0) = 0$. They will be perfectly coherent if $\mathrm{C}_{xy}(f_0) = 1$.

Bibliography

[1] B. Berglund, T. Lindvall, and D. H. Schwela. New Who Guidelines for Community Noise. *World Health Organization, Geneva*, 31:24–29, 2000. 2

[2] Airbus. Global Market Forecast. Cities, Airports and Aircraft. 2019-2038. 2

[3] ICAO. Manual of aerodrome certification procedures. 2002. 2

[4] Review of the quota count (QC) system used for administering the night noise quotas at Heathrow, Gatwick and Stansted airports. 2003. 2

[5] https://www.airway1.com/virgin-atlantic-gets-its-first-a350-1000/footprint/. 2019. 3

[6] https://www.libdemvoice.org/sponsored-post-the-plan-for-a-quieter-heathrow-expansion-37153.html. 2013. 3

[7] A. Sengissen. Noise induced by grazing flow over cavities. *Airbus EEA6,Ref. PR0613451*, pages 1–10, 2006. 3

[8] W. Dobrzynski. Almost 40 years of airframe noise research: What did we achieve? *Journal of Aircraft*, 47:353–367, 2010. 5, 6

[9] J.-C. Giret. *Simulations aux grandes échelles des écoulements instationnaires turbulents autour des trains d'atterrissage pour la prédiction du bruit aérodynamique.* PhD thesis, 2013. 5, 6, 7, 102, 162, 164, 179, 180, 181, 192, 194, 195, 202

[10] W. K. Blake. *Mechanics of Flow-Induced Sound and Vibration*, volume 2. 2017. 5

[11] M. Pott-Pollenske, W. Dobrzynski, H. Buchholz, et al. Airframe noise characteristics from flyover measurements and predictions. *Collection of Technical Papers - 12th AIAA/CEAS Aeroacoustics Conference*, 4(May):2069–2082, 2006. 5

[12] T. J. Heffernon. *Aircraft Noise Installation Effect.* PhD thesis, 2013. 5

[13] Y. Martelet. *Jet mixing noise model based on geometrical acoustics for the prediction of installation effects.* PhD thesis, 2020. 5, 121

[14] M. Mosher. Phased arrays for aeroacoustic testing: Theoretical development. *2nd AIAA/CEAS Aeroacoustics Conference*, 1996. 6, 168, 195

[15] T. F. Brooks and W. M. Humphreys. A deconvolution approach for the mapping of acoustic sources (DAMAS) determined from phased microphone arrays. *Journal of Sound and Vibration*, 294:856–879, 2006. 6, 168, 195

[16] P. Sijtsma. CLEAN based on spatial source coherence. *13th AIAA/CEAS Aeroacoustics Conference*, 6:357–374, 2007. 6, 168, 195

[17] M. Y. Zaytsev, V. F. Kopiev, S. A. Velichko, and I. V. Belyaev. Fly-over noise source localization during acoustic flight tests of advanced passenger aircraft. *25th AIAA/CEAS Aeroacoustics Conference, 2019*, pages 1–12, 2019. 6

[18] M. R. Fink. Noise component method for airframe noise. *Journal of Aircraft*, 16:659–665, 1979. 6

[19] M. G. Smith and L. C. Chow. Prediction method for aerodynamic noise from aircraft landing gear. *4th AIAA/CEAS Aeroacoustics Conference*, pages 153–161, 1998. 6

[20] Y. Guo. A study on local flow variations for landing gear noise research. *14th AIAA/CEAS Aeroacoustics Conference*, (May):5–7, 2008. 6

[21] C. Zhang. *Amélioration de Loi de Paroi de Simulation aux Grands Échelles pour des Applications Aéroacoustiques*. PhD thesis, 2019. 7, 8, 102, 164, 172, 181, 192, 195

[22] P. Sagaut and S. Deck. Large eddy simulation for aerodynamics: Status and perspectives. *Philosophical Transactions of the Royal Society A: Mathematical, Physical and Engineering Sciences*, 367(1899):2849–2860, 2009. 7, 8, 164, 167

[23] O. Reynolds. On the Dynamical Theory of Incompressible Viscous Fluids and the Determination of the Criterion. *Philosophical Transactions of the Royal Society of London A.*, (186):123–164, 1895. 7

[24] P. R. Spalart, S. R. Allmaras, and J. Reno. One-Equatlon Turbulence Model for Aerodynamic Flows. *30th AIAA Aerospace Sciences Meeting and Exhibit*, 1992. 7, 8

[25] W. P. Jones and B. E. Launder. The prediction of laminarization with a two-equation model of turbulence. *Journal of Heat and Mass Transfer*, 15:301–314, 1972. 7

[26] D. C. Wilcox. Formulation of the k-ω turbulence model revisited. *AIAA Journal*, 46:2823–2838, 2008. 7

[27] S. Deck. Recent improvements in the Zonal Detached Eddy Simulation (ZDES) formulation. *Theoretical and Computational Fluid Dynamics*, 26:523–550, 2012. 7, 8, 225

[28] W. M. Dobrzynski, B. Schöning, L. C. Chow, et al. Design and testing of low noise landing gears. *Collection of Technical Papers - 11th AIAA/CEAS Aeroacoustics Conference*, 4:2619–2633, 2005. 7

[29] D. P. Lockard, M. R. Khorrami, and F. Li. Aeroacoustic analysis of a simplified landing gear. *9th AIAA/CEAS Aeroacoustics Conference and Exhibit*, 2003. 7

[30] J. Smagorinsky. General Circulation Experiments with the Primitive Equations. Part I, the Basic Experiment. *Monthly Weather Review*, 38:99–164, 1963. 8, 116

[31] H. Choi and P. Moin. Grid-point requirements for large eddy simulation: Chapman's estimates revisited. *Physics of Fluids*, 24:1–6, 2012. 8

[32] J. C. Giret, A. Sengissen, S. Moreau, and J. C. Jouhaud. Prediction of LAGOON landing-gear noise using an unstructured LES solver. *19th AIAA/CEAS Aeroacoustics Conference*, page 110, 2013. 8, 164, 165, 166, 179, 192

[33] X. I. Yang and K. P. Griffin. Grid-point and time-step requirements for direct numerical simulation and large-eddy simulation. *Physics of Fluids*, 33, 2021. 8

[34] Y. Hou, D. Angland, and A. Scotto. The ability of a weakly compressible solver to predict landing gear noise with flow-acoustic interactions. *23rd AIAA/CEAS Aeroacoustics Conference*, 2017. 8, 165, 167

[35] Y. Hou, D. Angland, and A. Scotto. A numerical study of installation effects of the rudimentary landing gear benchmark problem. *24th AIAA/CEAS Aeroacoustics Conference*, pages 1–13, 2018. 8

[36] A. Sengissen, J.-C. Giret, C. Coreixas, and J.-F. Boussuge. Simulations of LAGOON landing-gear noise using Lattice Boltzmann Solver. *21st AIAA/CEAS Aeroacoustics Conference*, pages 1–22, 2015. 8, 10, 11, 12, 83, 116, 122, 164, 166, 169, 180, 184, 218

[37] R. Brionnaud, G. Trapani, M. Chávez Modena, and D. M. Holmanx. Direct noise computation with a lattice-boltzmann method and application to industrial test cases. *22nd AIAA/CEAS Aeroacoustics Conference*, pages 1–20, 2016. 8, 9, 10, 127

[38] P. R. Spalart, W. H. Jou, M. K. Strelets, and S. R. Allmaras. Comments on the feasibility of LES for wings and on a hybrid RANS/LES approach. *Advances in DNS/LES*, pages 4–8, 1997. 8, 165

[39] F. R. Menter and M. Kuntz. Adaptation of Eddy-Viscosity Turbulence Models to Unsteady Separated Flow Behind Vehicles. *The Aerodynamics of Heavy Vehicles: Trucks, Buses, and Trains*, pages 339–352, 2004. 8

[40] P. R. Spalart, S. Deck, M. L. Shur, et al. A new version of detached-eddy simulation, resistant to ambiguous grid densities. *Theoretical and Computational Fluid Dynamics*, 20:181–195, 2006. 8

[41] S. Deck. Zonal-detached-eddy simulation of the flow around a high-lift configuration. *AIAA Journal*, 43:2372–2384, 2005. 8, 163

[42] C. Uribe. *Développement d'une approche ZDES á deux équations de transport et application turbomachines*. PhD thesis, 2018. 8

[43] L. Sanders, E. Manoha, S. Ben Khelil, and C. François. LAGOON: CFD/CAA coupling for landing gear noise and comparison with experimental database. *17th AIAA/CEAS Aeroacoustics Conference*, (June):5–8, 2011. 8, 163, 199

[44] L. Sanders, E. Manoha, S. Ben Khelil, and C. François. LAGOON: New mach landing gear noise computation and further analysis of the CAA process. *18th AIAA/CEAS Aeroacoustics Conference (33rd AIAA Aeroacoustics Conference)*, (June), 2012. 8, 163, 164

[45] L. Sanders, E. Manoha, S. Ben Khelil, and C. François. CFD/CAA coupling on the LAGOON #2 landing gear using a structured multi-block solver with the Chimera technique. *19th AIAA/CEAS Aeroacoustics Conference*, 2013. 8, 163, 202, 203, 214

[46] W. Liu, J. W. Kim, X. Zhang, and B. Caruelle. Simulation of a generic two-wheel nose landing gear using high-order finite difference schemes. *18th AIAA/CEAS Aeroacoustics Conference*, 2012. 8, 163

[47] W. Liu, J. Wook Kim, X. Zhang, D. Angland, and B. Caruelle. Landing-gear noise prediction using high-order finite difference schemes. *Journal of Sound and Vibration*, 332:3517–3534, 2013. 8, 163

[48] F. de la Puente, L. Sanders, and F. Vuillot. On LAGOON nose landing gear CFD/CAA computation over unstructured mesh using a ZDES approach. *20th AIAA/CEAS Aeroacoustics Conference*, (June):1–14, 2014. 8, 164, 199

[49] F. de la Puente Cerezo, L. Sanders, F. Vuillot, P. Druault, and E. Manoha. Zonal Detached Eddy Simulation of a simplified nose landing-gear for flow and noise predictions using an unstructured Navier-Stokes solver. *Journal of Sound and Vibration*, 405, 2017. 8, 164, 172, 173, 189

[50] T. R. Ricciardi, W. R. Wolf, and R. Speth. Acoustic prediction of lagoon landing gear: Cavity noise and coherent structures. *AIAA Journal*, 56:4379–4399, 2018. 8, 189

[51] A. F. P. Ribeiro, C. Damiano, F. Ehab, and S. Nölting. CFD / CAA Analysis of the LAGOON Landing Gear. *19th AIAA/CEAS Aeroacoustics Conference Paper 2013-2256*, pages 1–24, 2013. 8, 9, 12, 162, 165, 179, 180, 181, 189, 192

[52] D. Casalino, A. F. P. Ribeiro, E. Fares, and S. Nölting. Lattice-Boltzmann Aeroacoustic Analysis of the LAGOON Landing-Gear Configuration. *AIAA Journal*, 52:1232–1248, 2014. 8, 9, 12, 162, 165, 179, 180, 181, 189, 192

[53] C. Seror, P. Sagaut, and A. Belanger. A numerical aeroacoustics analysis of a detailed landing gear. *Collection of Technical Papers - 10th AIAA/CEAS Aeroacoustics Conference*, 2(May):970–976, 2004. 9

[54] D. Casalino, S. Nölting, E. Fares, et al. Towards numerical aircraft noise certification: Analysis of a full-scale landing gear in fly-over configuration. *18th AIAA/CEAS Aeroacoustics Conference*, pages 4–6, 2012. 9

[55] D. B. Armstrong and V. Raymond. Numerical Simulations of Flow over a Landing Gear with Noise Reduction Devices using the Lattice-Boltzmann Method. *19th AIAA/CEAS Aeroacoustics Conference*, pages 1–12, 2013. 9

[56] M. F. Barad, J. G. Kocheemoolayil, and C. C. Kiris. Lattice boltzmann and navier-stokes cartesian CFD approaches for airframe noise predictions. *23rd AIAA Computational Fluid Dynamics Conference*, pages 1–16, 2017. 9, 109, 110, 166, 167

[57] Y. Hou, D. Angland, A. Sengissen, and A. Scotto. Lattice-Boltzmann and Navier-Stokes Simulations of the Partially Dressed, Cavity-Closed Nose Landing Gear Benchmark Case. *AIAA/CEAS Aeroacoustics Conference*, 2019. 9, 11, 109, 149, 221

[58] P. Sagaut. Toward advanced subgrid models for Lattice-Boltzmann-based Large-eddy simulation : Theoretical formulations. *Computers and Mathematics with Applications*, 59:2194–2199, 2010. 9, 17

[59] H. Touil, D. Ricot, and E. Lévêque. Direct and large-eddy simulation of turbulent flows on composite multi-resolution grids by the lattice Boltzmann method. *Journal of Computational Physics*, 256:220–233, 2014. 9, 11, 58, 59, 60, 127, 128, 132, 136, 139, 149

[60] J. Jacob, O. Malaspinas, and P. Sagaut. A new hybrid recursive regularised Bhatnagar-Gross-Krook collision model for Lattice Boltzmann method-based large eddy simulation. *Journal of Turbulence*, 5248, 2018. 9, 70, 72, 78, 88, 94, 105, 112

[61] P. A. Ravetta, M. R. Khorrami, B. Konig, and E. Fares. Analysis of Simulated and Experimental Noise Sources of Boeing 777 Main Gear Model via CLEAN in 3D. *24th AIAA/CEAS Aeroacoustics Conference*, pages 1–19, 2018. 9, 17, 83, 135

[62] C. A. Niedermeier, C. F. Janssen, and T. Indinger. Massively-parallel multi-GPU simulations for fast and accurate automotive aerodynamics. *Proceedings of the 6th European Conference on Computational Mechanics*, pages 2005–2012, 2018. 9

[63] E. Leveque, H. Touil, S. Malik, D. Ricot, and A. Sengissen. Wall-modeled large-eddy simulation of the flow past a rod-airfoil tandem by the lattice boltzmann method. *International Journal of Numerical Methods for Heat & Fluid Flow*, 2018. 9, 10, 95, 122

[64] H. Chen, S. A. Orszag, I. Staroselsky, and S. Succi. Expanded analogy between Boltzmann kinetic theory of fluids and turbulence. *Journal of Fluid Mechanics*, 519:301–314, 2004. 9, 165

[65] Y. H. Qian, D. D'Humières, and P. Lallemand. Lattice BGK models for Navier-Stokes equation. *Europhysics Letters*, 17:479–484, 1992. 9, 10, 18

[66] S. Wilhelm, J. Jacob, and P. Sagaut. An explicit power-law-based wall model for lattice Boltzmann method-Reynolds-averaged numerical simulations of the flow around airfoils. *Physics of Fluids*, 30, 2018. 9, 10, 11, 39, 147

[67] S. G. Cai, J. Degrigny, J. F. Boussuge, and P. Sagaut. Coupling of turbulence wall models and immersed boundaries on Cartesian grids. *Journal of Computational Physics*, 429, 2021. 9, 11, 172, 225

[68] J. Degrigny, S.-G. Cai, J.-F. Boussuge, and P. Sagaut. Improved Wall Model Treatment for Aerodynamic Flows in LBM. *Computers & Fluids*, 2021. 9, 10, 11, 172, 225

[69] F. Gendre, D. Ricot, G. Fritz, and P. Sagaut. Grid refinement for aeroacoustics in the Lattice Boltzmann Method : a new directionnal splitting approach. *Physical Review E*, 96, 2017. 9, 58, 65, 86, 91, 126, 127, 137

[70] F. Gendre. *Développement de méthodes de Boltzmann sur réseau en maillages non-uniformes pour l'aéroacoustique automobile*. PhD thesis, 2018. 9, 25, 59, 70, 95, 108, 119, 127, 128

[71] A. Keating, P. Dethioux, R. Satti, et al. Computational aeroacoustics validation and analysis of a nose landing gear. *15th AIAA/CEAS Aeroacoustics Conference*, 2009. 9

[72] S. Noelting, G. Bres, and P. Dethioux. A Hybrid Lattice-Boltzmann/FW-H Method to Predict Sources and Propagation of Landing Gear Noise. *16th AIAA/CEAS Aeroacoustics Conference*, pages 1–16, 2010. 9

[73] M. Murayama, Y. Yokokawa, H. Kato, et al. Computational and experimental study on noise generation from tire-axle regions of a two-wheel main landing gear. *17th AIAA/CEAS Aeroacoustics Conference*, pages 1–11, 2011. 9

[74] B. König and E. Fares. A Comparative Study of Simulated and Measured Main Landing Gear Noise for Large Civil Transports. (June):1–19, 2017. 9, 83, 149, 187

[75] E. Manoha and B. Caruelle. Summary of the LAGOON solutions from the benchmark problems for airframe noise computations-III workshop. *21st AIAA/CEAS Aeroacoustics Conference*, pages 1–19, 2015. 9, 158, 162, 163, 167, 168, 172, 173, 181

[76] A. De Rosis and C. Coreixas. Multiphysics flow simulations using D3Q19 lattice Boltzmann methods based on central moments. *Physics of Fluids*, 32, 2020. 10, 32

[77] E. Lévêque, F. Toschi, L. Shao, and J.-p. Bertoglio. Shear-improved Smagorinsky model for large-eddy simulation of wall-bounded turbulent flows, year = 2010. *Journal of Fluid Mechanics*. 10, 88, 166

[78] N. Afzal. Wake layer in a thermal turbulent boundary layer with pressure gradient. *International Journal of Heat and Mass Transfer*, 1999. 10, 39, 88, 147, 165

[79] F. Chevillotte and D. Ricot. Development and Evaluation of Non-Reflective Boundary Conditions for Lattice Boltzmann Method. *AIAA/CEAS Aeroacoustics Conference*, 2016. 10, 40, 83, 89, 137, 148, 169

[80] P. A. Skordos. Initial and boundary conditions for the lattice Boltzmann method. *Phys. Rev. E*, 48:4823–4842, 1993. 11, 88, 89, 148

[81] J. Lätt and B. Chopard. Straight velocity boundaries in the lattice Boltzmann method. *Physical Review E*, 77, 2008. 11, 88, 89, 95, 148

[82] J. C. Verschaeve and B. Müller. A curved no-slip boundary condition for lattice Boltzmann method. *Journal of Computational Physics*, 229, 2010. 11, 88, 89, 148

[83] D. Lagrava, O. Malaspinas, J. Lätt, and B. Chopard. Advances in multi-domain lattice boltzmann grid refinement. *Journal of Computational Physics*, 231(14):4808–4822, 2012. 11, 57, 58, 59, 60, 127, 131, 132, 134, 149

[84] M. Hasert. *Multi-scale lattice boltzmann simulations on distributed octrees*. PhD thesis, 2014. 12, 40, 94, 127

[85] E. Kors. OPENAIR Aerodays. Madrid. 2011. 14

[86] https://www.dlr.de/at/en/desktopdefault.aspx/tabid-12784/22395_read-51555/. 14

[87] T. Astoul, G. Wissocq, J.-F. Boussuge, A. Sengissen, and P. Sagaut. Analysis and reduction of spurious noise generated at grid refinement interfaces with the lattice Boltzmann method. *Journal of Computational Physics*, 418, 2020. 14, 136, 137, 141, 148

[88] T. Astoul, G. Wissocq, J.-f. Boussuge, A. Sengissen, and P. Sagaut. Lattice Boltzmann method for computational aeroacoustics on non-uniform meshes: a direct grid coupling approach. *arXiv2004.14887*, 2020. 15

[89] H. Yu, S. S. Girimaji, and L.-S. Luo. Lattice Boltzmann simulations of decaying homogeneous isotropic turbulence. *Physical Review E*, 71:1–5, 2005. 17

[90] X. Shan and S. Rothman. Lattice Boltzmann model for simulating flows with multiple phases and components. *Physical Review E*, 47, 1993. 17

[91] L.-S. Luo. Unified Theory of Lattice Boltzmann Models for Nonideal Gases. *Physical Review Letter*, 81:0–3, 1998. 17

[92] J. Bernsdorf, G. Brenner, and F. Durst. Numerical analysis of the pressure drop in porous media flow with lattice Boltzmann (BGK) automata. *Computer Physics Communications*, 129:247–255, 2000. 17

[93] T. Ye, N. Phan-thien, and C. Teck. Particle-based simulations of red blood cells - A review. *Journal of Biomechanics*, pages 1–12, 2015. 17

[94] M. Schnherr, K. Kucher, M. Geier, et al. Multi-thread implementations of the lattice Boltzmann method on non-uniform grids for CPUs and GPUs. *Computers and Mathematics with Applications*, 61:3730–3743, 2011. 17, 38

[95] C. Feichtinger, J. Habich, H. Köstler, U. Rüde, and T. Aoki. Performance modeling and analysis of heterogeneous lattice Boltzmann simulations on CPU-GPU clusters. *Parallel Comput.*, 46:1 – 13, 2015. 17, 38

[96] F. Schornbaum and U. Rüde. Massively parallel algorithms for the lattice Boltzmann method on nonuniform grids. *SIAM J. Sci. Comput*, pages C96–C126, 2016. 17

[97] J. C. Maxwell. On the dynamical theory of gases. *Philos. Trans. Roy. Soc. London*, 157:49–88, 1867. 17, 18

[98] L. Boltzmann. Weitere Studien über das Wärmegleichgewicht unter Gasmolekülen. *Wien. Ber.*, 66:275370, 1872. 17, 18, 19

[99] J. Hardy, Y. Pomeau, and O. de Pazzis. Time evolution of a two-dimensional model system. I. Invariant states and time correlation functions. *J. Math. Phys.*, 14(12):1746–1759, 1973. 17

[100] U. Frisch, B. Hasslacher, and Y. Pomeau. Lattice-gas automata for the Navier-Stokes equation. *Phys. Rev. Lett.*, 56:1505–1508, 1986. 17

[101] D. d'Humieres, P. Lallemand, and U. Frisch. Lattice gas models for 3D hydrodynamics. *Europhys. Lett.*, 2(4):291, 1986. 17

[102] G. R. McNamara and G. Zanetti. Use of the Boltzmann Equation to Simulate Lattice-Gas Automata. *Physical Review Letters*, 61(20):2332–2335, 1988. 17

[103] F. Higuera and J. Jimenez. Boltzmann approach to lattice gas simulations. *Europhys. Lett.*, 663, 1989. 18

[104] H. Chen, S. Chen, and W. H. Matthaeus. Recovery of the Navier-Stokes equations using a lattice-gas Boltzmann method. *Physical Review A*, 45:5339–5342, 1992. 18

[105] P. L. Bhatnagar, E. P. Gross, and M. Krook. A model for collision processes in gases. I. Small amplitude processes in charged and neutral one-component systems. *Physical Review*, 94:511–525, 1954. 18, 20

[106] X. He and L.-S. Luo. A *priori* derivation of the lattice Boltzmann equation. *Physical Review E*, 55(6), 1997. 18, 26, 29

[107] K. Huang. *Statistical mechanics.* John Wiley & Sons, 1987. 18

[108] R. Zwanzig. *Nonequilibrium statistical mechanics.* Oxford University Press, 2001. 18

[109] D. Hilbert. Begründung der kinetischen gastheorie. *Mathematische Annalen*, 72:562–577, 1912. 22, 23

[110] S. Chapman and T. Cowling. The Mathematical Theory of Non-uniform Gases: An Account of the Kinetic Theory and of Viscosity. Thermal Conduction and Diffusion in Gases. *Cambridge Mathematical Library, Cambridge University Press*, 1970. 22, 72

[111] F. Golse. The boltzmann equation and its hydrodynamic limits. *Handbook of Differential Equations : Evolutionary Equations 2*, pages 159–301, 2006. 23

[112] X. Shan, X.-F. Yuan, and H. Chen. Kinetic theory representation of hydrodynamics: a way beyond the navier-stokes equation. *Journal of Fluid Mechanics*, 550(-1):413, 2006. 24, 25, 26, 28, 29, 31, 71

[113] G. Wissocq. *Investigation of lattice Boltzmann methods for turbomachinery secondary air system simulations.* PhD thesis, 2019. 25, 37, 50, 104, 105

[114] P.-A. Masset and G. Wissocq. Linear hydrodynamics and stability of the discrete velocity boltzmann equations. *Journal of Fluid Mechanics*, 897:A29, 2020. 25, 37, 45, 104, 112

[115] X. Shan and H. Chen. A general multiple-relaxation-time Boltzmann collision model. *International Journal of Modern Physics C*, 18:635–643, 2007. 26

[116] F. Chen, A. Xu, G. Zhang, Y. Li, and S. Succi. Multiple-relaxation-time lattice boltzmann approach to compressible flows with flexible specific-heat ratio and prandtl number. *Europhysics Letters*, 90, 2010. 26

[117] X. He, X. Shan, and G. D. Doolen. Discrete boltzmann equation model for nonideal gases. *Phys. Rev. E*, 57, 1998. 26, 34

[118] Q. Li, Y. L. He, Y. Wang, and W. Q. Tao. Coupled double-distribution-function lattice boltzmann method for the compressible navier-stokes equations. *Phys. Rev. E*, 76, 2007. 26

[119] Z. Guo, C. Zheng, B. Shi, and T. S. Zhao. Thermal lattice Boltzmann equation for low Mach number flows: Decoupling model. *Physical Review E - Statistical, Nonlinear, and Soft Matter Physics*, 75(3):1–15, 2007. 26

[120] Y. Feng, P. Boivin, J. Jacob, and P. Sagaut. Hybrid recursive regularized thermal lattice Boltzmann model for high subsonic compressible flows. *Journal of Computational Physics*, 2019. 26, 102, 103, 105, 112

[121] F. Renard, Y. Feng, J.-F. Boussuge, and P. Sagaut. Improved compressible Hybrid Lattice Boltzmann Method on standard lattice for subsonic and supersonic flows. *Journal of Computational Physics*, 219, 2021. 26, 112

[122] S.-L. Guo, Y.-L. Feng, J. Jacob, F. Renard, and P. Sagaut. An efficient lattice boltzmann method for compressible aerodynamics on d3q19 lattice. *Journal of Computational Physics*, 2020. 26

[123] X. Shan and X. He. Discretization of the velocity space in the solution of the boltzmann equation. *Phys. Rev. Lett.*, 80:65–68, 1998. 26

[124] H. Grad. Note on N-dimensional Hermite polynomials. *Commun. Pure Appl. Math.*, 2(4):325–330, 1949. 26

[125] C. Coreixas, B. Chopard, and J. Latt. Comprehensive comparison of collision models in the lattice boltzmann framework: Theoretical investigations. *Phys. Rev. E*, 100, 2019. 28

[126] O. Malaspinas. Increasing stability and accuracy of the lattice Boltzmann scheme : recursivity and regularization. *ArXiv e-prints:1505.06900*, pages 1–31, 2015. 28, 70, 71, 72, 106

[127] X. Shan. The mathematical structure of the lattices of the lattice Boltzmann method. *Journal of Computational Science*, 17:475–481, 2016. 31

[128] P. J. Dellar. Bulk and shear viscosities in lattice Boltzmann equations. *Physical Review E - Statistical Physics, Plasmas, Fluids, and Related Interdisciplinary Topics*, 64:11, 2001. 33, 34

[129] L. D. Landau and E. M. Lifshitz. Fluid mechanics: Landau and Lifshitz: course of theoretical physics. *Pergamon, Oxford*, 2nd edition:539, 1987. 34

[130] T. Krüger, H. Kusumaatmaja, A. Kuzmin, et al. *The Lattice Boltzmann Method - Principles and Practice.* 2016. 36

[131] M. Wittmann, T. Zeiser, G. Hager, and G. Wellein. Comparison of different propagation steps for the lattice boltzmann method. *Computers & Mathematics with Applications*, 65, 2011. 38

[132] J. Latt, C. Coreixas, and J. Beny. Cross-platform programming model for many-core lattice Boltzmann simulations. *arXiv:2010.11751*, 2020. 38

[133] F. Schornbaum and U. Rüde. Massively parallel algorithms for the lattice boltzmann method on nonuniform grids. *SIAM Journal on Scientific Computing*, 38(2):96–126, 2016. 38, 127

[134] D. D'Humieres, I. Ginzburg, M. Krafczyk, P. Lallemand, and L.-S. Luo. Multiple-relaxation-time lattice Boltzmann models in three dimensions. *Philosophical Transactions of the Royal Society A: Mathematical, Physical and Engineering Sciences*, 360(1792):437–451, 2002. 39, 52, 70, 75, 108

[135] P. J. Dellar. Nonhydrodynamic modes and a priori construction of shallow water lattice Boltzmann equations. *Physical Review E - Statistical Physics, Plasmas, Fluids, and Related Interdisciplinary Topics*, 65:1–12, 2002. 39, 50, 95

[136] C. Coreixas. *High-order extension of the recursive regularized lattice Boltzmann method*. PhD thesis, 2018. 39, 45, 71, 72, 104, 105, 122

[137] Y. Jin, F. Liao, and J. Cai. Numerical simulation of 30p30n multi-element airfoil using delayed detached-eddy simulation. *Aiaa Aviation 2020 Forum*, pages 1–24, 2020. 40

[138] J. von Neumann and R. D. Richtmyer. A Method for the Numerical Calculation of Hydrodynamic Shocks. *Journal of Applied Physics*, 21:232–237, 1950. 45, 46

[139] C. W.tam, J. C.webb, and Zhongdong. A study of the short wave components in computational acoustics. *Journal of Computational Acoustics*, 01:1–30, 1992. 45, 109

[140] C. Bogey and C. Bailly. A family of low dispersive and low dissipative explicit schemes for flow and noise computations. *Journal of Computational Physics*, 194:194–214, 2004. 45, 109

[141] J. Berland, C. Bogey, O. Marsden, and C. Bailly. High-order, low dispersive and low dissipative explicit schemes for multiple-scale and boundary problems. *Journal of Computational Physics*, 224(2):637–662, 2007. 45

[142] L. Muscat, G. Puigt, M. Montagnac, and P. Brenner. A coupled implicit-explicit time integration method for compressible unsteady flows. *Journal of Computational Physics*, 398:108883, 2019. 45

[143] S. Marié. *Etude de la méthode Boltzmann sur Réseau pour les simulations en aéroacoustique*. PhD thesis, 2008. 45, 47, 64, 108

[144] P. Lallemand and L.-S. Luo. Theory of the lattice Boltzmann method: Dispersion, dissipation, isotropy,Galilean invariance, and stability. *Physical Review E*, 61(6):6546–6562, 2000. 46, 52, 70, 75, 104

[145] P. Lallemand and L.-S. Luo. Theory of the lattice boltzmann method: Acoustic and thermal properties in two and three dimensions. *Physical review. E, Statistical, nonlinear, and soft matter physics*, 68, 2003. 46

[146] H. Xu and P. Sagaut. Optimal low-dispersion low-dissipation LBM schemes for computational aeroacoustics. *J. Comput. Phys.*, 230:5353–5382, 2011. 46, 70

[147] M. Chavez, E. Ferrer, and G. Rubio. Improving the stability of multiple-relaxation lattice boltzmann methods with central moments. *Computers & Fluids*, 2018. 46

[148] G. Wissocq, P. Sagaut, and J.-f. Boussuge. An extended spectral analysis of the lattice Boltzmann method : modal interactions and stability issues. *Journal of Computational Physics*, 2019. 46, 47, 48, 49, 50, 52, 65, 106, 108

[149] G. Wissocq, C. Coreixas, and J.-f. Boussuge. Linear stability and isotropy properties of athermal regularized lattice Boltzmann methods. *Physical Review E*, 102, 2020. 46, 70, 76, 104, 105, 106, 112, 114, 122, 223, 235

[150] J. D. Sterling and S. Chen. Stability analysis of lattice boltzmann methods. *Journal of Computational Physics*, 123(1):196–206, 1996. 46

[151] R. Adhikari and S. Succi. Duality in matrix lattice Boltzmann models. *Physical Review E - Statistical, Nonlinear, and Soft Matter Physics*, 78(6):1–9, 2008. 50, 53, 95

[152] I. V. Karlin, F. Bösch, and S. S. Chikatamarla. Gibbs' principle for the lattice-kinetic theory of fluid dynamics. *Physical Review E - Statistical, Nonlinear, and Soft Matter Physics*, 90:1–5, 2014. 52, 109

[153] B. Dorschner, N. Frapolli, S. S. Chikatamarla, and I. V. Karlin. Grid refinement for entropic lattice Boltzmann models. *Physical Review E - Statistical, Nonlinear, and Soft Matter Physics*, 94, 2016. 52, 109

[154] R. Benzi, S. Succi, and M. Vergassola. Turbulence modelling by nonhydrodynamic variables. *Europhysics Letters*, 13, 1990. 52

[155] J. Latt and B. Chopard. Lattice Boltzmann method with regularized pre-collision distribution functions. *Mathematics and Computers in Simulation*, 72:165–168, 2006. 53, 71, 95

[156] A. Dupuis and B. Chopard. Theory and applications of an alternative lattice boltzmann grid refinement algorithm. *Physical Review E.*, 67, 2003. 57, 127, 128, 131

[157] O. Filippova and D. Hänel. Grid Refinement for Lattice-BGK Models. *Journal of Computational Physics*, 147:219–228, 1998. 58, 125, 127, 128

[158] M. Rohde, D. Kandhai, J. J. Derksen, and H. E. A. van den Akker. A generic, mass conservative local grid refinement technique for lattice-Boltzmann schemes. *International Journal for Numerical Methods in Fluids*, 51:439–468, 2006. 59, 127, 128

[159] H. Chen, O. Filippova, J. Hoch, et al. Grid refinement in lattice Boltzmann methods based on volumetric formulation. *Physica A: Statistical Mechanics and its Applications*, 362:158–167, 2006. 59, 126, 127, 128

[160] D. Yu, R. Mei, and W. Shyy. A multi-block lattice Boltzmann method for viscous fluid flows. *International Journal of Numerical Methods in Fluids*, 120:99–120, 2002. 59, 127

[161] B. Crouse, E. Rank, M. Krafczyk, and J. T. Olke. A LB-based approach for adaptive flow simulations. *International Journal of Modern Physics*, 17:10—112, 2003. 59, 127

[162] D. Ricot, S. Marié, P. Sagaut, and C. Bailly. Lattice Boltzmann method with selective viscosity filter. *Journal of Computational Physics*, 228:4478–4490, 2009. 70, 95, 96, 102, 113

[163] S. Marié and X. Gloerfelt. Adaptive filtering for the lattice Boltzmann method. *Journal of Computational Physics*, 333, 2017. 70

[164] Y.-H. Qian. Fractional Propagation and the Elimination of Staggered Invariants in Lattice-BGK Models. *International Journal of Modern Physics C*, 08:753–761, 1997. 70, 96

[165] G. R. McNamara, A. L. Garcia, and B. J. Alder. Stabilization of thermal lattice Boltzmann models. *Journal of Statistical Physics*, 81:395–408, 1995. 70, 96

[166] Z. Guo, B. Shi, and C. Zheng. Chequerboard effects on spurious currents in the lattice Boltzmann equation for two-phase flows. *Philosophical Transactions of the Royal Society A: Mathematical, Physical and Engineering Sciences*, 369:2283–2291, 2011. 70, 96

[167] D. D'Humières. Generalized Lattice-Boltzmann Equations. *Rarefied Gas Dynamics: Theory and Simulations*, 159:450–459, 2012. 70

[168] M. Geier, A. Greiner, and J. G. Korvink. Cascaded digital lattice Boltzmann automata for high Reynolds number flow. *Physical Review E - Statistical, Nonlinear, and Soft Matter Physics*, 73, 2006. 70

[169] M. Geier, A. Greiner, and J. G. Korvink. A factorized central moment lattice Boltzmann method. *The European Physical Journal Special Topics*, 171:55–61, 2009. 70

[170] F. Dubois, T. Février, and B. Graille. On the stability of a relative velocity lattice Boltzmann scheme for compressible Navier-Stokes equations. *Comptes Rendus - Mecanique*, 343, 2015. 70

[171] A. De Rosis. Nonorthogonal central-moments-based lattice boltzmann scheme in three dimensions. *Phys. Rev. E*, 95, 2017. 70

[172] M. Geier, M. Schönherr, A. Pasquali, and M. Krafczyk. The cumulant lattice Boltzmann equation in three dimensions: Theory and validation. *Computers and Mathematics with Applications*, 70:507–547, 2015. 70

[173] J. Latt. *Hydrodynamic limit of lattice Boltzmann equations.* PhD thesis, 2007. 70, 71, 106, 108

[174] F. Brogi, O. Malaspinas, B. Chopard, and C. Bonadonna. Hermite regularization of the Lattice Boltzmann Method for open source computational aeroacoustics. *Journal of the Acoustical Society of America*, 2332, 2017. 70, 83

[175] C. Coreixas, G. Wissocq, G. Puigt, J. F. Boussuge, and P. Sagaut. Recursive regularization step for high-order lattice Boltzmann methods. *Physical Review E*, 96:1–22, 2017. 72

[176] L. Rego, F. Avallone, D. Ragni, and D. Casalino. Jet-installation noise and near-field characteristics of jet - surface interaction. *Journal of Fluid Mechanics*, 895. 83

[177] D. Casalino, A. Hazir, and A. Mann. Turbofan broadband noise prediction using the lattice boltzmann method. *AIAA Journal*, 56:609–628, 2018. 83, 127

[178] C. Coreixas. Round Cavity Noise Simulations using Lattice-Boltzmann Solver. *2015 PEGASUS-AIAA Aeroacoustics Conference*, 2015. 83, 116, 122

[179] D. Singh, A. Ribeiro, B. Knig, and E. Fares. Lattice boltzmann simulations of a supersonic cavity. *35th AIAA Applied Aerodynamics Conference*, 2017. 83

[180] S. Mancini, A. Kolb, I. Gonzalez-Martino, and D. Casalino. Very-large eddy simulations of the m219 cavity at high-subsonic and supersonic conditions. *AIAA Scitech 2019 Forum*, 2019. 83

[181] H. Lamb. Hydrodynamics. *6th edition. Cambridge University Press, Cambridge*, 1932. 83

[182] C. Oseen. Neuere Methoden und Ergebnisse in der Hydrodynamik. *(Akademie Verlag)*, 1927. 83

[183] G. Wissocq, J. F. Boussuge, and P. Sagaut. Consistent vortex initialization for the athermal lattice Boltzmann method. *Physical Review E*, 101:1–11, 2020. 83, 137

[184] R. Zhang, H. Chen, Y. H. Qian, and S. Chen. Effective volumetric lattice Boltzmann scheme. *Physical Review E - Statistical, Nonlinear, and Soft Matter Physics*, 63, 2001. 96

[185] O. Colin. *Simulations aux grandes échelles de la combustion turbulente prémélangée dans les statoréacteurs.* PhD thesis, 2000. 102

[186] K. Morton and S. Stringer. *Artificial Viscosity for the Cell Vertex Method*, pages 111–116. 2007. 102

[187] V. Bonneau, C. Polacsek, R. Barrier, et al. Tonal noise prediction of a turbofan with heterogeneous stator and bifurcations. *AIAA Journal*, 52:3354–3369, 2015. 102

[188] G. Delattre, F. Falissard, L. Vion, and L. Jacquin. Open rotor interaction noise reduction through front rotor wake modification. *International Journal of Aeroacoustics*, 15:207–227, 2016. 102

[189] F. Falissard, R. Boisard, R. Gaveriaux, et al. Influence of blade deformations on open-rotor low-speed and high-speed aerodynamics and aeroacoustics. *Journal of Aircraft*, 55:2267–2281, 2018. 102

[190] M. R. Visbal and D. V. Gaitonde. Very high-order spatially implicit schemes for computational acoustics on curvilinear meshes. *Journal of Computational Acoustics*, 9(4):1259–1286, 2001. 102

[191] S. Le Bras. *Modélisation de paroi et traitement aux interfaces des maillages non conformes pour les simulations aéroacoustiques avec une approche numérique d'ordre élevé*. PhD thesis, 2016. 102

[192] X. Nie, X. Shan, and H. Chen. Lattice-Boltzmann/ Finite-Difference Hybrid Simulation of Transonic Flow. *47th AIAA Aerospace Sciences Meeting*, page 2009, 2009. 102

[193] R. Vichnevetsky and J. B. Bowles. *Fourier analysis of numerical approximations of hyperbolic equations*. Studies in Applied Mathematics, 1982. 102

[194] D. N. Siebert, L. A. Hegele, and P. C. Philippi. Lattice Boltzmann equation linear stability analysis: Thermal and athermal models. *Physical Review E - Statistical, Nonlinear, and Soft Matter Physics*, 77:1–9, 2008. 104

[195] C. Coreixas, G. Wissocq, B. Chopard, and J. Latt. Impact of collision models on the physical properties and the stability of lattice Boltzmann methods. *Philosophical transactions. Series A, Mathematical, physical, and engineering sciences*, 378, 2020. 104

[196] A. Montessori, G. Falcucci, P. Prestininzi, M. La Rocca, and S. Succi. Regularized lattice Bhatnagar-Gross-Krook model for two- and three-dimensional cavity flow simulations. *Physical Review E - Statistical, Nonlinear, and Soft Matter Physics*, 89:1–8, 2014. 106

[197] K. K. Mattila, L. A. Hegele, and P. C. Philippi. Investigation of an entropic stabilizer for the lattice-Boltzmann method. *Physical Review E - Statistical, Nonlinear, and Soft Matter Physics*, 91(6):1–10, 2015. 106

[198] Z. Li, W. Cao, and D. Le Touzé. On the coupling of a direct-forcing immersed boundary method and the regularized lattice Boltzmann method for fluid-structure interaction. *Computers and Fluids*, 190:470–484, 2019. 106

[199] S. Marié, D. Ricot, and P. Sagaut. Comparison between lattice Boltzmann method and Navier-Stokes high order schemes for computational aeroacoustics. *Journal of Computational Physics*, 228:1056–1070, 2009. 108

[200] J. Butcher. Implicit runge-kutta processes. *Math. Comp.*, 18, 1964. 109

[201] S. K. Lele. Compact finite difference schemes with spectral-like resolution. *Journal of Computational Physics*, 103(1):16–42, 1992. 109

[202] C. Tam and J. Webb. Dispersion-relation-preserving finite difference schemes for computational acoustics. *J. Comput. Phys.*, 107:262–281, 1993. 109, 119

[203] F. Hu, M. Hussaini, and J. Manthey. Low-dissipation and low-dispersion runge-kutta schemes for computational acoustics. *Journal Computational Physics*, 124:177–191, 1996. 109

[204] J. Berland, C. Bogey, and C. Bailly. Optimized explicit schemes: Matching and boundary schemes and 4th-order Runge-Kutta algorithm. *Collection of Technical Papers - 10th AIAA/CEAS Aeroacoustics Conference*, 1:176–209, 2004. 109

[205] J. Berland, C. Bogey, and C. Bailly. Low-dissipation and low-dispersion fourth-order Runge-Kutta algorithm. *Computers and Fluids*, 35(10):1459–1463, 2006. 109

[206] C. Kiris, J. A. Housman, M. F. Barad, et al. Computational framework for Launch, Ascent, and Vehicle Aerodynamics (LAVA). *Aerospace Science and Technology*, 55:189–219, 2016. 109

[207] F. Bösch, S. S. Chikatamarla, and I. V. Karlin. Entropic multirelaxation lattice Boltzmann models for turbulent flows. *Physical Review E - Statistical, Nonlinear, and Soft Matter Physics*, 92:1–15, 2015. 109

[208] V. G. Weirs and G. V. Candlert. Optimization of Weighted ENO Schemes for DNS of Compressible Turbulence. *American Institute of Aeronautics and Astronautics*, pages 528–538, 1997. 109

[209] https://www.openfoam.com/documentation/. 109

[210] F. Renard, G. Wissocq, J.-F. Boussuge, and P. Sagaut. A linear stability analysis of compressible hybrid lattice Boltzmann methods. *arXiv:2006.08477*, 2020. 112

[211] T. Hainaut, T. L. Garrec, C. Polacsek, D. C. Mincu, and S. Deck. Aerodynamic and Aeroacoustic Numerical Investigation of an Axial Fan using Lattice Boltzmann Methods. *2018 AIAA/CEAS Aeroacoustics Conference*, 2018. 122

[212] L. Sandoval and D. Walter. *Revisiting grid refinement algorithms for the lattice Boltzmann method*. PhD thesis, 2012. 125, 127, 132, 152, 223

[213] D. Staubach. Static Block-Structured Grid Refinement for Parallel Lattice Boltzmann Simulations. 10. 126, 127

[214] M. Hasert, K. Masilamani, S. Zimny, et al. Complex fluid simulations with the parallel tree-based lattice boltzmann solver musubi. *Journal of Computational Science*, 5(5):784 – 794, 2014. 126

[215] G. Eitel-Amor, M. Meinke, and W. Schröder. A lattice-Boltzmann method with hierarchically refined meshes. *Computers and Fluids*, 75:127–139, 2013. 127

[216] S. M. Guzik, T. H. Weisgraber, P. Colella, and B. J. Alder. Interpolation methods and the accuracy of lattice-Boltzmann mesh refinement. *Journal of Computational Physics*, 259:461–487, 2014. 127

[217] J. Qi, H. Klimach, and S. Roller. Implementation of the compact interpolation within the octree based Lattice Boltzmann solver Musubi. *Computers and Mathematics with Applications*, 78:1131–1141, 2019. 127

[218] K. N. Premnath, M. J. Pattison, and S. Banerjee. Dynamic subgrid scale modeling of turbulent flows using lattice-Boltzmann method. *Physica A*, 388(13):2640–2658, 2009. 127

[219] D. M. Holman, R. M. Brionnaud, F. J. Martínez, and M. Mier-Torrecilla. Advanced aerodynamic analysis of the NASA high-lift trap wing with a moving flap configuration. *30th AIAA Applied Aerodynamics Conference 2012*, pages 1341–1359, 2012. 127

[220] K. N. Premnath, M. J. Pattison, and S. Banerjee. Computation of transitional flow past a circular cylinder using multiblock lattice Boltzmann method with a dynamic subgrid scale model. *Fluid Dynamics Research*, 45(5), 2013. 127

[221] G. Trapani, R. Brionnaud, and D. M. Holman. XFlow contribution to the third high-lift prediction workshop. *Applied Aerodynamics Conference*, pages 1–19, 2018. 127

[222] B. König, E. Fares, M. Murayama, and Y. Ito. PowerFLOW simulations for the third AIAA high lift prediction workshop. *AIAA Aerospace Sciences Meeting, 2018*, (210059):1–16, 2018. 127, 149

[223] P. T. Lew, A. Lyrintzis, B. Crouse, et al. Noise prediction of a subsonic turbulent round jet using the lattice-Boltzmann method. *13th AIAA/CEAS Aeroacoustics Conference (28th AIAA Aeroacoustics Conference)*, pages 1–23, 2007. 127

[224] A. Mann, M. S. Kim, B. Neuhierl, et al. Exhaust and Muffler Aeroacoustics Predictions using Lattice Boltzmann Method. *SAE International Journal of Passenger Cars - Mechanical Systems*, 8(3):1009–1017, 2015. 127

[225] D. P. Lockard, M. M. Choudhari, V. N. Vatsa, et al. Noise simulations of the high-lift common research model. *23rd AIAA/CEAS Aeroacoustics Conference, 2017*, pages 1–18, 2017. 127

[226] W. C. Van Der Velden, D. Casalino, P. Gopalakrishnan, et al. Jet noise prediction: Validation and physical insight. *2018 AIAA/CEAS Aeroacoustics Conference*, 2018. 127

[227] G. Romani, Q. Ye, F. Avallone, D. Ragni, and D. Casalino. Numerical analysis of fan noise for the NOVA boundary-layer ingestion configuration. *Aerospace Science and Technology*, 2019. 127

[228] G. Romani and D. Casalino. Rotorcraft blade-vortex interaction noise prediction using the Lattice-Boltzmann method. *Aerospace Science and Technology*, 88:147–157, 2019. 127

[229] D. Acevedo-Giraldo, L. Botero-Bolívar, L. Pereira, et al. Experimental and numerical aeroacoustic analyses of a large-scale flap side-edge model. *48th International Congress and Exhibition on Noise Control Engineering*, 2019. 127

[230] H. M. Noh. Numerical analysis of aerodynamic noise from pantograph in high-speed trains using lattice Boltzmann method. *Advances in Mechanical Engineering*, 11(7):1–12, 2019. 127

[231] O. Filippova, S. Succi, F. Mazzocco, et al. Multiscale Lattice Boltzmann Schemes with Turbulence Modeling. *Journal of Computational Physics*, 829:812–829, 2001. 127

[232] D. Yu, R. Mei, L.-s. Luo, and W. Shyy. Viscous flow computations with the method of lattice Boltzmann equation. *Progress in Aerospace sciences*, 39:329–367, 2003. 127

[233] Y. Peng and C. Shu. Application of multi-block approach in the immersed boundary - lattice Boltzmann method for viscous fluid flows. *Journal of Computational Physics*, 218:460–478, 2006. 127

[234] Lattice Boltzmann solver from NUMECA's, developed with FlowKit. *https://www.numeca.com/index/latticeboltzmann*. 127

[235] J. Latt, A. Parmigiani, E. Zurich, et al. Palabos: Parallel Lattice Boltzmann Solver. *Computers and Mathematics with Applications*, 2020. 127

[236] Y. Kuwata and K. Suga. Imbalance-correction grid-refinement method for lattice Boltzmann flow simulations. *Journal of Computational Physics*, 311:348–362, 2016. 127

[237] X. He and L.-S. Luo. Lattice Boltzmann Model for the Incompressible Navier-Stokes Equation. *Journal of Statistical Physics*, 88, 1997. 127

[238] Y. Tjalling J. Historical development of the Newton-Raphson method. *SIAM Review*, 37:531–551, 1995. 130

[239] W. H. Press, S. A. Teukolsky, W. T. Vetterling, and B. P. Flannery. *Numerical recipes: The art of scientific computing.* Cambridge University Press, 3rd ed edition, 2007. 130

[240] *http://maxima.sourceforge.net/download.html.* 131

[241] Lapack is a software package provided by univ. of tennessee; univ. of california, berkeley. univ. of colorado denver and nag ltd. 131

[242] B. Dorschner, F. Bösch, S. S. Chikatamarla, K. Boulouchos, and I. V. Karlin. Entropic multi-relaxation time lattice Boltzmann model for complex flows. *Journal of Fluid Mechanics*, 801:623–651, 2016. 134

[243] E. M. Viggen. Acoustic multipole sources for the lattice Boltzmann method. *Physical Review E.*, pages 1–5, 2013. 139

[244] C. Zhuo and P. Sagaut. Acoustic multipole sources for the regularized lattice Boltzmann method : Comparison with multiple-relaxation-time models in the inviscid limit. *Physical Review E.*, 063301:1–22, 2017. 139

[245] E. Achenbach. Influence of surface roughness on the cross-flow around a circular cylinder. *Journal of fluid mechanics*, 46, 1971. 147

[246] E. Achenbach. Total and local heat transfer from a smooth circular cylinder in cross-flow at high reynolds number. *International Journal of Heat and Mass Transfer*, 18, 1975. 147

[247] C. Zhang, S. Moreau, and M. Sanjosé. Turbulent flow and noise sources on a circular cylinder in the critical regime. *AIP Advances 9*, 2019. 147

[248] E. Manoha, J. Bulté, and B. Caruelle. LAGOON: An experimental database for the validation of CFD/CAA methods for landing gear noise prediction. *14th AIAA/CEAS Aeroacoustics Conference*, 2008. 156

[249] E. Manoha, J. Bulté, V. Ciobaca, and B. Caruelle. LAGOON: Further analysis of aerodynamic experiments and early aeroacoustics results. *15th AIAA/CEAS Aeroacoustics Conference*, 2009. 156, 157

[250] M. Raffel, C. Willert, and J. Kompenhans. *Particle Image Velocimetry. A practical guide*, volume 2. Springer, 1998. 157

[251] R. Beauvais. *Laser-Doppler Velocimetry (LDV).* Springer, 1994. 157

[252] S. Kai, R. Gunnar, V. János, and V. N. Peter. *Industrial Ventilation Design Guidebook.* Academic Press, 2001. 157

[253] X. Gloerfelt. Bruit Rayonné par un écoulement affleurant une cavité: simulation aéroacoustique directe et application de méthodes intégrales. *Thesis*, page 277, 2001. 158, 159, 160, 161

[254] M. J. Lighthill. On sound generated aerodynamically I. General theory. *Proceedings of the Royal Society A: Mathematical, Physical and Engineering Sciences*, 211:564–587, 1951. 158, 160, 162, 187

[255] M. J. Lighthill. On sound generated aerodynamically II. Turbulence as a source of sound. *Proceedings of the Royal Society A: Mathematical, Physical and Engineering Sciences*, 222(February), 1954. 158, 187

[256] V. Fleury, C. Bailly, E. Jondeau, M. Michard, and D. Juve. Space-time correlations in two subsonic jets using dual particle image velocimetry measurements. *AIAA Journal*, 46:2498–2509, 2008. 160

[257] C. Seror, P. Sagaut, C. Bailly, and D. Juvé. On the radiated noise computed by large-eddy simulation. *Physics of Fluids*, 13:476–487, 2001. 160

[258] C. Bogey, C. Bailly, and D. Juve. Noise Investigation of a High Subsonic,Moderate-Reynolds-Number Jet Using Compressible LES. *Theoretical and Computational Fluid Dynamics*, 16:273–297, 2003. 160

[259] M. Goldstein. *Aeroacoustics, McGraw-Hill, New York.*, 1976. 160

[260] N. Curle. The influence of solid boundaries upon aerodynamic sound. *Proceedings of the Royal Society A*, 231:505–514, 1955. 160, 162, 187

[261] H. D. L. Ffowcs Williams J E. Sound generation by turbulence and surfaces in arbitrary motion. *Philosophical Transactions of The Royal Society A Mathematical and Physical Sciences*, 264:321–342, 1969. 160, 187

[262] P. Di Francescantonio. A new boundary integral formulation for the prediction of sound radiation. *Journal of Sound and Vibration*, 202:491–509, 1997. 161

[263] K. S. Brentner and F. Farassat. Analytical comparison of the acoustic analogy and Kirchhoff formulation for moving surfaces. *AIAA Journal*, 36:1379–1386, 1998. 161

[264] F. Farassat and G. Succi. The Prediction of Helicopter Rotor Discrete Frequency Noise. *Vertica*, pages 309–320, 1983. 162

[265] F. Farassat. Derivation of Formulations 1 and 1A of Farassat. *NASA/TM-2007-214853*, 2007. 162

[266] K. Brentner. Prediction of helicopter discrete frequency rotor noise - A computer program incorporating realistic blade motions and advanced formulation. *NASA, Technical Report TM-87721*, 1986. 162

[267] D. Casalino. An advanced time approach for acoustic analogy predictions. *Journal of Sound and Vibration*, 261:583–612, 2003. 162

[268] J. Prieur and G. Rahier. Aeroacoustic integral methods, formulation and efficient numerical implementation. *Aerospace Science and Technology*, 5:457–468, 2001. 162, 188

[269] G. Rahier, J. Prieur, F. Vuillot, N. Lupoglazoff, and A. Biancherin. Investigation of integral surface formulations for acoustic post-processing of unsteady aerodynamic jet simulations. *Aerospace Science and Technology*, 8:453–467, 2004. 162, 188

[270] F. De La Puente Cerezo. *Aeroacoustic simulations of landing gears with unstructured grids and a ZDES turbulence model.* PhD thesis, 2018. 162, 164, 180, 195

[271] G. Ashcroft and X. Zhang. Optimized prefactored compact schemes. *Journal of Computational Physics*, 190(2):459 – 477, 2003. 163

[272] S. A. Hamid and B. Lakshmanan. Application of navier-stokes code PAB3D with ke turbulence model to attached and separated flows. *NASA Technical Paper 3480*, 1995. 163

[273] P. R. Spalart, K. V. Belyaev, M. L. Shur, and M. K. Strelets. On the differences in noise predictions based on solid and permeable surface Ffowcs Williams - Hawkings integral solutions. 2019. 164, 168, 187, 188, 190, 192, 199, 200, 223

[274] O. Colin and M. Rudgyard. Development of High-Order Taylor-Galerkin Schemes for LES. *Journal of Computational Physics*, 162(2):338–371, 2000. 164

[275] P. J. Schmid. Dynamic mode decomposition of numerical and experimental data. *Journal of Fluid Mechanics*, 656:5–28, 2010. 164

[276] P. J. Schmid, L. Li, M. P. Juniper, and O. Pust. Applications of the dynamic mode decomposition. *Theoretical and Computational Fluid Dynamics*, 25(1-4):249–259, 2011. 164

[277] F. Nicoud, L. Benoit, C. Sensiau, and T. Poinsot. Acoustic modes in combustors with complex impedances and multidimensional active flames. *AIAA Journal*, 45(2):426–441, 2007. 164

[278] C. Zhang, M. Sanjosé, and S. Moreau. Wall-modeled Large Eddy Simulation with adverse pressure gradients : Application to bluff bodies. *CFD Canada*, 2018. 165

[279] V. Yakhot and S. A. Orszag. Renormalization group analysis of turbulence. I. Basic theory. *Journal of Scientific Computing*, 1(1):3–51, 1986. 165

[280] J. Marie and C. Carpaye. *Contribution à la parallélisation et au passage à l'échelle du code FLUSEPA*. PhD thesis, 2016. 167

[281] B. Lessani, J. Ramboer, and C. Lacor. Efficient large-eddy simulations of low mach number flows using preconditioning and multigrid. *International Journal of Computational Fluid Dynamics*, 18:221–233, 2004. 167

[282] N. Alkishriwi, M. Meinke, and W. Schröder. A large-eddy simulation method for low Mach number flows using preconditioning and multigrid. *Computers and Fluids*, 35:1126–1136, 2006. 167

[283] A. Hajczak, L. Sanders, F. Vuillot, and P. Druault. A comparison between off and on-body control surfaces for the FW-H equation: Application to a non-compact landing gear wheel. *Journal of Sound and Vibration*, 490, 2021. 168, 170, 188, 191, 192, 200

[284] A. Hajczak, L. Sanders, F. Vuillot, and P. Druault. Investigation of the Ffowcs-Williams and hawkings analogy on an isolated landing gear wheel. *2018 AIAA/CEAS Aeroacoustics Conference*, 2018. 168

[285] P. R. Spalart. On the precise implications of acoustic analogies for aerodynamic noise at low Mach numbers. *Journal of Sound and Vibration*, 332(11):2808–2815, 2013. 168, 187, 199

[286] P. D. Welch. The use of FFT for the estimation of power spectra. *IEEE transactions on audio and electroacoustics*, 15, 1967. 170

[287] E. Achenbach. Distribution of local pressure and skin friction around a circular cylinder in cross-flow up to Re = 5 106. *Journal of Fluid Mechanics*, 34:625–639, 1968. 172

[288] R. Koch, M. Sanjosé, and S. Moreau. Large-eddy simulation of a single airfoil tip-leakage flow. *AIAA Aviation 2020 Forum*, pages 1–18, 2020. 187

[289] D. P. Lockard and J. H. Casper. Permeable surface corrections for Ffowcs Williams and Hawkings integrals. *Collection of Technical Papers - 11th AIAA/CEAS Aeroacoustics Conference*, 4:2467–2479, 2005. 187

[290] G. Rahier, M. Huet, and J. Prieur. Additional terms for the use of Ffowcs Williams and Hawkings surface integrals in turbulent flows. *Computers and Fluids*, 120:158–172, 2015. 187

[291] T. Ikeda, S. Enomoto, K. Yamamoto, and K. Amemiya. Quadrupole corrections for the permeable-surface ffowcs williams-hawkings equation. *AIAA Journal*, 55(7):2307–2320, 2017. 187

[292] T. R. Ricciardi, W. R. Wolf, N. J. Moffitt, J. R. Kreitzman, and P. Bent. Numerical noise prediction and source identification of a realistic landing gear. *Journal of Sound and Vibration*, 496:115933, 2021. 192

[293] L. F. L. Rego, L. T. L. Pereira, and F. M. Catalano. Aerodynamic and Aeroacoustic Experimental Investigation of a Simplified Nose Landing Gear. *AIAA Aerospace Sciences Meeting*, pages 1–13, 2018. 195, 200

[294] M. R. Khorrami and C. A. Branch. An Overview of Contributions for Nose Landing Gear Configuration - BANC-III Workshop Background - Gulfstream Aircraft Nose Landing Gear Model. *21st AIAA/CEAS Aeroacoustics Conference*, 2015. 221

[295] G. Pont. *Self adaptive turbulence models for unsteady compressible flows Modèles de turbulence auto-adaptatifs pour la simulation des ecoulements compressibles instationnaires*. PhD thesis, 2016. 225

[296] M. Geier, A. Greiner, and J. G. Korvink. Bubble functions for the lattice Boltzmann method and their application to grid refinement. *The European Physical Journal Special Topics*, 171:173–179, 2009. 225

[297] S. Deck and R. Laraufie. Numerical investigation of the flow dynamics past a three-element aerofoil. *Journal of Fluid Mechanics*, 732:401–444, 2013. 225